INSTITUTO SUPERIOR DE ENGENHARIA DO PORTO
MESTRADO EM ENGENHARIA MECÂNICA




Análise Não Linear de Estruturas Metálicas Industriais Utilizando Técnicas Computacionais

HUGO DANIEL PEREIRA TORRES
outubro de 2025

POLITÉCNICO
DO PORTO

ISEP INSTITUTO SUPERIOR DE ENGENHARIA DO PORTO

Nonlinear Analysis of Industrial Frame Structures Using Computational Techniques

Hugo Daniel Pereira Torres

Dissertation for the attainment of the Master's degree in Mechanical Engineering, Specialization Area in Mechanical Constructions

Supervisor: Professor Jorge Américo de Oliveira Pinto Belinha, PhD

Jury:
President: Professor Hernâni Miguel Reis Lopes, PhD, ISEP
Member of the Committee: Professor Daniel do Espírito Santo Rodrigues, PhD, UA
Supervisor: Professor Jorge Américo de Oliveira Pinto Belinha, PhD, ISEP

Porto, October 2025

Dedication

To my loving uncle Casimiro, the best person I will ever meet. You left us too soon, however you'll always be between with us.

Aknowledgemnts

The completion of this thesis would not have been possible without the help, guidance, and support of many individuals.

I would like to express my gratitude to my supervisor, Professor Jorge Américo de Oliveira Pinto Belinha, for his various recommendations, teachings, and patience. His unique insight was immensely valuable to the understanding, problem-solving, and completion of this work.

For my parents, José Carlos Oliveira Torres and Maria Emília Pereira do Couto, I want to thank them for all the life-teaching moments, sacrifices, and life-enforcing encouragements. Without them, I would have tripped many more times in this journey called life, and I wouldn't learn to get up and move forward.

To my brother and girlfriend for their important presence, even though I can love you and get very frustrated with you. Thankfully, my frustration can be as quick as the wind, and only affects one at a time.

And finally, to all my friends who helped me distract from the day-to-day problems and stress.

To all who have contributed, in some way, to the realization of this work, I salute you. My appreciation will be eternal and always with you.

Abstract

Industrial frame structures, such as those used in manufacturing plants and warehouses, are often subjected to a wide range of loading conditions, including static and dynamic loads. These structures are also subject to various forms of nonlinear behavior, including geometric and material nonlinearities. The accurate analysis of these structures is crucial for ensuring their safety and performance. In recent years, computational techniques have become increasingly popular for the analysis of industrial frame structures due to their ability to model complex behavior and failure modes such as buckling and yielding.

In this study, the computation analysis method selected is the meshless method and the mechanical state in focus is the nonlinearity in an industrial frame structure. To fully understand the present work, we begin by studying meshless methods and elastoplasticity.

In this work, 2D and 3D simple beams and more complex structures are studied using meshless methods and elasto-plastic material assumptions.

The results of the analysis provide insight into the behavior of industrial frame structures under various loading conditions. The study will also highlight the potential advantages of meshless methods in the analysis of complex structures, such as the ability to model geometric nonlinearities, the ability to accurately predict failure modes, and the potential for further research in this area.

KEYWORDS: Meshless Methods; Finite Element Methods; Nonlinear Deformation; Elastoplasticity; Radial Point Interpolation Method; Natural Neighbour Radial Point Interpolation Method.

Resumo

Estruturas de pórtico industriais, como as utilizadas em fábricas e armazéns, são frequentemente sujeitas a uma vasta gama de condições de carga, incluindo cargas estáticas e dinâmicas. Estas estruturas estão também sujeitas a várias formas de comportamento não linear, incluindo não linearidades geométricas e materiais. A análise precisa destas estruturas é crucial para garantir a sua segurança e desempenho. Nos últimos anos, as técnicas computacionais tornaram-se cada vez mais populares para a análise de estruturas de pórtico industriais devido à sua capacidade de modelar comportamentos complexos e modos de falha como a encurvadura e a cedência.

Neste estudo, a ferramenta de análise computacional escolhida é o método sem malha e o estado mecânico em foco é a não linearidade numa estrutura de pórtico industrial. Assim, para compreender plenamente o trabalho realizado, começaremos por estudar os métodos sem malha e a elastoplasticidade.

Neste trabalho, vigas simples 2D e 3D e estruturas mais complexas são estudadas usando métodos sem malha e pressupostos de material elastoplástico.

Os resultados da análise fornecem uma visão sobre o comportamento de estruturas de pórtico industriais sob várias condições de carga. O estudo também destacará as potenciais vantagens dos métodos sem malha na análise de estruturas complexas, como a capacidade de modelar não linearidades geométricas, a capacidade de prever com precisão os modos de falha e o potencial para futuras investigações nesta área.

PALAVRAS-CHAVE: Método sem Malha; Método de Elementos Finitos; Deformação Não Linear; Elastoplasticidade; Método de Interpolação Radial de Pontos; Método de Interpolação Radial de Pontos com Vizinhos Naturais.

Index

List of Figures

List of Tables

Acronyms and Symbols

List of Acronyms

ANM Asymptotic Numerical Method

EFG Element Free Galerkin

FEM Finite Element Method

GFDM Generalized Finite Difference Method

ISEP Instituto Superior de Engenharia do Porto

MFEM Meshless Finite Element Method

MLPG Meshless Local Petrov-Galerkin

MLS Moving Least-Squares

NNFEM Natural Neighbor Finite Element Method

NNRPIM Natural Neighbor Radial Point Interpolation Method

OSD Optimal Sampling Density

P.PORTO Instituto Politécnico do Porto

PIM Point Interpolation Method

RKPM Reproducing Kernel Particle Method

RNEM Radial Natural Element Method

RPIM Radial Point Interpolation Method

SHP Smooth Particle Hydrodynamics

1 Introdution

In this work, we present a thorough examination of the application and comparative results from meshless methods to finite element method (FEM), with the meshless methods being the radial point interpolation method (RPIM) and natural neighbor radial point interpolation method (NNRPIM). This study comprises linear and nonlinear study cases, which were run using FEMAS software. The engineering world is constantly seeking more precise and economic solutions and while the FEM is being the industry standard for many years, the meshless methods can position themselves as a possible competitor to the FEM.

1.1 Meshless Methods

Meshless methods have been significantly developed since the late 20^{th} century, which makes them an alternative to the older FEM, having the possible advantages of lower computational times and the ability to simulate more precisely, complex geometries[8, 9, 10]. Meshless methods differ from the FEM because the FEM problem domain is related to the elements while the meshless methods problem domain is related to the surrounding nodes[4].

There are several meshless methods, some examples are:

- Smooth Particle Hydrodynamics (SHP), first created to resolve complex physics problems and later adapted to resolve mechanical simulations[11, 12, 13, 14];
- Element Free Galerkin (EFG), one of the first weak form meshless methods[15];
- Moving Least-Squares (MLS)[16];
- Reproducing Kernel Particle Method (RKPM)[17];
- Meshless Local Petrov-Galerkin (MLPG)[18];
- Generalized Finite Difference Method (GFDM)[19];
- Asymptotic Numerical Method (ANM)[20];
- Optimal Sampling Density (OSD)[21],

these are just some of the meshless methods examples.

In meshless methods, the Kronecker delta property, a mathematical property of the shape function, allows us to impose, directly, the boundary conditions values. The meshless methods work using approximation functions; because of this, the Kronecker delta property can not be satisfied, which has forced a new generation of meshless methods to emerge that use interpolation functions.[12, 22, 23, 4]. This new meshless method generation was born to overtake this obstacle:

- Point Interpolation Method (PIM)[24, 25];
- Radial Point Interpolation Method (RPIM)[26, 27];
- Natural Neighbor Finite Element Method (NNFEM)[28, 29];
- Meshless Finite Element Method (MFEM)[30];
- Radial Natural Element Method (RNEM)[31, 32];
- Natural Neighbor Radial Point Interpolation Method (NNRPIM)[33, 34].

1.1.1 Radial Point Interpolation Method (RPIM)

The RPIM is a meshless method with the ability to solve partial differential equations from unstructured nodes[27]. With RPIM the approximation function passes through every node in the influence domain, which makes it easier to implement the boundary conditions[27]. In complex and irregular structures, RPIM has the ability to offer potentially more accurate results comparable to FEM[27].

1.1.2 Natural Neighbour Radial Point Interpolation Method (NNRPIM)

The meshless method NNRPIM utilizes the RPIM concept, combined with the natural neighbour method where background integration is achieved through Voronoi Diagrams[4]. Although the NNRPIM is a relatively recent meshless method, it has already been applied in diverse computational mechanical fields, like isotropic and orthotropic static analysis, grade material plate analysis, 3D shell approach, and more[35, 36, 37, 38, 39]. One of the most popular field applications of the NNRPIM is the solid mechanical problem[36, 40, 41]. In this field, the NNRPIM has performed the most variant types of studies, including studies addressing large deformations and bone tissue remodeling[33, 34].

1.2 Purpose of the Thesis

The purpose of this thesis is to study the nonlinearity, in an industrial frame structure, using meshless methods computational techniques. To achieve this, several representative examples are analyzed to validate and corroborate the software used and the different methods in question. After the required confirmations, the nonlinearity of an industrial frame structure is analyzed. To all the different simulations elaborated in this work, the stress, strain, displacement, are analyzed and, with the exception of the linear state analysis, the plastic strain.

1.3 Thesis Structure

Structurally, this thesis is divided into 9 chapters, being this introduction the first one. Chapter 2presents meshless methods, explaining their mechanical and mathematical formulations. In the next chapter 3, the solid mechanics and their applications in the meshless methods are shown. Chatper 4 presents a literature review of the meshless methods applications in solid mechanics problems. Chapter 5 examines the results of several linear analyses, in a standard beam, with different mesh sizes and types. From chapters 6 to 8 the nonlinear analysis in different cases are examined, in chapter 6 the nonlinear analysis in the standard Cook's Membrane and different beams in 2D and 3D is applied, ending it with a comparative study of the same beam simulations in the different dimensions. In the following chapter 7, the goal is to prove the accuracy of the software in use, and in this way validate it. In conclusion, chapters 8 and 9 are to study an industrial frame structure nonlinear analysis and the thesis's conclusion, respectively.

2 Meshless Methods

When studying a meshless method problem, the approach consists of the following[1]:

1. studying the problem's geometry, the solid domain;
2. identify the essentials and natural boundary conditions;
3. numerical discretizing the domain and boundary, by a nodal set (this can be regular or irregularly distributed)[1].

In recent years, meshless methods have emerged as an alternative to the already existing and older, FEM[42].

2.1 Meshless Methods' Introduction

To understand what a meshless method is and how it works, we have to attain the notions of the solid domain and nodal discretization[1].

By examining the figure 2.1**(a)** we can visualize an example of a solid domain, a solid domain can be understood as the space that the solid domain is taken up, in other words, by the space occupied by the solid[1]. There are 2 types of nodal discretization, the first one is visible in figure 2.1**(b)** and it is the regular nodal distribution[1]. The second nodal distribution is irregular and it is called irregular nodal distribution, and can be observed in figure 2.1**(c)**[1]. Analysing the figure 2.1 is visible, an arbitrary distribution with a greater nodal concentration in areas that require more attention, like boundary conditions and complex or discontinuous geometries[1].

In the meshless methods, the nodal density and spatial distribution are critical and directly correlate with the computer performance necessary, as well as the results' reliability [1]. A more accurate result can be obtained with an notable nodal distribution, however, it also has the necessity of requiring more computational power, where these computational costs has a direct correlation with the number of nodes used, however, the same can not be affirmed for the results' accuracy, in fact, if we have an unbalanced nodal's distribution the accuracy of the results will decrease [1].

The nodal connectivity of the FEM is defined by 'elements', on the other hand, the meshless methods are known for not resorting to 'elements' [1]. The shape and size of the influence domain have an enormous impact on the result's quality [1]. The course of action that produces the best results depends on the meshless method used, as we will examine in subchapter 2.2[1].

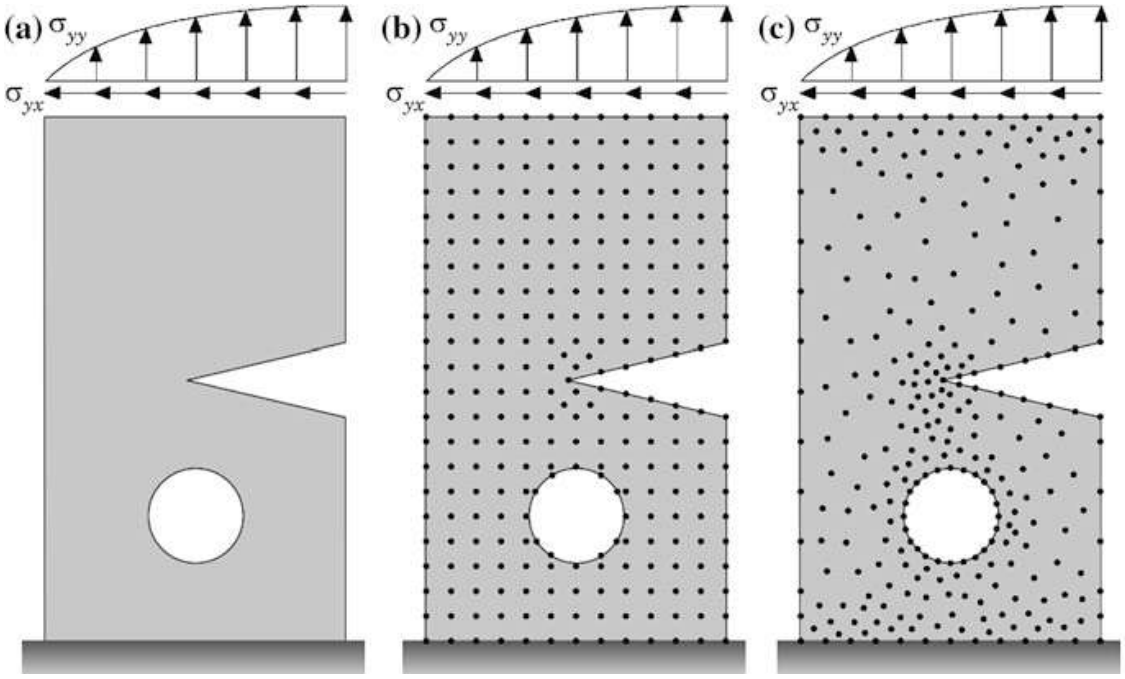

Figure 2.1: **(a)** Solid domain; **(b)** Regular nodal discretization; **(c)** Irregular nodal discretization.[1]

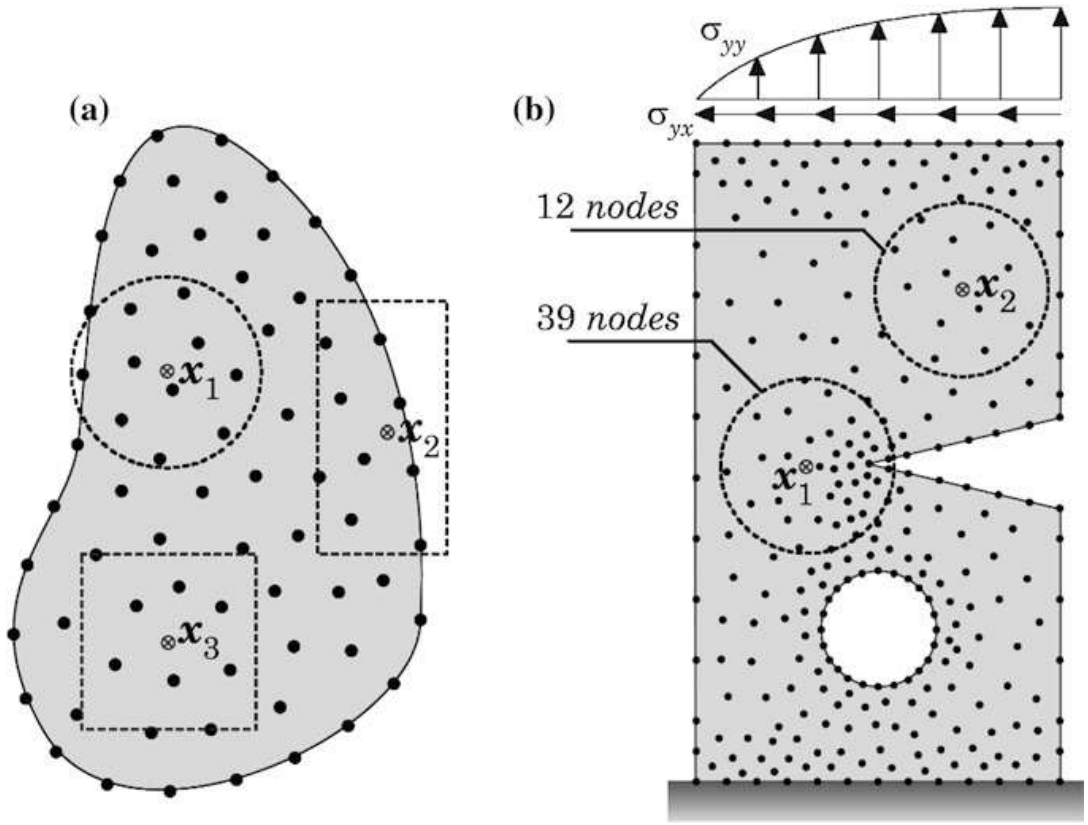

Figure 2.2: **(a)** Example of an interest domain with different size and shapes **(b)** Example of a poor choice of influence domain[1]

In figure 2.2 we can observe 2 examples of how the influence domain shouldn't be chosen, in example **(a)** we can observe that the influence domains are all with different shapes[1]. In example **(b)** we can clearly see that the number of nodes existing inside the 2 different influence domains is very different [1].

The field variable can be approximated as follows. The displacement components $u_I = (u_x, u_y, u_z)$ of any interest point $\boldsymbol{x_I}$ in the problem domain are, approximated using the displacement nodes inside the influence domain[1]:

$$\boldsymbol{u}(\boldsymbol{x_I}) = \sum_{i=1}^{n} \boldsymbol{\varphi_i}(\boldsymbol{x_I})\boldsymbol{u}(\boldsymbol{x_i}) \tag{2.1}$$

were n is the number of nodes inside the influence domain in question, $\boldsymbol{u}(\boldsymbol{x_i})$ is the displacement of its node inside the influence domain, and $\boldsymbol{\varphi_i}(\boldsymbol{x_I})$ is the approximation of interpolation functions value of i^{th} node inside the influence-domain[1].

2.2 Nodal Connectivity

2.2.1 Influence Domain

The influence domain can be generated by searching a determined number of nodes inside the fixed area or volume[1]. As previously discussed in the previous subchapter 2.1, the size and shape of the influence domain have a very important and significant impact on the final results and their accuracy, for that reason, all the influence domains must have the same, or at least an approximated, number of nodes[1].

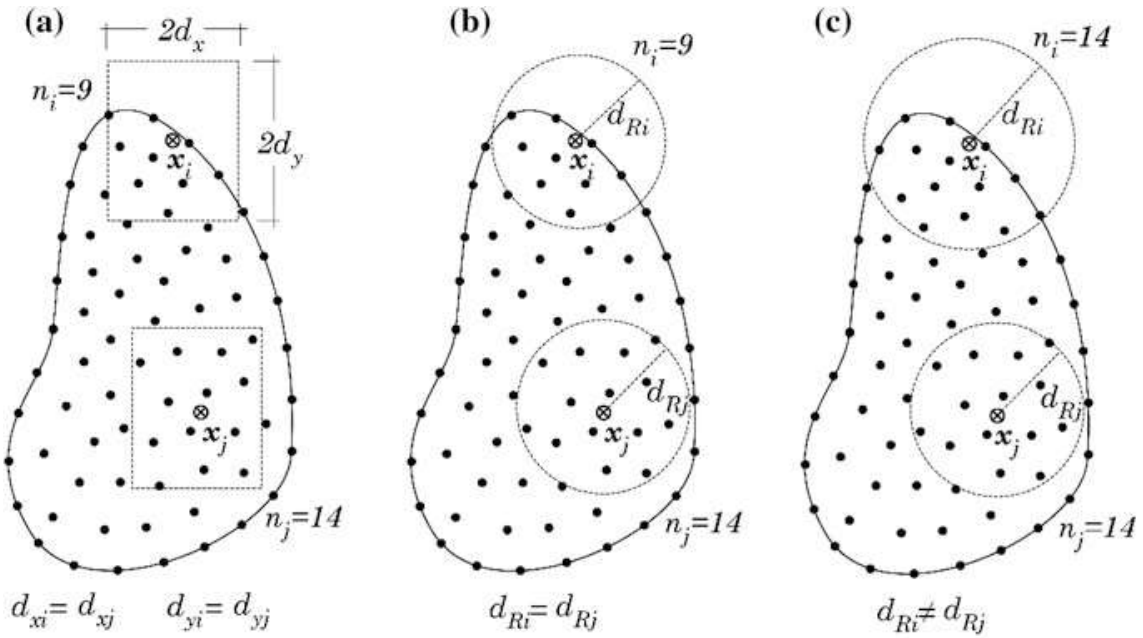

Figure 2.3: **(a)** Fixed rectangular shape with different number of nodes inside the influence-domain, **(b)** Fixed circular shape with different number of nodes inside the influence-domain, **(c)** Adjustable circular shape with a fixed number of nodes inside the influence-domain[1]

Independently of the technique of the meshless method used, the number of nodes inside the influence domain must be between 9 and 16; these numbers were proposed by previous works of literature [1]. The influence domain is a key parameter applied in the RPIM technique[1].

In figure 2.3 **(a)** and **(b)**, we can observe two influence domains that have the same shape and the same size, with different nodes inside. On the other hand, we can also see in **(c)** an example of two influence domains with the same number of nodes, but different sizes, which will provide a much better option for simulations with meshless methods[1].

2.2.2 Influence Cells

In 2007, a team led by Jorge Belinha presented a new method to establish influence-domains in meshless methods[1]. This new method determines these domains based on Delaunay triangulation and Voronoï diagrams, instead of using blind influence domain.[1] These parameters (influence cells) work in the NNRPIM technique[1].

Contrary to the blind methods that are related to the radial distances, influence cells are applicable in any Euclidean space[1]. There are two types of influence cells, as we can see in the figure 2.4[1]:

a) First-degree neighbourhood;

b) Second-degree neighbourhood.

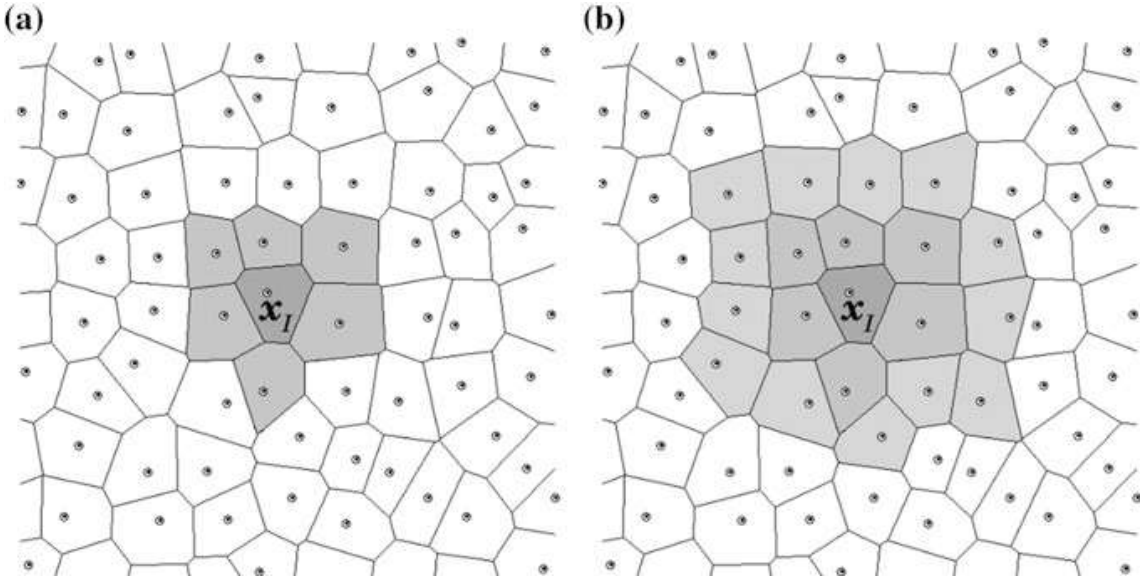

Figure 2.4: **(a)** First degree of influence cells, **(b)** Second degree of influence cells[1]

Because the influence cells with the second degree of the neighborhood influence has more cells, it's natural that these types of influence cells provide better results[1].

2.3 Radial Point Interpolators

The radial point interpolation functions are obtained using a combination of elemental radial functions with polynomial functions[1, 43].

2.3.1 Radial Point Interpolation Methods

Considering T as a space function defined in the analysis domain $\Omega \subset \mathbb{R}^d$, and T^h as the finite dimension space $T^h \subset T$ were $T^h := \langle r(\boldsymbol{x}-\boldsymbol{x}_i) : i \in \mathbb{N} \wedge i \leq N \rangle + p_m(\boldsymbol{x})$ where $r : \mathbb{R}^d \mapsto \mathbb{R}$ and $p_m : \mathbb{R}^d \mapsto \mathbb{R}$ is characterised as a polynomial of degree smaller that m [1, 43]. The nodal set is defined in $\boldsymbol{X} = \{\boldsymbol{x}_1, \boldsymbol{x}_2, ..., \boldsymbol{x}_N\} \in \Omega \wedge \boldsymbol{x}_i \in \mathbb{R}^d$ and discretization by $N_I = \{n_1, n_2, ..., n_N\}$ [1, 43]. To calculate the $\boldsymbol{X}$ density, the following equation is used:

$$h = min\|\boldsymbol{x}_j - \boldsymbol{x}_i\|, \forall\{i,j\} \in : \{i,j\} \leq N \wedge i \neq j \tag{2.2}$$

being $\|.\|$ the Euclidean norm [43].

The interpolation function $u^h(\boldsymbol{x}) \in T$ passes through all nodes existent in the influence domain, and is calculated using the equation[1, 44]:

$$u^h = \sum_{i=1}^{n} r_i(\boldsymbol{x_I})a_i + \sum_{j=1}^{m} p_j(\boldsymbol{x_I})b_j = \mathbf{r}(\boldsymbol{x_I})^T\mathbf{a} + \mathbf{p}(\boldsymbol{x_I})^T\mathbf{b} = u(\boldsymbol{x_I}) \tag{2.3}$$

where a_i and b_i are the non-constants of $r_i(\boldsymbol{x_I})$ and $p_j(\boldsymbol{x_I})$ respectively, n is the number of nodes inside the support-domain and m is the number of monomials of the polynomial basis $p_j(\boldsymbol{x_I})$ [1, 43]. The vectors are characterised as:

$$\mathbf{a}^T = \{a_1, a_2, ..., a_n\} \tag{2.4}$$

$$\mathbf{b}^T = \{b_1, b_2, ..., b_m\} \tag{2.5}$$

$$\mathbf{r}(\mathbf{x})^T = \{r(\mathbf{x})_1, r(\mathbf{x})_2, ..., r(\mathbf{x})_n\} \tag{2.6}$$

$$\mathbf{p}(\mathbf{x})^T = \{p(\mathbf{x})_1, p(\mathbf{x})_2, ..., p(\mathbf{x})_m\} \tag{2.7}$$

where $\boldsymbol{x}_i$ can be characterized by $\mathbf{x}_i = \{x_i, y_i\}$ [1, 43]. This way, the radial basis function can be defined as,

$$\begin{gathered}\mathbf{r}(\mathbf{x}_I) = \{r_1(\mathbf{x}_I) \quad r_2(\mathbf{x}_I) \quad ... \quad r_n(\mathbf{x}_I)\}^T = \\ \{r(\boldsymbol{x}_1 - \boldsymbol{x}_I) \quad r(\boldsymbol{x}_2 - \boldsymbol{x}_I) \quad ... \quad r(\boldsymbol{x}_n - \boldsymbol{x}_I)\}^T\end{gathered} \tag{2.8}$$

were we can find in the literature various ways to calculate $r(\boldsymbol{x}_I)$, as for example the Multiquadric Radial Basis Function [1]:

$$\mathbf{r}_i(\mathbf{x}_I) = (d_{iI}^2 + (\gamma d_a)^2)^p \tag{2.9}$$

the Gaussian function[1]:

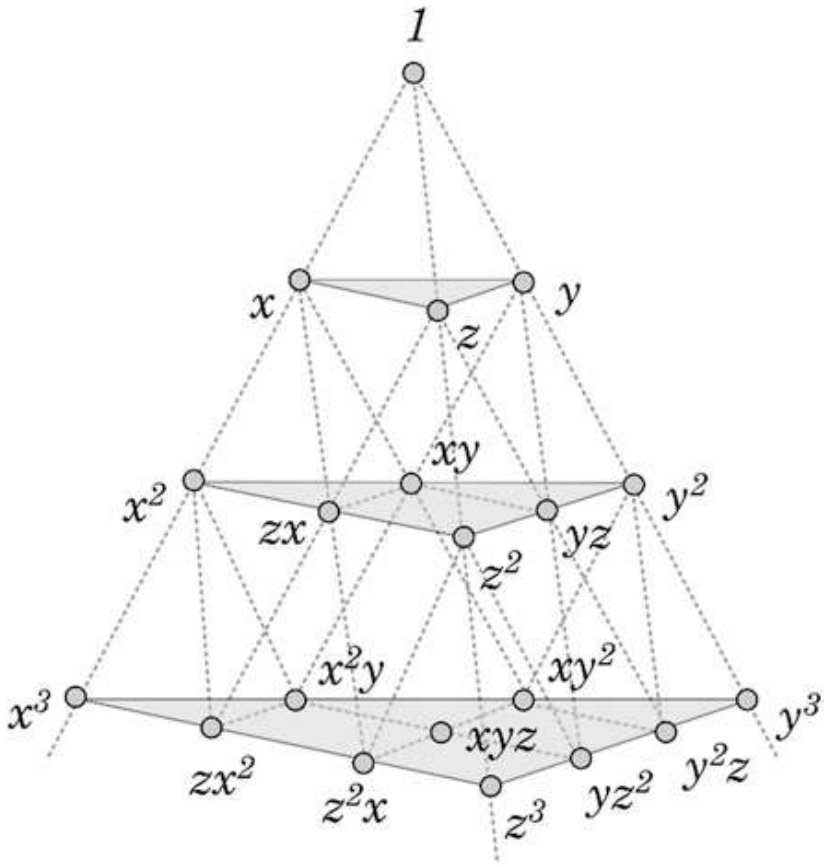

Figure 2.5: Pascal Triangle [1]

$$\mathbf{r}_i(\mathbf{x}_I) = e^{(-\gamma(d_{iI}/d_a)^2)} \tag{2.10}$$

and the thin plate spline function[1]:

$$\boldsymbol{r}_i(\boldsymbol{x}_I) = d_{iI}^p \tag{2.11}$$

were γ and p represent shape parameters, d_a the size coefficient and x_I represents the influence size of the interest [1].

As we can see by the equation 2.2, the only variable is the Euclidean norm that can be defined by d_{iI} and calculated by:

$$d_{iI} = \sqrt{(x_i - x_I)^2 + (y_i - y_I)^2 + (z_i - z_I)^2} \tag{2.12}$$

which represents the distance between the field node and the interesting point, in a 3-dimensional space[1].

Initially, the RPIM formulation had the need to be a complete polynomial basic function, which means that for 1 dimension we have the [1]:

$$\mathbf{p}(\mathbf{x}_I)^T = \{1 \quad x_I \quad x_I^2\} \tag{2.13}$$

for 2 dimensions the equation is [1]:

$$\mathbf{p}(\mathbf{x}_I)^T = \{1 \quad x_I \quad y_I \quad x_I^2 \quad x_I y_I \quad y_I^2\} \tag{2.14}$$

and finally, for 3 dimensions [1]:

$$\mathbf{p}(\mathbf{x}_I)^T = \{1 \quad x_I \quad y_I \quad z_I \quad x_I^2 \quad x_I y_I \quad y_I^2 \quad y_I z_I \quad z_I^2 \quad z_I x_I\} \tag{2.15}$$

by analysing the 3 different equations, we can observe that for 1 dimension $m = 3$, for 2 dimensions $m = 6$, and for 3 dimensions $m = 10$, where m represents the term's number[1].

The figure 2.5 is a great example that helps understand the different numbers of terms depending on the number of dimensions[1]. Let's assume that inside the influence domain are k number of nodes, and to enforce that the interpolation passes through all of them, we determined the a_i and b_j in a way that enforced it[43]. The interpolation function is[1, 43, 45, 46]:

$$\mathbf{u}^h(\boldsymbol{x}_I) = \sum_{i=1}^{n} \mathbf{r}_i(\boldsymbol{x}_i - \boldsymbol{x}_I)\mathbf{a}_i(x_I) + \sum_{j=1}^{m} \mathbf{p}_j(\boldsymbol{x}_I)\mathbf{b}_j(\boldsymbol{x}_I) = u(\boldsymbol{x}_1) \tag{2.16}$$

and in the matrix form as,

$$\mathbf{u}^h(\mathbf{x}) = \begin{Bmatrix}\mathbf{r}(\mathbf{x})^T & \mathbf{p}(\mathbf{x})^T\end{Bmatrix} \begin{Bmatrix}\mathbf{a}(\mathbf{x}) \\ \mathbf{b}(\mathbf{x})\end{Bmatrix} \tag{2.17}$$

The computations of the shape function can be written in a matrix form[1, 47]:

$$\begin{bmatrix}\mathbf{R} & \mathbf{P} \\ \mathbf{P}^T & \mathbf{Z}\end{bmatrix} \begin{Bmatrix}\mathbf{a}(\mathbf{x}_I) \\ \mathbf{b}(\mathbf{x}_I)\end{Bmatrix} = \mathbf{M}_T \begin{Bmatrix}\mathbf{a}(\mathbf{x}_I) \\ \mathbf{b}(\mathbf{x}_I)\end{Bmatrix} = \begin{Bmatrix}\mathbf{u}^h(\mathbf{x}) \\ \mathbf{z}_P\end{Bmatrix} \tag{2.18}$$

where $\mathbf{R}$ is the radial moment matrix, $\mathbf{M}_T$ is the total moment matrix and $\mathbf{Z}$ is a null matrix that can be defined by $Z_{ij} = 0, \forall\{\{i, j\} \in: \{i, j\} \leq m\}$ and $\mathbf{P}$ can be presented in a matrix form [1, 43, 48, 49]:

$$\mathbf{P}^T = 0 \tag{2.19}$$

$$\mathbf{R} = \begin{Bmatrix} r_1(x_1, y_1, z_1) & r_1(x_2, y_2, z_2) & \cdots & r_1(x_n, y_n, z_n) \\ r_2(x_1, y_1, z_1) & r_2(x_2, y_2, z_2) & \cdots & r_2(x_n, y_n, z_n) \\ \vdots & \vdots & \ddots & \vdots \\ r_n(x_1, y_1, z_1) & r_n(x_2, y_2, z_2) & \cdots & r_n(x_n, y_n, z_n) \end{Bmatrix} \tag{2.20}$$

$$\mathbf{P} = \begin{Bmatrix} p_1(x_1, y_1, z_1) & p_2(x_1, y_1, z_1) & \cdots & p_m(x_1, y_1, z_1) \\ p_1(x_2, y_2, z_2) & p_2(x_2, y_2, z_2) & \vdots & p_m(x_2, y_2, z_2) \\ \vdots & \vdots & \ddots & \vdots \\ p_1(x_n, y_n, z_n) & p_2(x_n, y_n, z_n) & \cdots & p_m(x_n, y_n, z_n) \end{Bmatrix} \tag{2.21}$$

Because the distance is directionless, it follows that $r_i(x_j, y_j, z_j) = r_j(x_i, y_i, z_i)$ which implies that $R_{ij} = R_{ji}$. Consequently, by obtaining the inverse of the moment matrix $\mathbf{M}_T$, the interpolation function can ultimately be derived as follows[1, 43, 45]:

$$\begin{Bmatrix}\mathbf{a}(\mathbf{x}_I) \\ \mathbf{b}(\mathbf{x}_I)\end{Bmatrix} = \mathbf{M}_T^{-1} \begin{Bmatrix}\mathbf{u}_s \\ \mathbf{z}\end{Bmatrix} \tag{2.22}$$

$$\begin{aligned}\boldsymbol{u}^h(x_I) &= \begin{bmatrix}\boldsymbol{r}(\boldsymbol{x}_I)^T & \boldsymbol{p}(\boldsymbol{x}_I)^T\end{bmatrix}\begin{bmatrix}\boldsymbol{a}(\boldsymbol{x}_I)\\ \boldsymbol{b}(\boldsymbol{x}_I)\end{bmatrix}\\ &= \begin{bmatrix}\boldsymbol{r}(\boldsymbol{x}_I)^T & \boldsymbol{p}(\boldsymbol{x}_I)^T\end{bmatrix}\boldsymbol{M}_T^{-1}\begin{bmatrix}\boldsymbol{u}_s\\ \boldsymbol{z}\end{bmatrix}\\ &= \begin{bmatrix}\boldsymbol{\varphi}(\boldsymbol{x}_I)^T & \boldsymbol{\Psi}(\boldsymbol{x}_I)^T\end{bmatrix}\begin{bmatrix}\boldsymbol{u}_s\\ \boldsymbol{z}\end{bmatrix}\end{aligned} \tag{2.23}$$

with the interpolation function vector $\varphi(x_I)^T$ defined as[1]:

$$\boldsymbol{\varphi}(\mathbf{x}_I)^T = \begin{Bmatrix}\varphi_1(\boldsymbol{x}_I) & \varphi_2(\boldsymbol{x}_I) & \cdots & \varphi_n(\boldsymbol{x}_I)\end{Bmatrix} \tag{2.24}$$

and the byproduct vector Ψ defined as[1]:

$$\boldsymbol{\Psi}(\mathbf{x}_I)^T = \begin{Bmatrix}\Psi_1(\boldsymbol{x}_I) & \Psi_2(\boldsymbol{x}_I) & \cdots & \Psi_m(\boldsymbol{x}_I)\end{Bmatrix} \tag{2.25}$$

Since

$$\boldsymbol{u}^h(\boldsymbol{x}_I) = \boldsymbol{\varphi}(\boldsymbol{x}_I)^T\boldsymbol{u}_s \tag{2.26}$$

in order to be possible to compute the partial derivatives of the interpolation field variables, we need to use a variable ζ, and assume $\zeta = x$ or $\zeta = y$, which can be determined with the expression[1]:

$$\begin{Bmatrix}\boldsymbol{\varphi}(\mathbf{x}_I)^T_{,\zeta} & \boldsymbol{\Psi}(\mathbf{x}_I)^T_{,\zeta}\end{Bmatrix} = \begin{Bmatrix}\mathbf{r}(\mathbf{x}_I)^T_{,\zeta} & \mathbf{p}(\mathbf{x}_I)^T_{,\zeta}\end{Bmatrix} M_T^{-1} \tag{2.27}$$

The first-order partial derivative of the RBF vector is defined by[1]:

$$\frac{\partial r_i(\boldsymbol{x}_I)}{\partial\zeta} = -2p(\zeta_i - \zeta_I)(d_{iI}^2 + (\gamma d_c)^2)^{p-1} \tag{2.28}$$

3 Solid Mechanics

In this chapter, we will discuss and study the mechanics' equations and behaviors, with the purpose of transitioning to elastoplasticity, nonlinearity, and computational mechanics. These will help us understand the work that will be presented.

3.1 Fundamental Equations

When a solid is under a load, it is automatically under stress, which in terms generates a deformation [2]. The Solid Mechanics field defines the tensions and deformations in a single solid point[1, 2].

There are 2 types of boundaries we need to consider when analyzing a solid as shown in the example of the figure 3.1[1, 2]:

1. essential boundary;
2. natural boundary.

In the essential boundary, we relate displacement imposition with an impediment, and in the natural border, the relationship is with force or loads imposition [2]. By analysing the figure 3.1 we can define Γ_t as a natural boundary and Γ_u as an essential boundary. Considering P as a point (with infinitesimal volume) inside the domain Γ with dimensions $dx \cdot dy \cdot dz$ [2, 50].

We can define the stress tensor with the expression[1, 2, 51]:

$$\mathbf{\Lambda} = \begin{bmatrix} \sigma_{xx} & \tau_{xy} & \tau_{xz} \\ \tau_{yx} & \sigma_{yy} & \tau_{yz} \\ \tau_{zx} & \tau_{zy} & \sigma_{zz} \end{bmatrix} \quad \wedge \quad \sigma_{ij} = \sigma_{ji} \quad if \quad i \neq j \tag{3.1}$$

with can also be represented in the vector form[1, 2, 50, 51]:

$$\boldsymbol{\sigma} = \begin{Bmatrix} \sigma_{xx} & \sigma_{yy} & \sigma_{zz} & \tau_{xy} & \tau_{yz} & \tau_{zx} \end{Bmatrix}^T \tag{3.2}$$

and because the strain field ε has a direct correlation with the stress field, we can define the strain as[1, 2, 50, 52, 51]:

$$\boldsymbol{\varepsilon} = \begin{Bmatrix} \varepsilon_{xx} & \varepsilon_{yy} & \varepsilon_{zz} & \gamma_{xy} & \gamma_{yz} & \gamma_{zx} \end{Bmatrix}^T \tag{3.3}$$

where,

$$\begin{array}{ll} \varepsilon_{xx} = \frac{\partial u}{\partial x} & \gamma_{xy} = \frac{\partial u}{\partial y} + \frac{\partial v}{\partial x} \\ \varepsilon_{yy} = \frac{\partial v}{\partial y} & \gamma_{yz} = \frac{\partial v}{\partial z} + \frac{\partial w}{\partial y} \\ \varepsilon_{zz} = \frac{\partial w}{\partial z} & \gamma_{zx} = \frac{\partial u}{\partial z} + \frac{\partial w}{\partial x} \end{array} \tag{3.4}$$

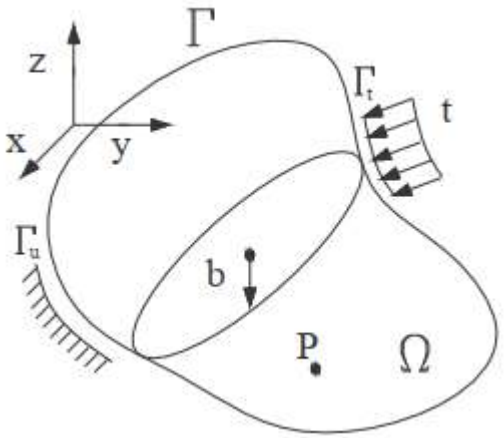

Figure 3.1: Solid volume with the domain Ω , surface Γ, force of volume b , field force t, surface where the field force is applied Γ_t and displacement area stopper Γ_u [2]

and where u is the displacements in the direction x, v is the displacement in the direction y and w are the displacement in the direction z[1, 2].

Another way to define displacement is referring to the differential operator L and to the displacement field vector u[1, 2, 51, 52]:

$$\boldsymbol{\varepsilon} = \mathbf{Lu} \tag{3.5}$$

where

$$\mathbf{L} = \begin{Bmatrix} \frac{\partial}{\partial x} & 0 & 0 & \frac{\partial}{\partial y} & 0 & \frac{\partial}{\partial z} \\ 0 & \frac{\partial}{\partial y} & 0 & \frac{\partial}{\partial x} & \frac{\partial}{\partial z} & 0 \\ 0 & 0 & \frac{\partial}{\partial z} & 0 & \frac{\partial}{\partial y} & \frac{\partial}{\partial x} \end{Bmatrix}^T \tag{3.6}$$

and

$$\mathbf{u} = \begin{Bmatrix} u \\ v \\ w \end{Bmatrix} \tag{3.7}$$

Using Hook's Law, we are capable of establishing a relationship between the strain and stresses, using the equation[4, 2]:

$$\boldsymbol{\sigma} = \boldsymbol{c\epsilon} \tag{3.8}$$

being $\mathbf{c}$ the matrix, obtained experimentally, of the material constants, we can affirm that[2]:

$$\boldsymbol{\epsilon} = \boldsymbol{s\sigma} \tag{3.9}$$

and being $\mathbf{c}^{-1} = \mathbf{s}$, its possible to define the $\mathbf{s}$ matrix[2]:

$$\mathbf{s} = \begin{bmatrix} \frac{1}{E_x} & -\frac{\upsilon_{yx}}{E_y} & -\frac{\upsilon_{zx}}{E_z} & 0 & 0 & 0 \\ -\frac{\upsilon_{xy}}{E_x} & \frac{1}{E_y} & -\frac{\upsilon_{zy}}{E_z} & 0 & 0 & 0 \\ -\frac{\upsilon_{xz}}{E_x} & -\frac{\upsilon_{yz}}{E_y} & \frac{1}{E_z} & 0 & 0 & 0 \\ 0 & 0 & 0 & \frac{1}{G_{xy}} & 0 & 0 \\ 0 & 0 & 0 & 0 & \frac{1}{G_{yz}} & 0 \\ 0 & 0 & 0 & 0 & 0 & \frac{1}{G_{zx}} \end{bmatrix} \tag{3.10}$$

The former equation is dependent on nine constants ($E_x, E_y, E_z, \upsilon_{xy}, \upsilon_{yz}, \upsilon_{zx}, G_{xy}, G_{yz}, G_{zx}$), that are obtained by experiments and uniquely dependent from the material[2]. These nine constants belong to 3 well-known material characteristics[2]:

1. E is Young's modulus;
2. υ is the Poisson coefficient;
3. G is the shear modulus.

These formulations are valid for linear deformation; however, when we study nonlinear deformation are other factors that need consideration.

3.2 Elastoplasticity

Nonlinear deformation occurs when the material is subject to a stress exceeding its yield stress, resulting in a permanent (unrecoverable) deformation[3]. Exist two tips of nonlinear deformations [3]:

1. nonlinear in the elastic region;
2. nonlinear in the plastic region.

In figure 3.2**(a)** it is possible to see two diagrams that show the behavior of two different materials in terms of stress-strain.

In material **(a)** is possible to observe 3 different regions [3]:

1. elastic region, where the deformation behavior is linear;
2. yield region, where it's visible the transition zone in terms of deformation behavior;
3. plastic region, where the deformation is nonlinear;

and in the material **(b)** of the figure 3.2**(b)** it is visible that the deformation behavior is nonlinear, either in the elastic and plastic regions [3]. As soon as a material experiences stress beyond the yield stress (linear limit), it will be permanently deformed from its original form, shape, or geometry[4]. If a material enters in nonlinear state, the deformation recovery will be just as much as the recovery possible in the linear state, as we can observe in figure 3.3[4].

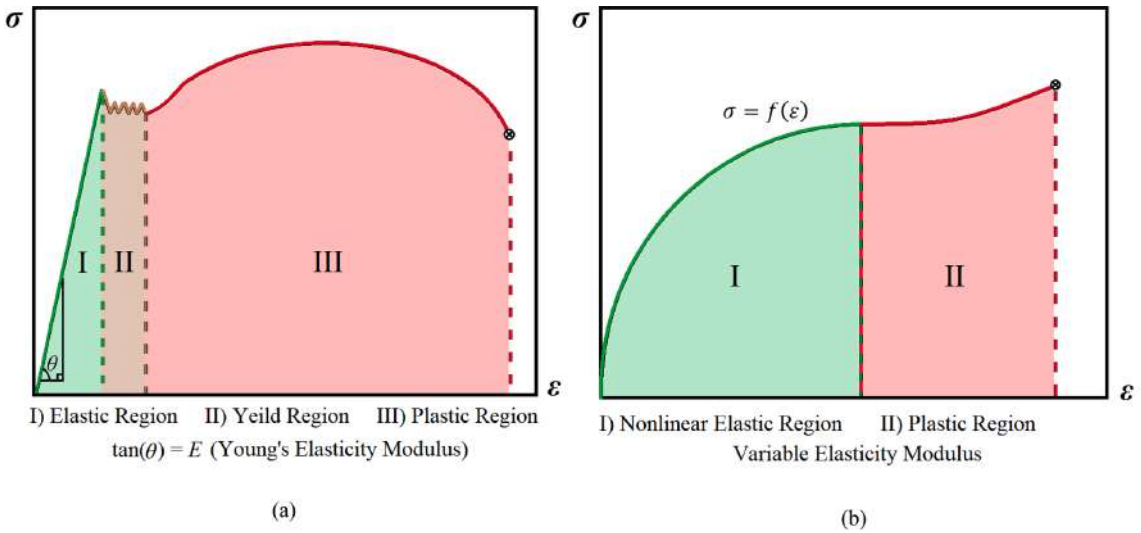

Figure 3.2: Examples of two stress-strain diagrams: **(a)** material with the linear elastic region; **(b)** material with nonlinear elastic region [3]

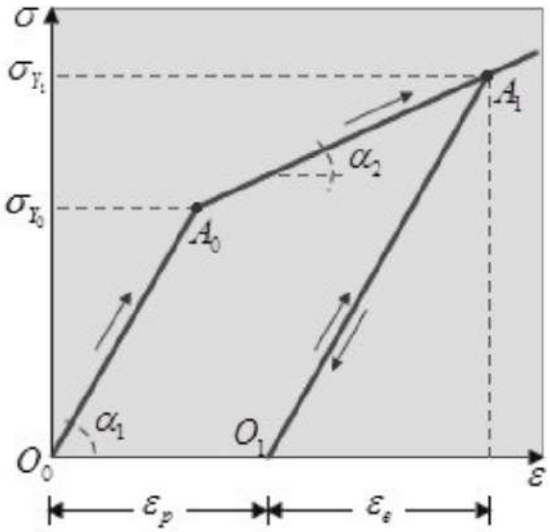

Figure 3.3: An example of a material deformation recovery after entering the nonlinear state [4]

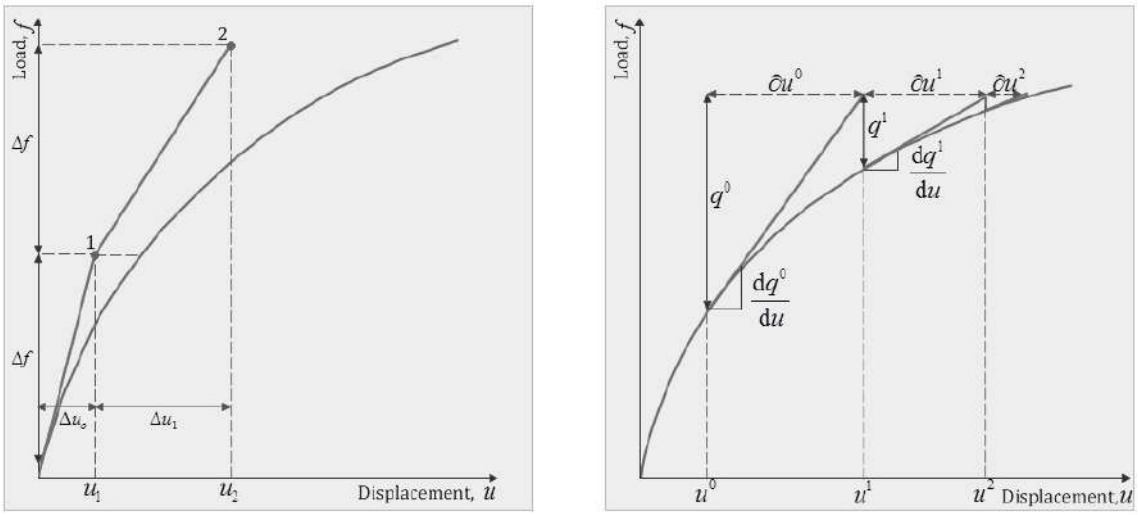

Figure 3.4: **(a)** Euler increment solution scheme; **(b)** Newton Raphson method[4]

To calculate the displacement of the linear deformation, the Young's Modulus is used; however, as soon as the deformations start being nonlinear, the Young's Modulus is no longer valid for the displacement calculation[4]. For this reason, the nonlinear calculation is done by calculating the deformations of small load increments[4, 53]:

$$\Delta u = \left(\frac{df}{du}\right)^{-1} \Delta f = K_T^{-1} \Delta f \tag{3.11}$$

where u is the displacement, f is the load, and K_T^{-1} is the inverse tangential stiffness matrix[1, 4].

There are errors that are associated, and will accumulate with every single load stage as is visible in figure 3.4 (a), where small errors will constantly accumulate[4].

The solution is more nonlinear when $\left(\left(\frac{df}{du}\right)^{-1} \to 0\right)$, which will make the solution less reliable and with more deteriorated results[4]. This generates a problem with the reliability of the results; however, the problem can be overcome with iterative solutions. In figure 3.4 (b) we can observe Newton Raphson method, this one only provides the displacement u to a fixed load f reducing, in this way, the errors associated with the Euler increment solution are visible in the figure 3.4 **(a)**[4]. If we consider j as the iteration of the Newton-Raphson method, then the equation is[4]:

$$\partial u^j = \left(\frac{dq^j}{du}\right)^{-1} q^j(u^j) \tag{3.12}$$

with can be transformed into an equation for displacement[4]:

$$u^j = u^{j-1} + \partial u^{j-1} \tag{3.13}$$

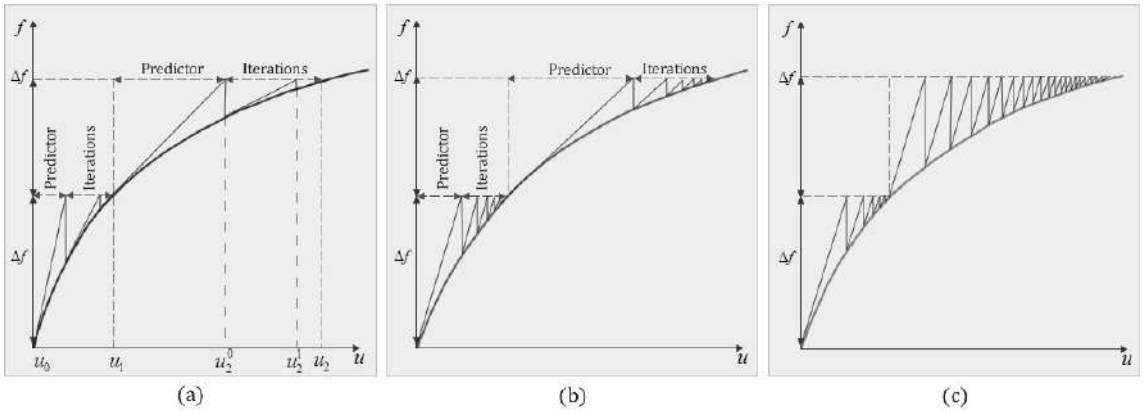

Figure 3.5: **(a)** Combined incremental and Newton Raphson method; **(b)** Combination of incremental predictors with modified Newton-Raphson iterations (KT1); **(c)** Initial stress method combined with an incremental solution (KT0)[4]

The Newton-Raphson iterative method (figure 3.4 **(b)**) can be combined with the Euler incremental method (figure 3.4 **(a)**)[4]. By combining these two methods, we can obtain a more accurate solution in the increment process[4]. In figure 3.5 **(a)** the increment method beavers as a predictor, producing an iterative initial solution u_i^0, that can be observed in the figure 3.5 **(a)**, where u_i^j is the iteration displacement j for an incremented load i[4]. Because of the predictor used, it is possible to reduce the number of interactions, and the reason behind this is related to the fact that the predictor improves the convergence of the iterative procedure, and because of this, the iteration numbers are reduced[4].

During nonlinear deformation, it is necessary to constantly update the stiffness matrix during the analysis[4]. As a result, the process requires greater computational power, longer computation time, and higher costs[4]. One such approach combines incremental predictors with modified Newton–Raphson iterations, known as the KT1 method[4]. In this method, the stiffness matrix is assumed to remain constant within each load increment, as illustrated in figure 3.5(b)[4]. By comparing the standard Newton–Raphson method with KT1, it can be observed that the tangent stiffness remains constant throughout each incremental step, making the process faster and less computationally demanding[4]. The KT1 method can be additionally simplified by keeping the stiffness matrix constant, not just within each load increment but for the entire analysis process; this new approach can be seen in figure 3.5(c), and it's called the KT0 method.[4]. The stiffness matrix from the first incremental solution is used for all increments. [4].

When comparing the Newton–Raphson (also known as KT-ALL), KT1, and KT0 methods, several important differences can be observed; in the Newton–Raphson method, the stiffness matrix is updated at every iteration within each load increment, ensuring high accuracy but significantly demanding more computational cost[4]. In the KT1 method, the stiffness matrix is kept constant throughout each load iteration and only updated between increments, therefore reducing the number of matrix

updates and improving computational efficiency[4]. Finally, in the KT0 method, the stiffness matrix obtained from the first increment is used for all subsequent load steps[4]. Although this approach greatly reduces computational effort, it also decreases accuracy and may require a greater number of load increments to achieve convergence[4]. Overall, the Newton–Raphson method provides the most accurate solution; KT1 and KT0 offer more efficient alternatives that trade some precision for computational speed, with KT0 being the method that is generally less precise[4].

3.3 Computational Nonlinearity

In this subsection, we will comprehend the variables and the algorithm implementation behind the nonlinear deformation[4].

The plastic behavior starts when the yield function f gives us the same value of the material's yield stress $\boldsymbol{\sigma}$. As soon as the material enters the plastic domain, the material's behavior will be conditioned by the yield function f and the respective stress $\boldsymbol{\sigma}$, which in terms can be written by the equation[4, 54]:

$$df = \left(\frac{\partial f}{\partial \boldsymbol{\sigma}}\right)^T d\boldsymbol{\sigma} \tag{3.14}$$

The von Mises yield criterion is[4]:

$$F(\boldsymbol{\sigma}, \boldsymbol{\varepsilon}^p, \boldsymbol{\kappa}) = f(\boldsymbol{\sigma}, \boldsymbol{\varepsilon}^p, \boldsymbol{\kappa}) - \sigma_Y(\boldsymbol{\kappa}) = 0 \tag{3.15}$$

where the $f(\boldsymbol{\sigma}, \boldsymbol{\varepsilon}^p, \boldsymbol{\kappa})$ is the yield function, and this function depends on the stress $\boldsymbol{\sigma}$, depends on the plastic strain $\boldsymbol{\varepsilon}^p$, and finally, depends on a hardening parameter $\boldsymbol{\kappa}$[4]. The parameter $\sigma_Y(\boldsymbol{\kappa})$ represents the yield stress, which is also dependent of the yield criterion[4, 55].

The differentiation of the yield criterion is,

$$dF = \left(\frac{\partial f}{\partial \boldsymbol{\sigma}}\right)^T d\boldsymbol{\sigma} - \frac{\partial \sigma_Y}{\partial \kappa} d\kappa = 0 \tag{3.16}$$

which can also be transformed in[4]:

$$dF = \mathbf{a}^T d\boldsymbol{\sigma} - A d\lambda = 0 \tag{3.17}$$

where $\boldsymbol{a}$ represents the flow vector, ($\boldsymbol{a} = \partial f / \partial \boldsymbol{\sigma}$) is the normal to the yield surface, $d\lambda$ represents the plastic strain-rate multiplier, and finally A is calculated by the equation[4, 54]:

$$A = \frac{1}{d\lambda} \frac{\partial \sigma_Y}{\partial \kappa} d\kappa \tag{3.18}$$

To calculate the von Mises yield criterion we need to refer to the Prandtl-Reuss flow rules; however, it is necessary first to understand the Prandtl-Reuss flow rule [4, 53].

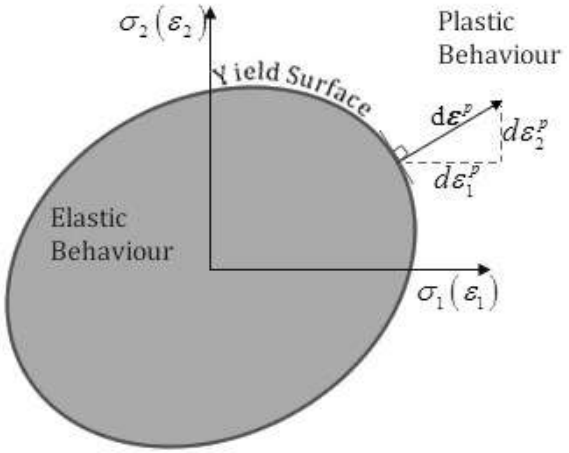

Figure 3.6: Plastic Flow Rule[4]

The Prandtl-Reuss flow rule equation can be calculated with the equation[4, 55, 53]:

$$d\boldsymbol{\varepsilon}^p = d\lambda \frac{\partial f}{\partial \boldsymbol{\sigma}} \tag{3.19}$$

where $d\lambda$ is the plastic strain-rate multiplier. The plastic flow can be represented by the figure 3.6.

By analyzing the figure 3.6 we can verify the plastic flow rule behavior (table 3.1) depending on the plastic strain-rate multiplier $d\lambda$[4, 56, 54, 2].

Table 3.1: Plastic Flow Rule Behaviour

$d\lambda$	Plastic Flow Behaviour
$d\lambda < 0$	the material's behaviour is elastic, which means that the material can recover all the current deformation and Hook's Law is still valid and applicable
$d\lambda = 0$	as it was already mentioned, in this situation the material enters the plastic behaviour state
$d\lambda > 0$	the material is inside the plastic behaviour state

Now, using the Prandtl-Reuss flow rules, we can define the von Mises equation[4]:

$$d\boldsymbol{\epsilon}^p = d\lambda \mathbf{a} = d\lambda \begin{Bmatrix} \frac{\partial f}{\partial \sigma_{xx}} \\ \frac{\partial f}{\partial \sigma_{yy}} \\ \frac{\partial f}{\partial \sigma_{zz}} \\ \frac{\partial f}{\partial \sigma_{xy}} \\ \frac{\partial f}{\partial \sigma_{yz}} \\ \frac{\partial f}{\partial \sigma_{zx}} \end{Bmatrix} = \frac{s\lambda}{2\overline{\sigma}} \begin{Bmatrix} 2\sigma_{xx} - \sigma_{yy} - \sigma_{zz} \\ 2\sigma_{yy} - \sigma_{xx} - \sigma_{zz} \\ 2\sigma_{zz} - \sigma_{xx} - \sigma_{yy} \\ 6\sigma_{xy} \\ 6\sigma_{yz} \\ 6\sigma_{zx} \end{Bmatrix}_{vonMises} \tag{3.20}$$

The stress and strain are connected through the equation[4]:

$$d\boldsymbol{\sigma} = \boldsymbol{c} \cdot d\boldsymbol{\epsilon}_e \tag{3.21}$$

which can be rewritten as:

$$d\boldsymbol{\sigma} = \mathbf{c} \cdot d\boldsymbol{\epsilon}_e - d\lambda \cdot \mathbf{c} \cdot \mathbf{a} \tag{3.22}$$

where $d\lambda$ is:

$$d\lambda = \frac{\mathbf{a}^T \mathbf{c} d\boldsymbol{\epsilon}}{\mathbf{a}^T \mathbf{c}\mathbf{a} + A} \tag{3.23}$$

Replacing the last two equations, we obtain:

$$d\boldsymbol{\sigma} = \mathbf{c} \cdot d\boldsymbol{\epsilon} - \frac{\mathbf{a}^T \mathbf{c} d\boldsymbol{\epsilon}}{\mathbf{a}^T \mathbf{c}\mathbf{a} + A\mathbf{c}\mathbf{a}} = \left(\mathbf{c} - \frac{\mathbf{c}\mathbf{a}\mathbf{a}^T\mathbf{c}}{\mathbf{a}^T\mathbf{c}\mathbf{a}+A}\right) d\boldsymbol{\epsilon} = \mathbf{c}^{ep} d\boldsymbol{\epsilon} \tag{3.24}$$

where c^{ep} is the elastoplastic tangential modular matrix[4].

The determination of the A parameter depends on the chosen hardening rule, which is the only remaining task[4]. To determine this parameter, isotropic work hardening will be applied and, as a result, the yield stress becomes a function of plastic work, where the plastic work W_p is calculated through the equation [4]:

$$\boldsymbol{\kappa} = W_p = \int \sigma_Y \, d\epsilon_p = \int \boldsymbol{\sigma}^T d\boldsymbol{\epsilon}_p = \int d\lambda \, \boldsymbol{\sigma}^T \boldsymbol{a} \tag{3.25}$$

$$d\kappa = dW_p = \sigma_Y d\epsilon_p = \boldsymbol{\sigma}^T d\boldsymbol{\epsilon}_p = d\lambda \, \boldsymbol{\sigma}^T \boldsymbol{a} \tag{3.26}$$

Using these equations, we can rewrite the hardening constant equation as[4]:

$$A = \boldsymbol{\sigma}^T \mathbf{a} \frac{\partial \sigma_Y}{\partial \boldsymbol{\kappa}} \tag{3.27}$$

If we define the explicit relationship between the uniaxial yield stress (σ_Y) and the hardening parameter κ, the value of A would be fully determined[4]. This relationship can be written as shown in the equation[4]:

$$\frac{\partial \sigma_Y}{\partial \kappa} = \frac{\partial \boldsymbol{\sigma}_Y}{\partial \boldsymbol{\epsilon}_p} \frac{\partial \epsilon_p}{\partial \boldsymbol{\kappa}} \tag{3.28}$$

$$\frac{\partial \sigma_Y}{\partial \kappa} = \frac{\partial \boldsymbol{\sigma}_Y}{\partial \boldsymbol{\epsilon}_p} \frac{1}{\sigma_Y} \tag{3.29}$$

where ϵ_p is the plastic strain[4].

The σ_Y and ϵ_p relation of the past equations can be taken from the uniaxial stress/plastic strain relationship, obtaining the next equations[4]:

$$\frac{\partial \sigma_Y}{\partial \epsilon_p} = \frac{d\sigma}{d\epsilon - d\epsilon_e} = \frac{1}{\frac{d\epsilon}{d\sigma} - \frac{d\epsilon_p}{d\sigma}} = \frac{1}{\frac{1}{E_T} - \frac{1}{E}} = \frac{E_T}{1 - \frac{E_T}{E}} = H' \tag{3.30}$$

$$\frac{\partial \sigma_Y}{\partial \kappa} = \frac{H'}{\sigma_Y} \tag{3.31}$$

where E_T is the tangent modulus, and H' is the plastic modulus[4].

And now, the hardening constant can be rewritten by the equation[4]:

$$A = \frac{H' \boldsymbol{\sigma}^T \mathbf{a}}{\sigma_Y} \tag{3.32}$$

If the yield function is a homogeneous function of order one, Euler's theorem states that[4]:

$$\frac{\partial f^T}{\partial \boldsymbol{\sigma}} = \mathbf{a}^T \boldsymbol{\sigma} = \sigma_Y \tag{3.33}$$

3.3.1 Stress Returning Algorithm

During the execution of the numerical program, it is important to ensure that the stresses remain within or close to the yield surface while implementing it. Otherwise, errors may accumulate, and the computed load will typically be overestimated, as previously mentioned in this chapter. To address this issue, stress-returning algorithms can be employed when the stresses are outside the yield surface[4]. The approach used in this work for such cases is the backward-Euler method, which can be observed in figure 3.7.

This method is used to solve the nonlinear equations at the Gauss point level and does not require knowledge of the intersection point between the incremental load and the yield surface[4]. After the incremental load is applied, the stress state at each Gauss point is checked to see if it is within or outside the yield surface[4]. This is done by evaluating the yield criterion by the equation[4]:

$$f(\boldsymbol{\sigma}) \leqslant \sigma_Y^* \tag{3.34}$$

where $f(\boldsymbol{\sigma})$ represents the yield surface and σ_Y^* is the updated yield stress, defined by the equation[4]:

$$\sigma_Y^* = \sigma_Y + \left[E_T \cdot \bar{\epsilon}_{i-1}^p \right] \tag{3.35}$$

The accumulated effective plastic strain from the previous increment $(i-1)$ is represented by $\bar{\epsilon}_{i-1}^p$[4]. If the Gauss point in question has not yet entered the plastic region, the second term of the equation used to calculate σ_Y^* will be zero, and the updated yield stress will be equal to the reference yield stress[4].

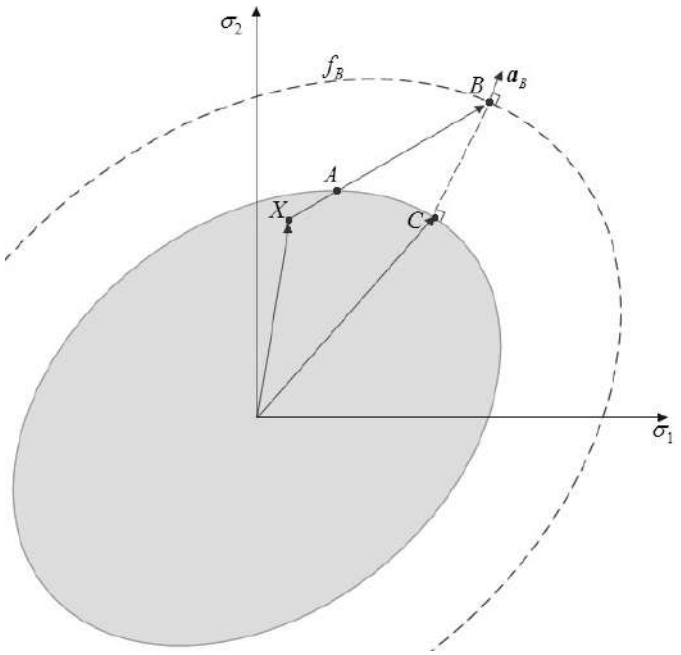

Figure 3.7: Backward Euler method[4]

The stress-returning algorithm is used whenever equation 3.34 is not satisfied[4]. In these cases, we are at point σ_B in figure 3.7, and this point must be moved to point σ_C on the yield surface[4]. To achieve this, the implemented algorithm begins with a predictor[4]. This predictor simulates that point σ_B is under a yield function f_B, thereby eliminating the need to compute the intersection point σ_A[4]. The flow vector, $\mathbf{a}$, is calculated for point σ_B, is computed for point σ_B, and the yield function at point σ_B is given by $f_B = \overline{\sigma}_B - \overline{\sigma}_Y^*$. After that, the plastic multiplier $d\lambda$ is calculated, using the flowed equation[4]:

$$d\lambda = \frac{f_B}{\mathbf{a}_B^T \mathbf{c} \mathbf{a}_B + H'} \tag{3.36}$$

where H' is defined in the former subchapter 3.2.

Now it is possible to estimate, through calculation, the stress in point σ_C, by using the equation:

$$\boldsymbol{\sigma}_C = \boldsymbol{\sigma}_B - d\lambda \mathbf{c} \mathbf{a}_B \tag{3.37}$$

The former equations give us just a starting estimation, to achieve the correct stress on point σ_C, it is necessary to use the flow vector of that same point[4]:

$$\boldsymbol{\sigma}_C = \boldsymbol{\sigma}_B - d\lambda \mathbf{c} \mathbf{a}_c \tag{3.38}$$

However, the flow vector σ_C cannot be calculated solely from the data information from points X and B[4]. Therefore, an iterative procedure using data from point σ_B must be utilized to correspond point σ_B to point σ_C[4]. During each iteration, the effective plastic strain is updated to apply to the equation $\sigma_Y^* = \sigma_Y + \left[E_T \cdot \bar{\epsilon}_{i-1}^p\right]$ and the full method is replicated[4]. In the limit, point σ_B will be very near to point

σ_C, and therefore, using the flow vector at point σ_C rather than at point σ_B will be nearly equivalent[4]. This is achieved by performing multiple iterations until a given tolerance is reached, which serves as the stopping criterion[4].

We can observe the implemented stress return algorithm through figure 3.8 [4].

3.3.2 KT0 Algorithm

The present study employs the initial stress method in combination with an incremental solution (KT0) to solve the nonlinear equations[4]. The algorithm used is described in this section [4]. It is necessary to keep in mind that this method involves calculating the stiffness matrix only once, during the first iteration of the first load increment[4]. To start the analysis, it is necessary to input certain data such as the dimensions of the problem, the desired type of nodal mesh, the material properties, the maximum load to be applied and its type, the essential boundary conditions, and the number of increments, iterations, and tolerance values[4]. With this information, a nodal mesh can be created and an integration mesh can be derived from it[4]. The influence domains are then determined, and interpolation functions are constructed. Using the material properties and the connectivity between nodes, the initial stiffness matrix is calculated[4]. The natural and essential boundary conditions are then applied to obtain the final stiffness matrix $\mathbf{K}_0$[4]. After this first process is finished, the KT0 algorithm starts to initiate, through the equation[4]:

$$\mathbf{f}_i = \frac{\mathbf{F}}{inc} \tag{3.39}$$

where the $\mathbf{f}_i$ is the incremental load applied, $\mathbf{F}$ is the maximum load and inc is the considered number of increments[4].

Now it is possible to calculate the displacement field and stress field using the equations[4]:

$$\mathbf{u}_i = \mathbf{K}_0^{-1}\mathbf{f}_i \tag{3.40}$$

$$\boldsymbol{\sigma}_i = \mathbf{cBu}_i \tag{3.41}$$

After that, the algorithm checks whether any of the Gauss points are outside of the yield surface, that is, whether any of the Gauss points have entered the plastic region[4]. At the end of this algorithm, the updated stress vector for the current increment, $\boldsymbol{\delta\sigma}$, is obtained[4]. The total stress vector can be computed using the following equation:

$$\boldsymbol{\sigma}_i = \boldsymbol{\sigma}_{i-1} + \boldsymbol{\delta\sigma} \tag{3.42}$$

where $\boldsymbol{\sigma}_i - 1$ is the total stress vector from the previous increment done[4].

If none of the Gauss points in the problem domain have been entered in the plastic region during the current load increment, it means that the entire incremental load was applied[4]. However, if any point has entered the plastic region, it means that the load increment value does not correspond to the applied load, due to the stress

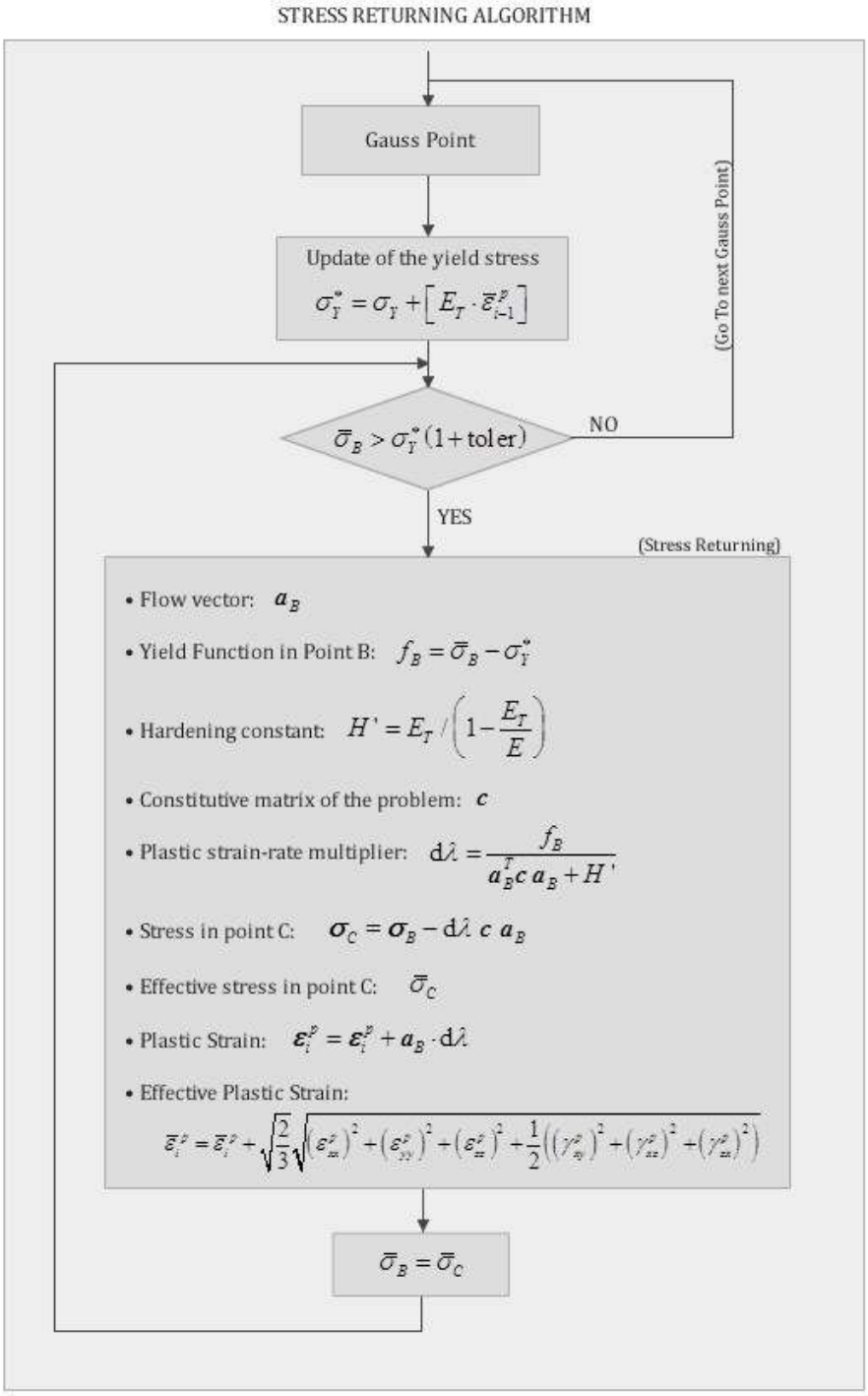

Figure 3.8: Stress returning algorithm process [4]

returning to the yield surface[4]. Therefore, whenever a Gauss point has entered the plastic region, it is necessary to calculate the value of the residual forces using the following equation,

$$\mathbf{f}_i^{res} = \mathbf{f}_i - \int_\Omega \mathbf{B}^T \boldsymbol{\delta\sigma} d\Omega \tag{3.43}$$

which will be equal to zero if no point has exceeded the yield surface[4].

When the calculation of the residual force is finished, it is necessary to assess its magnitude to determine whether it is significant or not[4]. This also serves as a stopping criterion, using a tolerance value *(toler)*[4]. If the *toler* equation is pleased, the algorithm proceeds to the next load increment[4]. Otherwise, the residual force must be applied, and an iterative procedure is initiated to do so[4].

$$\frac{\left\{\frac{\sum_{l=1}^{n} f_i^{res}}{n}\right\}}{\left\{\sum_{m=1}^{j} \frac{\sum_{l=1}^{n} f_i^{res}}{n}\right\}} < toler \tag{3.44}$$

where n is the number of nodes and j is the number of iterations[4].

Upon completion of all the load increments, it is possible to obtain the load-displacement curves as well as the stress and displacement fields[4]. The figure 3.9 illustrates the KT0 algorithm implemented in this study[4].

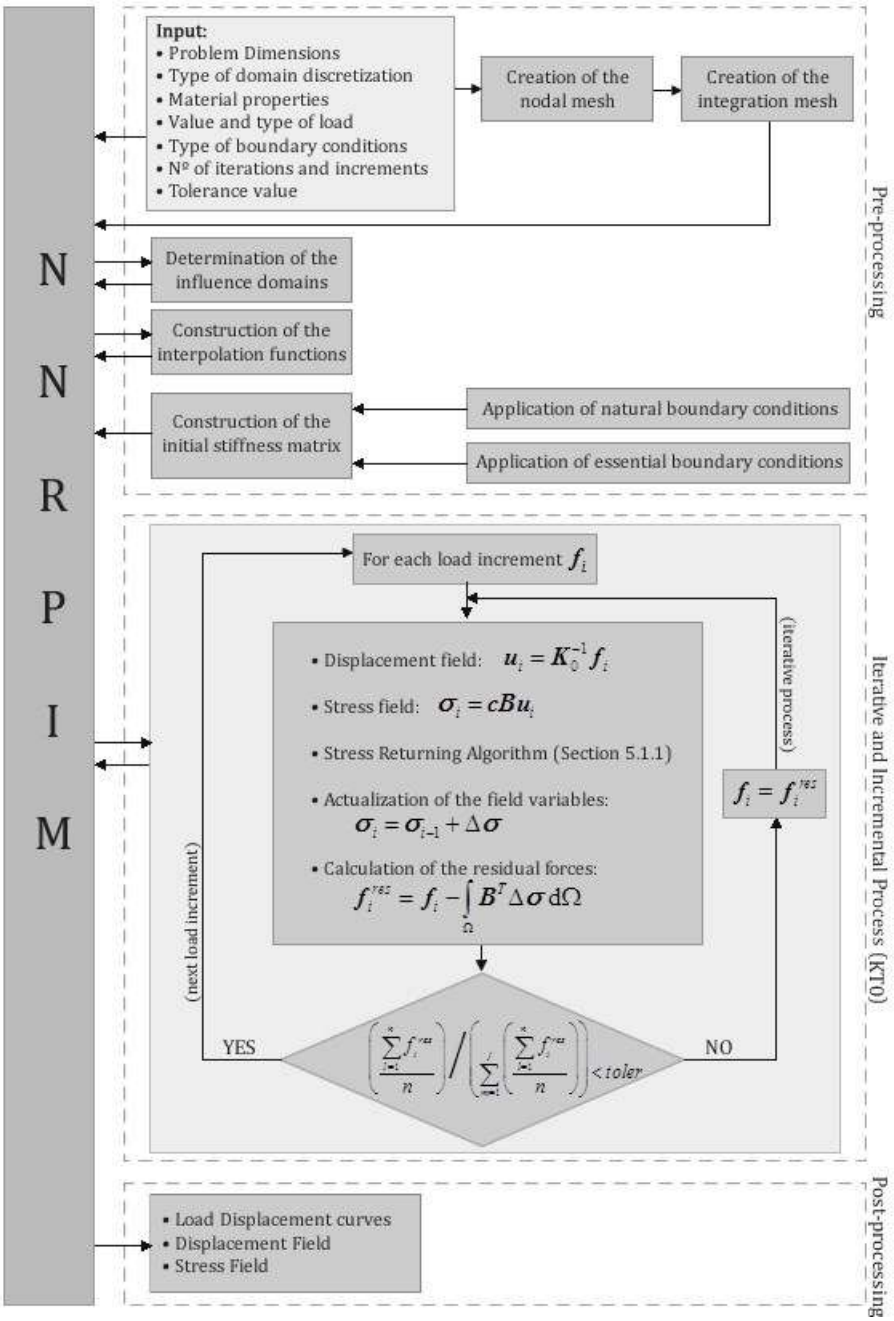

Figure 3.9: KT0 algorithm process [4]

4 State of the Art

The field of nonlinear analysis of industrial frame structures has seen significant advancements in recent years, with the development of advanced computational techniques. As we know, there are two important computational techniques [57]:

1. finite element methods;
2. meshless methods.

By doing a quick analysis, on June 15^{th} of 2025, with the comparative interest, in the prestigious online website *Science Direct*, we can analyse and compare the results from the four different searches, using the words [58]:

- *("finite element analysis" or "finite element methods")*;
- *("meshfree method" or "meshless method")*;
- *("finite element analysis" or "finite element method") and "plasticity"*;
- *("meshfree method" or "meshless method") and "plasticity"*.

After the search completion, it's possible to see that the results are, surprisingly, discrepant and can be visualized in figure 4.1 and figure 4.2.

By analysis of both diagrams (figure 4.1 and figure 4.2), it is clear that the FEM method is in a maturity state much more advanced, both in terms of years of existence and time spent perfecting. If we take into account that the finite element methods are easier to program and require less computational power makes sense, from an industrial point of view, to develop programs with FEM. FEM appeared in the end of the 1950's, and meshless methods only in the beginning of the 1990's." The fact that the program code required is more complex, makes it difficult for the meshless methods to surpass the finite element methods, even thou the meshless method has the potencial to be more precise, and can deal with the elastoplasticity and complex forms with more easiness.

There are several advantages that make the meshless methods an alternative to the FEM, like the fact that meshless methods are much more precise with their results which can make a big difference in some industries, like for example, the aeronautic industry, where weight is always an important factor and an aeroplane is design with only the necessary material/weight. Having a tool like the meshless method can help companies reduce the weight of the most diversified structures, which in turn will have positive impacts on the world.

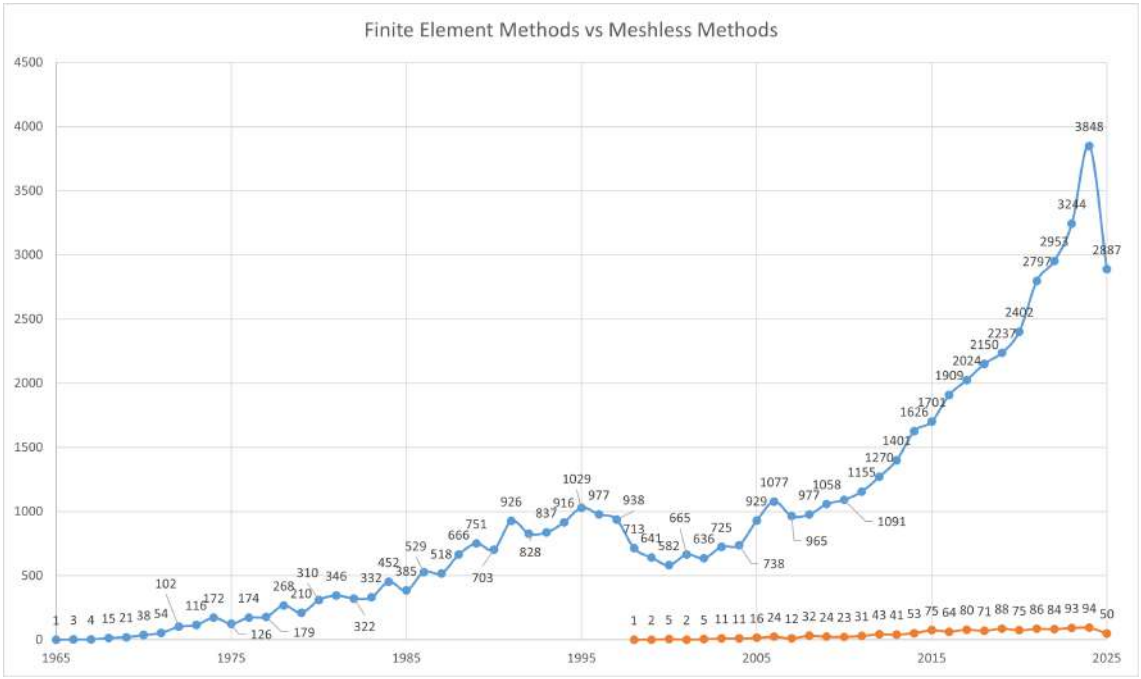

Figure 4.1: Comparison diagram with the published paper about Finite Element Methods vs Meshless methods, through the years

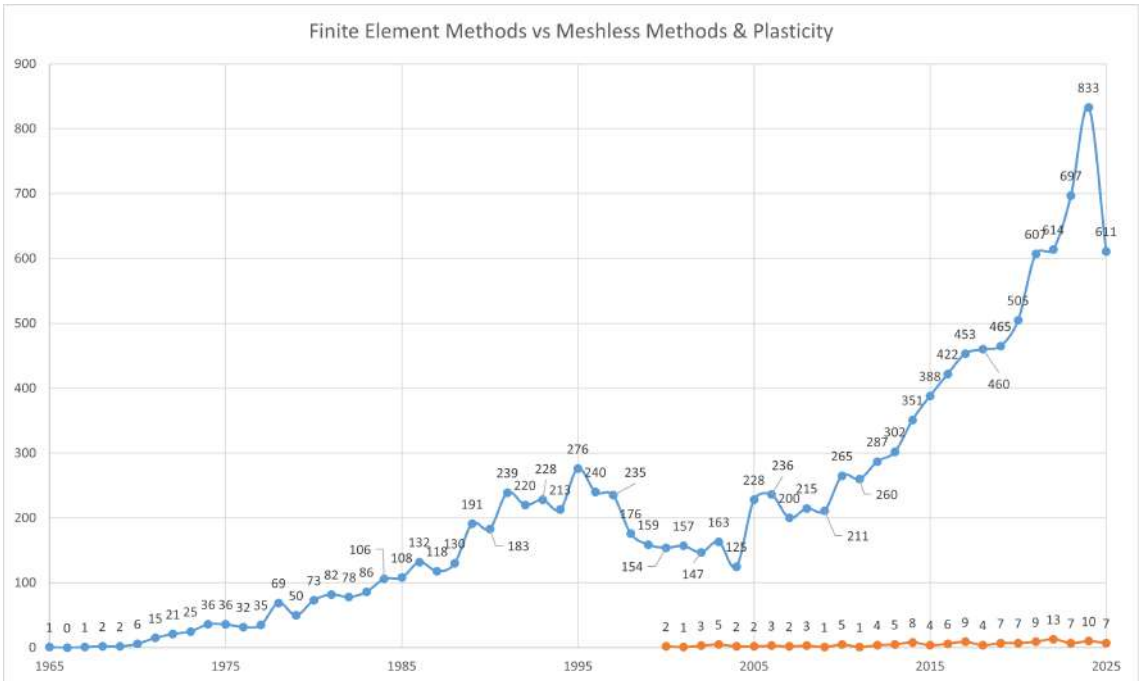

Figure 4.2: Comparison diagram with the published paper about plasticity with Finite Element Methods vs Meshless methods, through the years

4.1 Previews Works Evolving Meshless Methods with Elastoplasticity

In January of the year 2023, the paper *"Application of generalized finite difference method for elastoplastic torsion analysis of prismatic bars"* was published[19]. This paper presents a numerical method called the generalized finite difference method (GFDM) for analyzing the behavior of prismatic bars under torsional loading, taking into account both elastic and plastic deformation[19]. The method is based on dividing the computational domain into a series of overlapping sub-domains and constructing a system of linear equations using Taylor series expansion and moving least squares[19]. The plastic nonhomogeneous term is then evaluated using radial basis function (RBF) interpolation[19]. The method is applied to numerical examples of square-section bars and linear guide rails, showing that the GFDM is a reliable and effective solution for elastic-plastic torsion problems of prismatic bars[19]. The main advantage of GFDM is that it does not require intra-domain integration and allows random distribution of nodes, making it suitable for dealing with complex geometric domains[19]. This study is relevant to the present work because it applies a meshless-type numerical technique to model elastoplastic behavior in structural components. The use of the method in question demonstrates how meshless formulations can effectively capture material nonlinearity, directly aligning with this work's focus on nonlinear analysis using RPIM and NNRPIM.

In 2017 the paper *"A numerical mesh-free model for elastoplastic contact problems"* was published[20]. In this paper, a numerical mesh-free model was developed for simulating elastoplastic structures with contact in the context of large deformation[20]. The model is based on the Asymptotic Numerical Method (ANM) and the meshless collocation framework to extend its application to elastoplastic problems with contact[20]. The efficiency of this model is in its ability to handle large deformations and avoid meshing distortion[20]. The approach was tested on several examples and found to be a reliable and less time-consuming alternative to iterative methods[20]. This model is an effective candidate for solving large deformation of elastoplastic contact[20]. The pertinence of this study can be found in the extension of meshless formulations to elastoplastic contact problems, effectively handling both material and boundary nonlinearities. Such capabilities are essential for the exact modeling of industrial frame structures, where contact and plastic deformation often occur under complex loading conditions, just like those considered in this dissertation.

In 2015 the paper *"A numerical meshless method of soliton-like structures model via an optimal sampling density based kernel interpolation"* presented a numerical method for solving problems involving soliton-like structures model[21]. The method is based on an adaptive meshless approach, which is a numerical method that does not rely on a fixed mesh, and it uses kernel interpolation to approximate the solution[21]. The method is also based on the use of optimal sampling density (OSD) to improve the accuracy of kernel interpolation[21]. The authors propose a two-step meshless method, which uses a predictor process in the first step and a final process in the second step[21]. The predictor process uses field nodes with the same node distribution, while the final process uses field nodes arranged adaptively

according to the OSD[21]. The method is applied to the sine-Gordon equation, which is an example of a soliton-like structures model, and the results show that the method is very effective in simulating a soliton-like structures model with good accuracy and a low computational cost[21]. This academic paper is related to the dissertation theme because it advances kernel interpolation techniques by optimizing sampling density, a concept responsible for the improvement of the stability and accuracy of meshless approximations. These developments are directly applicable to the refinement of RPIM and NNRPIM formulations used for nonlinear structural analysis in this research.

In May of 2002, the paper *"Meshless methods for large deformation analysis-a reproducing kernel particle approach"* used the meshless method approach for analyzing the behavior of structures under large displacements.[59] The method is based on reproducing kernel particle estimates, and it is applied to solve typical two-dimensional large displacement problems.[59] The penalty method is used to enforce essential boundary conditions in this method.[59] The results of the numerical examples show that the meshless model has at least similar effectiveness and accuracy as compared to the finite element method.[59] The paper concludes that the meshless algorithm for large deformation analyses proposed in this work is efficient and accurate for large deformation beam problems, and are comparable to the standard FEM analysis in all the case exemples studied.[59] This paper contributes to the state of the art by handling geometric nonlinearity through the reproducing kernel particle method (RKPM). This method formulation for large deformation problems provides a strong theoretical and numerical basis for the nonlinear framework adopted in this dissertation, which similarly employs kernel-based meshless techniques such as RPIM and NNRPIM, being used for the elaboration of this work.

5 Linear Analysis

In this chapter, we will run some linear analysis simulations to understand the behavior and influence of different types and sizes of meshes in the same object. We will also use different types of simulations, those being Finite Element Method (FEM) simulations, RPIM with constant and linear polynomials, and NNRPIM with first and second degrees of neighborhood.

5.1 Cantilever Beam

In this subchapter, a linear analysis was conducted for a cantilever beam with dimensions of 2 by 1 meter in the 2D plane. For this analysis, the domain $\mathbf{\Omega} \subset \mathbb{R}^2$ was considered, with material properties $E = 1000$ Pa and $\nu = 0.3$.

5.1.1 Simulations

For this linear analysis, the cantilever beam simulations began with a 4×2 element configuration, doubling the number of elements until it reached 128×64. Table 5.1 provides us with a clearer understanding of the different cantilever beams configurations analyzed, showing the number of nodes and elements for each mesh used. In all simulations, the applied force was a uniformly distributed load (P), with a unitary value of 1 [N], as shown in figure 5.1, where the dimensions are represented in millimeters. Since the load is uniformly distributed and forces must be applied at the nodes, increasing the number of nodes improves the accuracy of simulating a uniformly distributed load. For example, in a 4×2 mesh, only 3 nodes are available to apply the force, whereas in a 128×64 mesh, up to 65 nodes can be used.

As previously mentioned, this work will be done with FEM, RPIM, and NNRPIM type simulations, and for these three types of simulations, we will be using square and triangular meshes except for NNRPIM simulations, which will be done exclusively with triangular meshes, and that means that for this chapter we have done a total of 12 FEM simulations, 24 are RPIM simulations and 12 NNRPIM simulations. For the RPIM simulations, it was used constant and linear bases were used with the terms c and p equal to 1.42 and 1.03, respectively, while for the NNRPIM simulations, the terms were 0.0001 and 0.9999, respectively, and only a constant base for both the first and second degrees of neighborhood. These parameter values are considered the norm for the respective simulation types, as stated earlier.

The points in analysis from these simulations are A, B, C, and finally, D, which can be observed in image 5.1, being those:

- point A, with the respective coordinate (0;0.5);

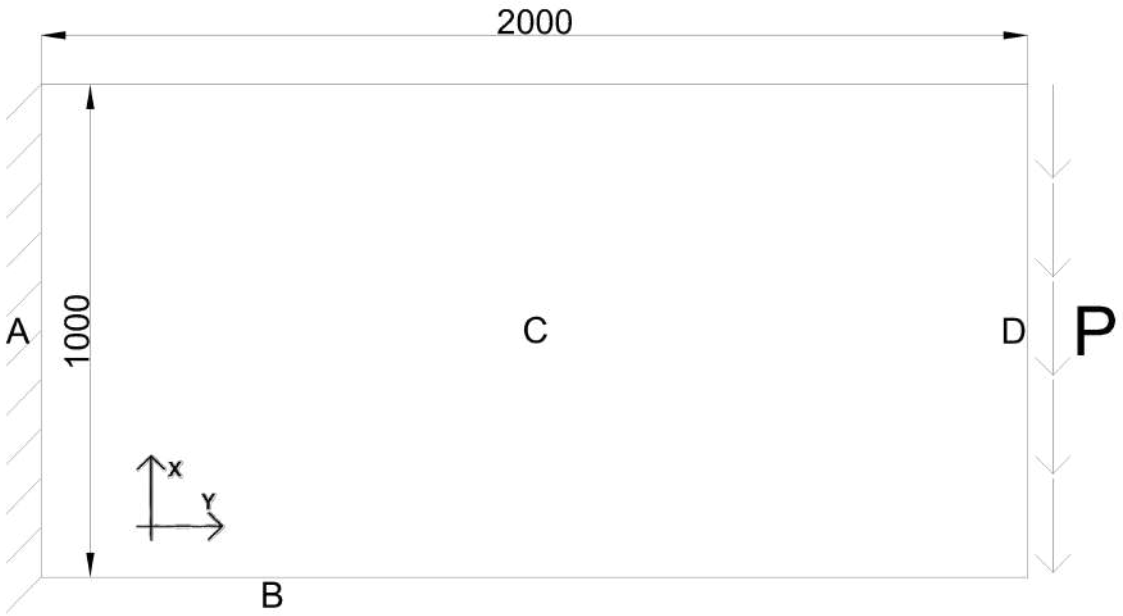

Figure 5.1: 2D simulated model for the linear analysis

- point B, with the respective coordinate (0.5;0);
- point C, with the respective coordinate (1;0.5);
- point D, with the respective coordinate (2;0.5).

In this study, we will focus on points B, C, and D, leaving point A out of the results study. At point B, the stress was analyzed; at point C, the shear stress was examined; and at point D, the vertical deflection was studied. The compressive stress analysis for point B was performed using σ_{xx} (compressive stress in the x-direction), σ_{11} (compressive stress in the first principal direction), and $\sigma_{\text{von Mises}}$ (equivalent stress). The following graphs illustrate how these stress values change depending on the mesh geometry, number of elements, and simulation type. However, by quickly analyzing the graphs presented in figures 5.2 to 5.6, it is possible to observe that as the number of nodes increases, the obtained values tend to converge to a mathematical limit.

By analyzing the different diagrams for the compression stress, it is possible to conclude that with the nodal number increment, the compression stress in point B is increasing, exactly as expected.

Continuing with the analysis, now on point C to the shear stress, and by analyzing the diagram present in figure 5.5, we can observe that while the shear stress appears to be decreasing, the absolute value is, indeed, increasing with behavior that tends to a limit and is converging; however, there is an unexpected fenomenum that is visible throughout all the RPIM and NNRPIM simulations, and occurs in the simulations with nodes' number equal to 45. What was expected was a shear stress Increase in the absolute value, with a curve with concavity up-tending to a limit;

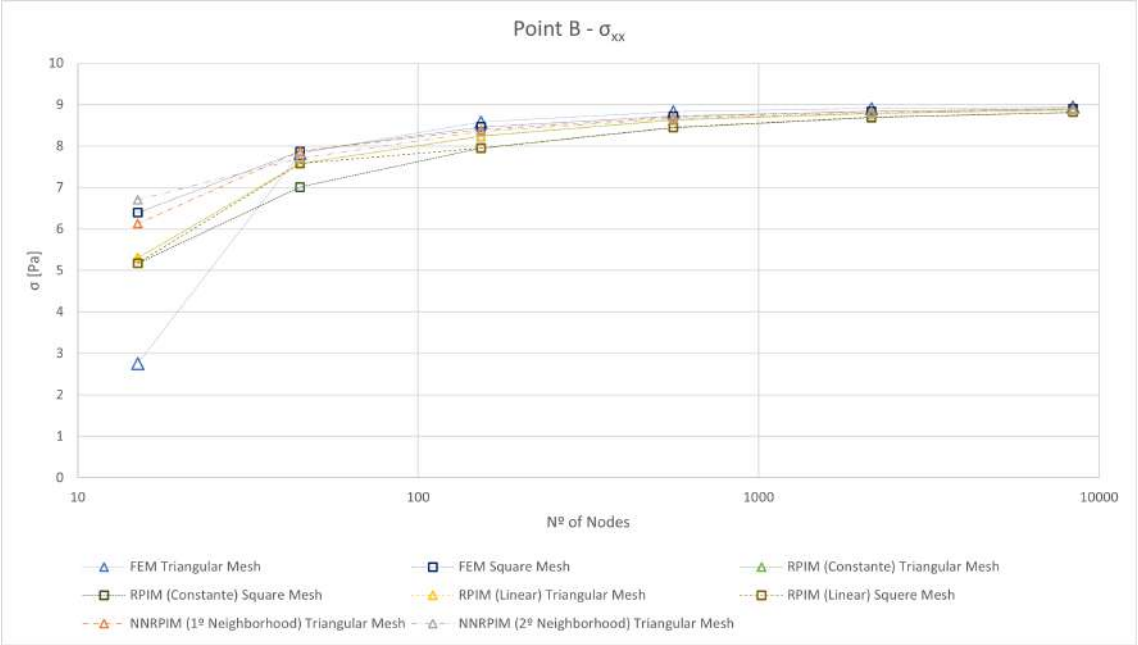

Figure 5.2: Comparison diagram of the compression stress (σ_{xx}) for the point B

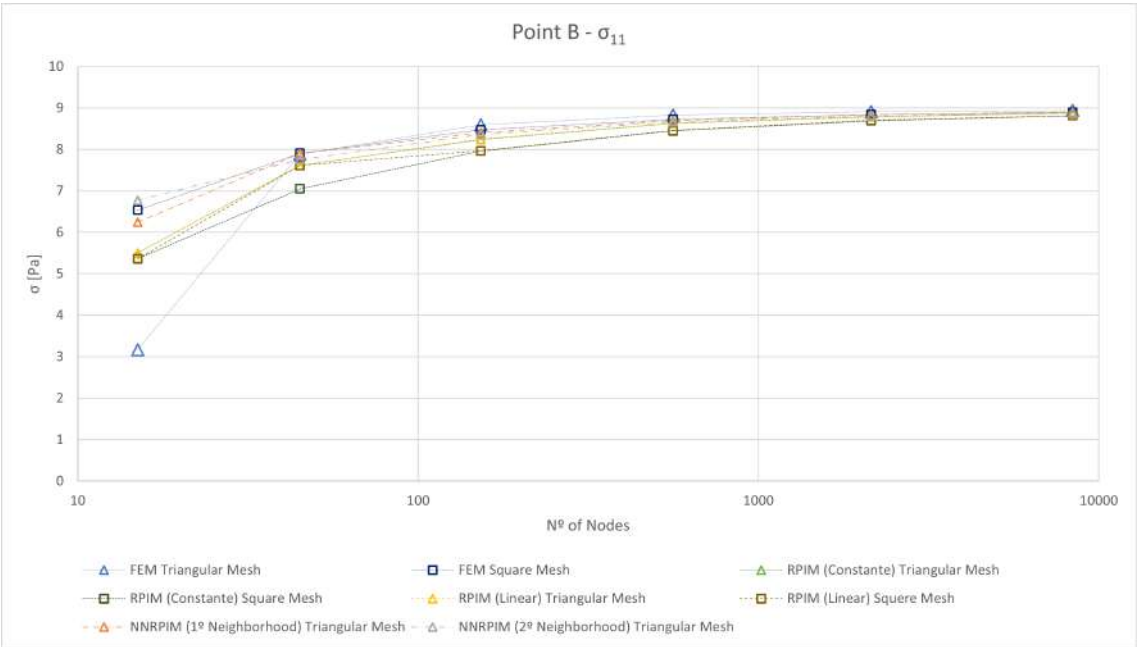

Figure 5.3: Comparison diagram of the compression stress (σ_{11}) for the point B

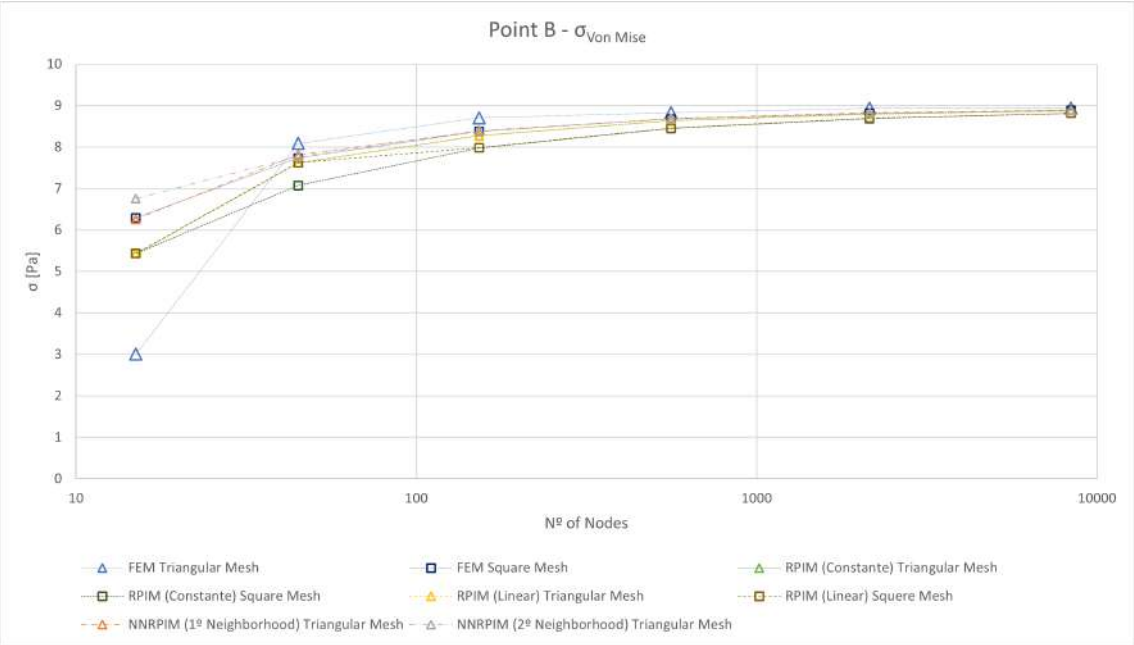

Figure 5.4: Comparison diagram of the compression stress ($\sigma_{VonMise}$) for the point B

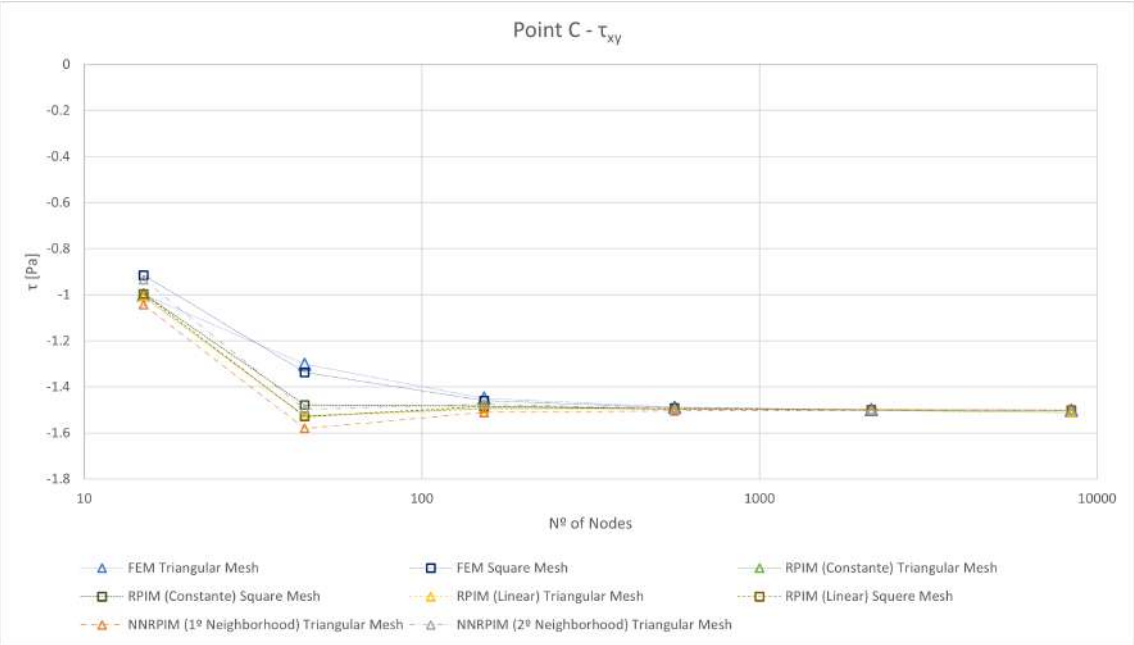

Figure 5.5: Comparison diagram of the shear stress (τ_{xy}) for the point C

Table 5.1: Number of nodes and elements depending on the cantilever beam type

Mesh Size	Type	Number of Nodes	Number of Elements
4×2	Square	15	8
	Triangular	15	16
8×4	Square	45	32
	Triangular	45	64
16×8	Square	153	128
	Triangular	153	265
32×16	Square	561	512
	Triangular	561	1024
64×32	Square	2145	2048
	Triangular	2145	4096
128×64	Square	8385	8192
	Triangular	8385	16384

however, the graphic in the analysis shows us that the absolute stress value decreases when we compare the results of the 45 nodes configurations to the 153 nodes configurations, which wasn't expected. Despite this, we can observe the achievement of the mathematical limit for the configurations with a larger number of nodes and elements.

To finalize the analysis of the three points in question, we must direct our attention to the graphics present in figure 5.6, this one for the vertical deflection suffered by point D. This last diagram appears to have, just like in the diagram from point C, a decreasing in value while in reality, it has an increase on the absolute value converging to a limit, there is however an interesting fact that can be visualized in the graphic in question, all the RPIM results have a very close value in all the different simulations executed, independently of mesh type, elements number and the type of base used the values are so close that by just looking to the graphic give the sensation of being a line and not a curve.

Let's now divert our attention to the contour plots acquired from these simulations. In figures 5.7 to 5.11, we can observe the color-coded results for the FEM simulation with trianguler meshes, the same can be done for FEM with square meshes in figures 5.12 to 5.16, for RPIM with constant base in figures 5.17 and 5.21 with triangular meshes and for square meshes in figures 5.22 and 5.26, for RPIM with linear base is possible to study the contour plots in figures 5.27 to 5.31 for triangular meshes and square meshes from 5.32 to 5.36 to finalize we have the color-coded images from the square meshes NNRPIM simulations in figures 5.37 to 5.41 for the simulations done with the first degree on neighborhood and for the second degree in figures 5.42 to 5.46. The maximum and minimum values for the respectives color bars are defined from tables 5.2 to 5.9.

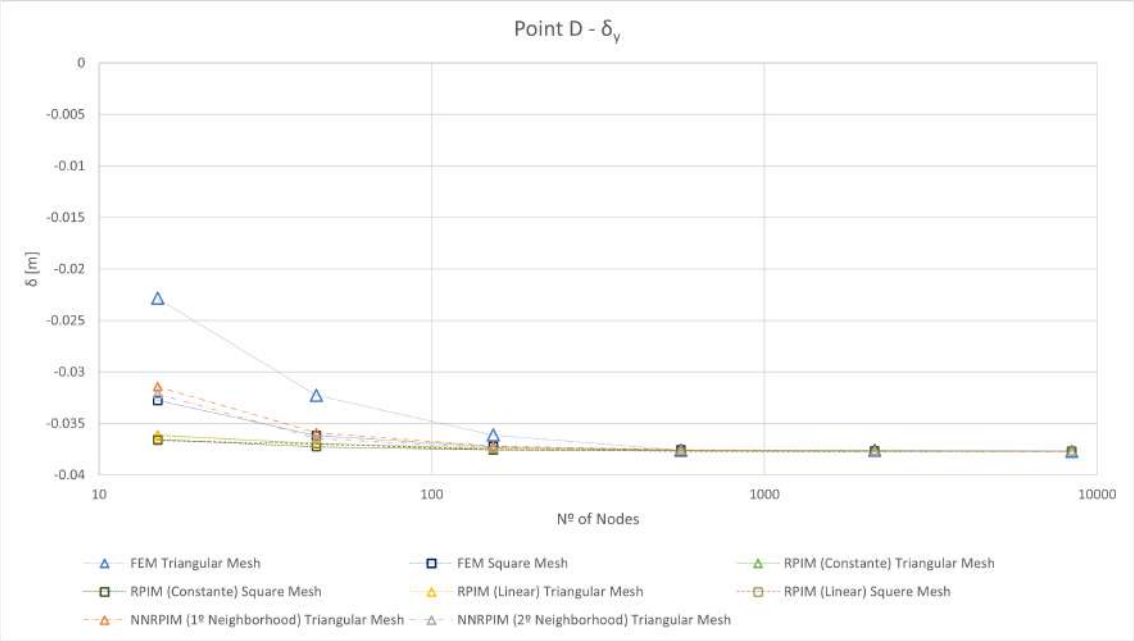

Figure 5.6: Comparison diagram of the displacement (δ_y) for the point D

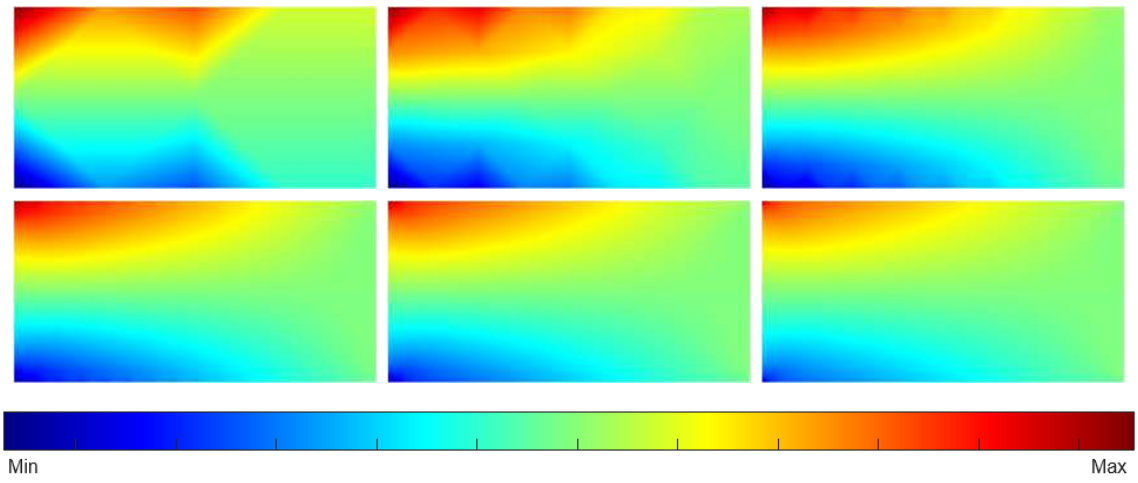

Figure 5.7: FEM simulation results: contour plots from triangular mesh of compressive stress in the x direction (σ_{xx}). From left to right, top to bottom: 4×2, 8×4, 16×8, 32×16, 64×32, and 128×64 meshes configurations

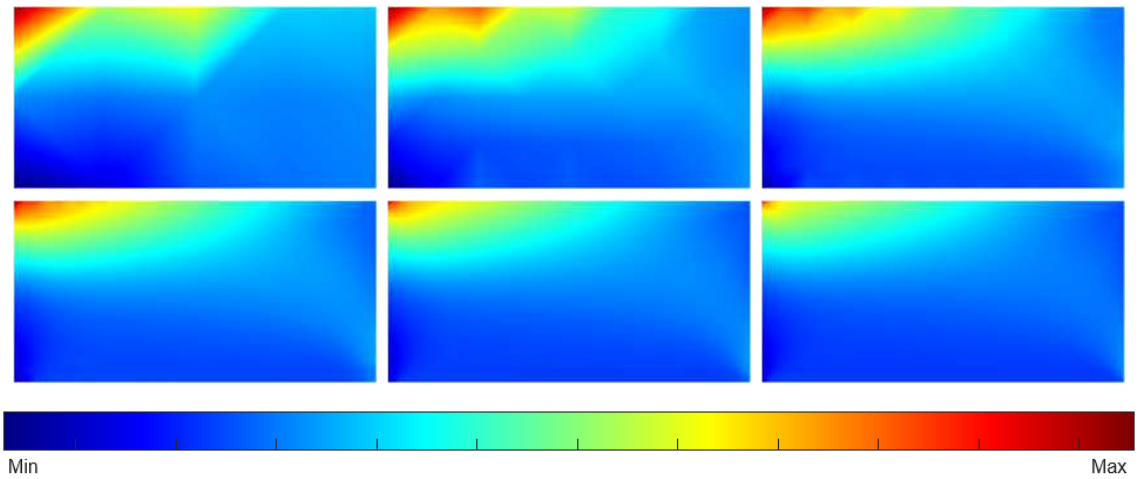

Figure 5.8: FEM simulation results: contour plots from triangular mesh for compressive stress in the first principal direction (σ_{11}). From left to right, top to bottom: 4×2, 8×4, 16×8, 32×16, 64×32, and 128×64 meshes configurations

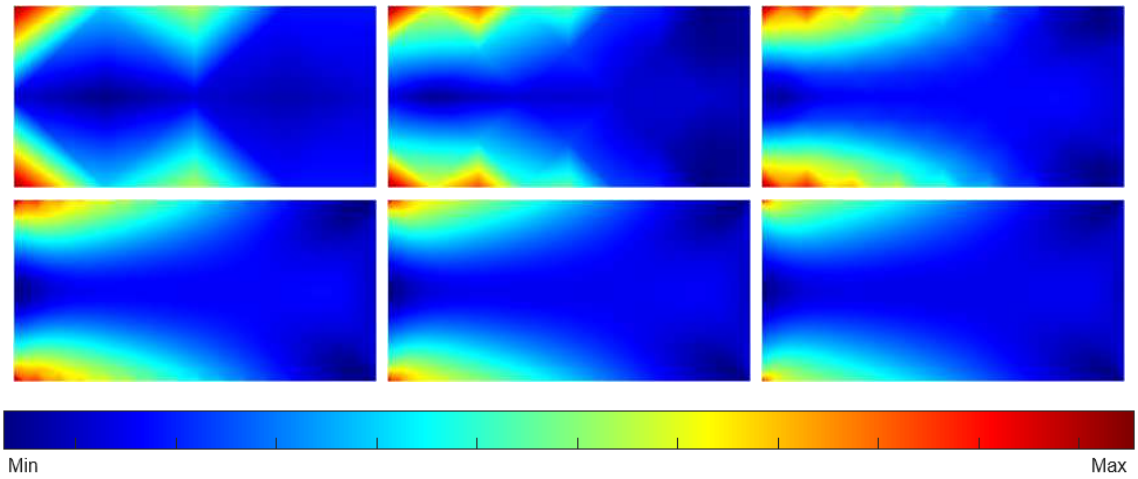

Figure 5.9: FEM simulation results: contour plots from triangular mesh for von Mises stress ($\sigma_{\text{von Mises}}$). From left to right, top to bottom: 4×2, 8×4, 16×8, 32×16, 64×32, and 128×64 meshes configurations

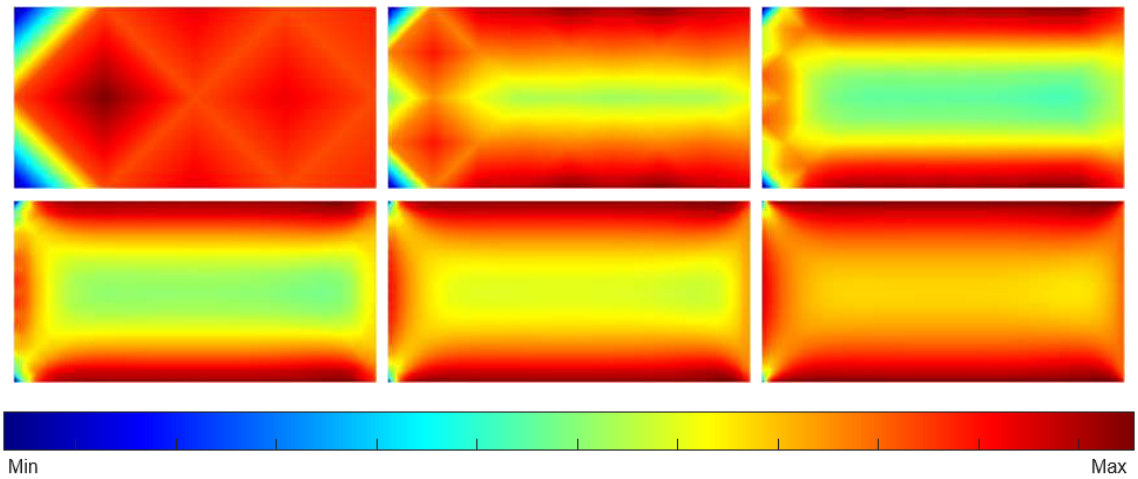

Figure 5.10: FEM simulation results: contour plots from triangular mesh for shear stress (τ_{xy}). From left to right, top to bottom: 4×2, 8×4, 16×8, 32×16, 64×32, and 128×64 meshes configurations

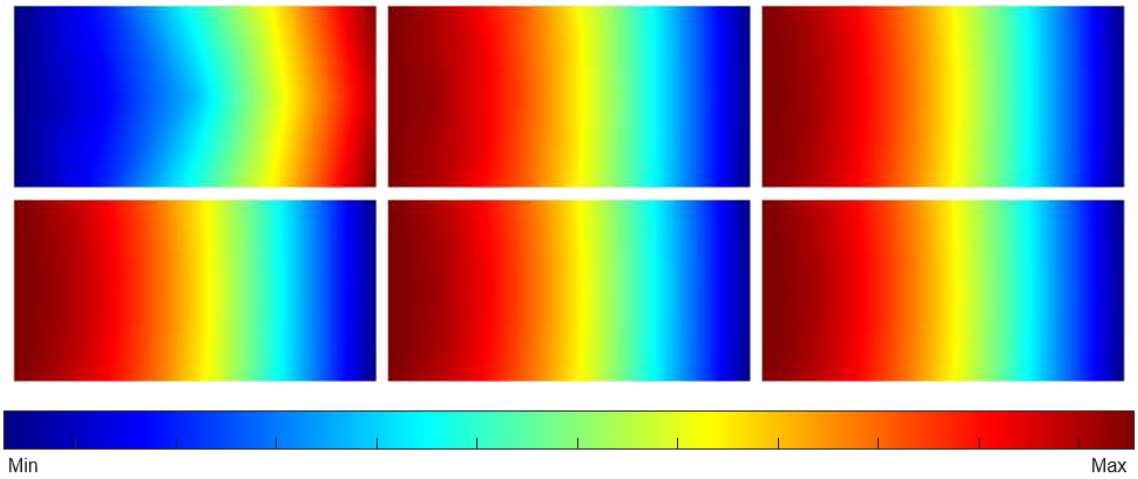

Figure 5.11: FEM simulation results: contour plots from triangular mesh for deflection (δ_y). From left to right, top to bottom: 4×2, 8×4, 16×8, 32×16, 64×32, and 128×64 meshes configurations

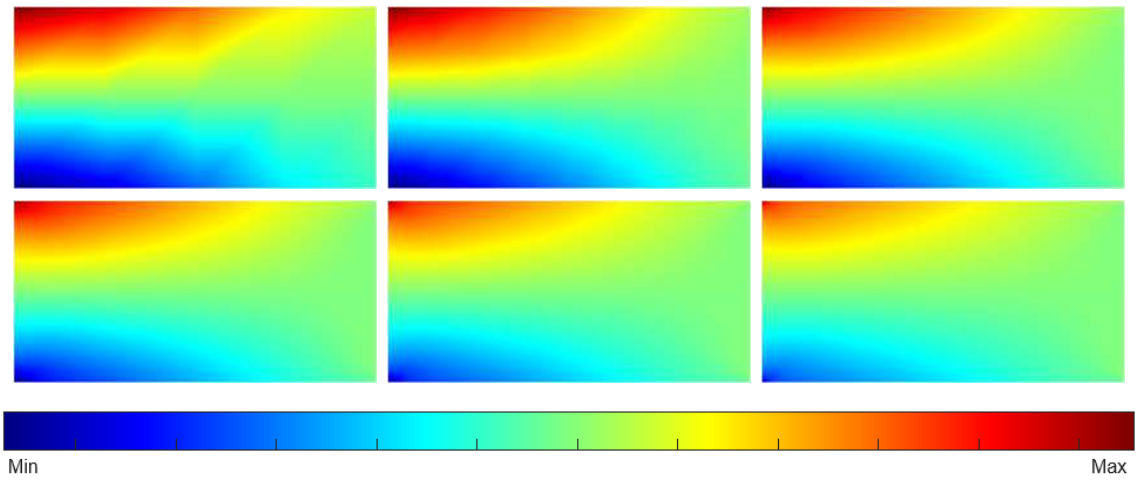

Figure 5.12: FEM simulation results: contour plots from square mesh of compressive stress in the x direction (σ_{xx}). From left to right, top to bottom: 4×2, 8×4, 16×8, 32×16, 64×32, and 128×64 meshes configurations

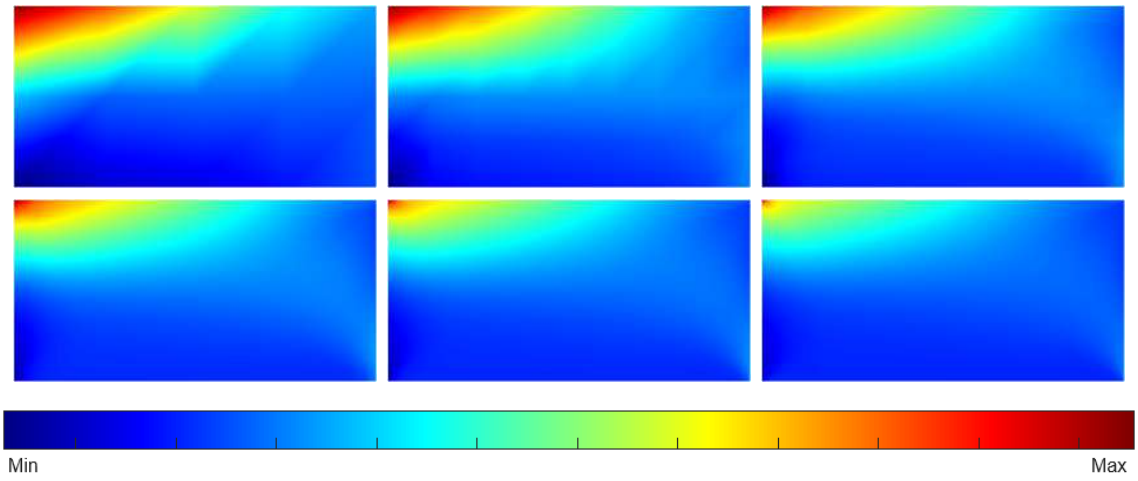

Figure 5.13: FEM simulation results: contour plots from square mesh for compressive stress in the first principal direction (σ_{11}). From left to right, top to bottom: 4×2, 8×4, 16×8, 32×16, 64×32, and 128×64 meshes configurations

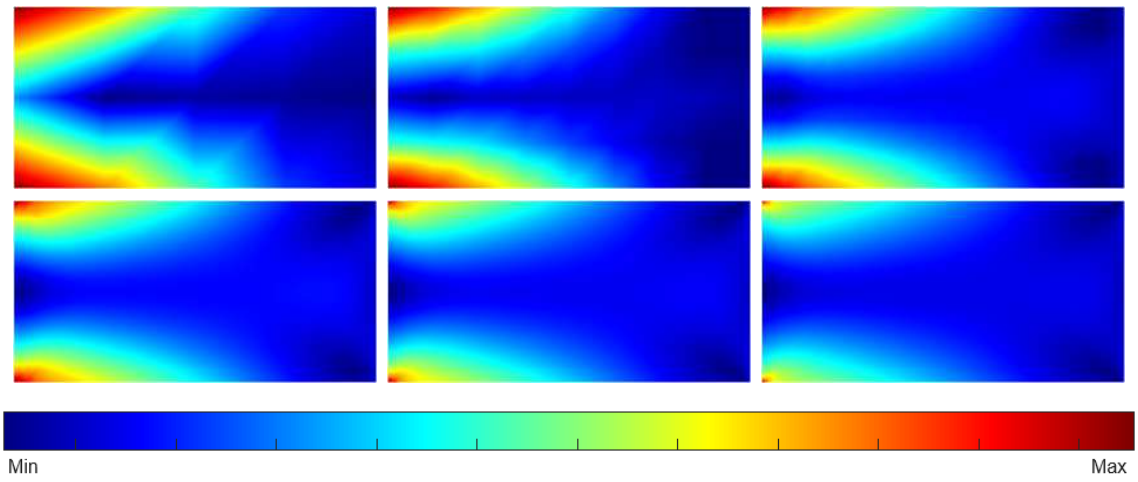

Figure 5.14: FEM simulation results: contour plots from square mesh for von Mises stress ($\sigma_{\text{von Mises}}$). From left to right, top to bottom: 4×2, 8×4, 16×8, 32×16, 64×32, and 128×64 meshes configurations

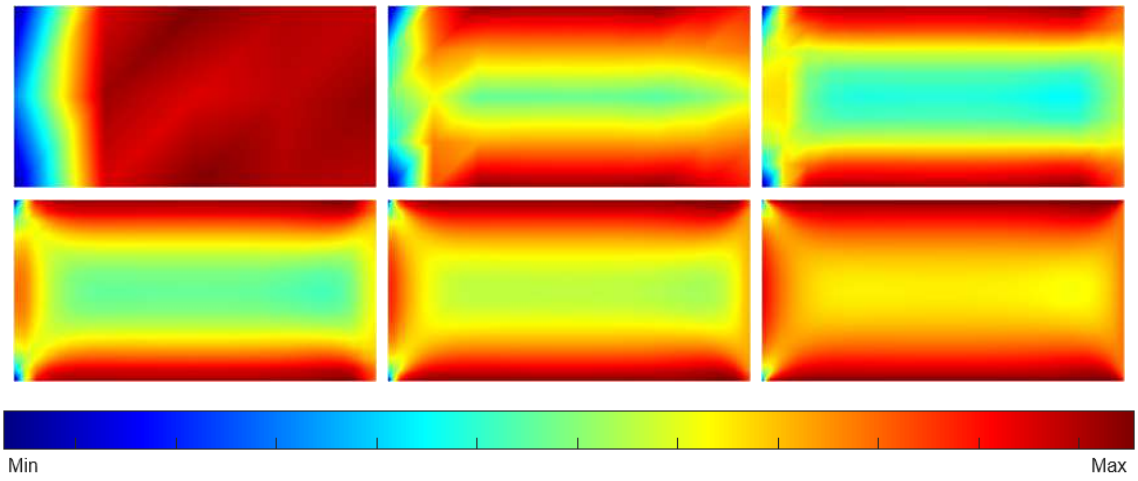

Figure 5.15: FEM simulation results: contour plots from square mesh for shear stress (τ_{xy}). From left to right, top to bottom: 4×2, 8×4, 16×8, 32×16, 64×32, and 128×64 meshes configurations

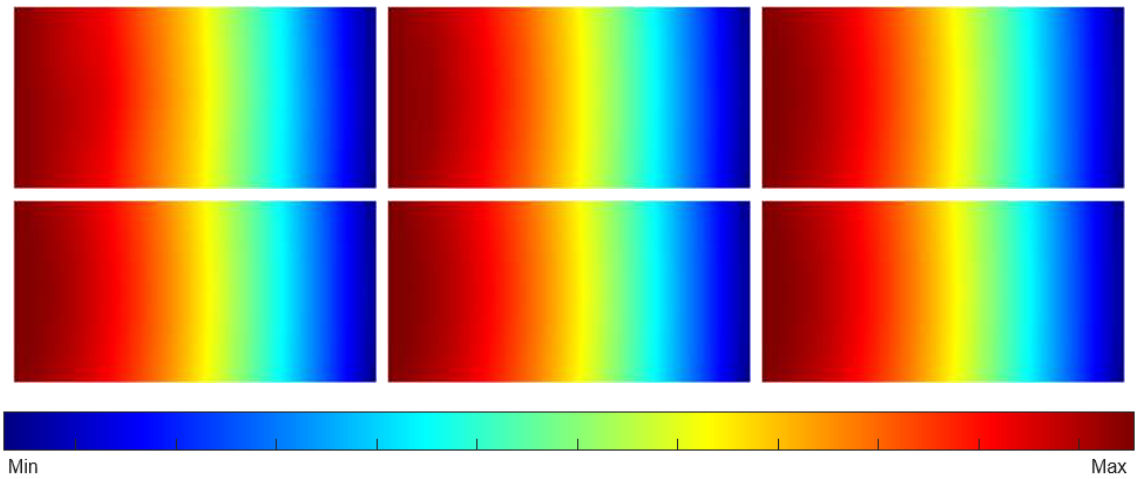

Figure 5.16: FEM simulation results: contour plots from square mesh for deflection (δ_y). From left to right, top to bottom: 4×2, 8×4, 16×8, 32×16, 64×32, and 128×64 meshes configurations

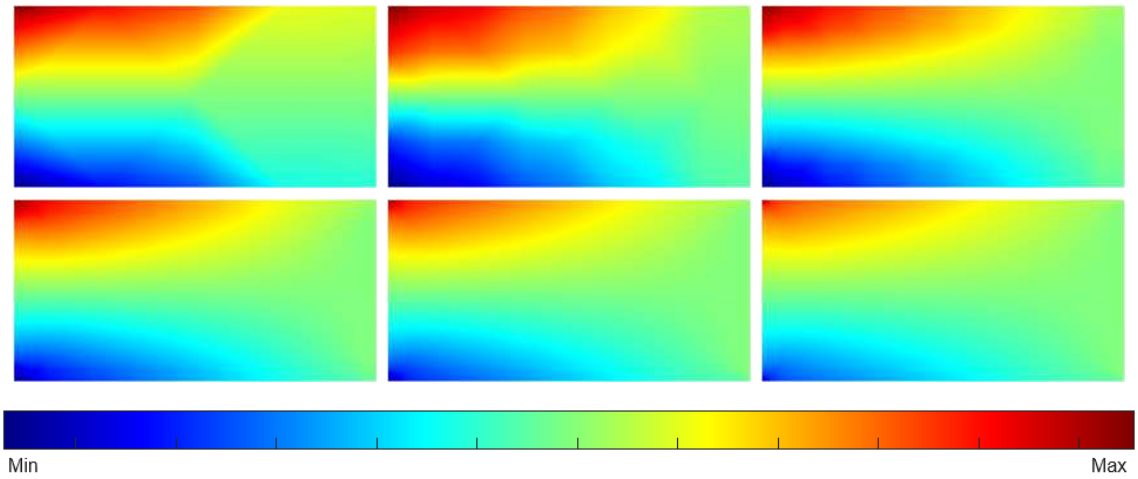

Figure 5.17: RPIM with constant base: contour plots from triangular mesh of compressive stress in the x direction (σ_{xx}). From left to right, top to bottom: 4×2, 8×4, 16×8, 32×16, 64×32, and 128×64 meshes configurations

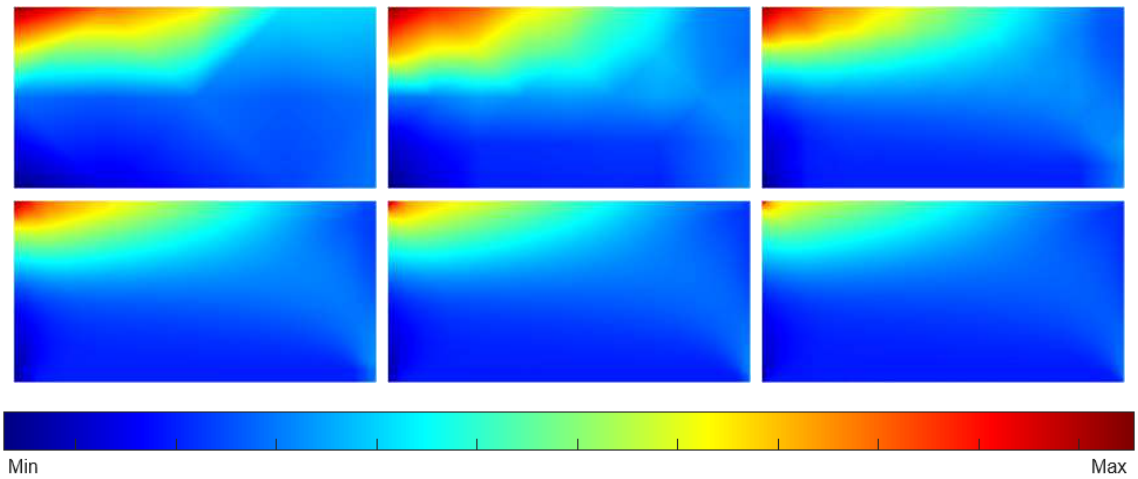

Figure 5.18: RPIM with constant base: contour plots from triangular mesh for compressive stress in the first principal direction (σ_{11}). From left to right, top to bottom: 4×2, 8×4, 16×8, 32×16, 64×32, and 128×64 meshes configurations

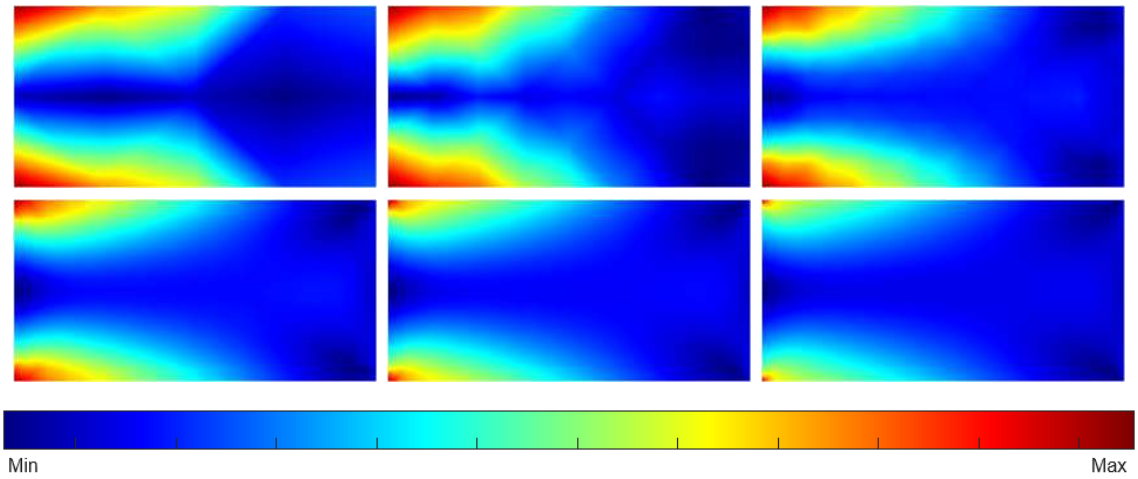

Figure 5.19: RPIM with constant base: contour plots from triangular mesh for von Mises stress ($\sigma_{\text{von Mises}}$). From left to right, top to bottom: 4×2, 8×4, 16×8, 32×16, 64×32, and 128×64 meshes configurations

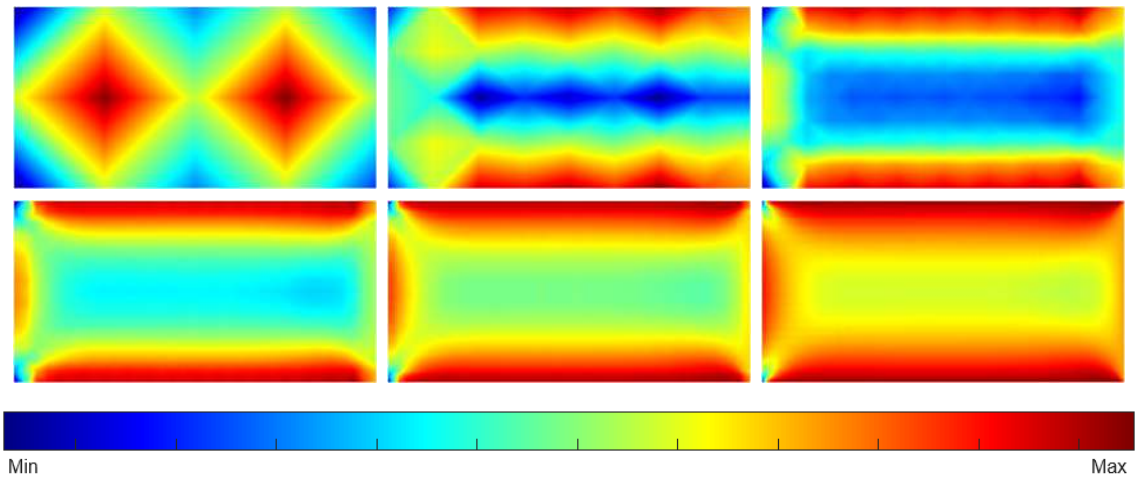

Figure 5.20: RPIM with constant base: contour plots from triangular mesh for shear stress (τ_{xy}). From left to right, top to bottom: 4×2, 8×4, 16×8, 32×16, 64×32, and 128×64 meshes configurations

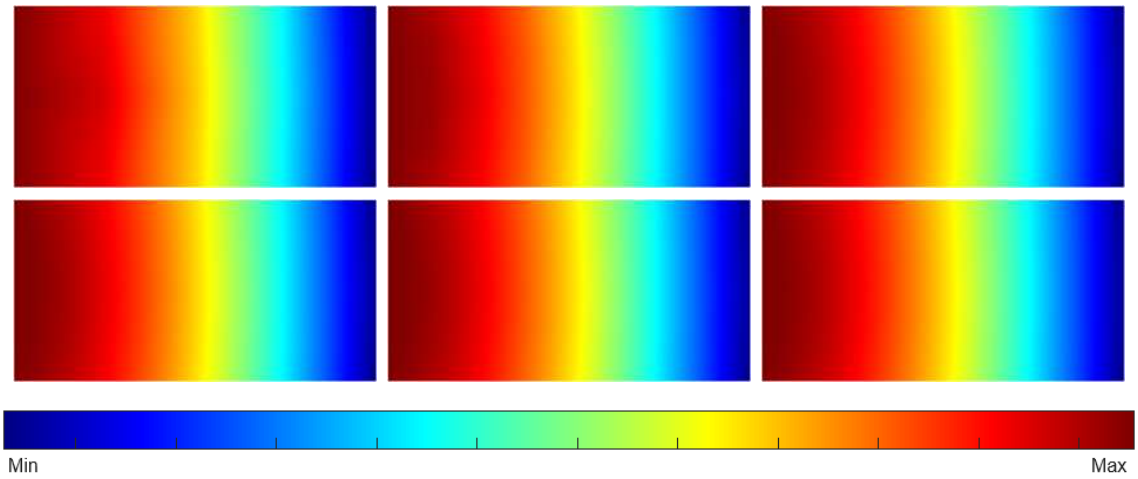

Figure 5.21: RPIM with constant base: contour plots from triangular mesh for deflection (δ_y). From left to right, top to bottom: 4×2, 8×4, 16×8, 32×16, 64×32, and 128×64 meshes configurations

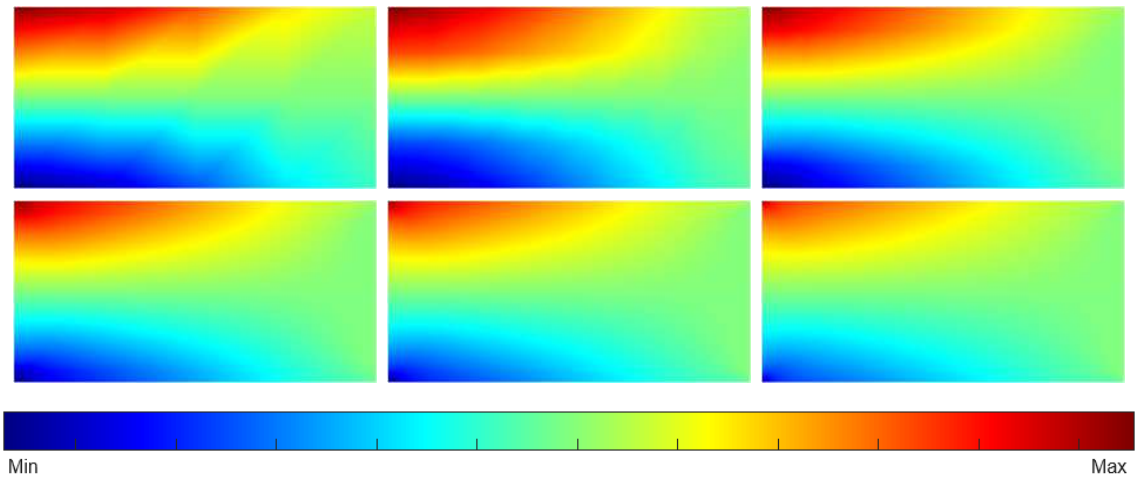

Figure 5.22: RPIM with constant base: contour plots from square mesh of compressive stress in the x direction (σ_{xx}). From left to right, top to bottom: 4×2, 8×4, 16×8, 32×16, 64×32, and 128×64 meshes configurations

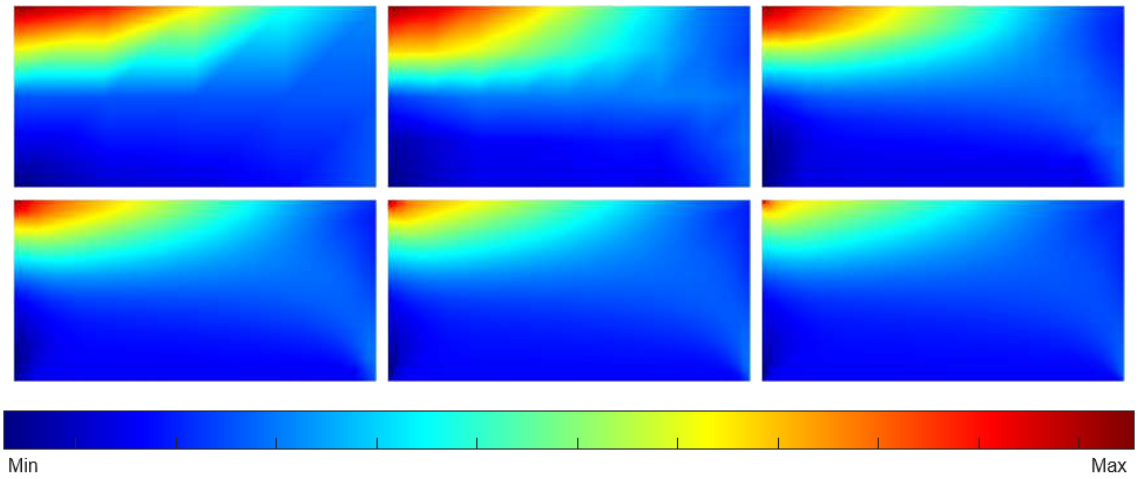

Figure 5.23: RPIM with constant base: contour plots from square mesh for compressive stress in the first principal direction (σ_{11}). From left to right, top to bottom: 4×2, 8×4, 16×8, 32×16, 64×32, and 128×64 meshes configurations

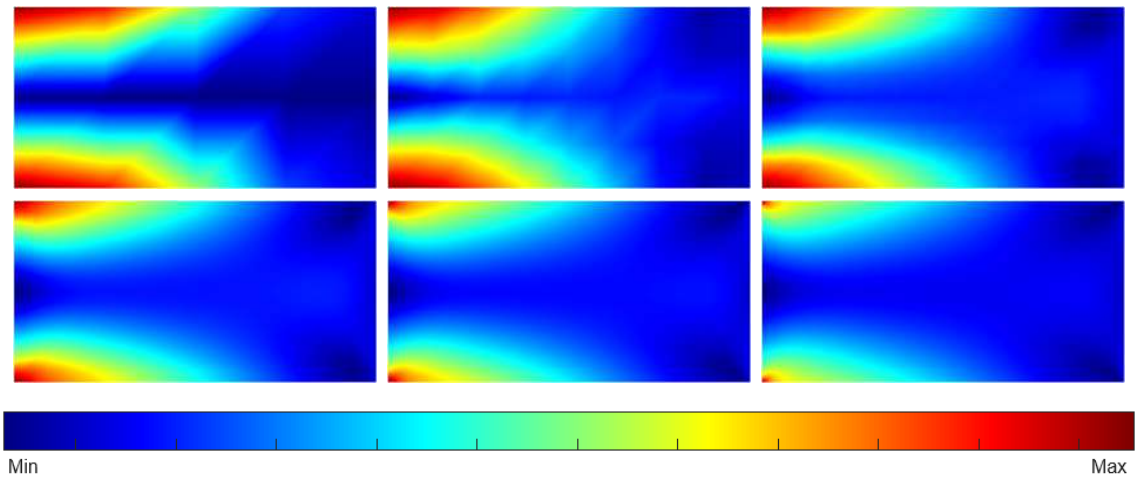

Figure 5.24: RPIM with constant base: contour plots from square mesh for von Mises stress ($\sigma_{\text{von Mises}}$). From left to right, top to bottom: 4×2, 8×4, 16×8, 32×16, 64×32, and 128×64 meshes configurations

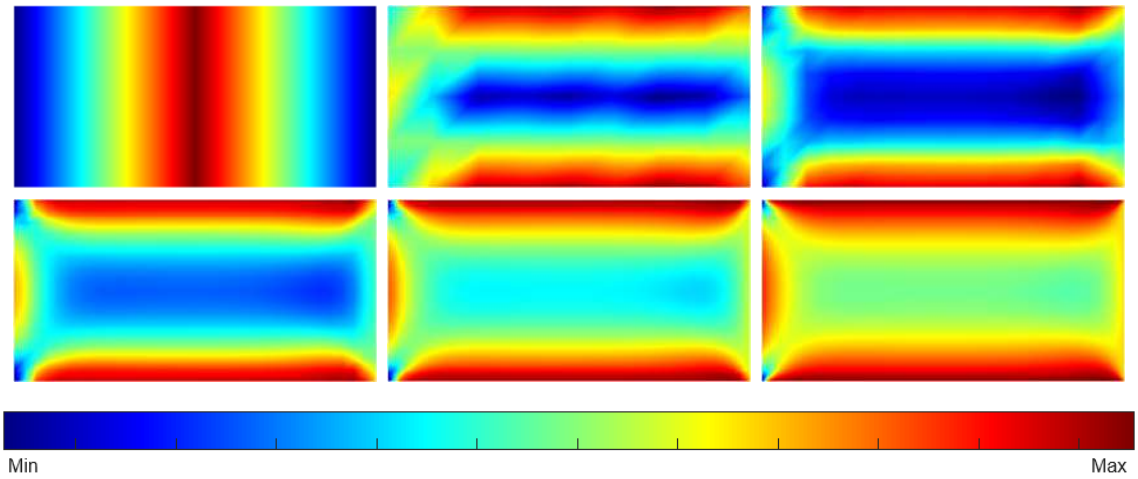

Figure 5.25: RPIM with constant base: contour plots from square mesh for shear stress (τ_{xy}). From left to right, top to bottom: 4×2, 8×4, 16×8, 32×16, 64×32, and 128×64 meshes configurations

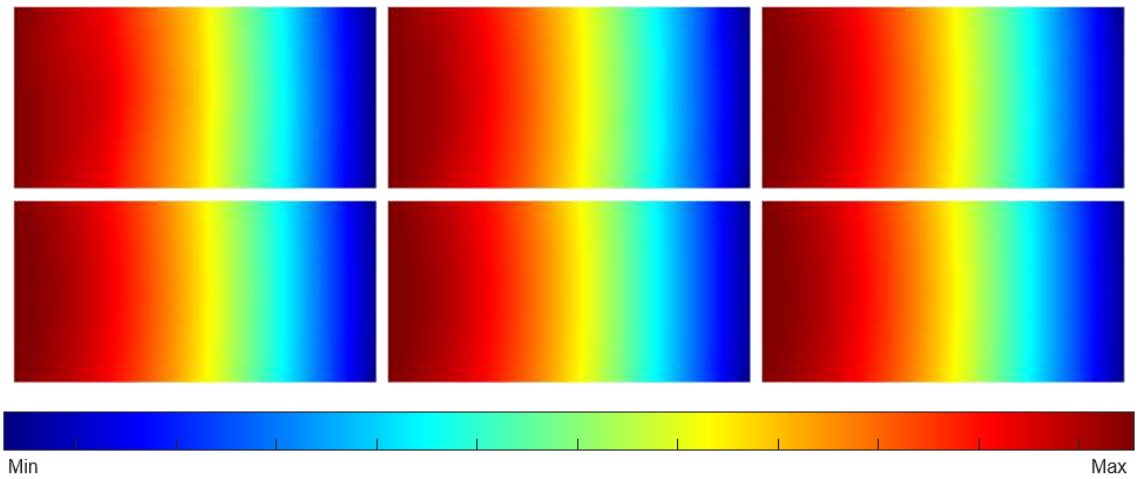

Figure 5.26: RPIM with constant base: contour plots from square mesh for deflection (δ_y). From left to right, top to bottom: 4×2, 8×4, 16×8, 32×16, 64×32, and 128×64 meshes configurations

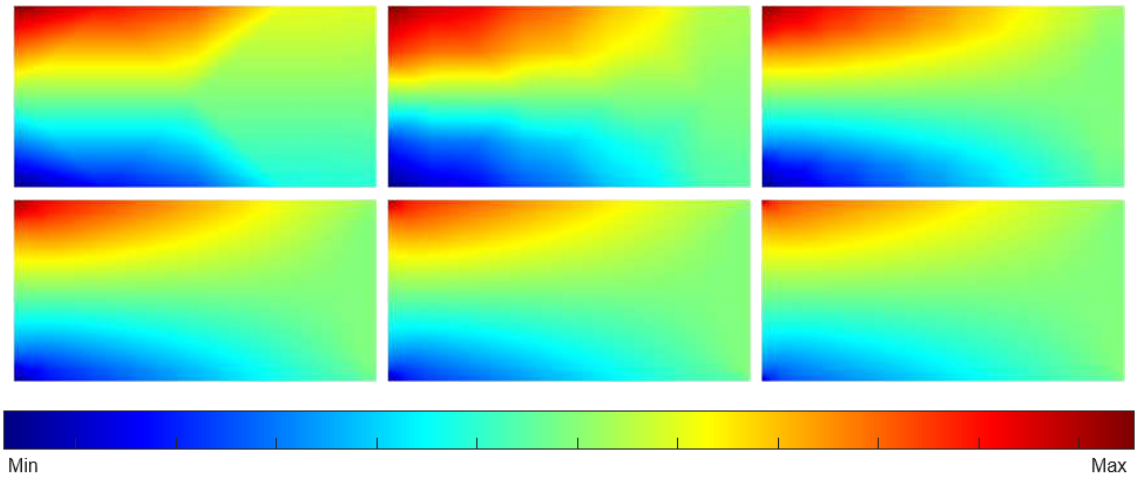

Figure 5.27: RPIM with linear base: contour plots from triangular mesh of compressive stress in the x direction (σ_{xx}). From left to right, top to bottom: 4×2, 8×4, 16×8, 32×16, 64×32, and 128×64 meshes configurations

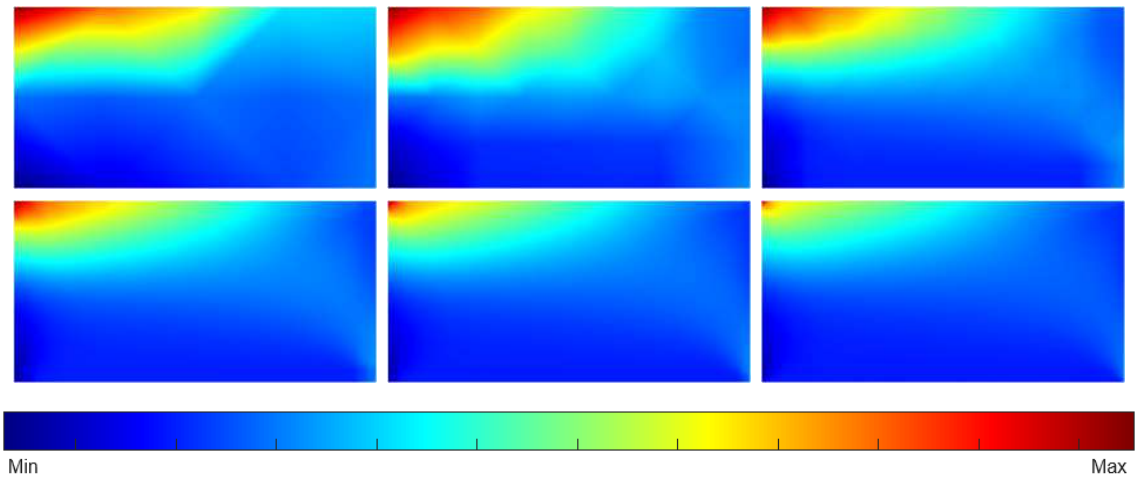

Figure 5.28: RPIM with linear base: contour plots from triangular mesh for compressive stress in the first principal direction (σ_{11}). From left to right, top to bottom: 4×2, 8×4, 16×8, 32×16, 64×32, and 128×64 meshes configurations

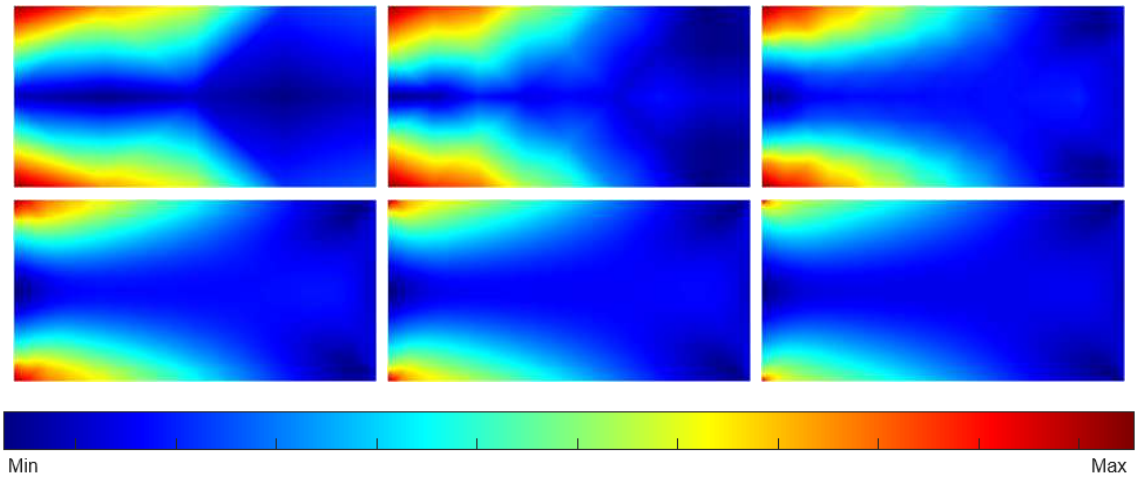

Figure 5.29: RPIM with linear base: contour plots from triangular mesh for von Mises stress ($\sigma_{\text{von Mises}}$). From left to right, top to bottom: 4×2, 8×4, 16×8, 32×16, 64×32, and 128×64 meshes configurations

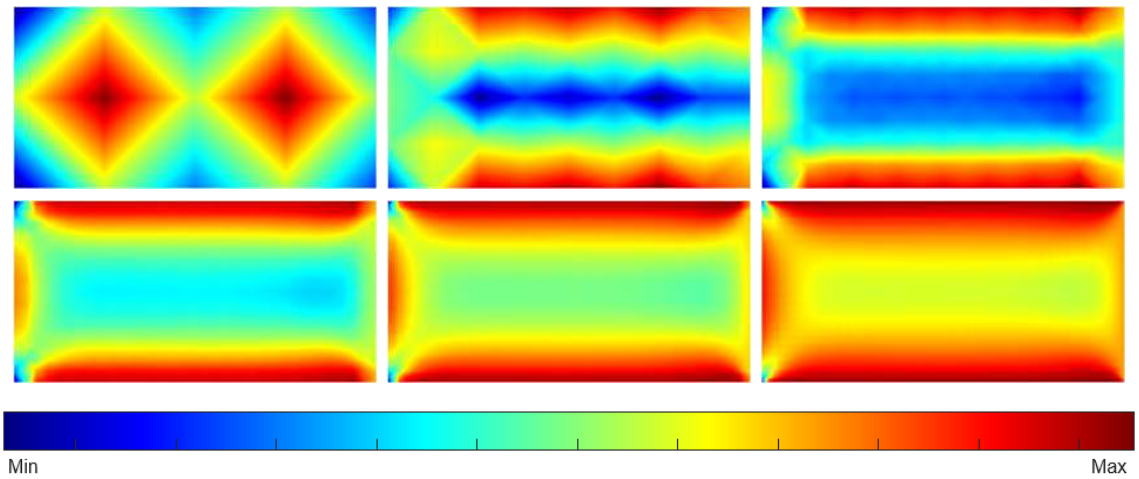

Figure 5.30: RPIM with linear base: contour plots from triangular mesh for shear stress (τ_{xy}). From left to right, top to bottom: 4×2, 8×4, 16×8, 32×16, 64×32, and 128×64 meshes configurations

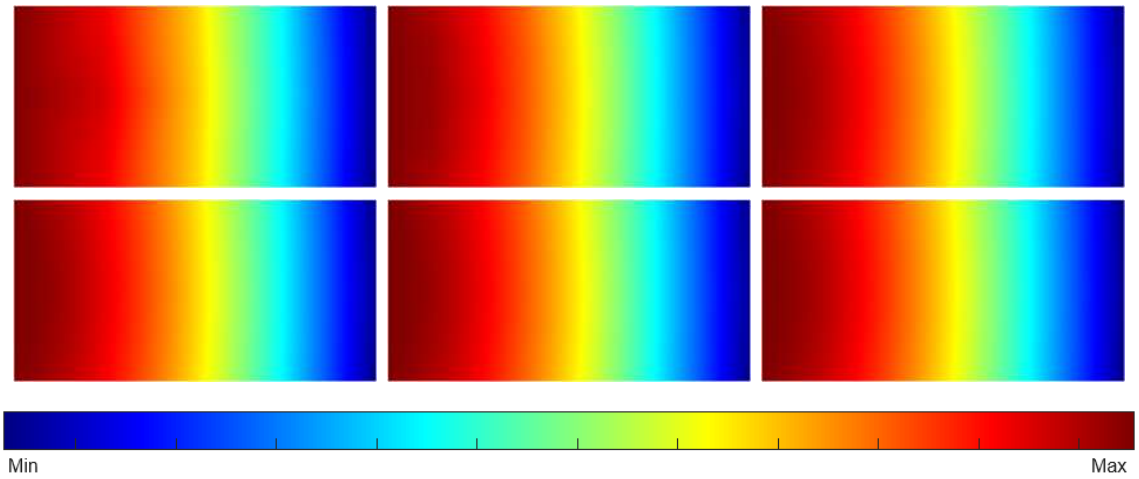

Figure 5.31: RPIM with linear base: contour plots from triangular mesh for deflection (δ_y). From left to right, top to bottom: 4×2, 8×4, 16×8, 32×16, 64×32, and 128×64 meshes configurations

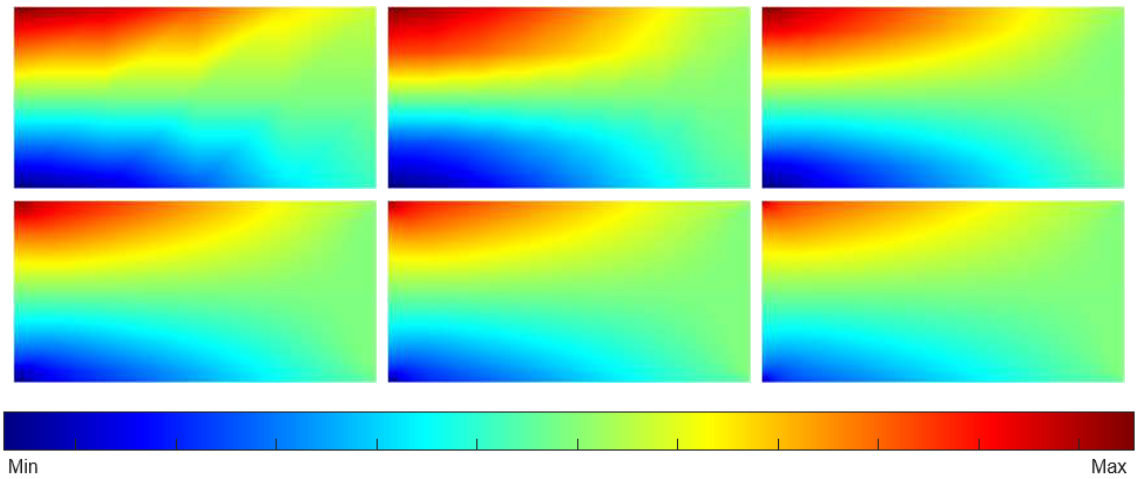

Figure 5.32: RPIM with linear base: contour plots from square mesh of compressive stress in the x direction (σ_{xx}). From left to right, top to bottom: 4×2, 8×4, 16×8, 32×16, 64×32, and 128×64 meshes configurations

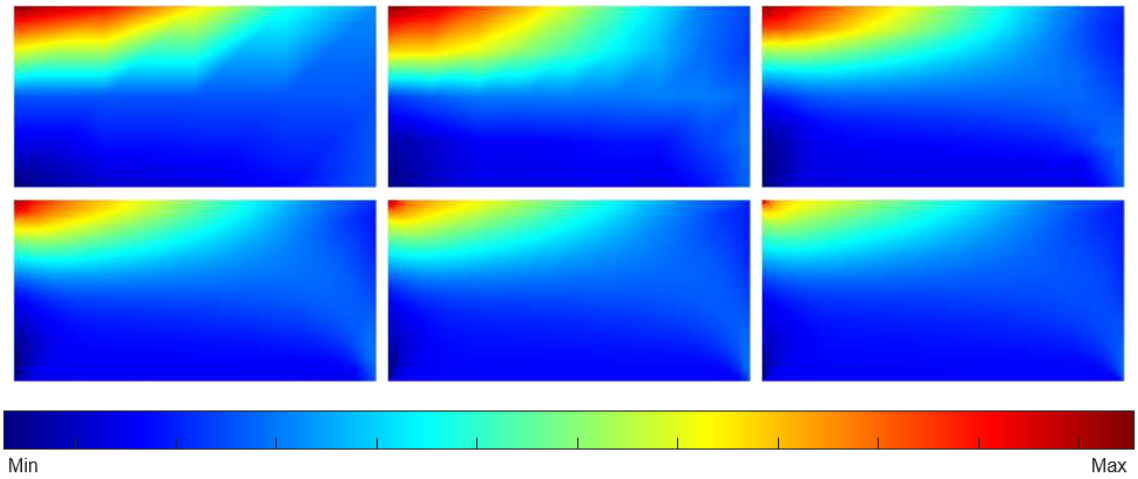

Figure 5.33: RPIM with linear base: contour plots from square mesh for compressive stress in the first principal direction (σ_{11}). From left to right, top to bottom: 4×2, 8×4, 16×8, 32×16, 64×32, and 128×64 meshes configurations

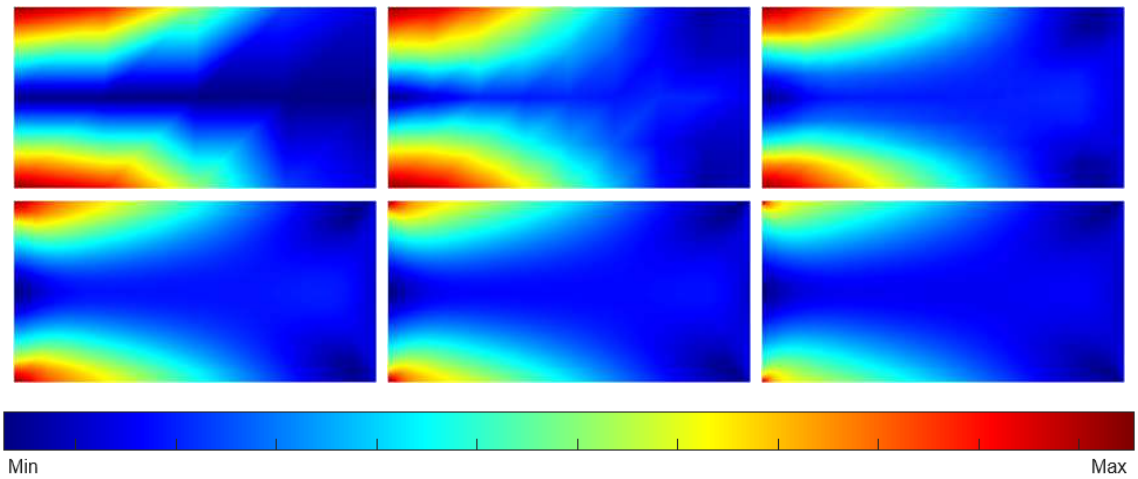

Figure 5.34: RPIM with linear base: contour plots from square mesh for von Mises stress ($\sigma_{\text{von Mises}}$). From left to right, top to bottom: 4×2, 8×4, 16×8, 32×16, 64×32, and 128×64 meshes configurations

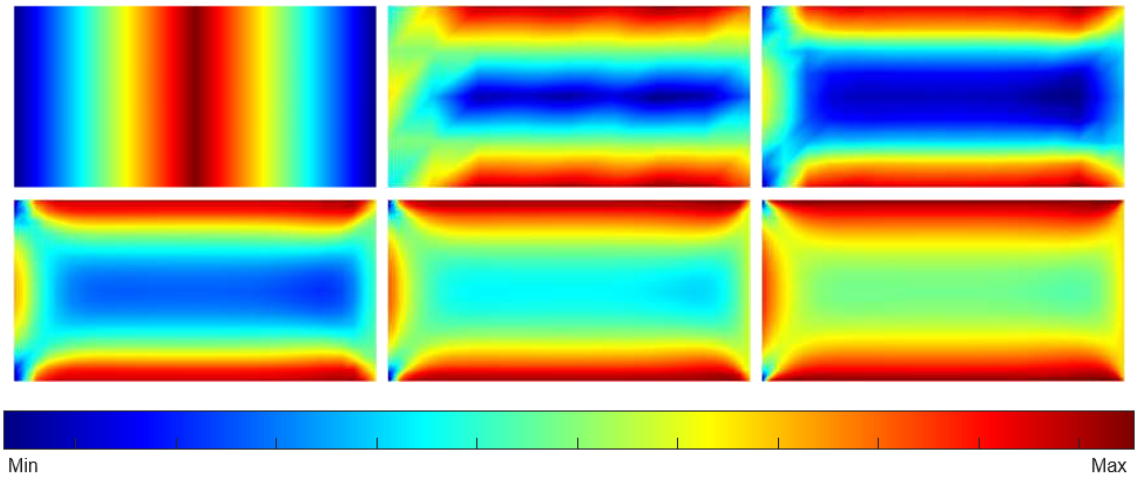

Figure 5.35: RPIM with linear base: contour plots from square mesh for shear stress (τ_{xy}). From left to right, top to bottom: 4×2, 8×4, 16×8, 32×16, 64×32, and 128×64 meshes configurations

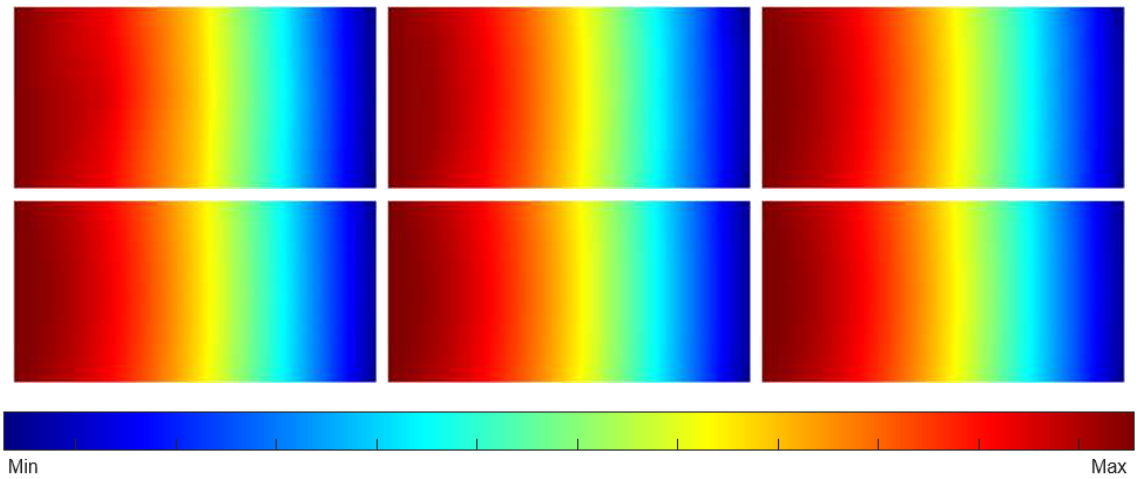

Figure 5.36: RPIM with linear base: contour plots from square mesh for deflection (δ_y). From left to right, top to bottom: 4×2, 8×4, 16×8, 32×16, 64×32, and 128×64 meshes configurations

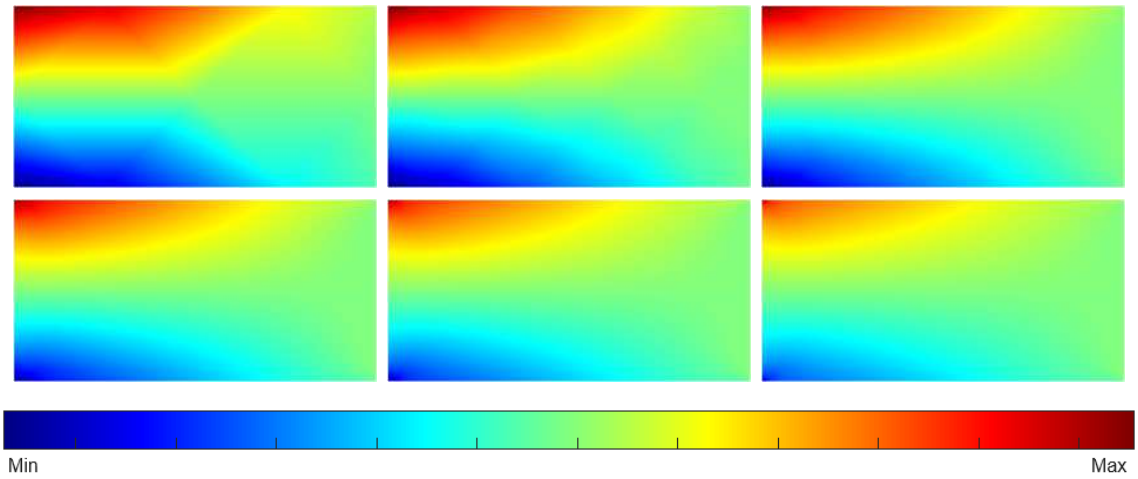

Figure 5.37: NNRPIM with first degree of neighborhood: contour plots from triangular mesh of compressive stress in the x direction (σ_{xx}). From left to right, top to bottom: 4×2, 8×4, 16×8, 32×16, 64×32, and 128×64 meshes configurations

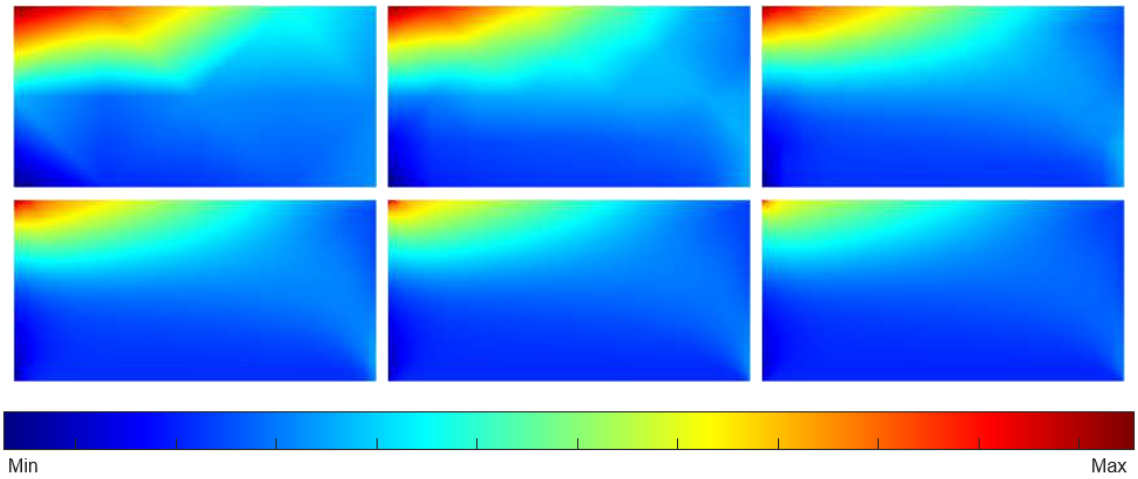

Figure 5.38: NNRPIM with first degree of neighborhood: contour plots from triangular mesh for compressive stress in the first principal direction (σ_{11}). From left to right, top to bottom: 4×2, 8×4, 16×8, 32×16, 64×32, and 128×64 meshes configurations

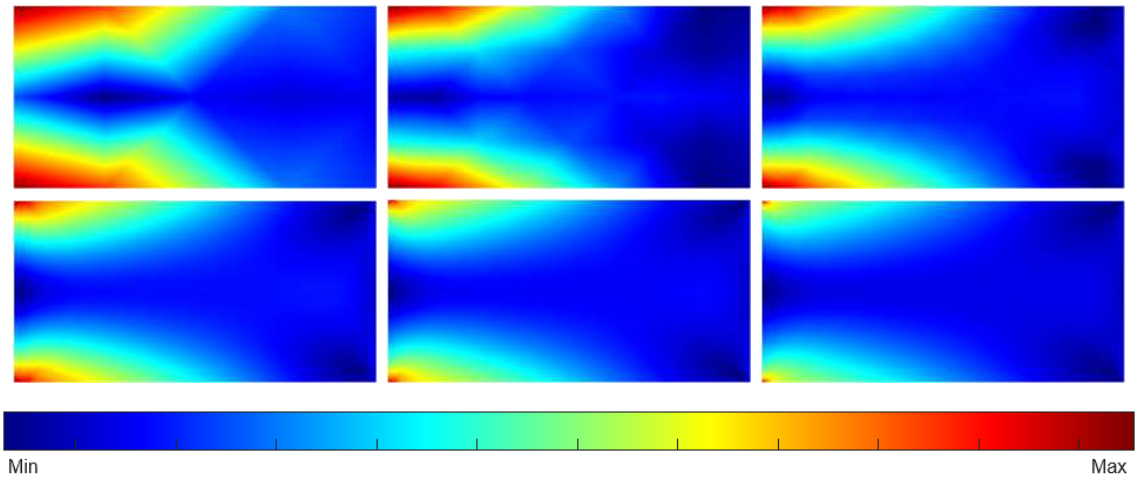

Figure 5.39: NNRPIM with first degree of neighborhood: contour plots from triangular mesh for von Mises stress ($\sigma_{\text{von Mises}}$). From left to right, top to bottom: 4×2, 8×4, 16×8, 32×16, 64×32, and 128×64 meshes configurations

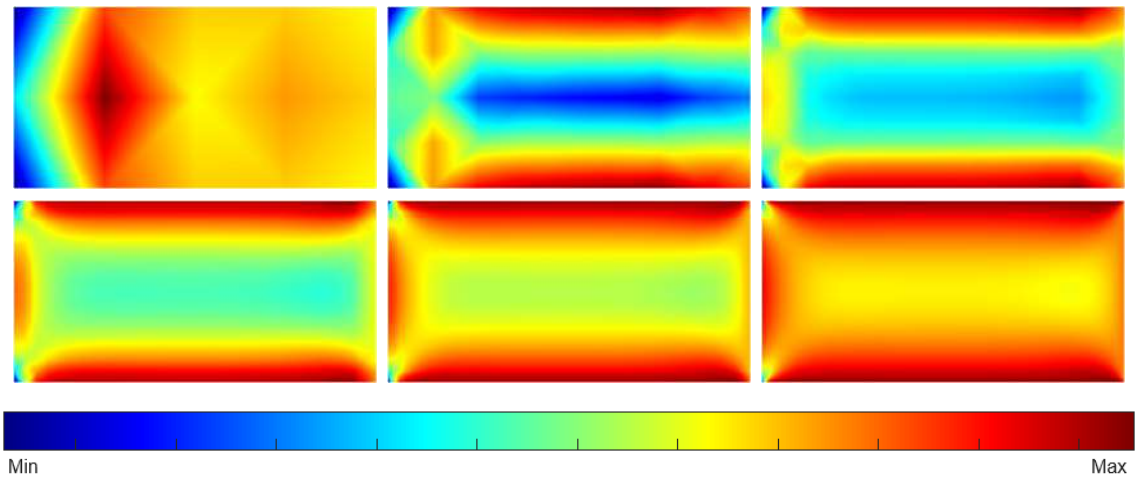

Figure 5.40: NNRPIM with first degree of neighborhood: contour plots from triangular mesh for shear stress (τ_{xy}). From left to right, top to bottom: 4×2, 8×4, 16×8, 32×16, 64×32, and 128×64 meshes configurations

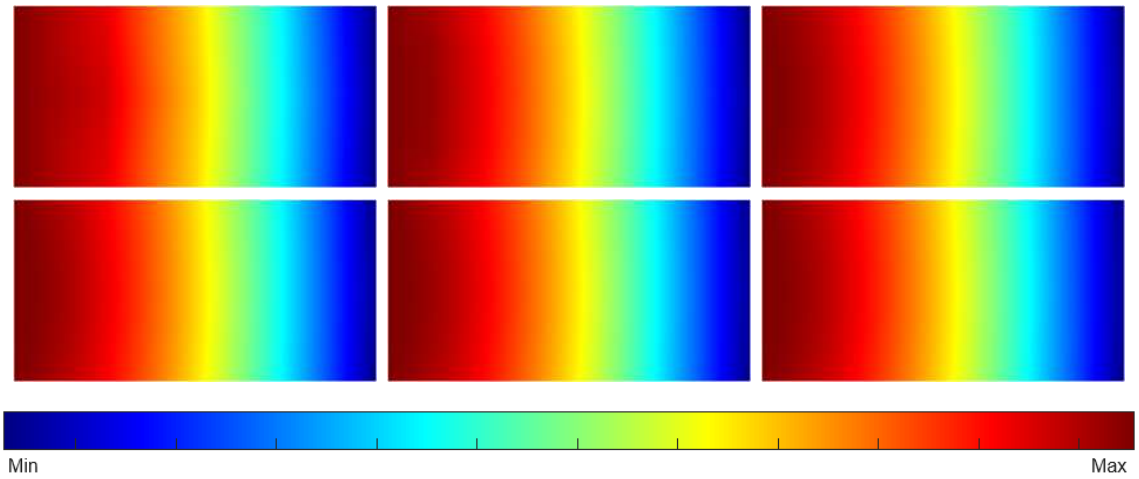

Figure 5.41: NNRPIM with first degree of neighborhood: contour plots from triangular mesh for deflection (δ_y). From left to right, top to bottom: 4×2, 8×4, 16×8, 32×16, 64×32, and 128×64 meshes configurations

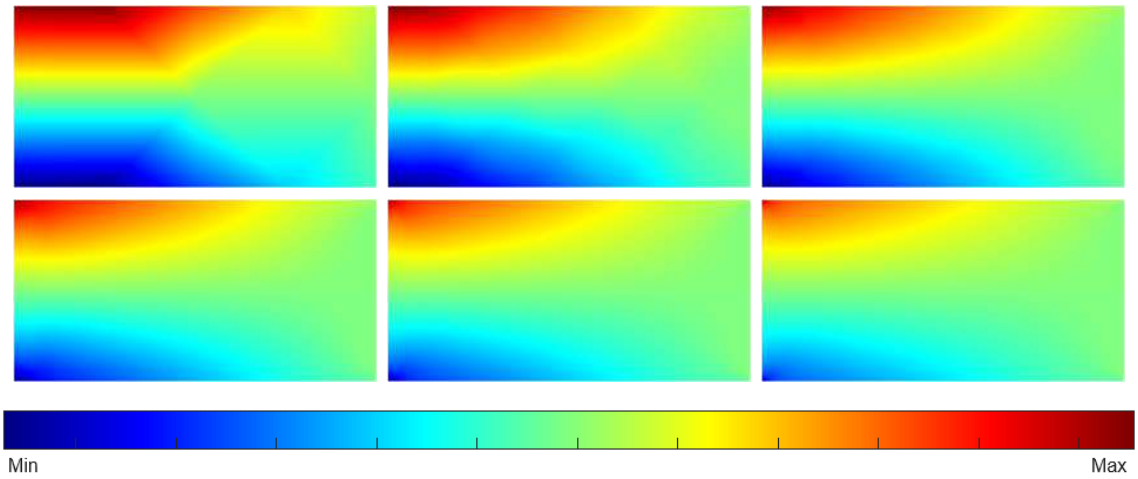

Figure 5.42: NNRPIM with second degree of neighborhood: contour plots from triangular mesh of compressive stress in the x direction (σ_{xx}). From left to right, top to bottom: 4×2, 8×4, 16×8, 32×16, 64×32, and 128×64 meshes configurations

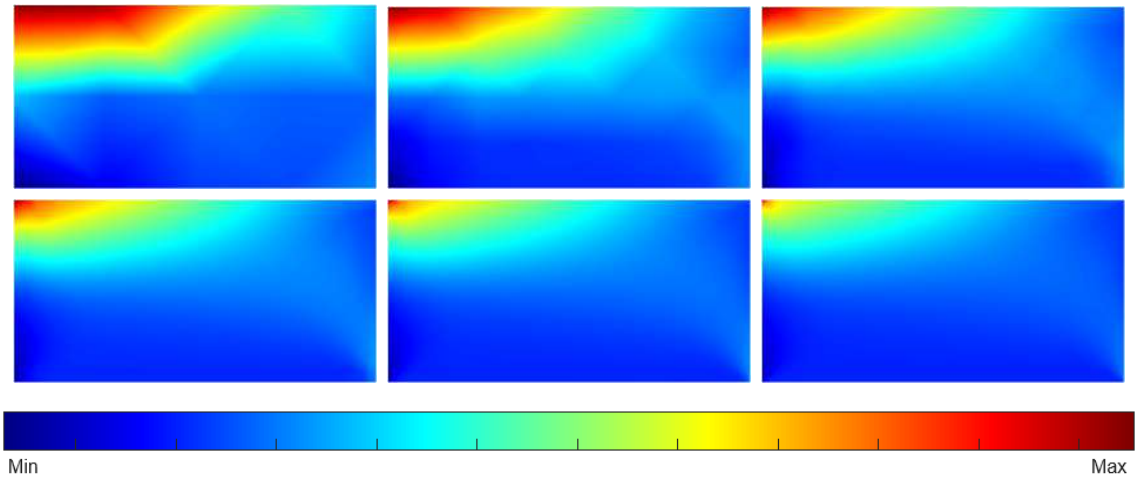

Figure 5.43: NNRPIM with second degree of neighborhood: contour plots from triangular mesh for compressive stress in the first principal direction (σ_{11}). From left to right, top to bottom: 4×2, 8×4, 16×8, 32×16, 64×32, and 128×64 meshes configurations

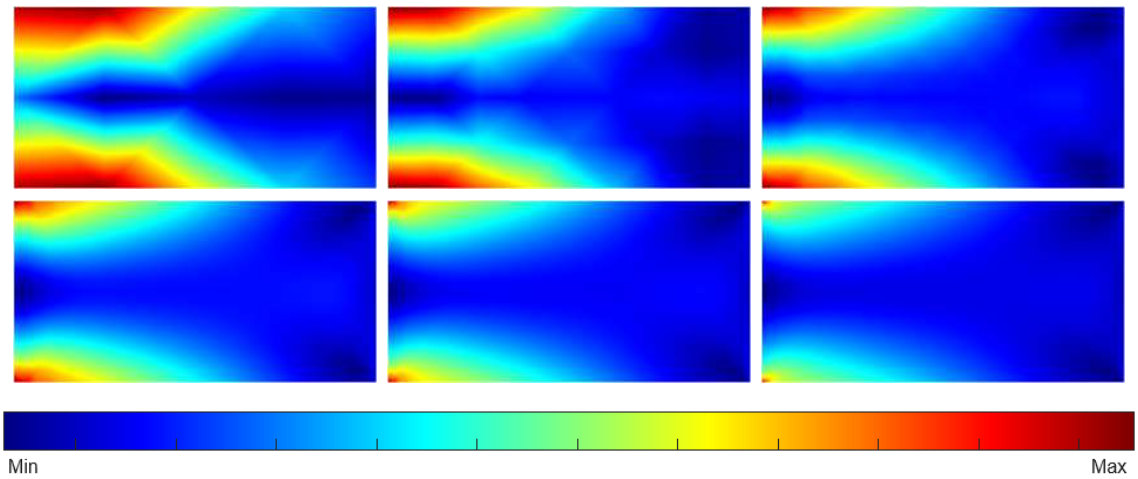

Figure 5.44: NNRPIM with second degree of neighborhood: contour plots from triangular mesh for von Mises stress ($\sigma_{\text{von Mises}}$). From left to right, top to bottom: 4×2, 8×4, 16×8, 32×16, 64×32, and 128×64 meshes configurations

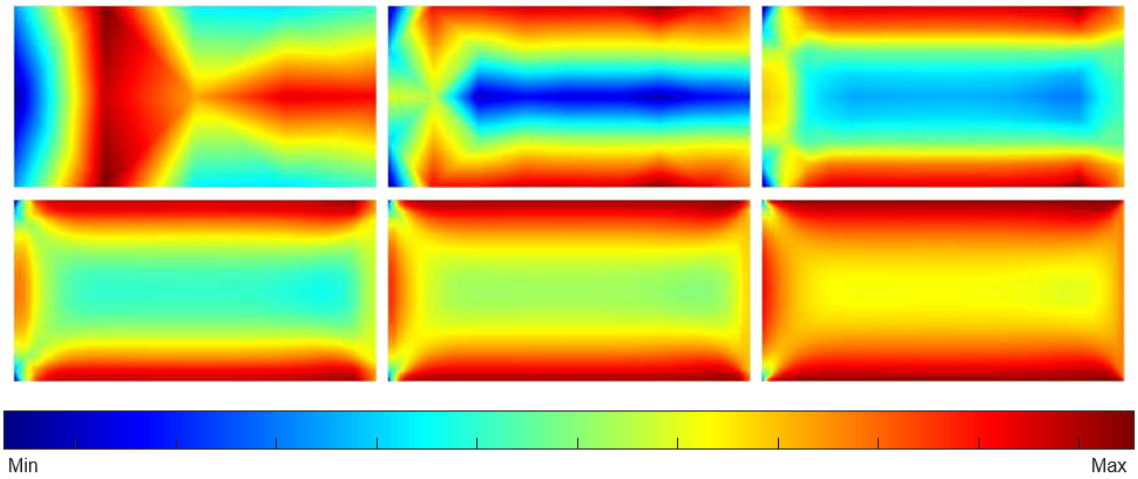

Figure 5.45: NNRPIM with second degree of neighborhood: contour plots from triangular mesh for shear stress (τ_{xy}). From left to right, top to bottom: 4×2, 8×4, 16×8, 32×16, 64×32, and 128×64 meshes configurations

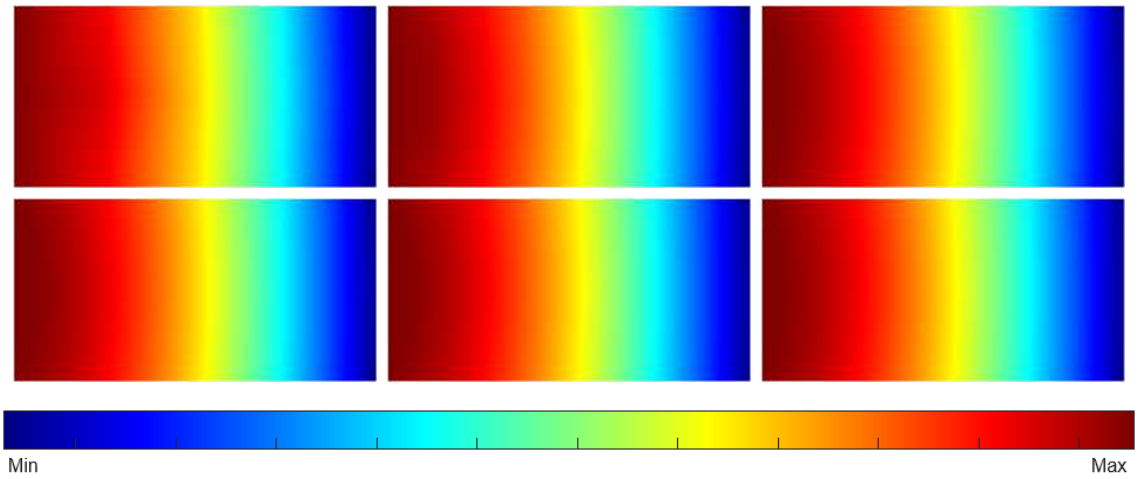

Figure 5.46: NNRPIM with second degree of neighborhood: contour plots from triangular mesh for deflection (δ_y). From left to right, top to bottom: 4×2, 8×4, 16×8, 32×16, 64×32, and 128×64 meshes configurations

Table 5.2: Maximum and minimum values acquired from the FEM simulations with triangular meshes

	FEM's Simulations to Triangular Meshes									
	σ_{xx}		σ_{11}		$\sigma_{vonMises}$		τ_{xy}		δy	
	Max	Min	Max	Min	Max	Min	Max	Min	Max	Min
Mesh 4×2	6.06	-6.06	6.81	-1.07	6.35	1.33	-0.77	-1.94	0	-0.02
Mesh 8×4	9.94	-9.94	10.55	-2.38	9.58	1.65	-0.6	-2.14	0	-0.03
Mesh 16×8	12.47	-12.47	13.12	-3.09	11.88	1.26	-0.3	-2.47	0	-0.04
Mesh 32×16	14.47	-14.47	15.29	-3.52	13.87	1.1	-0.1	-2.99	0	-0.04
Mesh 64×32	16.65	-16.65	17.71	-3.94	16.11	0.96	-0.02	-3.67	0	-0.04
Mesh 128×64	19.32	-19.32	20.67	-4.45	18.85	0.84	0.01	-4.48	0	-0.04

By analyzing the information presented in the contour plots, we observe a refinement in precision and a progressive improvement toward a more accurate representation of the beam's state as the mesh is refined. These changes are particularly evident in the shear stress images, where significant evolution can be seen from the initial coarse mesh (4×2) to the finest mesh (128×64). In contrast, for the vertical deflection, there are no substantial differences visible in the contour plots as the mesh is refined.

The following tables from 5.2 to 5.9 show us the maximum and minimum values for the contour plots images, where table 5.2 and 5.3 are for the FEM simulations to triangular and square meshes respectively, the tables 5.4 and 5.5 for the RPIM with base's constant to triangular and square meshes respectively, the tables RPIM with linear's base is 5.6 to the triangular meshes simulations and the 5.7 for the square ones. Finally, table 5.8 is for the NNRPIM simulations with the first degree of the neighborhood, while the 5.9 is for the simulations with the second degree of the neighborhood.

Table 5.3: Maximum and minimum values acquired from the FEM simulations with square meshes

	FEM's Simulations to Square Meshes									
	σ_{xx}		σ_{11}		$\sigma_{vonMises}$		τ_{xy}		δy	
	Max	Min	Max	Min	Max	Min	Max	Min	Max	Min
Mesh 4×2	7.71	-7.71	8.43	-1.27	7.87	1.4	-0.79	-2.15	0	-0.03
Mesh 8×4	10.54	-10.54	11.05	-2.13	10.16	1.8	-0.53	-2.07	0	-0.04
Mesh 16×8	12.6	-12.6	13.12	-2.6	12.04	1.39	-0.24	-2.29	0	-0.04
Mesh 32×16	14.53	-14.53	15.19	-2.96	13.94	1.02	-0.09	-2.76	0	-0.04
Mesh 64×32	16.74	-16.74	17.59	-3.34	16.18	0.9	-0.03	-3.38	0	-0.04
Mesh 128×64	19.43	-19.43	20.52	-3.79	18.91	0.82	-0.01	-4.13	0	-0.04

Table 5.4: Maximum and minimum values acquired from the RPIM from constant's base simulations with triangular meshes

	RPIM with Constant Base's Simulations to Triangular Meshes									
	σ_{xx}		σ_{11}		$\sigma_{vonMises}$		τ_{xy}		δy	
	Max	Min	Max	Min	Max	Min	Max	Min	Max	Min
Mesh 4×2	7.1	-7.1	7.36	-0.91	6.95	1.43	-0.82	-1.25	0	-0.04
Mesh 8×4	9.88	-9.91	10.13	-1.76	9.41	1.72	-0.39	-1.61	0	-0.04
Mesh 16×8	12	-12.02	12.34	-2.2	11.42	1.25	-0.1	-1.84	0	-0.04
Mesh 32×16	13.96	-13.99	14.45	-2.54	13.39	1.04	0.03	-2.39	0	-0.04
Mesh 64×32	16.14	-16.18	16.82	-2.9	15.61	0.88	0.06	-3	0	-0.04
Mesh 128×64	18.77	-18.82	19.66	-3.32	18.26	0.81	0.06	-3.7	0	-0.04

Table 5.5: Maximum and minimum values acquired from the RPIM from constant's base simulations with square meshes

	RPIM with Constant Base's Simulations to Square Meshes									
	σ_{xx}		σ_{11}		$\sigma_{vonMises}$		τ_{xy}		δy	
	Max	Min	Max	Min	Max	Min	Max	Min	Max	Min
Mesh 4×2	5.94	-5.94	6.12	-0.32	5.96	1.73	-1	-1.01	0	-0.04
Mesh 8×4	8.77	-8.77	8.93	-0.95	8.52	1.47	-0.5	-1.51	0	-0.04
Mesh 16×8	11.01	-11.02	11.23	-1.25	10.7	1.19	-0.18	-1.57	0	-0.04
Mesh 32×16	12.95	-12.96	13.26	-1.75	12.64	1.01	-0.03	-1.9	0	-0.04
Mesh 64×32	15	-15.01	15.43	-2.2	14.73	0.86	0	-2.39	0	-0.04
Mesh 128×64	17.42	-17.42	17.97	-2.53	17.19	0.79	0	-2.94	0	-0.04

Table 5.6: Maximum and minimum values acquired from the RPIM from linear's base simulations with triangular meshes

	RPIM with Linear Base's Simulations to Triangular Meshes									
	σ_{xx}		σ_{11}		$\sigma_{vonMises}$		τ_{xy}		δy	
	Max	Min	Max	Min	Max	Min	Max	Min	Max	Min
Mesh 4×2	7.11	-7.11	7.36	-0.91	6.95	1.42	-0.82	-1.25	0	-0.04
Mesh 8×4	9.88	-9.91	10.13	-1.76	9.41	1.72	-0.39	-1.61	0	-0.04
Mesh 16×8	11.99	-12.01	12.33	-2.19	11.41	1.24	-0.11	-1.84	0	-0.04
Mesh 32×16	13.94	-13.97	14.44	-2.54	13.37	1.03	0.02	-2.38	0	-0.04
Mesh 64×32	16.13	-16.17	16.81	-2.89	15.59	0.88	0.05	-2.99	0	-0.04
Mesh 128×64	18.76	-18.8	19.64	-3.32	18.24	0.81	0.05	-3.69	0	-0.04

Table 5.7: Maximum and minimum values acquired from the RPIM from linear's base simulations with square meshes

	RPIM with Linear Base's Simulations to Triangular Meshes									
	σ_{xx}		σ_{11}		$\sigma_{vonMises}$		τ_{xy}		δy	
	Max	Min	Max	Min	Max	Min	Max	Min	Max	Min
Mesh 4×2	5.94	-5.94	6.12	-0.32	5.97	1.73	-1	-1	0	-0.04
Mesh 8×4	8.77	-8.77	8.93	-0.95	8.52	1.47	-0.5	-1.51	0	-0.04
Mesh 16×8	11.01	-11.01	11.23	-1.25	10.69	1.19	-0.18	-1.57	0	-0.04
Mesh 32×16	12.95	-12.95	13.26	-1.75	12.64	1	-0.03	-1.9	0	-0.04
Mesh 64×32	15.01	-15.01	15.43	-2.2	14.74	0.86	0	-2.4	0	-0.04
Mesh 128×64	17.42	-17.42	17.97	-2.53	17.19	0.79	0	-2.94	0	-0.04

Table 5.8: Maximum and minimum values acquired from the NNRPIM with first degree of neighborhood with triangular meshes

	NNRPIM with First Degree of Neighborhood									
	σ_{xx}		σ_{11}		$\sigma_{vonMises}$		τ_{xy}		δy	
	Max	Min	Max	Min	Max	Min	Max	Min	Max	Min
Mesh 4×2	7.47	-7.47	7.97	-1.46	7.35	1.08	-0.63	-1.74	0	-0.03
Mesh 8×4	10.61	-10.61	10.99	-2.35	10.02	1.62	-0.35	-1.76	0	-0.04
Mesh 16×8	12.64	-12.64	13.11	-2.74	11.98	1.28	-0.07	-2.15	0	-0.04
Mesh 32×16	14.58	-14.58	15.23	-3.05	13.96	0.92	0.04	-2.74	0	-0.04
Mesh 64×32	16.83	-16.83	17.72	-3.41	16.28	0.81	0.06	-3.44	0	-0.04
Mesh 128×64	19.6	-19.6	20.74	-3.88	19.09	0.81	0.06	-4.23	0	-0.04

Table 5.9: Maximum and minimum values acquired from the NNRPIM with second degree of neighborhood with triangular meshes

	NNRPIM with Second Degree of Neighborhood									
	σ_{xx}		σ_{11}		$\sigma_{vonMises}$		τ_{xy}		δy	
	Max	Min	Max	Min	Max	Min	Max	Min	Max	Min
Mesh 4×2	6.7	-6.7	6.96	-0.91	6.76	1.31	-0.69	-1.52	0	-0.03
Mesh 8×4	9.91	-9.91	10.22	-1.83	9.44	1.64	-0.5	-1.59	0	-0.04
Mesh 16×8	12.24	-12.24	12.66	-2.39	11.65	1.28	-0.15	-2.04	0	-0.04
Mesh 32×16	14.4	-14.4	14.98	-2.83	13.79	0.94	0	-2.6	0	-0.04
Mesh 64×32	16.71	-16.71	17.49	-3.23	16.12	0.83	0.04	-3.26	0	-0.04
Mesh 128×64	19.45	-19.45	20.46	-3.7	18.89	0.82	0.04	-4	0	-0.04

5.1.2 Analytic Solution

Let's compare the results obtained with the analytical mathematical values for stress and displacement. Starting with the stress values, we can calculate them with the expression presented in the expression 5.1:

$$\sigma = \frac{-My}{I} \tag{5.1}$$

, where the M is the bending moment, the y is the distance from the plate neutral point and I is the moment of inertia[60]. The former expression can be transformed into the formula 5.2:

$$\sigma_{xx} = \frac{-P \times (L - x) \times y}{I} \tag{5.2}$$

, where the bending moment can be replaced by the force versus the length point position ($M \times (L - x)$) [60]. Because we are working on a 2D problem, the compression stress, resulting from the bending moment, on the xx axis is visible on the formula 5.2 while the compression stress on the yy axis is null, expression 5.3:

$$\sigma_{yy} = 0 \tag{5.3}$$

The shear stress is calculated with the expression 5.4:

$$\tau = \frac{VQ}{It} \tag{5.4}$$

, where V represents the shear force applied on the point, t is the thickness of the plate or the cross-section width, I is the moment of inertia and Q represents the first moment of area of the portion of the cross-section above the point at distance (y) from the neutral axis[60]. The formulation in question can be transformed by replacing the V and Q formulas visible in the expressions 5.5 and 5.6 respectively:

$$V = -P \tag{5.5}$$

$$Q = \overline{y} \times \overline{A} \tag{5.6}$$

, where P is the variable used to express the force applied, $\overline{A}$ is the area of the top or bottom portions of the member cross-sections and $\overline{y}$ is the distance from the neutral axis to the center of the area $\overline{A}$[60]. By replacing the variables $\overline{A}$ and $\overline{y}$ for their formulas (5.7 and 5.8 respectively) on equation 5.6 we obtain the following expression[60, 1]:

$$\overline{A} = t \times (\frac{D}{2} - y) \tag{5.7}$$

$$\overline{y} = \frac{\frac{D}{2} + y}{2} \tag{5.8}$$

$$\begin{aligned} Q = \overline{y} \times \overline{A} &= \frac{\frac{D}{2} + y}{2} \times t \times (\frac{D}{2} - y) \\ &= \left(\frac{D}{4} + \frac{y}{2}\right) \times \left(\frac{tD}{2} - yt\right) = \frac{tD^2}{8} - \frac{Dyt}{4} + \frac{Dyt}{4} - \frac{y^2t}{2} \\ &= \frac{tD^2}{8} - \frac{y^2t}{2} = \frac{t}{2} \times \left(\frac{D^2}{4} - y^2\right) \end{aligned} \tag{5.9}$$

, where the variable D is the plate's height.

Finally, by replacing the expressions 5.9 and 5.5 on formula 5.4, we obtained the final shear stress expression[60, 1]:

$$\begin{aligned} \tau = \sigma_{xy} = \frac{VQ}{It} &= \frac{-P \times \frac{t}{2} \times (\frac{D^2}{4} - y^2)}{It} \\ &= \frac{-P \times \frac{D^2}{8} + \frac{Py^2}{2}}{I} = \frac{-PD^2}{8I}\left(1 - \frac{4y^2}{D^2}\right) \end{aligned} \tag{5.10}$$

Moving our attention now to the deflection formulas, for this problem, we can see, in the work of Jorbe Belinha, that[1]:

$$u(x) = \frac{2P}{ED^3}\left[3x(2L - x)y + (2 + \upsilon)\left(y^2 - \frac{D^2}{4}\right)y\right] \tag{5.11}$$

$$v(x) = \frac{2P}{ED^3}\left[x^2(3L - x) + 3\upsilon(L - x)y^2 + x(4 + 5\upsilon)\frac{D^2}{4}\right] \tag{5.12}$$

For this problem, the variable I, inertia is $I = \frac{D^3}{12}$, and the variable y, is the distance from the neutral axis, where $y \in \left\{-\frac{D}{2} \vee \frac{D}{2}\right\}$[1].

Now we can initiate the analytic calculation analysis, and we will start with the point B stress analysis. Apling now, the equation 5.2 we can calculate the normal stress:

$$\sigma_{xx} = \frac{-P \times (L - x) \times y}{I} = \frac{-1 \times (2 - 0.5) \times 0.5}{\frac{1^3}{12}} = -9.0[MPa] \tag{5.13}$$

, where, as we can observe, the converging simulated results are very close to the analytically calculated value.

Moving now to analytic analysis from point C, we will initiate the shear stress calculation. By using equation 5.10 we can calculate the shear stress:

$$\sigma_{xy} = \frac{-PD^2}{8I}\left(1 - \frac{4y^2}{D^2}\right) = \frac{-1 \times 1^2}{\frac{8 \times 1^3}{12}\left(1 - \frac{4 \times 0^2}{\frac{1^3}{12}}\right)} = -1.5[MPa] \tag{5.14}$$

, where we can also conclude that the analytic calculations correspond to the obtained values.

Finally, we can analyze the displacement in point D using the equations 5.11 and 5.12:

$$\begin{aligned} u(x) &= \frac{2P}{ED^3}\left[3x(2L-x)y + (2+\upsilon)\left(y^2 - \frac{D^2}{4}\right)y\right] \\ &= \frac{2\times(-1)}{1000\times 1^3}\left[3\times 2(2\times 2-2)\times 0 + (2+0.3)\left(0^2 - \frac{1^2}{4}\right)\times 0\right] = 0 \end{aligned} \tag{5.15}$$

$$\begin{aligned} v(x) &= \frac{2P}{ED^3}\left[x^2(3L-x) + 3\upsilon(L-x)y^2 + x(4+5\upsilon)\frac{D^2}{4}\right] \\ &= \frac{2\times(-1)}{1000\times 1^3}\left[2^2(3\times 2-2) + 3\times 0.3(2-2)\times 0^2 + 2(4+5\times 0.3)\frac{1^2}{4}\right] \\ &= -0.0375\,\mathrm{m} = -37.5\,\mathrm{mm} \end{aligned} \tag{5.16}$$

, and with these results, we can notice that the analytically calculated values are either very close or the same as the ones resulting from the linear simulations.

5.2 Conclusions

During this chapter, we intend to analyze the different results obtained between different mesh sizes and element types, and to achieve that goal, we used a standard cantilever beam problem.

During the mesh size increments from 4×2 to 128×64 elements, it was possible to observe a correlation between the number of elements and the results' precision, which means that the more refined the mesh is, the better the simulation results will be. However, we could also witness that a mesh with extreme refinement will not necessarily achieve a result that is much more reliable and trustworthy when compared with a mesh a little less refined. That means that when we are talking about meshes excessively refined, we will be using more computational power and resources to achieve the same results and conclusions with a slightly less refined mesh. Another possible conclusion is that for less refined and elaborated meshes, the square elements mesh gives us more approximate results.

To conclude this chapter about linear analysis, we can observe two more things, first that all the methods used (FEM, RPIM, and NNRPIM) converge to give us the same result, with the mesh elements' increment and size, and secondly the meshless methods, that is the RPIM and NNRPIM methods', tendentially gives us better results, in comparison to the FEM method's, with the less refined meshes.

6 Non Linear Analysis

In this chapter, we will analyze non-linear deformations in different geometric beams, along with the respective von Mises stress and strains. Various beams will be simulated in three dimensions and in two dimensions to allow for comparative analysis. These simulations have been performed using the FEM, RPIM, and NNRPIM methods with the KT-ALL algorithm, as we will observe.

However, before we initiate the 3D nonlinear simulations, we must use a cook membrane to understand and visualize the difference between KT0, KT1, and KT-ALL.

6.1 Cook's Membrane

The Cook's membrane is a standard problem for simulating bending moments with shear stress[61]. As we can see in figures 6.1 and 6.2, the membrane is fixed through a face with 44 mm on the left side and has an applied vertical uniform distribution load of a 16 mm face on the right side of the membrane, that can be observed in figure 6.1[61]. For this problem, the material's properties are considered 10 GPa for Young's modulus, 1 MPa for the tangent modulus, 0.33 for the Poisson's ratio, and 200 MPa for the yield stress. For these simulations, we used a Cook's Membrane with 2970 nodes and with 2860 square elements.

In this particular study, we will focus on two points, let's call them point A and point B. Point A is located in the node right after the ones fixed and right below the one on the border, and that gives us the node with a coordinate (0.738, 43.256). Point B, however, is located in the right extremity of the cook membrane with the coordinates (48, 52). Because point A is practically a fixed node, we will study the von Mises stress involved in it, while in point B, we will study not just the von Mises stress but also the displacement suffered. The following figures 6.3 and 6.2 will help us to better understand the points' locations in the Cook's membrane.

Let's now discuss the simulations executed in the Cook's membrane problem. For this particular problem, simulations were performed using FEM, RPIM with linear and constant bases, and NNRPIM with 1^{st}- and 2^{nd} degree neighborhoods. The algorithms used in these methods' simulations were the KT0, KT1, and KT-ALL.

The following figures 6.4 to 6.12 show us the graphics extracted from the Cook's membrane problems simulations results previously mentioned. As we already discussed, the KT-ALL algorithm is the most precise mathematically and the most reliable for non-linear simulations, when compared to the three discussed algorithms. However, when we quickly analyze the results visible in the graphics from figures 6.4

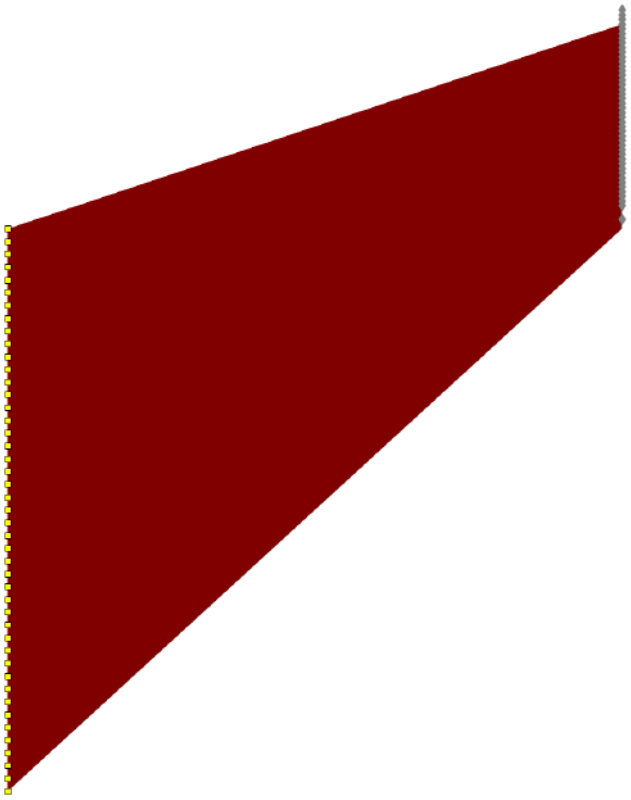

Figure 6.1: In this image, it's possible to observe the applied force in the right nodes as well as the fixed nodes on the left side

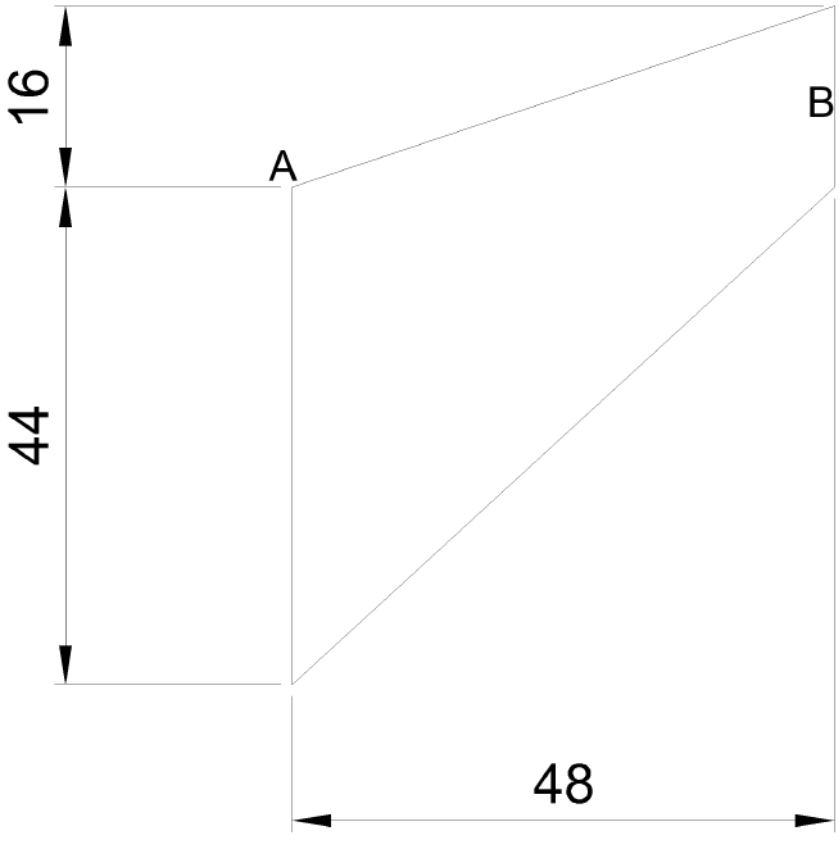

Figure 6.2: Cook's membrane dimensions

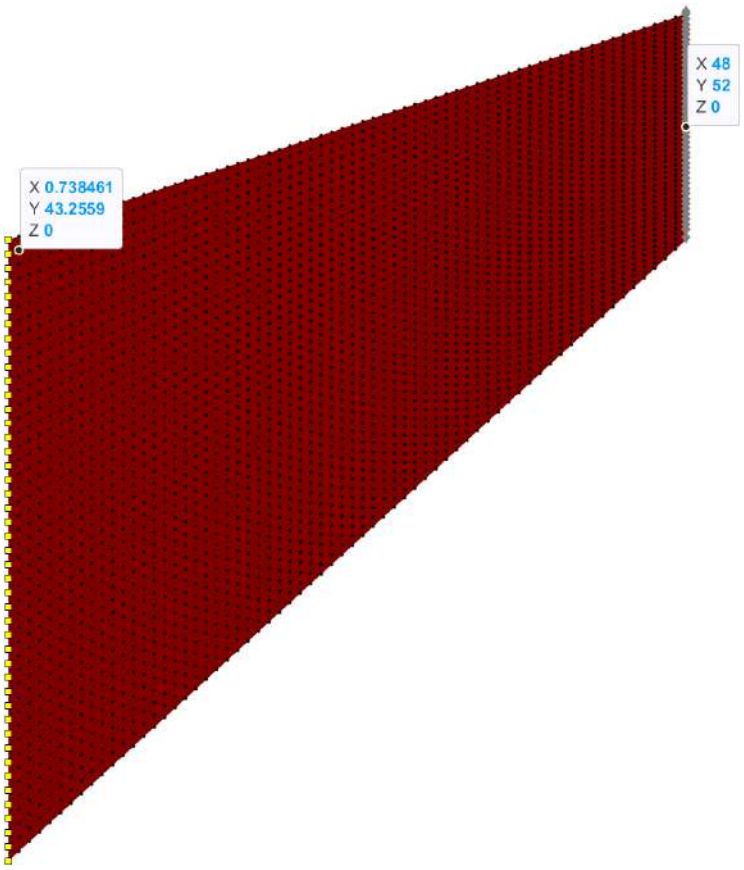

Figure 6.3: Cook's membrane points A and B positions

to 6.12, we can see the KT-ALL algorithm results are not what was to be expected. One of the possible explanations is that the incremental force was too large for the simulations with the KT-ALL algorithm, which means that for more believable results, we should increment the load less per increment, for this problem.

The following figures 6.4 to 6.6 show us the point A von Mises stress results, where 6.4 is for FEM simulations, 6.5 for RPIM simulations, and 6.6 for NNRPIM simulations. These three graphics are all stress vs strain. When we analyze the first graphic in figure 6.4, we can conclude that all three FEM simulations are very close matches, with a well-defined curve passing from a linear to a non-linear state. Analyzing figure 6.5 from the RPIM simulations, we note that the two KT-ALL algorithm simulations do not form a curve as expected, and unlike the other two algorithms, after achieving the first point in the graphic (that is, reaching the yield stress point), the simulation shows the Cook's membrane entering a complete state of rupture and collapse. To finish the point A analysis, let's divert our attention to figure 6.6, where we can see the graphic from the NNRPIM simulations. In this case, all the simulations present a very well-defined curve, with very similar results obtained.

The next analysis focuses on point B, where we will study both the stress and the displacement generated from the simulations. Let's begin with the stress analysis, where figures 6.7, 6.8, and 6.9 show stress versus deformation graphs for the FEM,

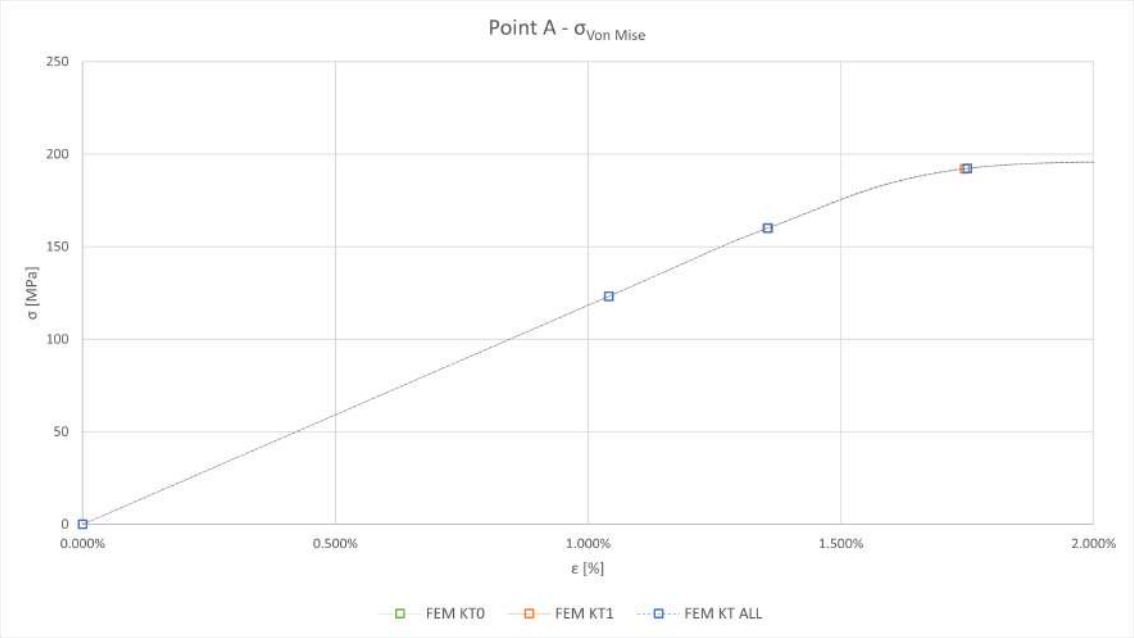

Figure 6.4: Results from FEM Cook's membrane simulations from point A in the form of a graphic stress versus deformation

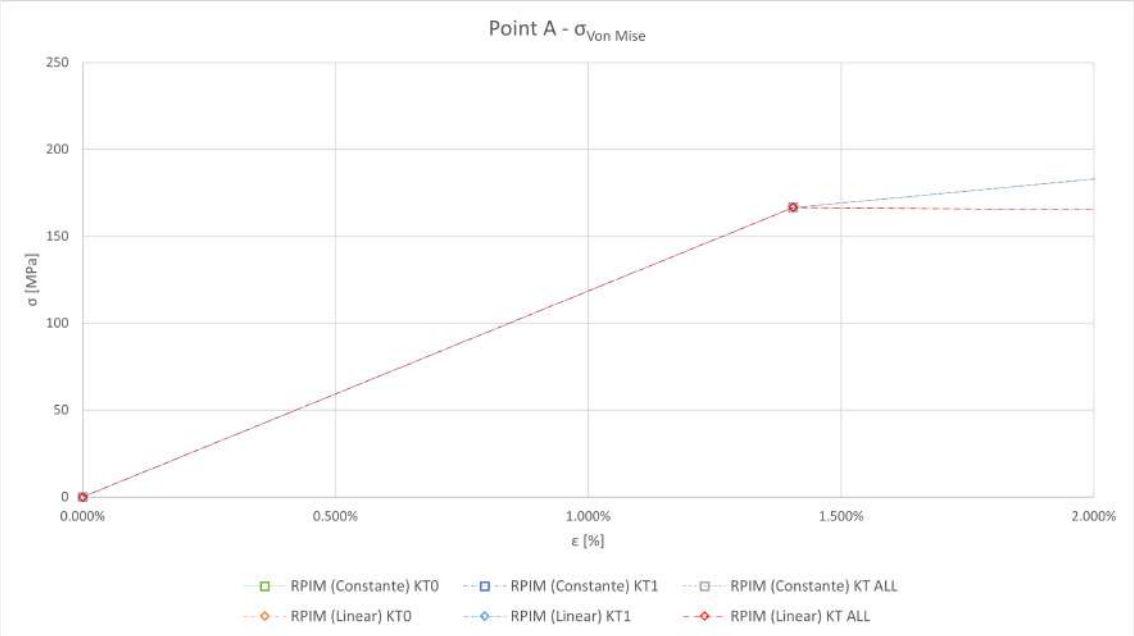

Figure 6.5: Results from RPIM Cook's membrane simulations from point A in the form of a graphic stress versus deformation

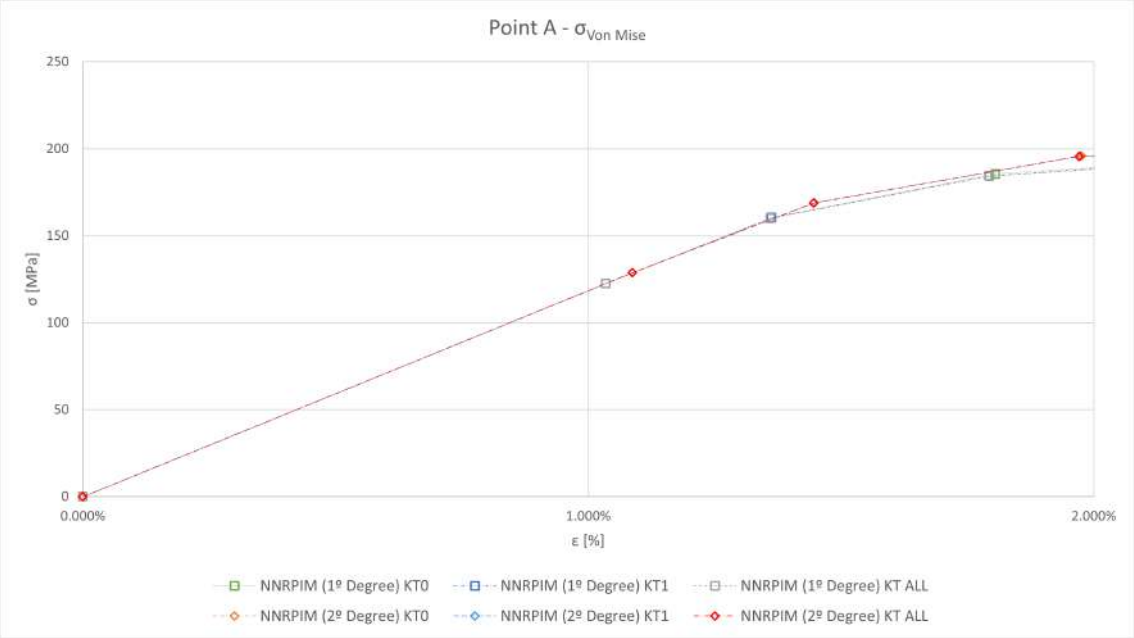

Figure 6.6: Results from NNRPIM Cook's membrane simulations from point A in the form of a graphic stress versus deformation

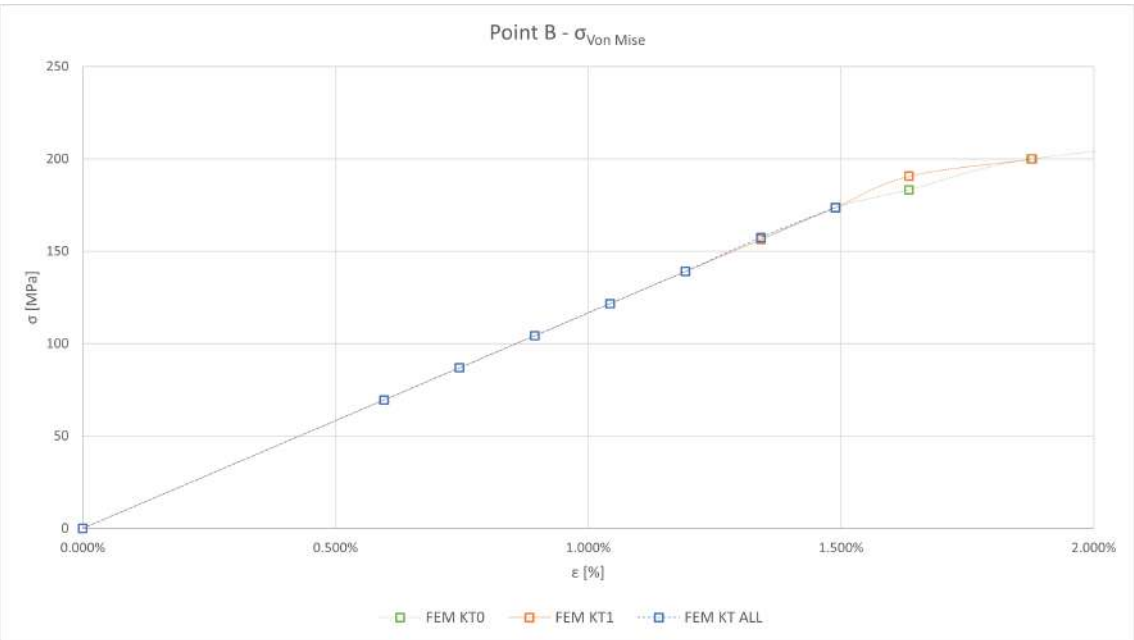

Figure 6.7: Results from FEM Cook's membrane simulations from point B in the form of a graphic stress versus deformation

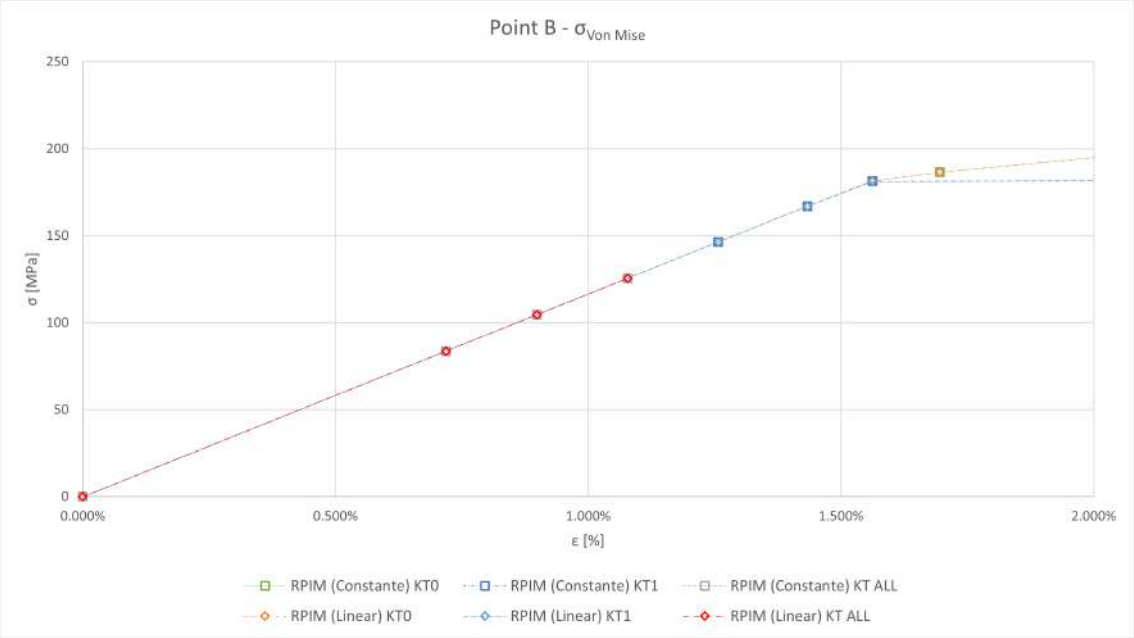

Figure 6.8: Results from RPIM Cook's membrane simulations from point B in the form of a graphic stress versus deformation

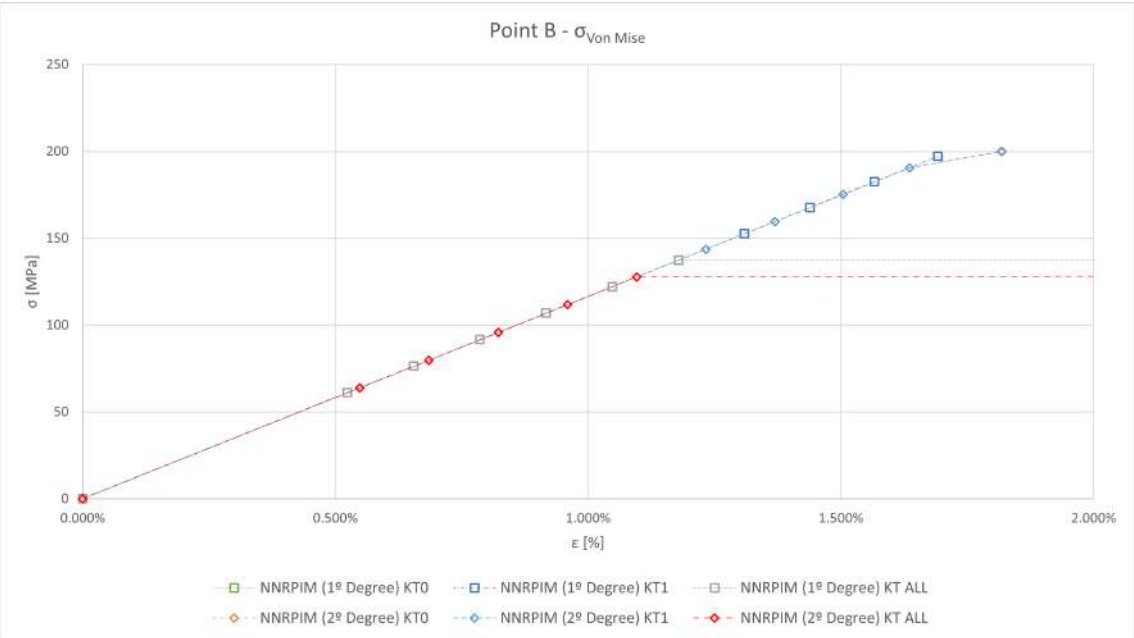

Figure 6.9: Results from NNRPIM Cook's membrane simulations from point B in the form of a graphic stress versus deformation

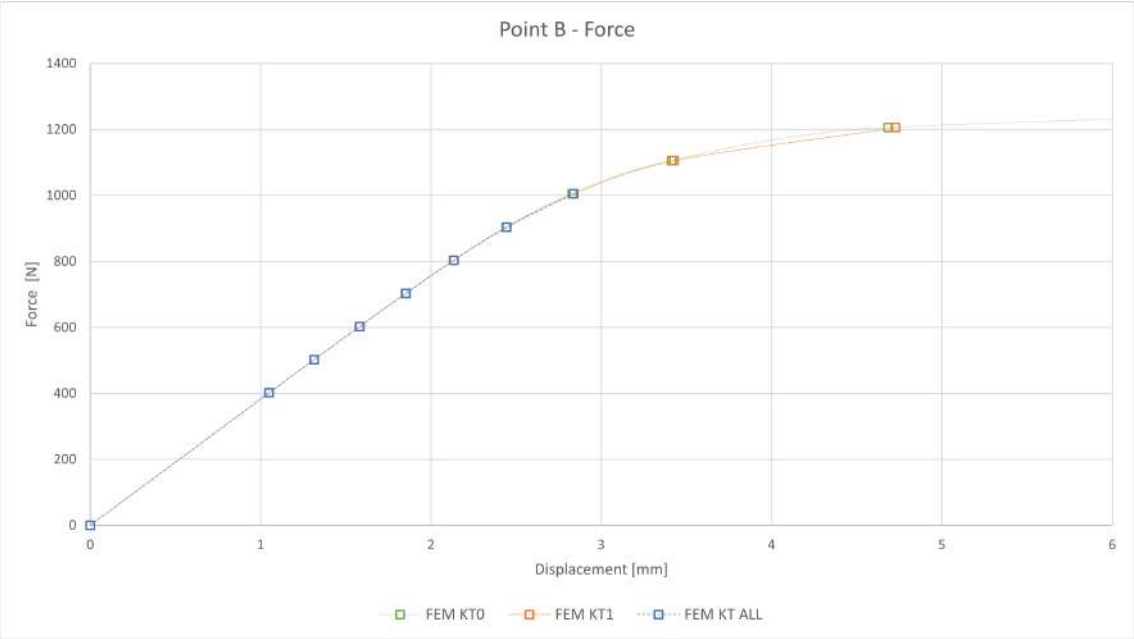

Figure 6.10: Results from FEM Cook's membrane simulations from point B in the form of a graphic stress versus deformation

RPIM, and NNRPIM simulations, respectively. In figure 6.7, we observe the stress versus strain from the FEM simulations, where the KT0 and KT1 algorithms initiate the representative curve that indicates the transition from linear to nonlinear behavior, while the KT-ALL simulation does not initiate the respective curve. In figure 6.8, we see the results from the RPIM simulations, where the KT0 algorithm gives a partial state change curve, the KT1 appears to enter a rupture state without forming this curve, and the KT-ALL algorithm does not enter the nonlinear state. To finalize the stress analysis at point B, focus on figure 6.9, where there is no well-defined state change curve in any of the simulations. Instead, the KT0 and KT1 simulations appear to start the transition to the nonlinear state, while the KT-ALL algorithm simulations indicate a change to a complete rupture state.

To finalize the B-point study, let's now focus our attention on the last three figures that show force versus displacement graphs. In figure 6.10, you can observe the extremely well-defined state change curve for the FEM simulations with the KT0 and KT1 algorithms. For the KT-ALL algorithm in the FEM simulation, we see an apparent intention to initiate the curve elaborated by the other two algorithms. In the next figure, 6.11, we draw a different conclusion from the previous RPIM's ones. In this graphic, we observe a very well-defined curve with the different states (linear and nonlinear) visible and identifiable. However, for the NNRPIM simulations, we see a behavior change in the KT-ALL simulations. In the NNRPIM simulations with the KT-ALL algorithm, they enter a rupture state without passing through the nonlinear state curve, something that didn't appear in the previous NNRPIM conclusions.

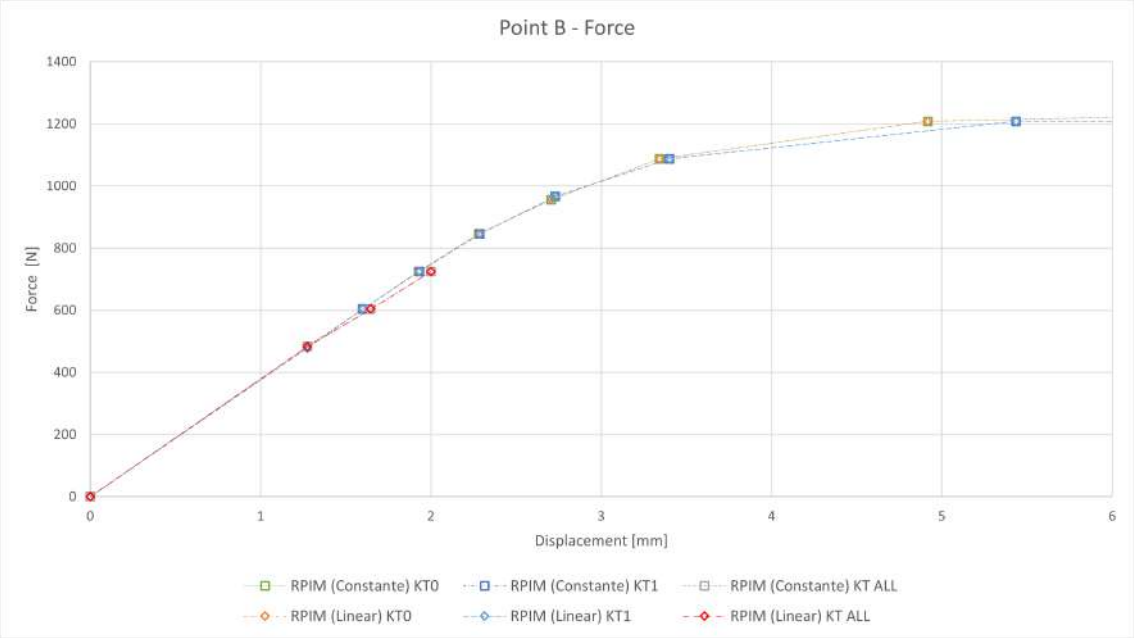

Figure 6.11: Results from RPIM Cook's membrane simulations from point B in the form of a graphic stress versus deformation

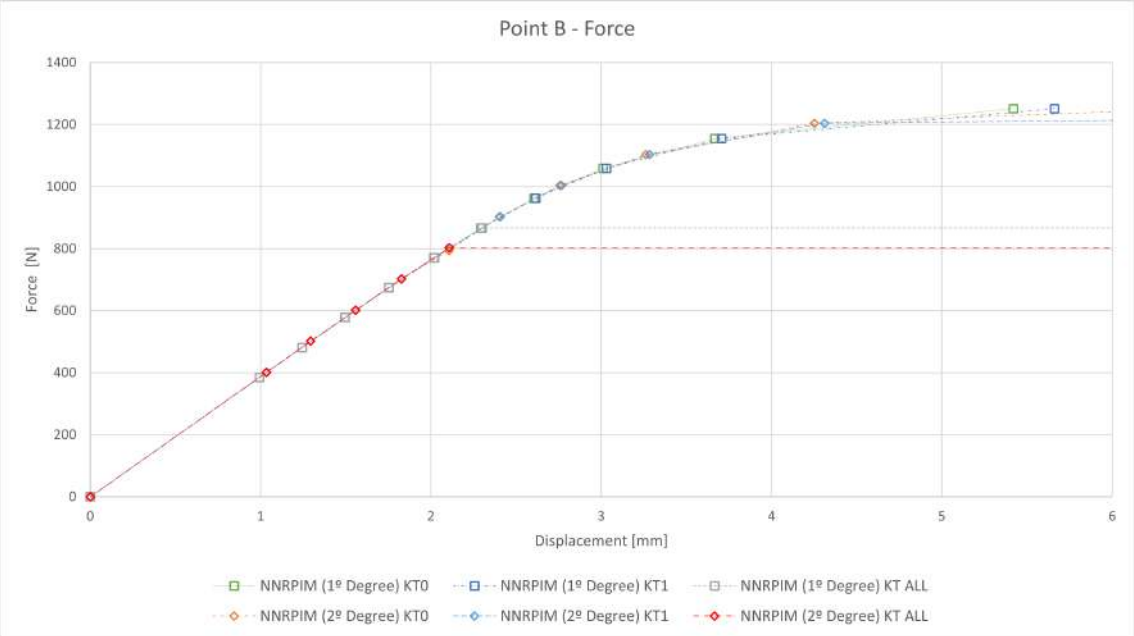

Figure 6.12: Results from NNRPIM Cook's membrane simulations from point B in the form of a graphic stress versus deformation

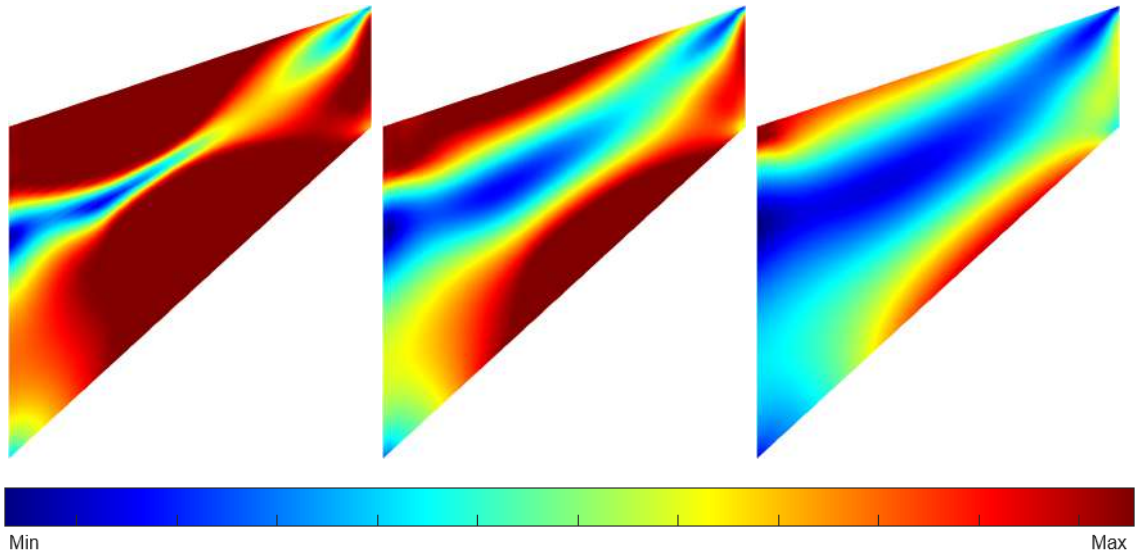

Figure 6.13: Von Mises stress contour plots resulting from the FEM simulations. From left to right, we have the FEM simulations done with the KT0 algorithm with a force of 1205.61 [N], KT1 with a combined force of 1105.14 [N], and, finally, with the KT-ALL algorithm with a combined force of 803.74 [N]

Table 6.1: Maximum and minimum von Mises values of the Cook's membrane FEM simulations

Von Mises stress values to FEM simulations					
KT0 algorithm		KT1 algorithm		KT-ALL algorithm	
Max	Min	Max	Min	Max	Min
200.36 [MPa]	12.89 [MPa]	203.18 [MPa]	5.32 [MPa]	208.86 [MPa]	16.71 [MPa]

In the following images, we can observe the contour plots for all the simulations regarding von Mises stress, plastic deformation, and shear stress. From figure 6.13 to 6.17, we can observe the von Mises stress contour plots. From figure 6.18 to 6.22, we can observe the shear stress contour plots. Finally, from figure 6.23 to 6.27, we can observe the plastic deformation contour plot images, generated by FEMAS. From table 6.1 to 6.10, we can study the maximum and minimum values of the respective contour plots' color bars. It's also important to mention that due to the different behaviour visible in the previous graphics, in the RPIM simulations elaborated with the KT-ALL algorithm, the tables 6.2, 6.3, 6.7, and 6.8 will not show those specific values.

Table 6.2: Maximum and minimum von Mises values of the Cook's membrane RPIM with constant base simulations

Von Mises stress values to RPIM with constant base simulations					
KT0 algorithm		KT1 algorithm		KT-ALL algorithm	
Max	Min	Max	Min	Max	Min
200.59 [MPa]	17.34 [MPa]	200.37 [MPa]	11.91 [MPa]	—	—

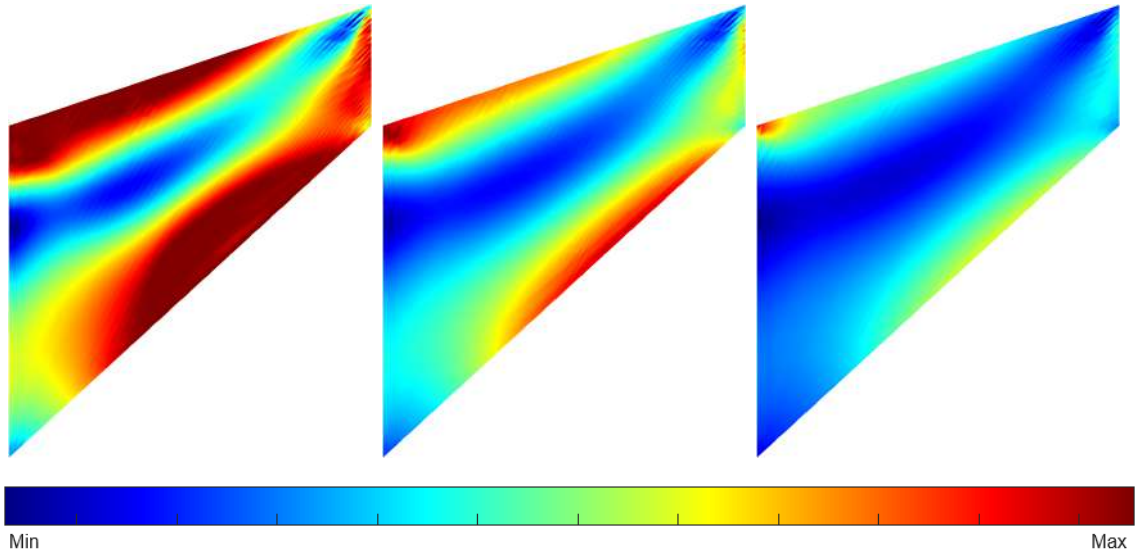

Figure 6.14: Von Mises stress contour plots resulting from the RPIM with constant base simulations. From left to right, we have the RPIM with constant base simulations done with the KT0 algorithm with a force of 1208.24 [N], KT1 with a combined force of 845.77 [N], and, finally, with the KT-ALL algorithm with a combined force of 483.30 [N]

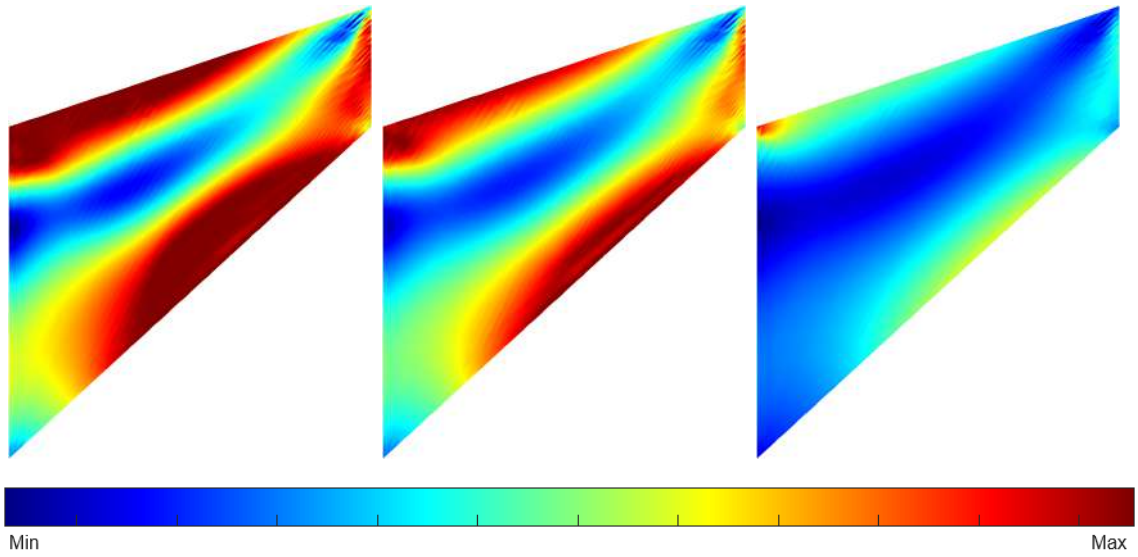

Figure 6.15: Von Mises stress contour plots resulting from the RPIM with linear base simulations. From left to right, we have the RPIM with linear base simulations done with the KT0 algorithm with a force of 1208.24 [N], KT1 with a combined force of 845.77 [N], and, finally, with the KT-ALL algorithm with a combined force of 483.29 [N]

Table 6.3: Maximum and minimum von Mises values of the Cook's membrane RPIM with linear base simulations

Von Mises stress values to RPIM with linear base simulations					
KT0 algorithm		KT1 algorithm		KT-ALL algorithm	
Max	Min	Max	Min	Max	Min
200.59 [MPa]	17.34 [MPa]	200.37 [MPa]	11.91 [MPa]	—	—

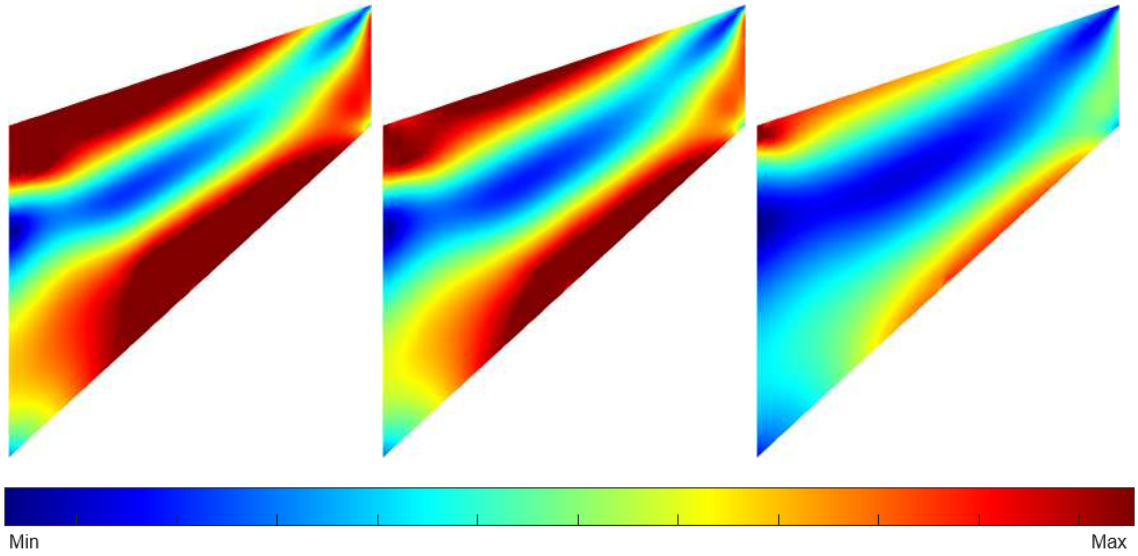

Figure 6.16: Von Mises stress contour plots resulting from the NNRPIM with first-degree neighborhood simulations. From left to right, we have the NNRPIM with first degree of neighborhood simulations done with the KT0 algorithm with a force of 1155.19 [N], KT1 with a combined force of 1058.92 [N], and, finally, with the KT-ALL algorithm with a combined force of 866.39 [N]

Table 6.4: Maximum and minimum von Mises values of the Cook's membrane NNRPIM first degree of neighborhood simulations

Von Mises stress values to NNRPIM first degree of neighborhood simulations					
KT0 algorithm		KT1 algorithm		KT-ALL algorithm	
Max	Min	Max	Min	Max	Min
200.07 [MPa]	12.62 [MPa]	200.06 [MPa]	9.89 [MPa]	307.76 [MPa]	11.96 [MPa]

Table 6.5: Maximum and minimum von Mises values of the Cook's membrane NNRPIM second degree of neighborhood simulations

Von Mises stress values to NNRPIM second degree of neighborhood simulations					
KT0 algorithm		KT1 algorithm		KT-ALL algorithm	
Max	Min	Max	Min	Max	Min
200.10 [MPa]	3.61 [MPa]	200.53 [MPa]	10.62 [MPa]	275.88 [MPa]	11.58 [MPa]

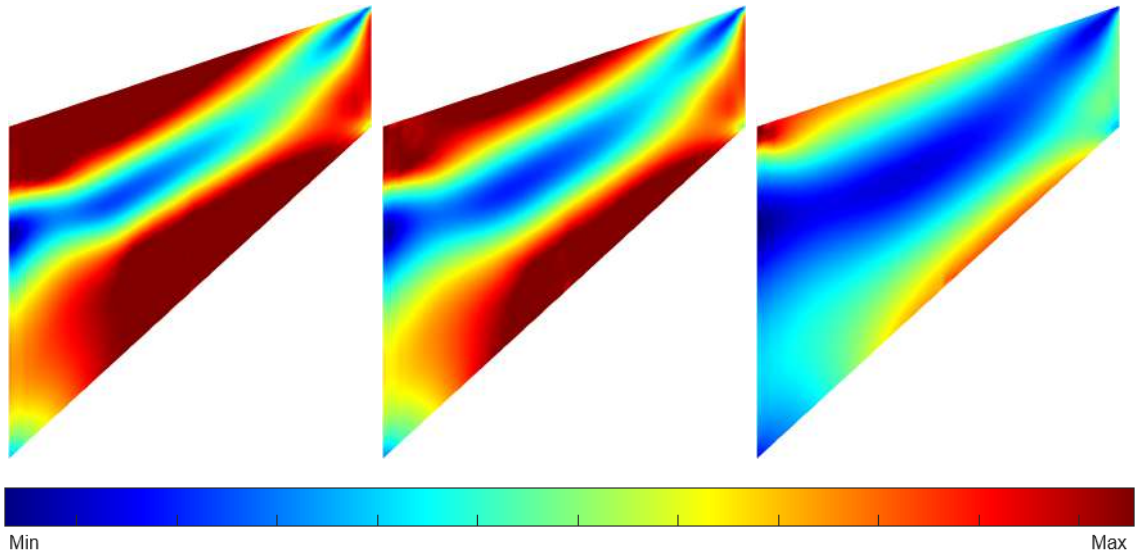

Figure 6.17: Von Mises stress contour plots resulting from the NNRPIM with second-degree neighborhood simulations. From left to right, we have the NNRPIM with a second degree of neighborhood simulations done with the KT0 algorithm with a force of 1204.23 [N], KT1 with a combined force of 1103.88 [N], and, finally, with the KT-ALL algorithm with a combined force of 802.82 [N]

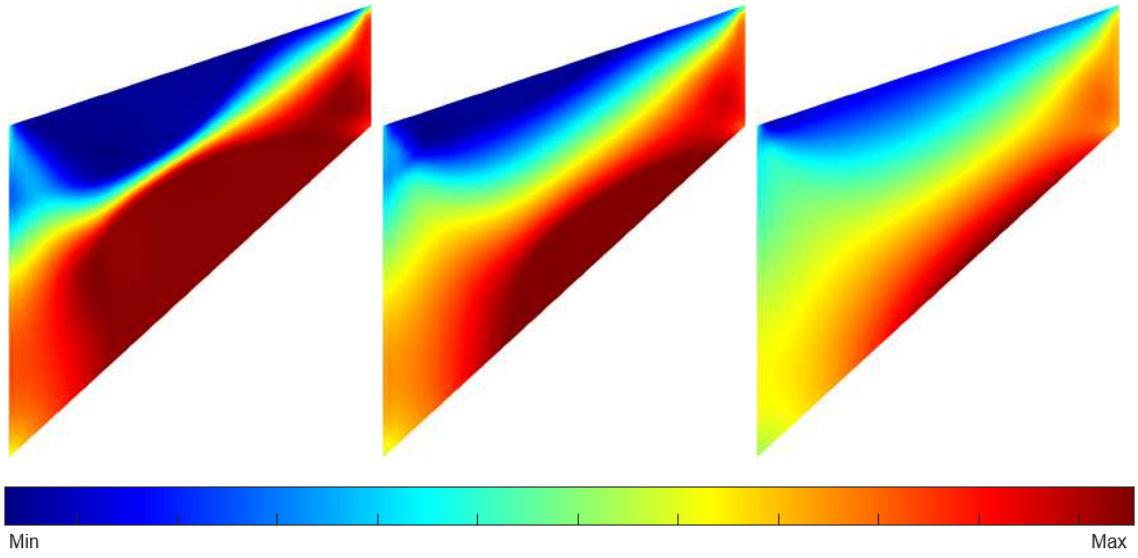

Figure 6.18: Shear stress contour plots resulting from the FEM simulations. From left to right, we have the FEM simulations done with the KT0 algorithm with a force of 1205.61 [N], KT1 with a combined force of 1105.14 [N], and, finally, with the KT-ALL algorithm with a combined force of 803.74 [N]

Table 6.6: Maximum and minimum shear stress values of the Cook's membrane FEM simulations

Shear stress values to FEM simulations					
KT0 algorithm		KT1 algorithm		KT-ALL algorithm	
Max	Min	Max	Min	Max	Min
105.51 [MPa]	-63.04 [MPa]	102.94 [MPa]	-67.71 [MPa]	108.65 [MPa]	-73.65 [MPa]

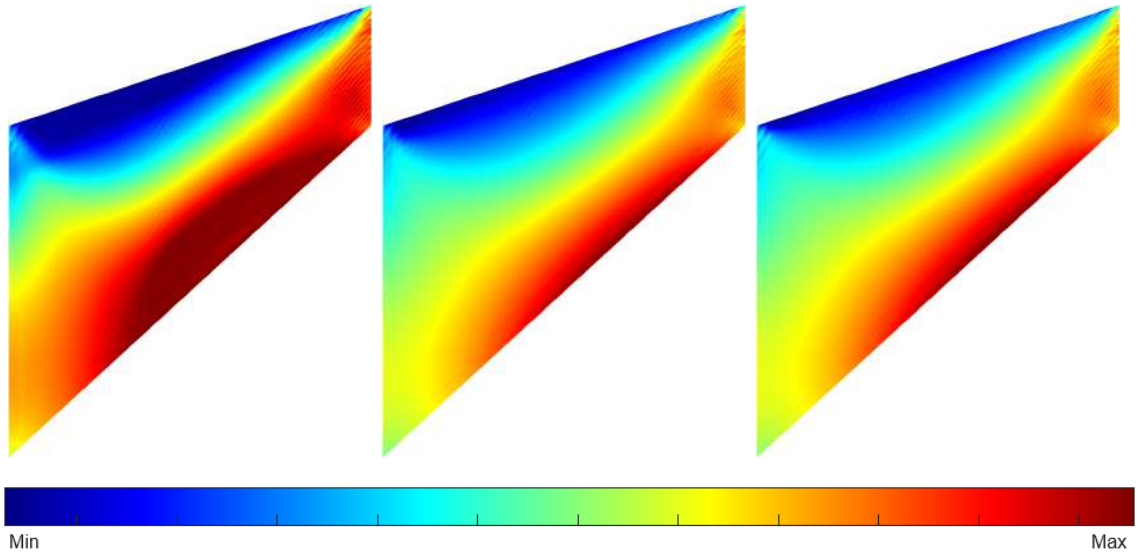

Figure 6.19: Shear stress contour plots resulting from the RPIM with constant base simulations. From left to right, we have the RPIM with constant base simulations done with the KT0 algorithm with a force of 1208.24 [N], KT1 with a combined force of 845.77 [N], and, finally, with the KT-ALL algorithm with a combined force of 483.30 [N]

Table 6.7: Maximum and minimum shear stress values of the Cook's membrane RPIM with a constant base simulations

Shear stress values to RPIM with a constant base simulations					
KT0 algorithm		KT1 algorithm		KT-ALL algorithm	
Max	Min	Max	Min	Max	Min
112.22 [MPa]	-73.63[MPa]	109.69 [MPa]	-73.13 [MPa]	—	—

Table 6.8: Maximum and minimum shear stress values of the Cook's membrane RPIM with a linear base simulations

Shear stress values to RPIM with a linear base simulations					
KT0 algorithm		KT1 algorithm		KT-ALL algorithm	
Max	Min	Max	Min	Max	Min
112.22 [MPa]	-73.63[MPa]	109.69 [MPa]	-73.13 [MPa]	—	—

Table 6.9: Maximum and minimum shear stress values of the Cook's membrane NNRPIM first degree of neighborhood simulations

Shear stress values to NNRPIM first degree of neighborhood simulations					
KT0 algorithm		KT1 algorithm		KT-ALL algorithm	
Max	Min	Max	Min	Max	Min
102.78 [MPa]	-72.48 [MPa]	101.68 [MPa]	-64.76 [MPa]	132.89 [MPa]	-103.09 [MPa]

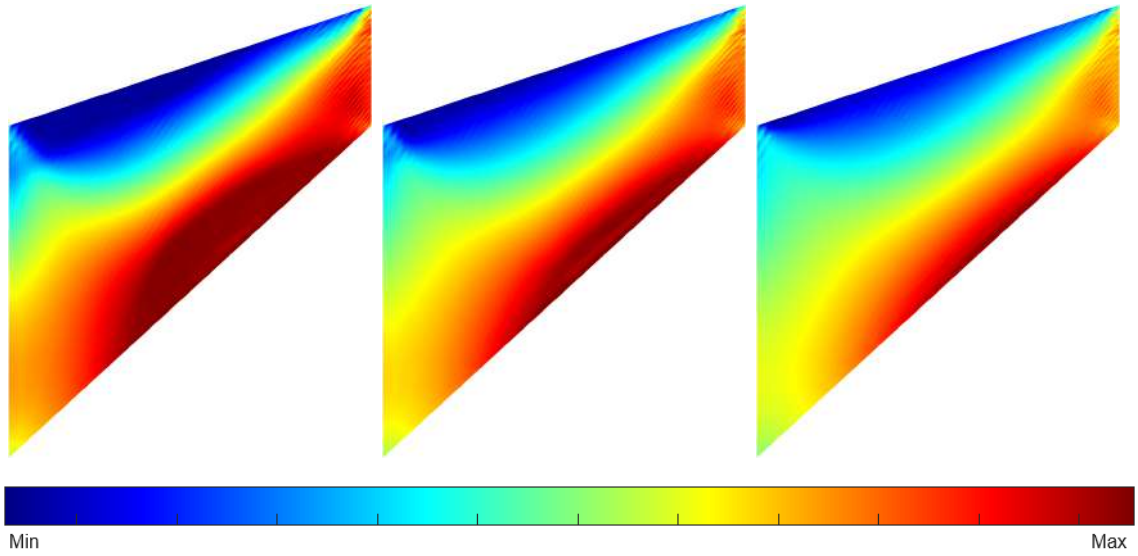

Figure 6.20: Shear stress contour plots resulting from the RPIM with linear base simulations. From left to right, we have the RPIM with linear base simulations done with the KT0 algorithm with a force of 1208.24 [N], KT1 with a combined force of 845.77 [N], and, finally, with the KT-ALL algorithm with a combined force of 483.29 [N]

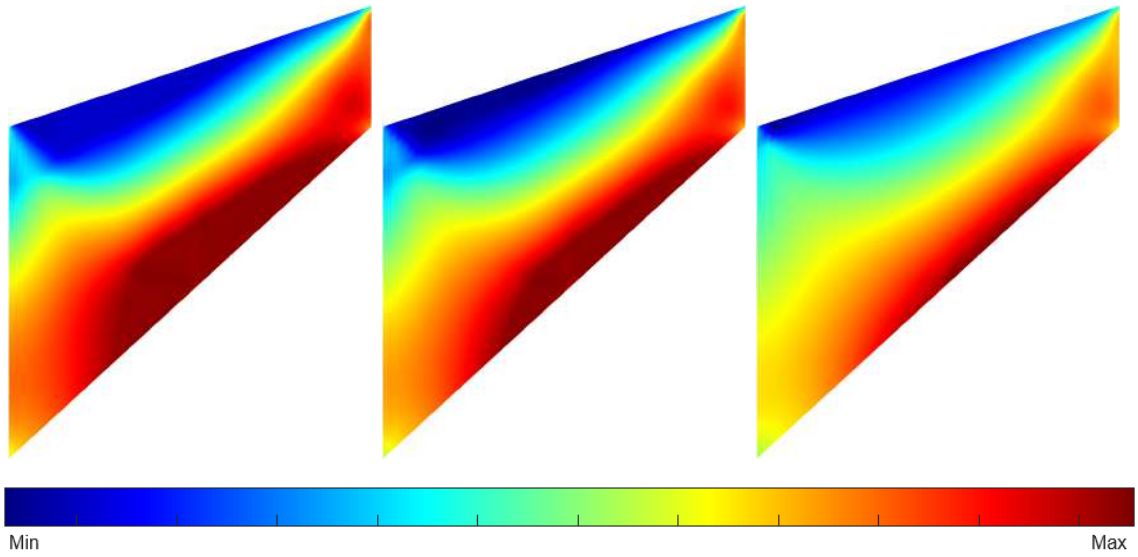

Figure 6.21: Shear stress contour plots resulting from the NNRPIM with first-degree neighborhood simulations. From left to right, we have the NNRPIM with first degree of neighborhood simulations done with the KT0 algorithm with a force of 1155.19 [N], KT1 with a combined force of 1058.92 [N], and, finally, with the KT-ALL algorithm with a combined force of 866.39 [N]

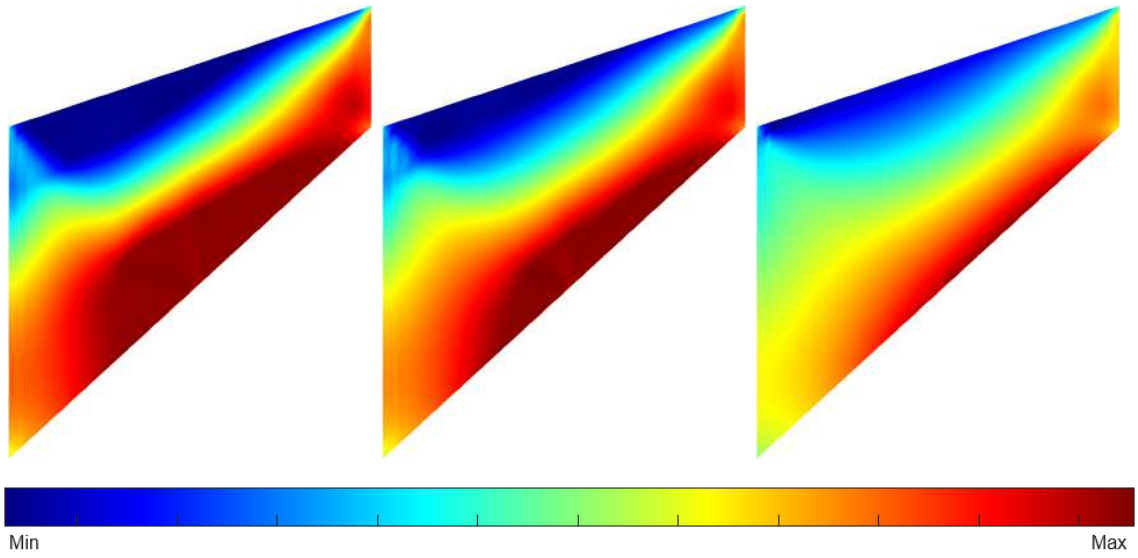

Figure 6.22: Shear stress contour plots resulting from the NNRPIM with second-degree neighborhood simulations. From left to right, we have the NNRPIM with a second degree of neighborhood simulations done with the KT0 algorithm with a force of 1204.23 [N], KT1 with a combined force of 1103.88 [N], and, finally, with the KT-ALL algorithm with a combined force of 802.82 [N]

Table 6.10: Maximum and minimum shear stress values of the Cook's membrane NNRPIM second degree of neighborhood simulations

Shear stress values to NNRPIM second degree of neighborhood simulations					
KT0 algorithm		KT1 algorithm		KT-ALL algorithm	
Max	Min	Max	Min	Max	Min
102.19 [MPa]	-60.81 [MPa]	101.65 [MPa]	-65.82 [MPa]	132.55 [MPa]	-104.68 [MPa]

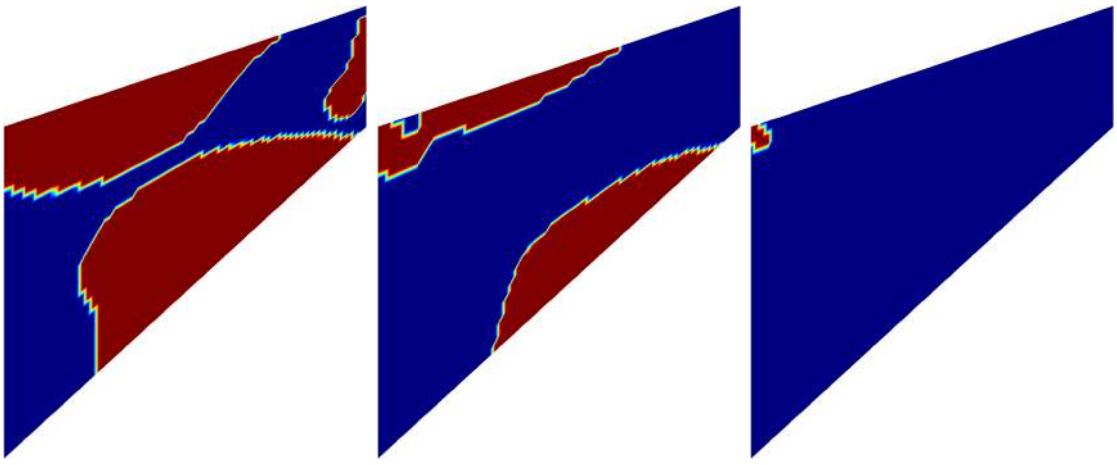

Figure 6.23: Plastic deformation contour plots resulting from the FEM simulations. From left to right, we have the FEM simulations done with the KT0 algorithm with a force of 1205.61 [N], KT1 with a combined force of 1105.14 [N], and, finally, with the KT-ALL algorithm with a combined force of 803.74 [N]

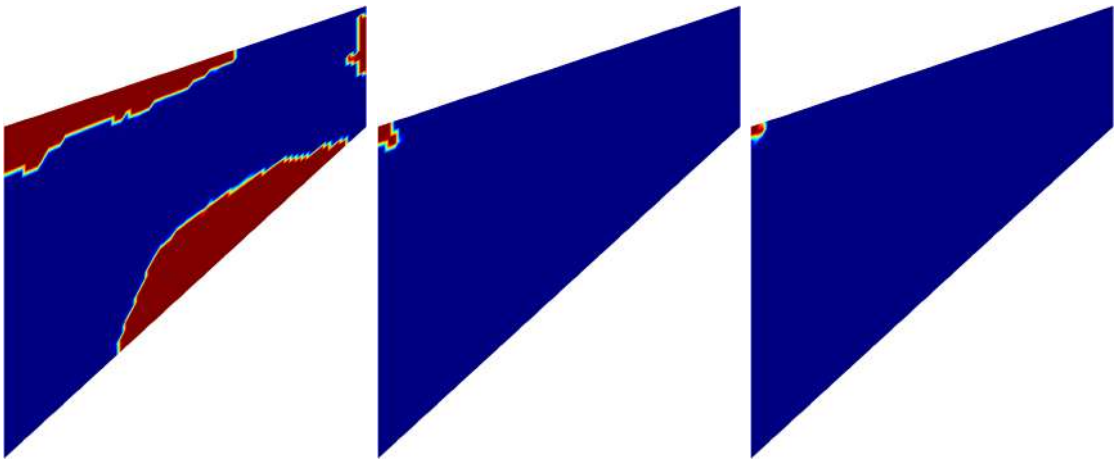

Figure 6.24: Plastic deformation contour plots resulting from the RPIM with constant base simulations. From left to right, we have the RPIM with constant base simulations done with the KT0 algorithm with a force of 1208.24 [N], KT with a combined force of 845.77 [N], and, finally, with the KT-ALL algorithm with a combined force of 483.30 [N]

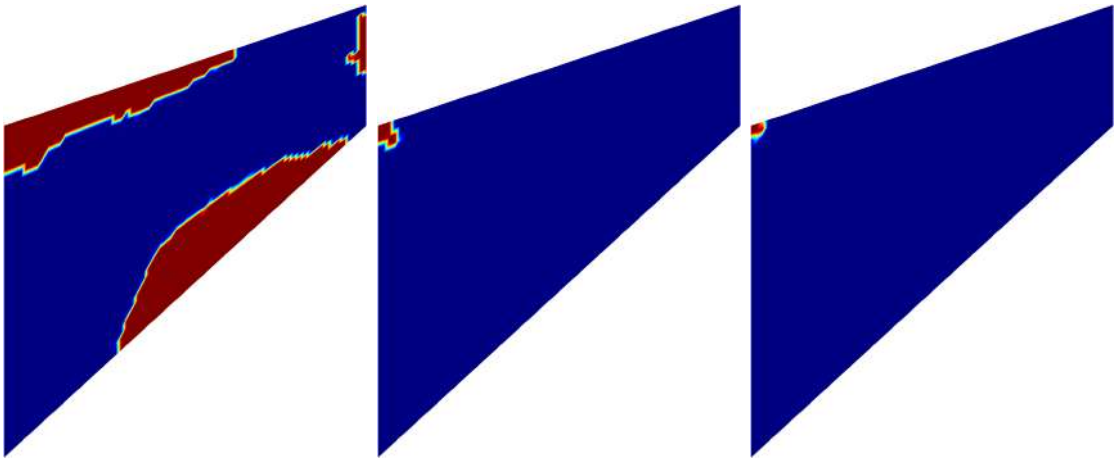

Figure 6.25: Plastic deformation contour plots resulting from the RPIM with linear base simulations. From left to right, we have the RPIM with linear base simulations done with the KT0 algorithm with a force of 1208.24 [N], KT1 with a combined force of 845.77 [N], and, finally, with the KT-ALL algorithm with a combined force of 483.29 [N]

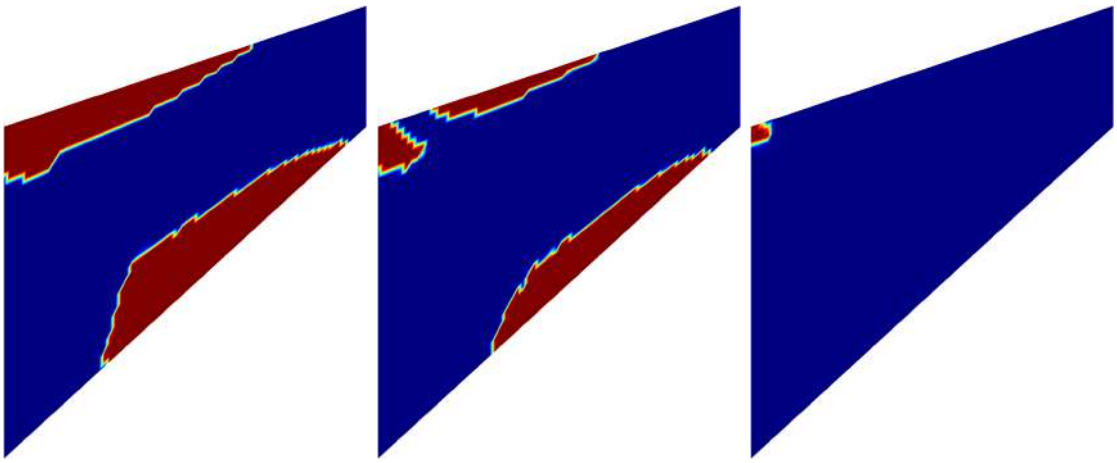

Figure 6.26: Plastic deformation contour plots resulting from the NNRPIM with first-degree neighborhood simulations. From left to right, we have the NNRPIM with first degree of neighborhood simulations done with the KT0 algorithm with a force of 1155.19 [N], KT1 with a combined force of 1058.92 [N], and, finally, with the KT-ALL algorithm with a combined force of 866.39 [N]

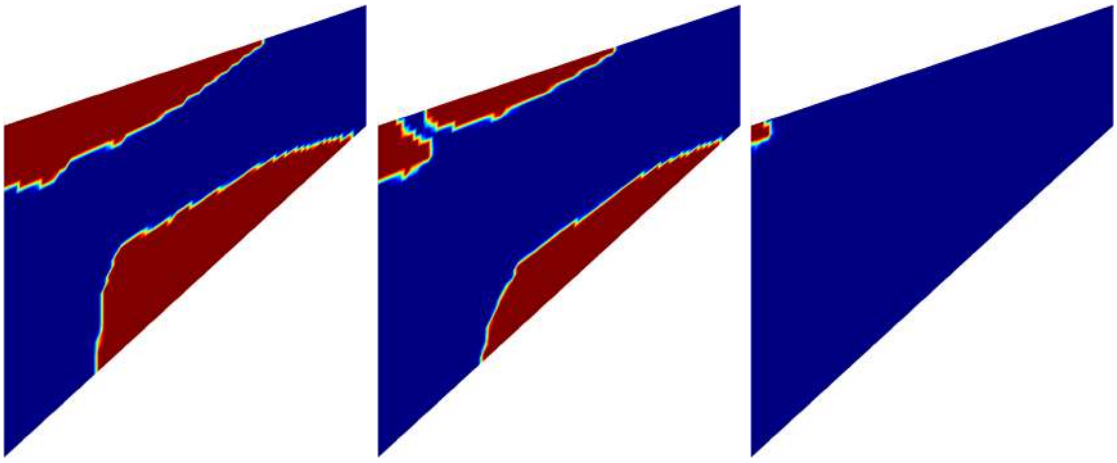

Figure 6.27: Plastic deformation contour plots resulting from the NNRPIM with second-degree neighborhood simulations. From left to right, we have the NNRPIM with a second degree of neighborhood simulations done with the KT0 algorithm with a force of 1204.23 [N], KT1 with a combined force of 1103.88 [N], and, finally, with the KT-ALL algorithm with a combined force of 802.82 [N]

By conducting a quick visual analysis, we can conclude that the simulations performed with the KT0 algorithm allow the membrane to withstand greater forces before collapsing. In contrast, the KT-ALL algorithm introduces collapse at a significantly smaller load in some instances. This conclusion is evident from the stress contour plot images, as a larger area is with or close to the yield stress in the KT0 simulations, while the KT-ALL simulations show a diminished yield stress area for the membrane. The same principle applies to the shear stress contour plot images; the KT0 simulations have a larger area with elevated shear stress, whereas the KT-ALL simulations result in a smaller area with elevated shear stress. Clearly, these conclusions indicate that the simulations using the KT0 algorithm can sustain a broader range of plastic deformations before the membrane collapses, compared to the KT-ALL simulations. The simulations from the KT1 algorithm fall between the two discussed in this paragraph. Because we know that the yield stress tends to be more concentrated,we can be considered that the KT-ALL algorithm is more precise, reliable, and returns more realistic physical behavior of the membrane.

6.2 2D and 3D Comparative Beams Study

Let's now initiate the cooperative study of the 2D and 3D simulations for the same beam. All subsequent simulations are carried out using the KT-ALL algorithm; this choice is justified by the conclusions and data analysis presented in the previous subsection.

All the cases were run with 2D and 3D simulations, which will show us the expected approximations and similarities that the two types of simulation have or lack. There are four different beam geometries used:

- an I-plate;
- a T-beam with a flange that extends 100 mm beyond the web (hereafter referred to as $b = 100$ mm);
- a T-beam with a flange that extends 200 mm beyond the web (hereafter referred to as $b = 200$ mm);
- a T-beam with a flange that extends 400 mm beyond the web (hereafter referred to as $b = 400$ mm).

The properties of the material being analyzed are Young's modulus (E), the tangent modulus (E_t), Poisson's coefficient (ν), and the yield stress (σ_{yield}), where:

- $E = 200000$ [MPa];
- $E_t = 20000$ [MPa];
- $\nu = 0,3$;
- $\sigma_{\text{yield}} = 200$ [MPa];

in general, these are the values corresponding to the steel properties values.

For the non-linear simulations, it is required to choose a ratio for the elastic limit value; this ratio is an indication of the increase in the yield stress force, which means that:

$$\mathbf{Force}_{\text{final}} = \mathbf{Force}_{\text{yield stress}} \times (1 + \text{Ratio}_{\text{elastic limit}}) \tag{6.1}$$

, with means that the ratio chosen for the simulations will be related to the yield force. The ratio for the elastic limit will be the same for all the simulations run with the same geometry, and the increments' number will be 10, independent of the geometry type. In table 6.11, we can observe the ratio values used for the different geometry types.

Table 6.11: Ratio for the elastic limit for different geometries

Beam Geometry	I Plate	T Beam ($b = 100\,\text{mm}$)	T Beam ($b = 200\,\text{mm}$)	T Beam ($b = 400\,\text{mm}$)
Ratio	0,75	1,25	1,45	1,65

The simulations operated in RPIM and NNRPIM needed to have the already discussed parameters c and p associated. As also already explained, the usual parameters used for the RPIM method are $c = 1,42$ and $p = 1,03$, for the NNRPIM method, the parameters usually used are $c = 0,0001$ and $p = 0,9999$. However, after the analysis of the RPIM simulations, it was clear that the usual parameter values were not giving satisfactory results, so the decision was made to rerun all the RPIM non-linear simulations with the NNRPIM parameters.

All the study cases that will be analyzed were run in these 5 ways:

- FEM;
- RRPIM (with a constant polynomial base);
- RRPIM (with a linear polynomial base);
- NNRRPIM (with a constant polynomial base and a first order of the influence-cell);
- NNRRPIM (with a constant polynomial base and a second order of the influence-cell).

6.3 3D Simulations

The mesh used in all the 3D simulations in this project consists of three-dimensional hexahedral cells.

Table 6.12 presents the number of elements and nodes for each simulation geometry in the study. By plotting these variables, we can confirm the linear relationship between the number of nodes and elements. Figure 6.28 displays this graph, where the vertical axis represents the number of elements and nodes, and the horizontal axis corresponds to the value of b. When b is zero, we are analyzing the values for the I-plate.

Table 6.12: Number of nodes and elements from each simulation's geometry in the study

Simulation's Geometry	I Plate	T Beam (b=100)	T Beam (b=200)	T Beam (b=400)
Nodes	2583	3075	3567	4551
Elements	1600	1920	2240	2880

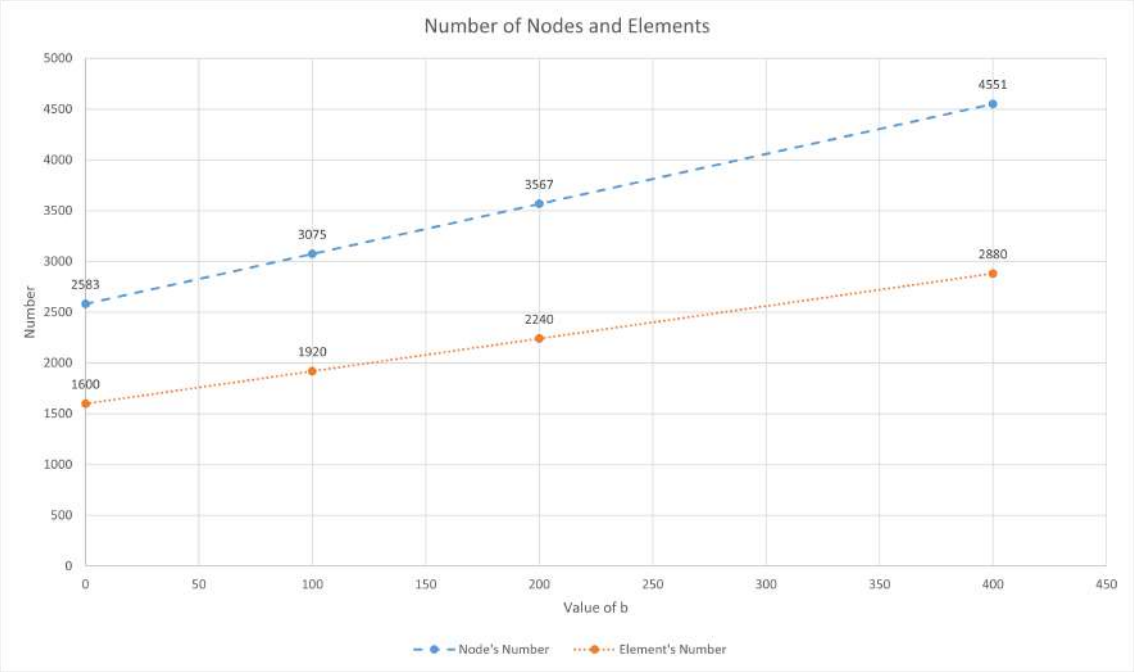

Figure 6.28: Comparison graphic of the number of nodes and elements for each simulation's geometry

6.3.1 I-Plate

The first example analyzed is the 3D I-plate. The dimensions of the I-plate are shown in figure 6.29, and the mesh can be observed in figure 6.30.

As discussed earlier, the I-plate study was subjected to various types of simulations, which means that the iterations differ from simulation to simulation. Table 6.13 shows the applied force at each iteration for every simulation performed on the 3D I-plate, while table 6.14 shows the percentual force difference between the FEM simulations and the meshless methods simulations.

We will begin this analysis by examining the von Mises stress. Table 6.15 presents the contour plot images with the maximum and minimum stress values in the I-plate throughout all the non-linear increments performed by the FEMAS software.

Table 6.13: Applied force in the 3D I-Plate

Iteration	FEM	RPIM (Constante)	RPIM (Linear)	NNRPIM (1º order)	NNRPIM (2º order)
01	818,0 [kN]	839,9 [kN]	839,9 [kN]	782,8 [kN]	782,8 [kN]
02	879,3 [kN]	901,9 [kN]	901,9 [kN]	841,5 [kN]	841,5 [kN]
03	940,7 [kN]	964,8 [kN]	964,8 [kN]	900,2 [kN]	900,2 [kN]
04	1 002,0 [kN]	1 027,7 [kN]	1 027,7 [kN]	958,9 [kN]	958,9 [kN]
05	1 063,4 [kN]	1 090,6 [kN]	1 090,6 [kN]	1 017,6 [kN]	1 017,6 [kN]
06	1 124,7 [kN]	1 153,6 [kN]	1 153,6 [kN]	1 076,3 [kN]	1 076,3 [kN]
07	1 186,1[kN]	1 216,5 [kN]	1 216,5 [kN]	1 135,0 [kN]	1 135,0 [kN]
08	1 247,4 [kN]	1 279,4 [kN]	1 279,4 [kN]	1 193,7 [kN]	1 193,7 [kN]
09	1 308,8 [kN]	1 342,3 [kN]	1 342,3 [kN]	1 252,4 [kN]	1 252,4 [kN]
10	1 370,1 [kN]	1 405,2 [kN]	1 405,2 [kN]	1 311,1 [kN]	1 311,1 [kN]

Table 6.14: Percentual force difference for the meshless methods simulations compared with the FEM simulation, for the 3D I-plate

Increment	RPIM Const.	RPIM Linear	NNRPIM 1º	NNRPIM 2º
01	2.56%	2.56%	4.30%	4.30%
02	2.57%	2.57%	4.30%	4.30%
03	2.56%	2.56%	4.31%	4.31%
04	2.56%	2.56%	4.30%	4.30%
05	2.56%	2.56%	4.31%	4.31%
06	2.57%	2.57%	4.30%	4.30%
07	2.56%	2.56%	4.31%	4.31%
08	2.57%	2.57%	4.30%	4.30%
09	2.56%	2.56%	4.31%	4.31%
10	2.56%	2.56%	4.31%	4.31%

Figure 6.29: I-Plate's Dimensions

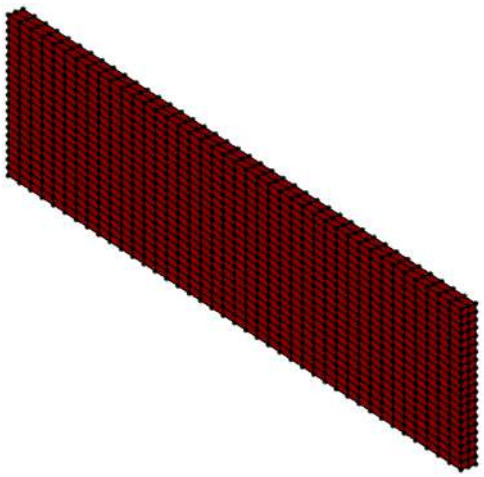

Figure 6.30: I-Plate's Mesh

Table 6.15: Von Mises stress contour plot images resulted from the 3D I plate simulations

	FEM	RPIM Constant	RPIM Linear	NNRPIM 1^{o} Order	NNRPIM 2^{o} Order
01	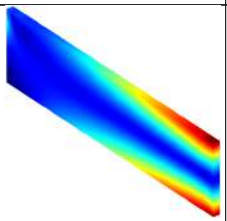 $Max = 191,59[MPa]$ $Min = 0,13[MPa]$	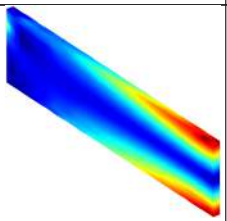 $Max = 195,41[MPa]$ $Min = 3,50[MPa]$	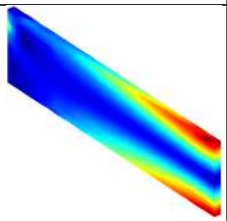 $Max = 195,41[MPa]$ $Min = 3,50[MPa]$	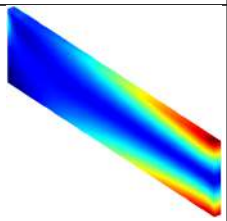 $Max = 189,53[MPa]$ $Min = 0,10[MPa]$	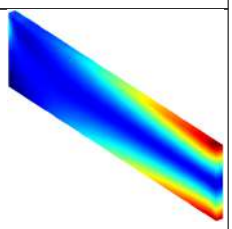 $Max = 189,53[MPa]$ $Min = 0,10[MPa]$
02	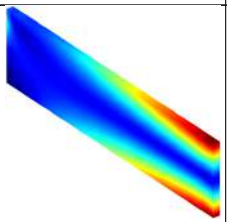 $Max = 199,84[MPa]$ $Min = 0,14[MPa]$	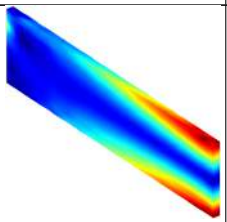 $Max = 200,35[MPa]$ $Min = 3,79[MPa]$	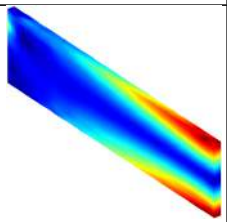 $Max = 200,35[MPa]$ $Min = 3,79[MPa]$	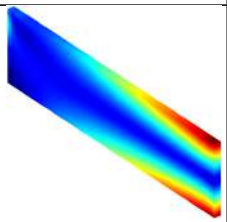 $Max = 199,71[MPa]$ $Min = 0,11[MPa]$	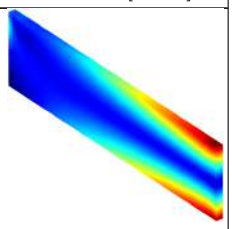 $Max = 199,71[MPa]$ $Min = 0,11[MPa]$

Table 6.15 continued from previous page

	FEM	RPIM Constant	RPIM Linear	NNRPIM 1^{o} Order	NNRPIM 2^{o} Order
03	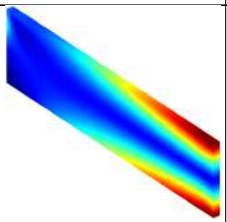 $Max = 200,35[MPa]$ $Min = 0,15[MPa]$	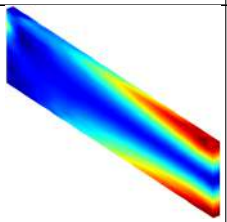 $Max = 200,60[MPa]$ $Min = 4,24[MPa]$	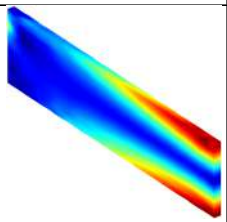 $Max = 200,60[MPa]$ $Min = 4,24[MPa]$	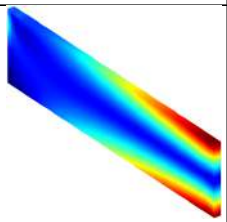 $Max = 200,18[MPa]$ $Min = 0,12[MPa]$	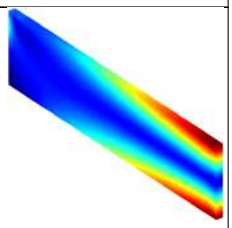 $Max = 200,18[MPa]$ $Min = 0,12[MPa]$
04	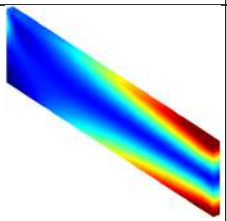 $Max = 200,53[MPa]$ $Min = 0,16[MPa]$	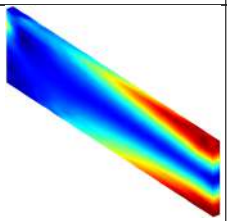 $Max = 201,16[MPa]$ $Min = 4,47[MPa]$	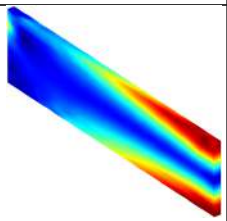 $Max = 201,16[MPa]$ $Min = 4,47[MPa]$	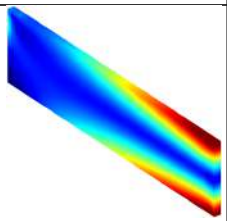 $Max = 200,39[MPa]$ $Min = 0,13[MPa]$	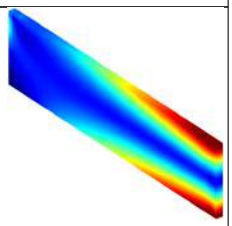 $Max = 200,39[MPa]$ $Min = 0,13[MPa]$
05	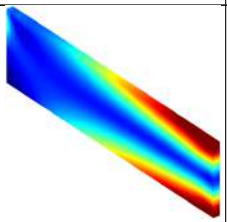 $Max = 200,74[MPa]$ $Min = 0,18[MPa]$	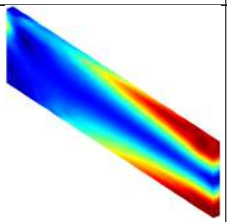 $Max = 201,55[MPa]$ $Min = 5,35[MPa]$	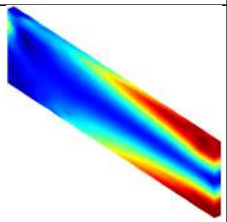 $Max = 201,55[MPa]$ $Min = 5,35[MPa]$	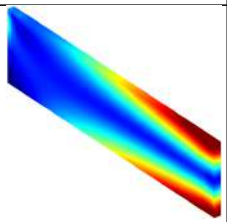 $Max = 200,44[MPa]$ $Min = 0,13[MPa]$	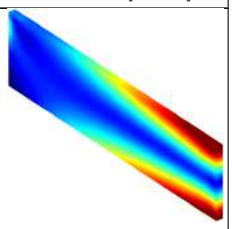 $Max = 200,44[MPa]$ $Min = 0,13[MPa]$
06	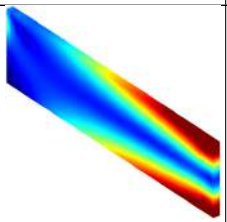 $Max = 200,84[MPa]$ $Min = 0,19[MPa]$	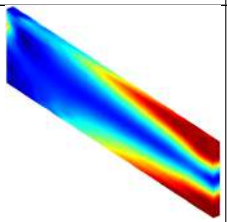 $Max = 201,92[MPa]$ $Min = 5,55[MPa]$	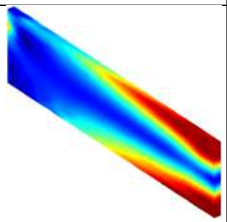 $Max = 201,92[MPa]$ $Min = 5,55[MPa]$	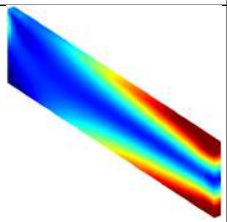 $Max = 200,46[MPa]$ $Min = 0,14[MPa]$	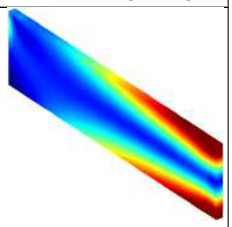 $Max = 200,46[MPa]$ $Min = 0,14[MPa]$
07	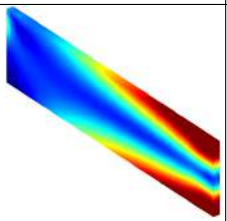 $Max = 200,86[MPa]$ $Min = 0,20[MPa]$	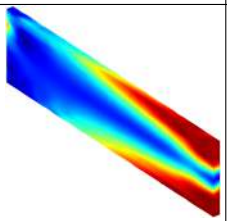 $Max = 203,39[MPa]$ $Min = 5,13[MPa]$	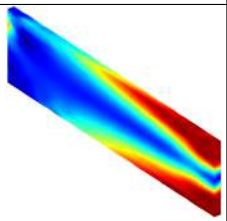 $Max = 203,39[MPa]$ $Min = 5,13[MPa]$	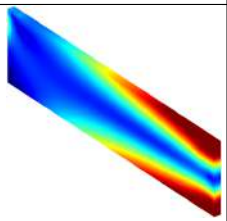 $Max = 200,58[MPa]$ $Min = 0,15[MPa]$	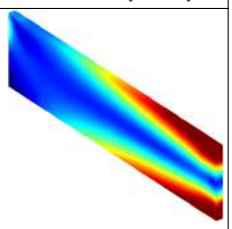 $Max = 200,58[MPa]$ $Min = 0,15[MPa]$

Table 6.15 continued from previous page

	FEM	RPIM Constant	RPIM Linear	NNRPIM 1^{o} Order	NNRPIM 2^{o} Order
08	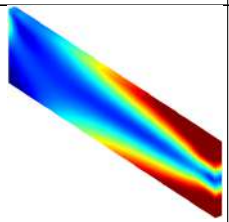 $Max = 201,43[MPa]$ $Min = 0,21[MPa]$	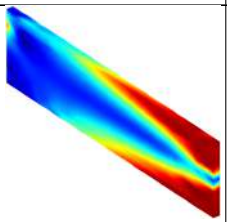 $Max = 206,08[MPa]$ $Min = 5,46[MPa]$	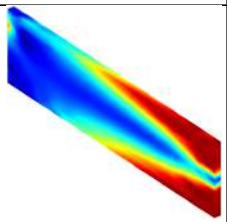 $Max = 206,08[MPa]$ $Min = 5,46[MPa]$	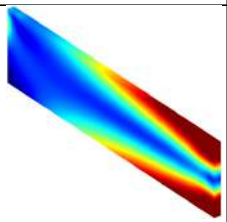 $Max = 200,87[MPa]$ $Min = 0,16[MPa]$	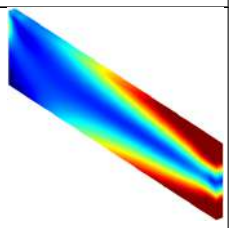 $Max = 200,87[MPa]$ $Min = 0,16[MPa]$
09	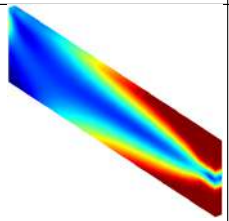 $Max = 202,49[MPa]$ $Min = 0,22[MPa]$	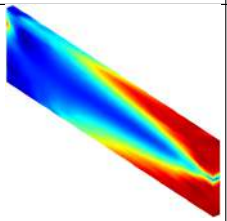 $Max = 215,92[MPa]$ $Min = 5,22[MPa]$	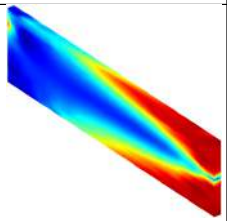 $Max = 215,92[MPa]$ $Min = 5,22[MPa]$	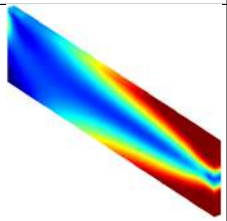 $Max = 201,37[MPa]$ $Min = 0,16[MPa]$	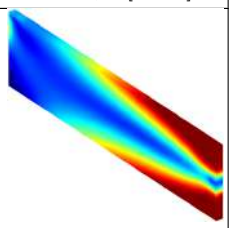 $Max = 201,37[MPa]$ $Min = 0,16[MPa]$
10	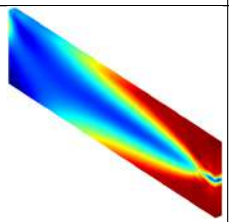 $Max = 209,72[MPa]$ $Min = 0,23[MPa]$	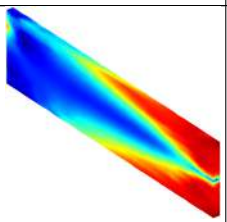 $Max = 231,06[MPa]$ $Min = 5,54[MPa]$	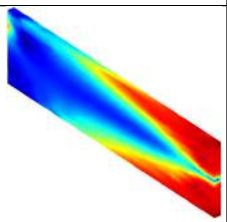 $Max = 231,06[MPa]$ $Min = 5,54[MPa]$	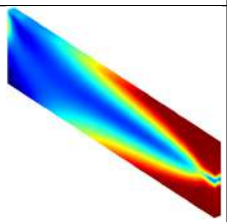 $Max = 203,68[MPa]$ $Min = 0,17[MPa]$	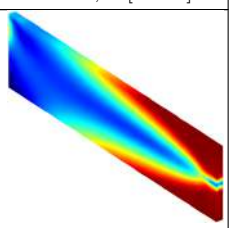 $Max = 203,68[MPa]$ $Min = 0,17[MPa]$
	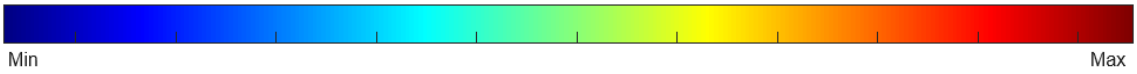				

By analyzing the images and values in table 6.15, we observe that the von Mises stress distribution is very similar across all five simulations' methods. However, by examining the colors in the images, we can visually identify that in the RPIM simulations, the area subjected to the highest stresses (the red region) is slightly less intense than the maximum von Mises stress value. This is evident as the red area in the RPIM simulations appears lighter compared to the FEM and NNRPIM simulations, and that means that the maximum values in the RPIM simulations are found in a more localized point, which means that the maximum stress value is confined to a smaller volume, compared to the other methods. Additionally, the maximum von Mises stress values in the RPIM simulations are slightly higher than those in the FEM and NNRPIM simulations. This means that, although the maximum von Mises stress is somewhat higher in the RPIM cases, the area experiencing the highest von Mises values (red region) is more comparable to the FEM and NNRPIM in terms of stress values. This observation is further supported by the lighter red color in the relevant simulation images. In the following table 6.16, we can observe the percentual difference between the FEM simulations and the meshless methods simulations (RPIM and NNRPIM) for the maximum von Mises stress.

Table 6.16: Percentual stress difference for the meshless methods simulations compared with the FEM simulation, for the 3D I-plate

Increment	RPIM Const.	RPIM Linear	NNRPIM 1º	NNRPIM 2º
01	1.99%	1.99%	1.08%	1.08%
02	0.26%	0.26%	0.07%	0.07%
03	0.12%	0.12%	0.08%	0.08%
04	0.31%	0.31%	0.07%	0.07%
05	0.40%	0.40%	0.15%	0.15%
06	0.54%	0.54%	0.19%	0.19%
07	1.26%	1.26%	0.14%	0.14%
08	2.31%	2.31%	0.28%	0.28%
09	6.63%	6.63%	0.55%	0.55%
10	10.18%	10.18%	2.88%	2.88%

Turning now to the plastic strain of the I-plate, we refer to table 6.17. In the first row (increment 1), we observe that the I-plate has no plastic strain. In all subsequent rows, the I-plate images display two colors: red and blue. The red color indicates areas under plastic strain, while the blue color indicates areas without plastic strain. This rule is applied to all the plastic strain analyses done in this work.

Table 6.17: Plastic strain contour plot images resulted from the 3D I-plate simulations

	FEM	RPIM Constant	RPIM Linear	NNRPIM 1º Order	NNRPIM 2º Order
01					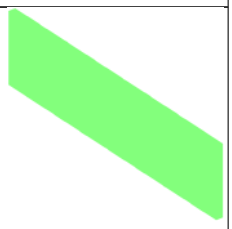
02	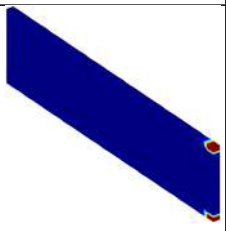	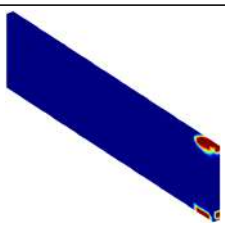	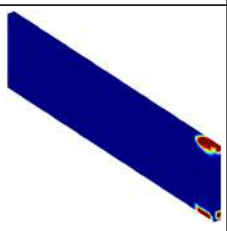	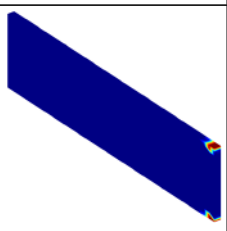	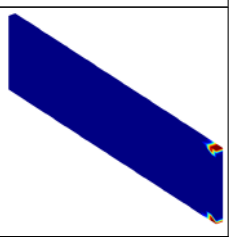
03	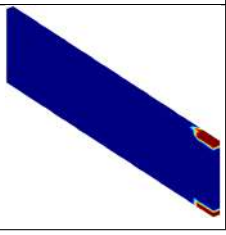	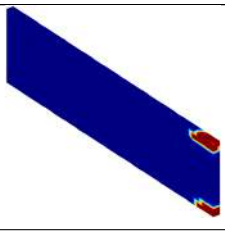	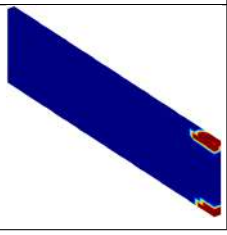	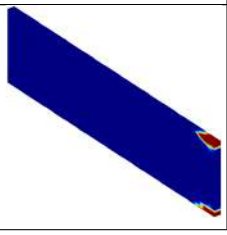	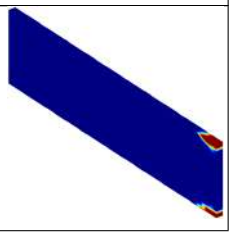

Table 6.17 continued from previous page

	FEM	RPIM Constant	RPIM Linear	NNRPIM 1^{o} Order	NNRPIM 2^{o} Order
04	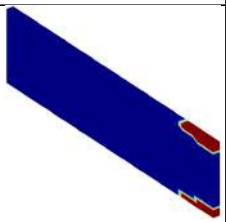	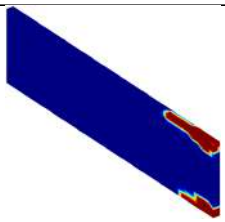	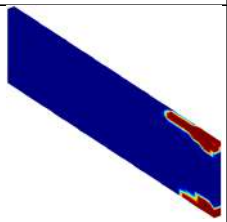	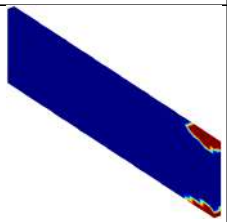	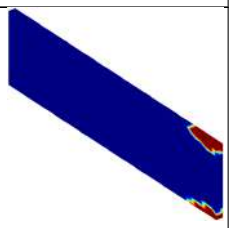
05	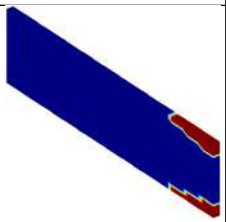	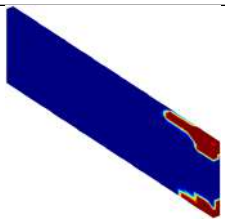	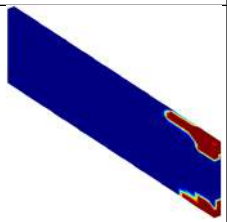	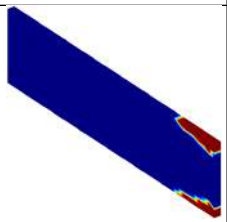	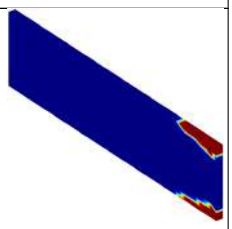
06	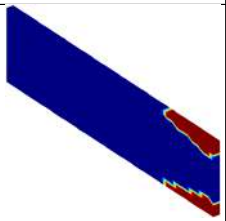	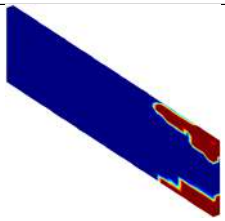	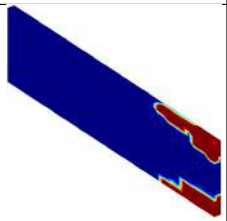	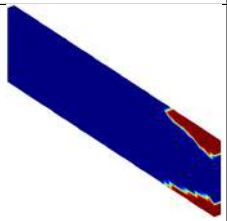	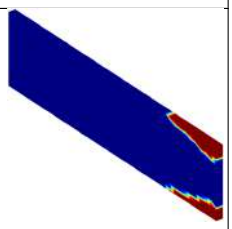
07	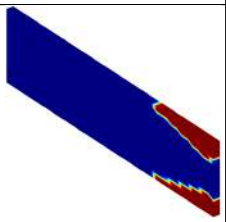	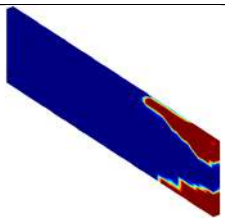	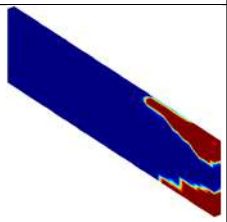	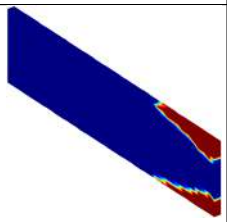	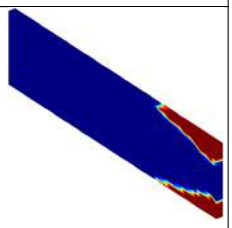
08	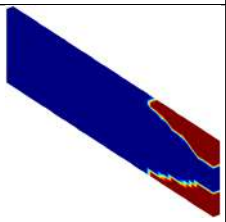	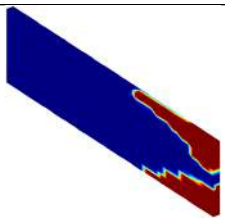	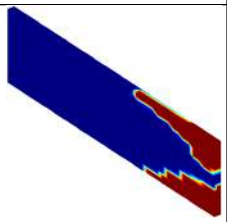	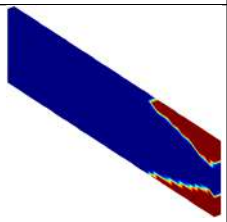	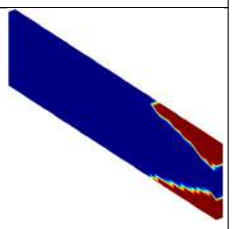
09	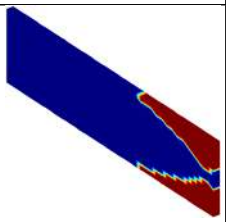	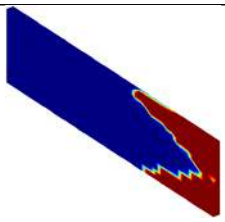	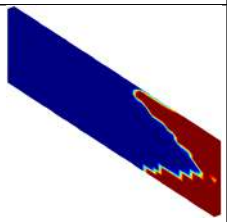	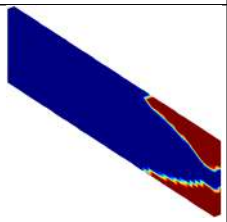	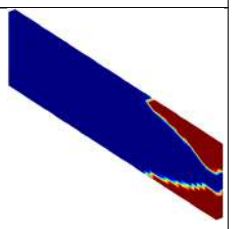
10	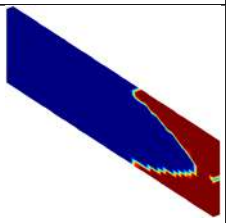	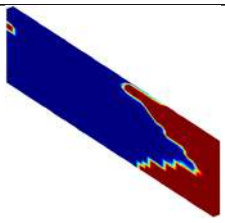	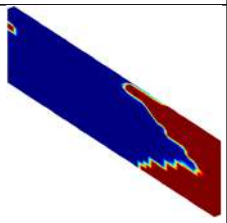	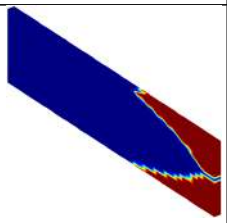	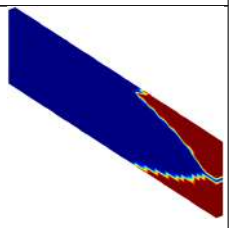

After analyzing table 6.17, we can observe that, similar to the stress analysis, the results are very consistent across all methods. All three methods' simulations generated results that are extremely close to each other.

Let us now conclude the 3D I-plate study by examining the equivalent strain.

Table 6.18: Total strain contour plot images resulted from the 3D I-plate simulations

	FEM	RPIM Constant	RPIM Linear	NNRPIM 1^{o} Order	NNRPIM 2^{o} Order
01	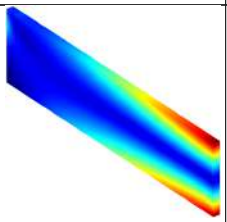 $Max = 0,08[\%]$ $Min = 0,00[\%]$	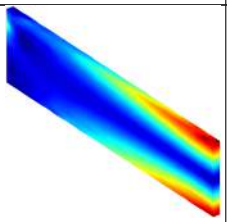 $Max = 0,08[\%]$ $Min = 0,00[\%]$	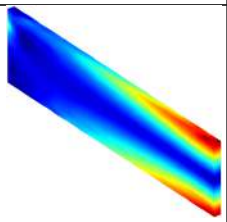 $Max = 0,08[\%]$ $Min = 0,00[\%]$	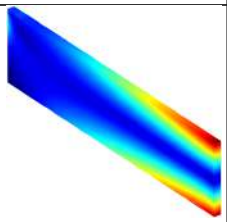 $Max = 0,08[\%]$ $Min = 0,00[\%]$	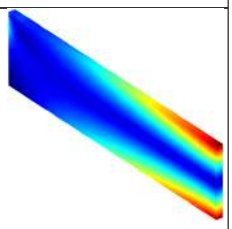 $Max = 0,08[\%]$ $Min = 0,00[\%]$
02	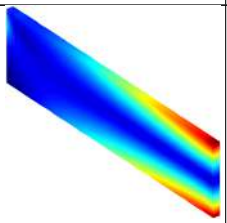 $Max = 0,09[\%]$ $Min = 0,00[\%]$	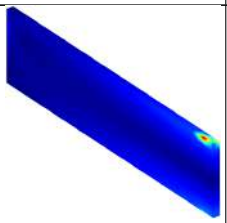 $Max = 0,41[\%]$ $Min = 0,00[\%]$	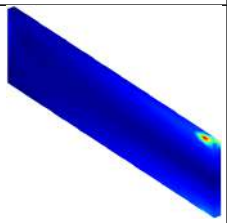 $Max = 0,41[\%]$ $Min = 0,00[\%]$	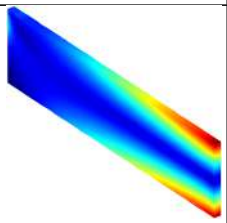 $Max = 0,09[\%]$ $Min = 0,00[\%]$	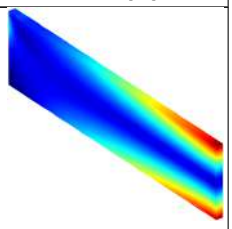 $Max = 0,09[\%]$ $Min = 0,00[\%]$
03	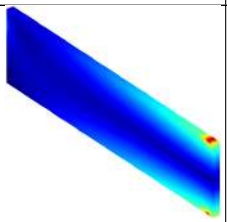 $Max = 0,18[\%]$ $Min = 0,00[\%]$	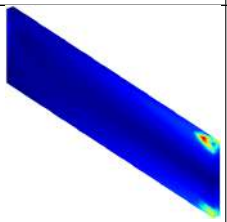 $Max = 0,43[\%]$ $Min = 0,00[\%]$	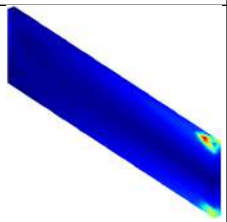 $Max = 0,43[\%]$ $Min = 0,00[\%]$	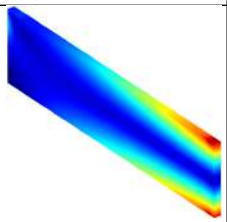 $Max = 0,11[\%]$ $Min = 0,00[\%]$	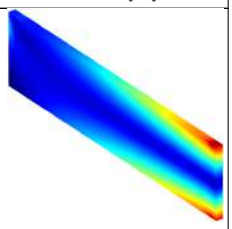 $Max = 0,11[\%]$ $Min = 0,00[\%]$
04	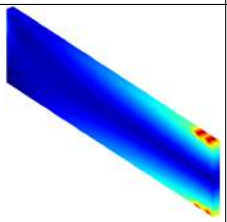 $Max = 0,18[\%]$ $Min = 0,00[\%]$	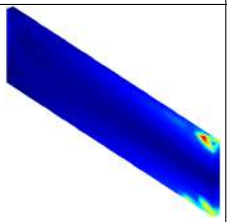 $Max = 0,45[\%]$ $Min = 0,00[\%]$	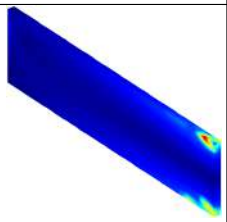 $Max = 0,45[\%]$ $Min = 0,00[\%]$	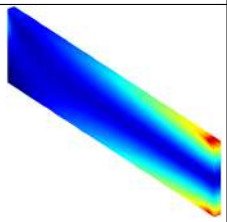 $Max = 0,13[\%]$ $Min = 0,00[\%]$	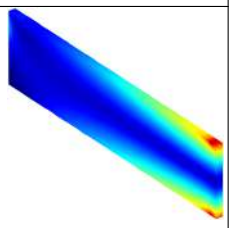 $Max = 0,13[\%]$ $Min = 0,00[\%]$
05	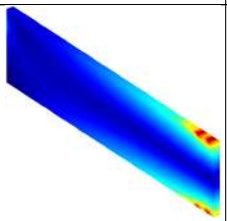 $Max = 0,19[\%]$ $Min = 0,00[\%]$	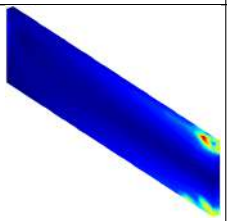 $Max = 0,46[\%]$ $Min = 0,00[\%]$	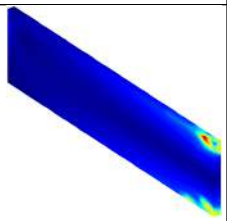 $Max = 0,46[\%]$ $Min = 0,00[\%]$	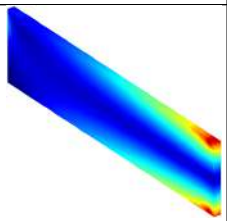 $Max = 0,14[\%]$ $Min = 0,00[\%]$	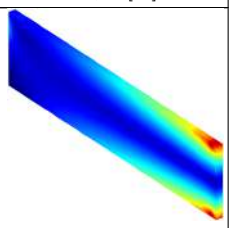 $Max = 0,14[\%]$ $Min = 0,00[\%]$

Table 6.18 continued from previous page

	FEM	RPIM Constant	RPIM Linear	NNRPIM 1^{o} Order	NNRPIM 2^{o} Order
06	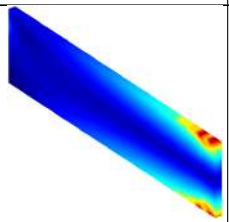 $Max = 0,20[\%]$ $Min = 0,00[\%]$	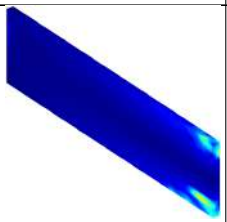 $Max = 0,86[\%]$ $Min = 0,00[\%]$	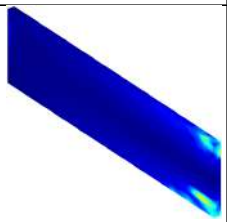 $Max = 0,86[\%]$ $Min = 0,00[\%]$	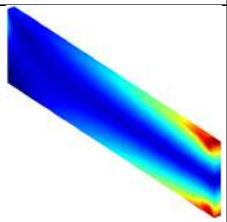 $Max = 0,15[\%]$ $Min = 0,00[\%]$	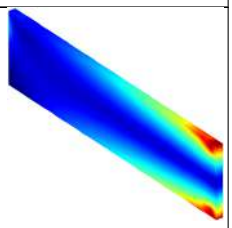 $Max = 0,15[\%]$ $Min = 0,00[\%]$
07	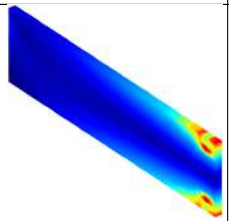 $Max = 0,25[\%]$ $Min = 0,00[\%]$	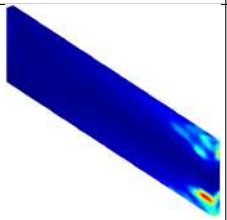 $Max = 1,00[\%]$ $Min = 0,00[\%]$	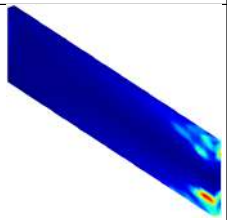 $Max = 1,00[\%]$ $Min = 0,00[\%]$	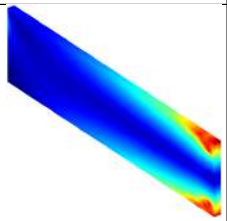 $Max = 0,17[\%]$ $Min = 0,00[\%]$	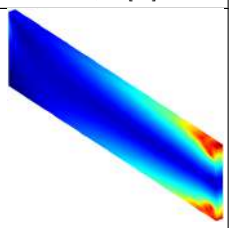 $Max = 0,17[\%]$ $Min = 0,00[\%]$
08	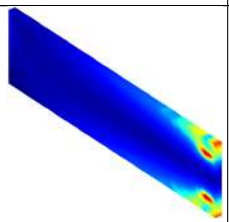 $Max = 0,37[\%]$ $Min = 0,00[\%]$	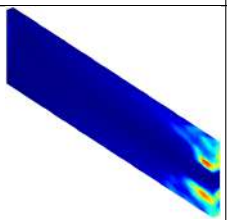 $Max = 1,34[\%]$ $Min = 0,00[\%]$	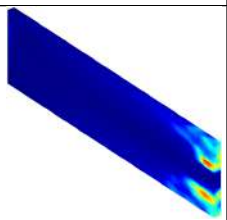 $Max = 1,34[\%]$ $Min = 0,00[\%]$	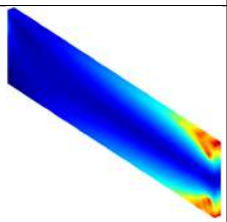 $Max = 0,22[\%]$ $Min = 0,00[\%]$	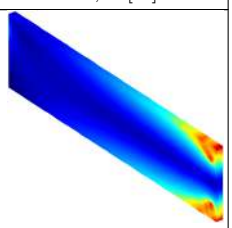 $Max = 0,22[\%]$ $Min = 0,00[\%]$
09	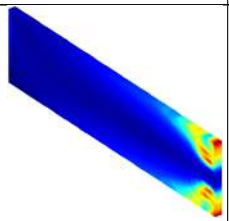 $Max = 0,46[\%]$ $Min = 0,00[\%]$	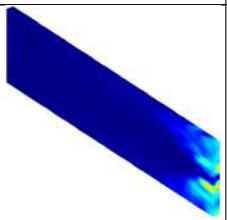 $Max = 2,89[\%]$ $Min = 0,00[\%]$	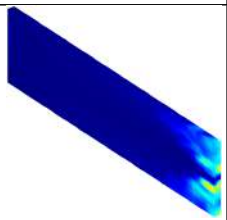 $Max = 2,89[\%]$ $Min = 0,00[\%]$	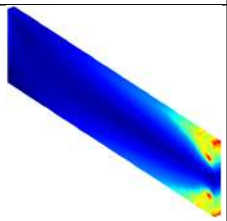 $Max = 0,33[\%]$ $Min = 0,00[\%]$	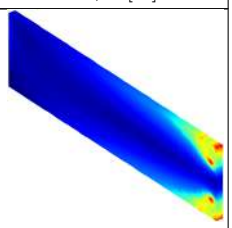 $Max = 0,33[\%]$ $Min = 0,00\%]$
10	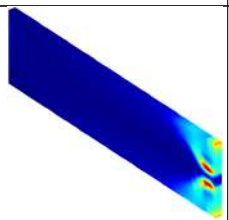 $Max = 1,72[\%]$ $Min = 0,00[\%]$	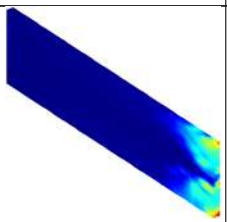 $Max = 3,65[\%]$ $Min = 0,00[\%]$	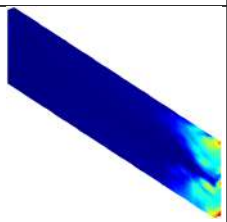 $Max = 3,65[\%]$ $Min = 0,00[\%]$	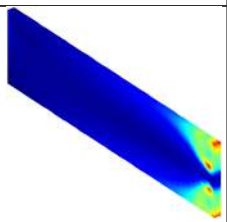 $Max = 0,67[\%]$ $Min = 0,00[\%]$	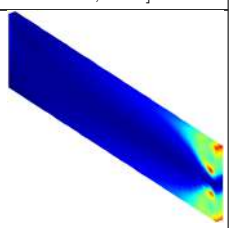 $Max = 0,67[\%]$ $Min = 0,00[\%]$

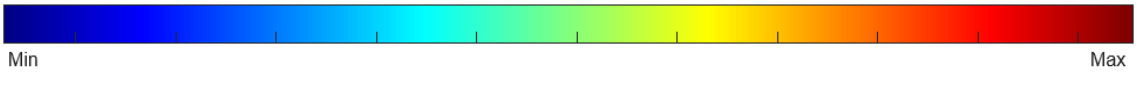

After analyzing table 6.18, we can conclude that, unlike the von Mises stress and plastic strain results, there are significant and visible differences between the three

Table 6.19: Percentual strain's difference for the meshless methods simulations compared with the FEM simulation, to the 3D I-plate

Increment	RPIM Const.	RPIM Linear	NNRPIM 1º	NNRPIM 2º
01	0.00%	0.00%	0.00%	0.00%
02	355.56%	355.56%	0.00%	0.00%
03	138.89%	138.89%	38.89%	38.89%
04	150.00%	150.00%	27.78%	27.78%
05	142.11%	142.11%	26.32%	26.32%
06	330.00%	330.00%	25.00%	25.00%
07	300.00%	300.00%	32.00%	32.00%
08	262.16%	262.16%	40.54%	40.54%
09	528.26%	528.26%	28.26%	28.26%
10	112.21%	112.21%	61.05%	61.05%

types of simulations (FEM, RPIM, and NNRPIM). This can be attributed to the fact that the maximum strain value in the RPIM simulation is much higher than the FEM value in the last iteration, which is undoubtedly a much greater percentage difference compared to the previously calculated von Mises stress, as we can see in the table 6.19.

6.3.2 T-Beams

Let us now analyze the different types of T-beam simulations. As expected, the results show an increase in the applied force on the beam as the value of dimension b increases, which is illustrated in figure 6.31.

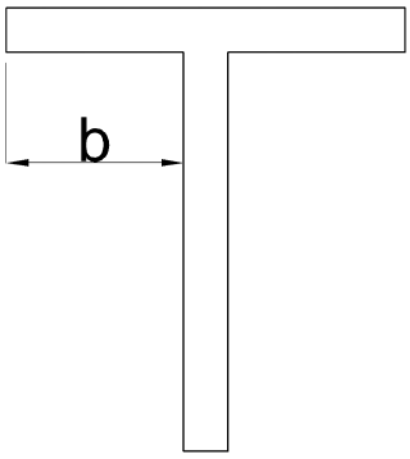

Figure 6.31: Dimension b of the T-Beam

T-Beam with b=100 [mm]

The first T-beam analyzed is the one with dimension $b = 100$ mm. The dimensions of this beam are shown in figure 6.32, and the corresponding mesh is presented in figure 6.33.

Figure 6.32: T-Beam (b=100 [mm]) Dimensions

The applied force on each iteration to each simulation can be compared in the table 6.20, while in table 6.21 we can observe the percentual difference between the FEM values simulation and the meshless methods simulations.

Let's start by analyzing the von Mises stress visible in table 6.22, where the images show us the evolution of the von Mises stress in the T Beam (b=100 mm).

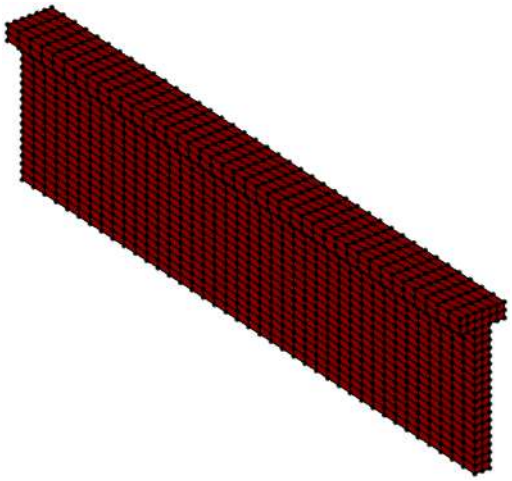

Figure 6.33: T-Beam (b=100 [mm]) Mesh

Table 6.20: Applied force in T-Beam with b=100 [mm]

Iteration	FEM	RPIM (Constante)	RPIM (Linear)	NNRPIM (1º order)	NNRPIM (2º order)
01	1 014,6 [kN]	983,4 [kN]	983,4 [kN]	975,8 [kN]	958,2 [kN]
02	1 141,5 [kN]	1 106,3 [kN]	1 106,3 [kN]	1 097,8 [kN]	1 077,9 [kN]
03	1 268,3 [kN]	1 229,2 [kN]	1 229,2 [kN]	1 219,8 [kN]	1 197,7 [kN]
04	1 395,1[kN]	1 352,2 [kN]	1 352,1 [kN]	1 341,8 [kN]	1 317,5 [kN]
05	1 521,9 [kN]	1 475,1 [kN]	1 475,1 [kN]	1 463,7 [kN]	1 437,2 [kN]
06	1 648,8 [kN]	1 598,0 [kN]	1 598,0 [kN]	1 585,7 [kN]	1 557,0 [kN]
07	1 775,6[kN]	1 720,9 [kN]	1 720,9 [kN]	1 707,7 [kN]	1 676,8 [kN]
08	1 902,4 [kN]	1 843,9 [kN]	1 843,8 [kN]	1 829,7 [kN]	1 796,6 [kN]
09	2 029,2 [kN]	1 966,8 [kN]	1 966,7 [kN]	1 951,7 [kN]	1 916,3 [kN]
10	2 156,1 [kN]	2 089,7 [kN]	2 089,7 [kN]	2 073,6 [kN]	2 036,1 [kN]

Table 6.21: Percentual force difference for the meshless methods simulations compared with the FEM simulation, to the 3D T beam with b=100 [mm]

Increment	RPIM Const.	RPIM Linear	NNRPIM 1º	NNRPIM 2º
01	3.08%	3.08%	3.82%	5.56%
02	3.08%	3.08%	3.83%	5.57%
03	3.08%	3.08%	3.82%	5.57%
04	3.08%	3.08%	3.82%	5.56%
05	3.08%	3.08%	3.82%	5.57%
06	3.08%	3.08%	3.83%	5.57%
07	3.08%	3.08%	3.82%	5.56%
08	3.08%	3.08%	3.82%	5.56%
09	3.08%	3.08%	3.82%	5.56%
10	3.08%	3.08%	3.83%	5.57%

Table 6.22: Von Mises stress images resulted from the 3D T beam with b=100 [mm] simulations

	FEM	RPIM Constant	RPIM Linear	NNRPIM 1^{o} Order	NNRPIM 2^{o} Order
01	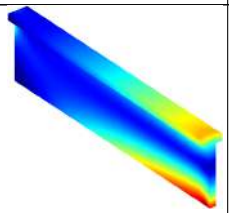 $Max = 194,82[MPa]$ $Min = 0,16[MPa]$	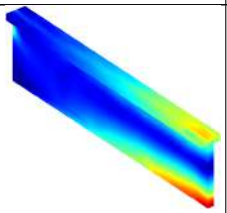 $Max = 199,99[MPa]$ $Min = 1,13[MPa]$	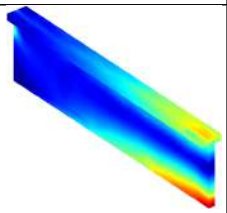 $Max = 199,99[MPa]$ $Min = 1,13[MPa]$	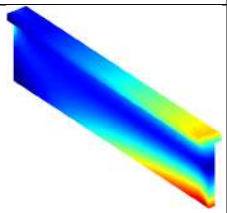 $Max = 193,11[MPa]$ $Min = 0,38[MPa]$	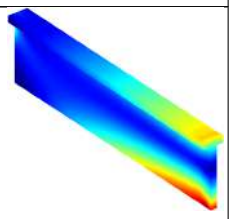 $Max = 187,23[MPa]$ $Min = 0,08[MPa]$
02	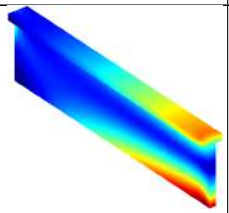 $Max = 201,29[MPa]$ $Min = 0,18[MPa]$	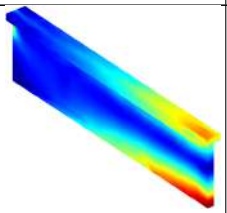 $Max = 203,01[MPa]$ $Min = 1,30[MPa]$	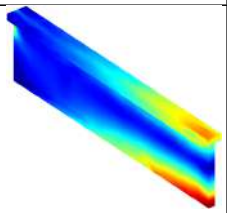 $Max = 203,01[MPa]$ $Min = 1,30[MPa]$	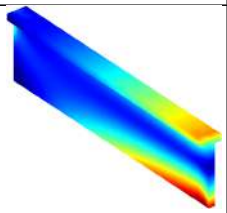 $Max = 201,26[MPa]$ $Min = 0,42[MPa]$	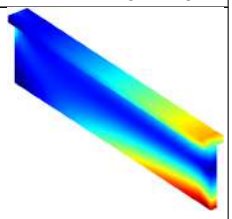 $Max = 199,28[MPa]$ $Min = 0,09[MPa]$
03	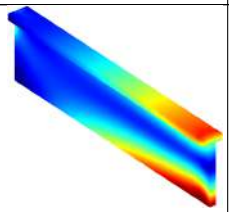 $Max = 202,70[MPa]$ $Min = 0,20[MPa]$	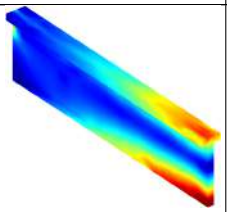 $Max = 205,08[MPa]$ $Min = 1,50[MPa]$	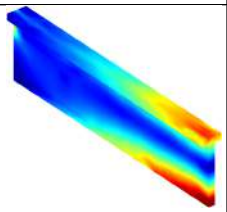 $Max = 205,08[MPa]$ $Min = 1,50[MPa]$	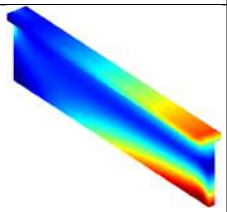 $Max = 202,76[MPa]$ $Min = 0,47[MPa]$	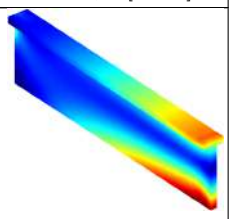 $Max = 201,74[MPa]$ $Min = 0,10[MPa]$
04	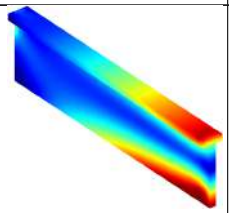 $Max = 205,34[MPa]$ $Min = 0,22[MPa]$	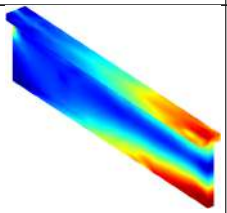 $Max = 208,97[MPa]$ $Min = 1,58[MPa]$	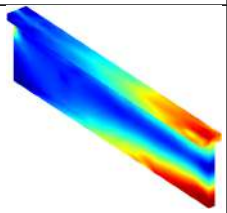 $Max = 208,97[MPa]$ $Min = 1,58[MPa]$	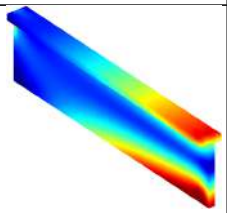 $Max = 205,34[MPa]$ $Min = 0,52[MPa]$	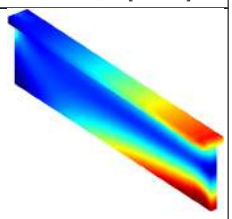 $Max = 204,20[MPa]$ $Min = 0,11[MPa]$
05	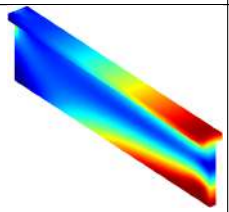 $Max = 207,78[MPa]$ $Min = 0,24[MPa]$	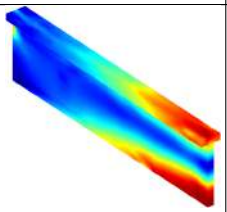 $Max = 213,47[MPa]$ $Min = 1,74[MPa]$	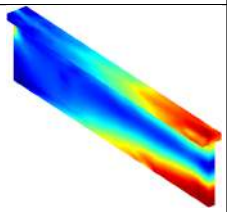 $Max = 213,47[MPa]$ $Min = 1,74[MPa]$	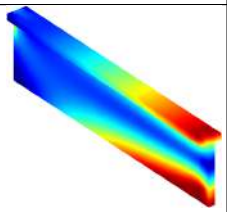 $Max = 207,74[MPa]$ $Min = 0,56[MPa]$	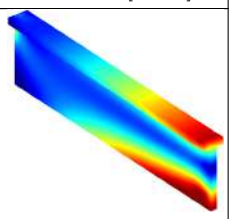 $Max = 206,31[MPa]$ $Min = 0,12[MPa]$

Table 6.22 continued from previous page

	FEM	RPIM Constant	RPIM Linear	NNRPIM 1^{o} Order	NNRPIM 2^{o} Order
06	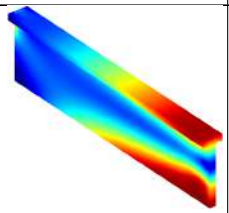 $Max = 211,39[MPa]$ $Min = 0,26[MPa]$	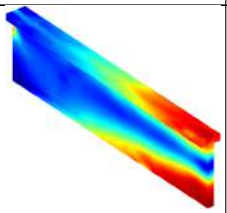 $Max = 219,11[MPa]$ $Min = 1,94[MPa]$	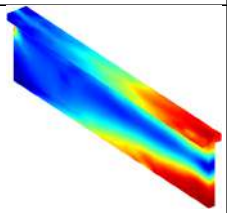 $Max = 219,11[MPa]$ $Min = 1,94[MPa]$	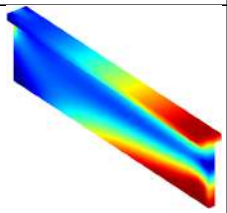 $Max = 210,79[MPa]$ $Min = 0,61[MPa]$	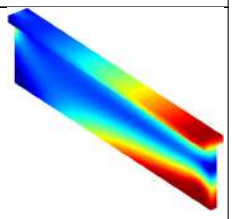 $Max = 209,16[MPa]$ $Min = 0,13[MPa]$
07	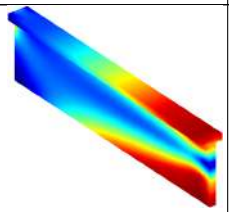 $Max = 217,86[MPa]$ $Min = 0,28[MPa]$	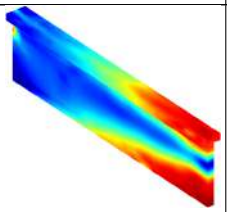 $Max = 226,17[MPa]$ $Min = 2,16[MPa]$	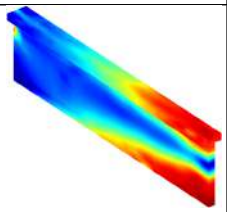 $Max = 226,17[MPa]$ $Min = 2,16[MPa]$	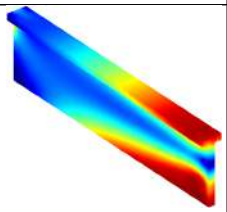 $Max = 216,02[MPa]$ $Min = 0,66[MPa]$	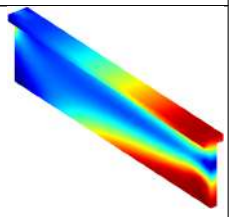 $Max = 213,41[MPa]$ $Min = 0,14[MPa]$
08	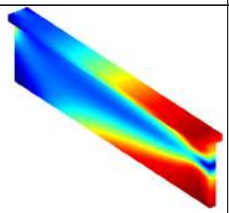 $Max = 228,65[MPa]$ $Min = 0,29[MPa]$	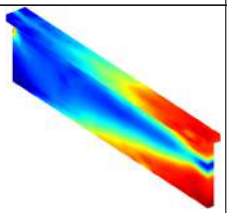 $Max = 240,57[MPa]$ $Min = 2,20[MPa]$	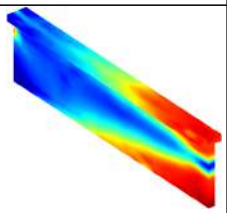 $Max = 240,57[MPa]$ $Min = 2,20[MPa]$	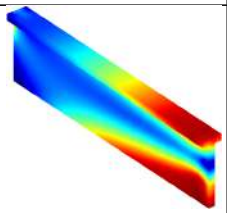 $Max = 224,34[MPa]$ $Min = 0,70[MPa]$	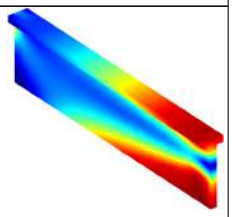 $Max = 220,91[MPa]$ $Min = 0,14[MPa]$
09	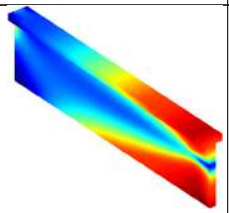 $Max = 246,16[MPa]$ $Min = 0,31[MPa]$	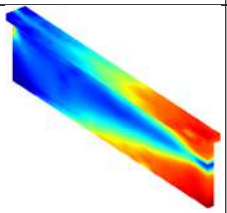 $Max = 260,41[MPa]$ $Min = 2,32[MPa]$	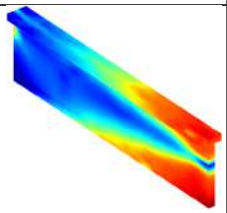 $Max = 260,41[MPa]$ $Min = 2,32[MPa]$	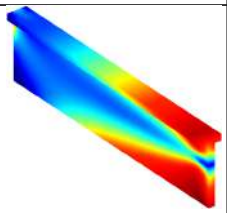 $Max = 238,10[MPa]$ $Min = 0,75[MPa]$	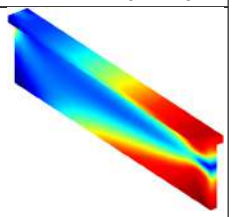 $Max = 233,78[MPa]$ $Min = 0,15[MPa]$
10	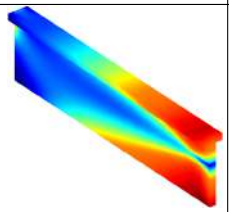 $Max = 266,74[MPa]$ $Min = 0,33[MPa]$	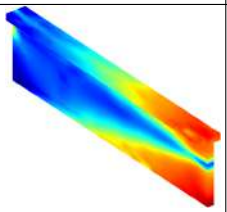 $Max = 283,47[MPa]$ $Min = 2,54[MPa]$	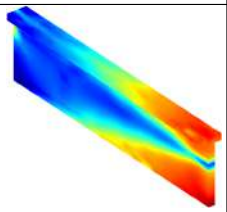 $Max = 283,47[MPa]$ $Min = 2,54[MPa]$	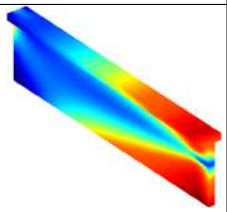 $Max = 257,20[MPa]$ $Min = 0,79[MPa]$	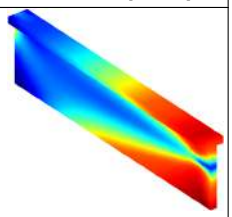 $Max = 252,06[MPa]$ $Min = 0,16[MPa]$
	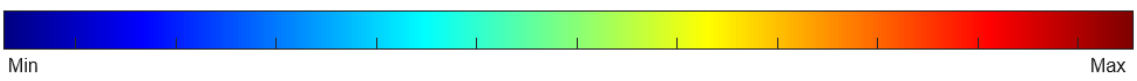 Min Max				

As in the I-plate simulations, we observe that the RPIM simulations yield slightly higher stress values. It is important to note that these higher values are due to nodal stresses, and, similar to the I-plate case, the areas with the highest stress values are

Table 6.23: Percentual stress' difference for the meshless methods simulations compared with the FEM simulation, to the 3D T beam with b=100 mm

Increment	RPIM Const.	RPIM Linear	NNRPIM 1º	NNRPIM 2º
01	2.65%	2.65%	0.88%	3.90%
02	0.85%	0.85%	0.01%	1.00%
03	1.17%	1.17%	0.03%	0.47%
04	1.77%	1.77%	0.00%	0.56%
05	2.74%	2.74%	0.02%	0.71%
06	3.65%	3.65%	0.28%	1.05%
07	3.81%	3.81%	0.84%	2.04%
08	5.21%	5.21%	1.88%	3.39%
09	5.79%	5.79%	3.27%	5.03%
10	6.27%	6.27%	3.58%	5.50%

quite comparable across all simulation types. By performing the same percentage calculation as in the I-plate study, we find the stress value difference with the FEM as standard, in table 6.23.

Let us now move on to the plastic strain analysis, which can be observed in table 6.24, where the same color scheme used for the I-plate is maintained.

Table 6.24: Plastic strain contour plot images resulted from the 3D T beam with b=100 [mm] simulations

	FEM	RPIM Constant	RPIM Linear	NNRPIM 1º Order	NNRPIM 2º Order
01	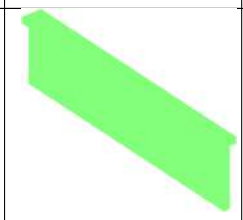	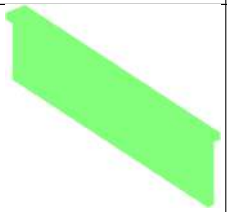	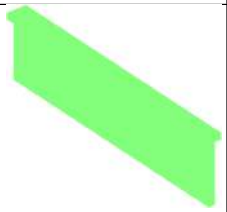	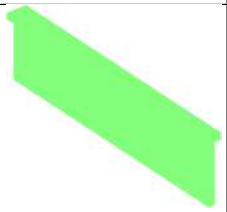	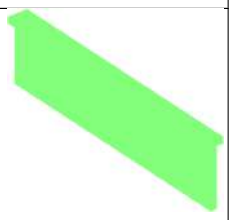
02	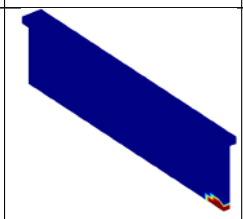	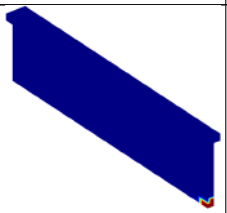	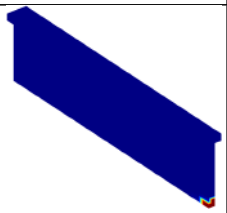	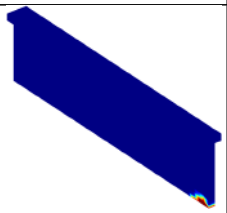	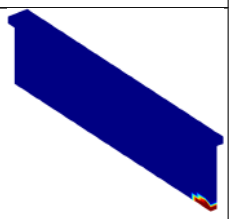
03	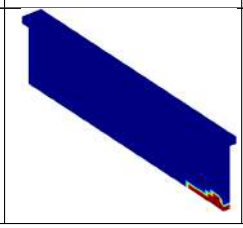	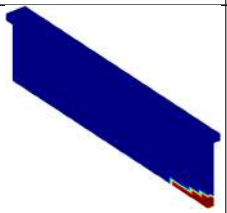	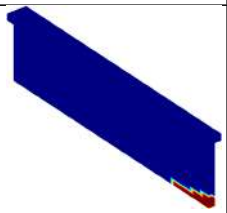	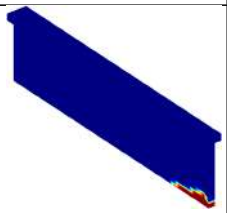	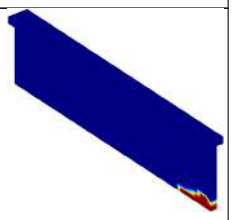

Table 6.24 continued from previous page

	FEM	RPIM Constant	RPIM Linear	NNRPIM 1^{o} Order	NNRPIM 2^{o} Order
04	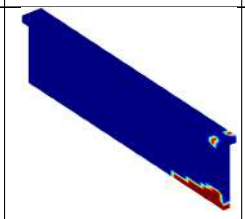	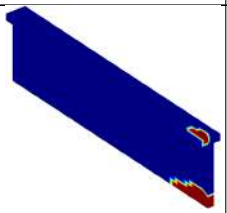	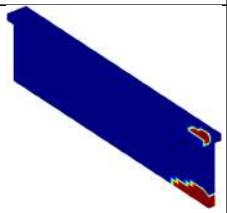	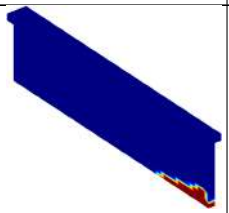	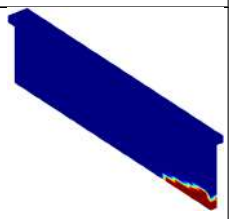
05	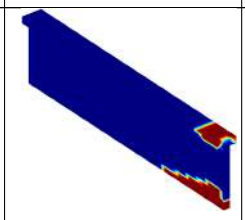	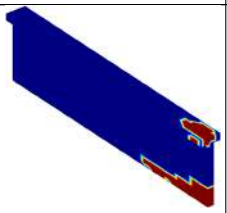	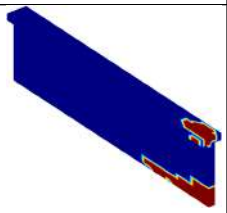	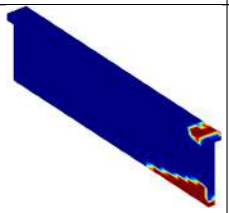	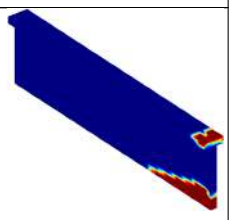
06	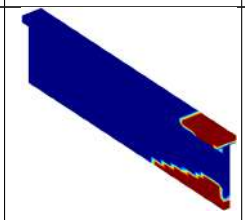	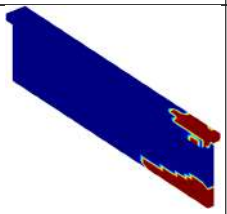	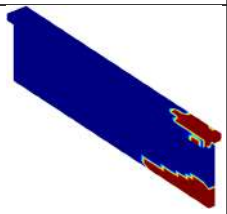	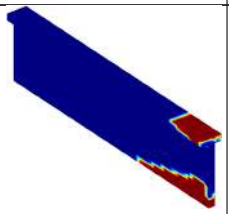	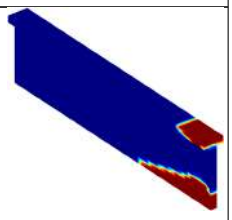
07	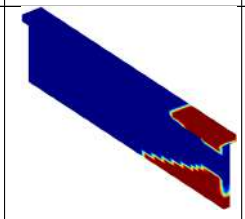	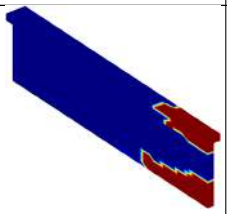	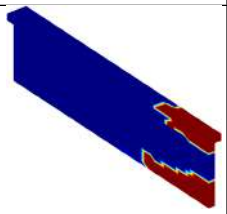	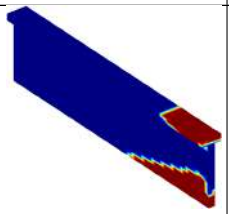	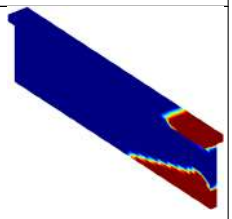
08	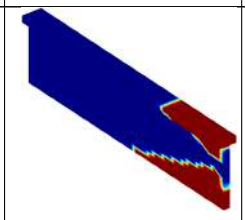	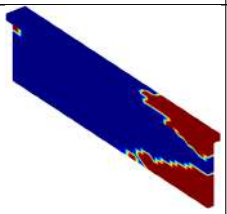	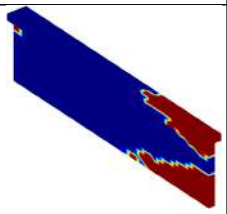	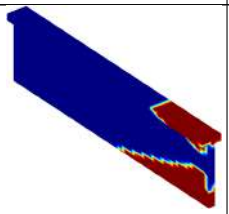	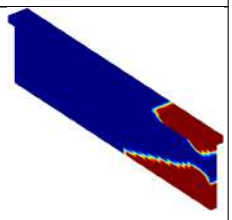
09	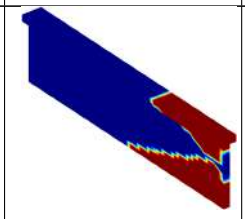	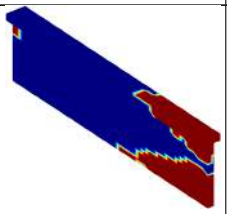	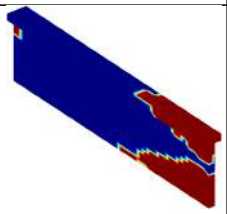	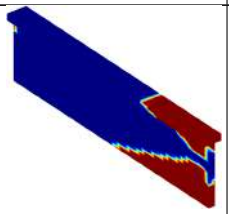	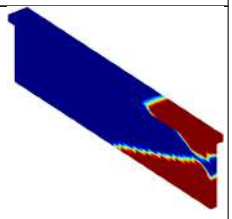
10	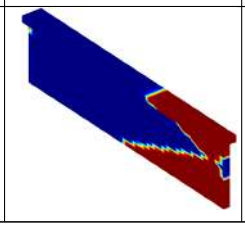	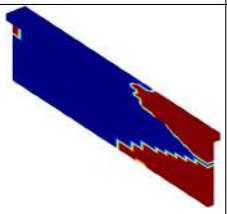	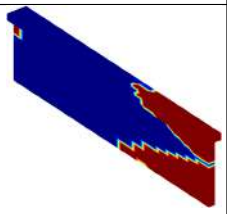	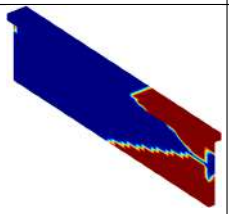	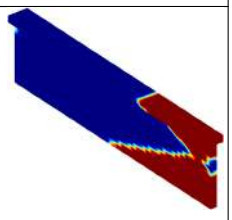

After analyzing the images in table 6.24, it is clear that the plastic strain behavior is very similar across all five simulations. It is also observable that, on the beam surface where the boundary force is applied, there is plastic strain in the final iterations; however, this can be disregarded, as it results from the applied force being concentrated at nodes near that area, so we can disregard that plastic strain on that

specific nodes.

To conclude the analysis of the T-beam with $b = 100$ mm, we will now examine the total strain, which is presented in table 6.25.

Table 6.25: Total strain contour plot images resulted from the 3D T beam with b=100 [mm] simulations

	FEM	RPIM Constant	RPIM Linear	NNRPIM 1^{o} Order	NNRPIM 2^{o} Order
01	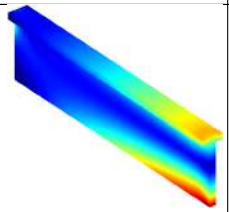 $Max = 0,09[\%]$ $Min = 0,00[\%]$	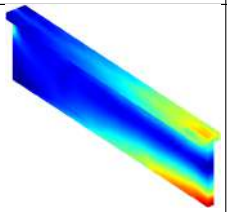 $Max = 0,09[\%]$ $Min = 0,00[\%]$	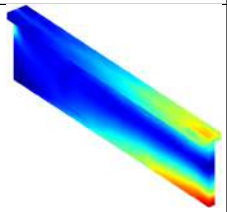 $Max = 0,09[\%]$ $Min = 0,00[\%]$	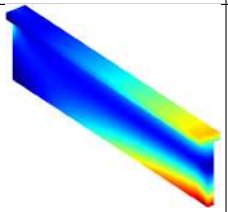 $Max = 0,09[\%]$ $Min = 0,00[\%]$	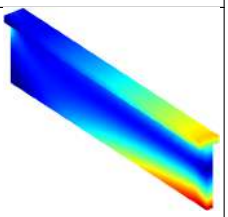 $Max = 0,08[\%]$ $Min = 0,00[\%]$
02	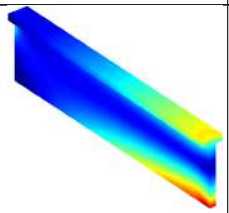 $Max = 0,11[\%]$ $Min = 0,00[\%]$	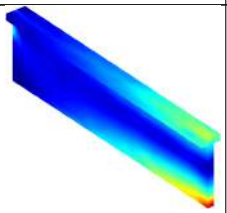 $Max = 0,12[\%]$ $Min = 0,00[\%]$	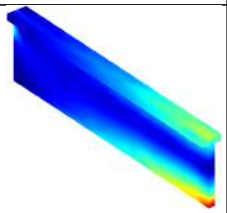 $Max = 0,12[\%]$ $Min = 0,00[\%]$	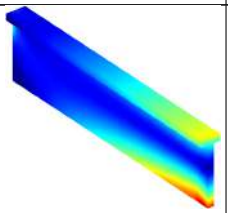 $Max = 0,11[\%]$ $Min = 0,00[\%]$	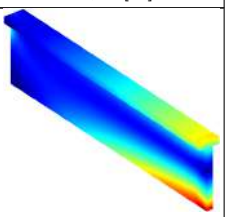 $Max = 0,10[\%]$ $Min = 0,00[\%]$
03	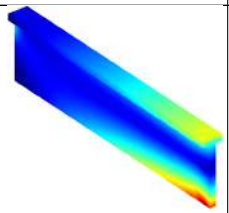 $Max = 0,13[\%]$ $Min = 0,00[\%]$	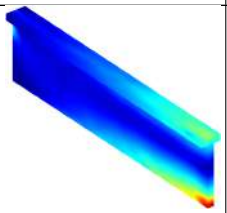 $Max = 0,15[\%]$ $Min = 0,00[\%]$	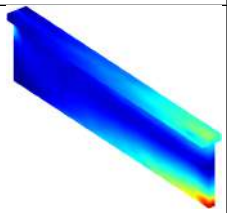 $Max = 0,15[\%]$ $Min = 0,00[\%]$	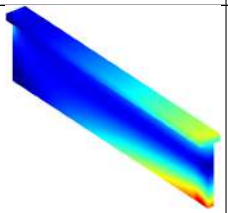 $Max = 0,12[\%]$ $Min = 0,00[\%]$	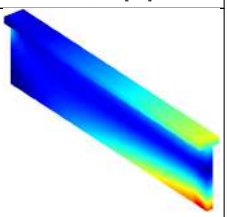 $Max = 0,12[\%]$ $Min = 0,00[\%]$
04	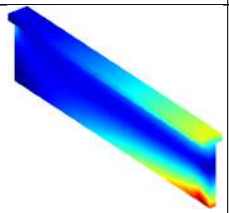 $Max = 0,14[\%]$ $Min = 0,00[\%]$	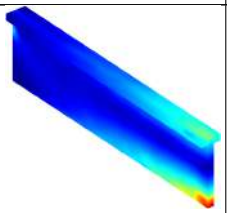 $Max = 0,18[\%]$ $Min = 0,00[\%]$	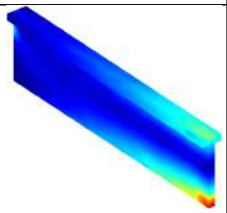 $Max = 0,18[\%]$ $Min = 0,00[\%]$	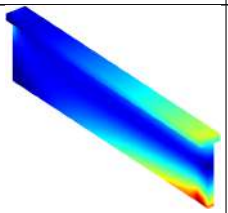 $Max = 0,14[\%]$ $Min = 0,00[\%]$	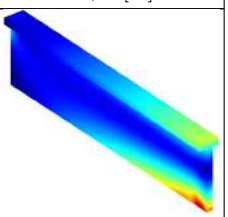 $Max = 0,14[\%]$ $Min = 0,00[\%]$
05	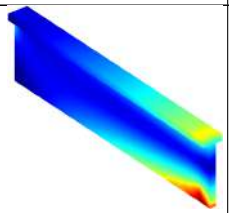 $Max = 0,16[\%]$ $Min = 0,00[\%]$	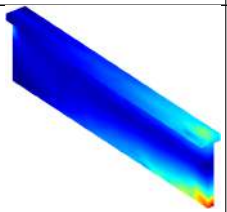 $Max = 0,23[\%]$ $Min = 0,00[\%]$	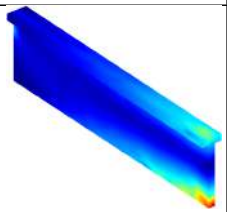 $Max = 0,23[\%]$ $Min = 0,00[\%]$	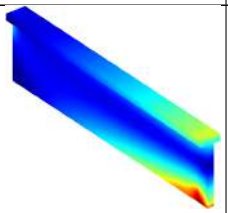 $Max = 0,16[\%]$ $Min = 0,00[\%]$	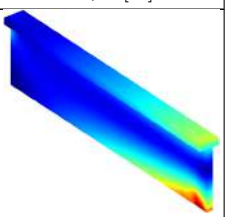 $Max = 0,16[\%]$ $Min = 0,00[\%]$

Table 6.25 continued from previous page

	FEM	RPIM Constant	RPIM Linear	NNRPIM 1^{o} Order	NNRPIM 2^{o} Order
06	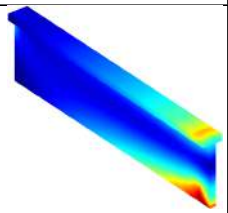 $Max = 0,20[\%]$ $Min = 0,00[\%]$	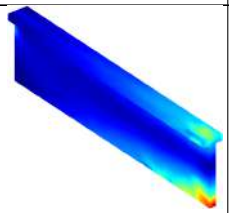 $Max = 0,27[\%]$ $Min = 0,00[\%]$	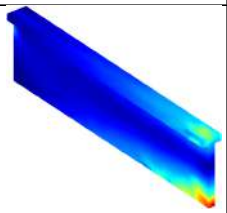 $Max = 0,27[\%]$ $Min = 0,00[\%]$	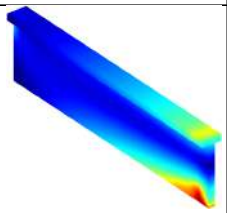 $Max = 0,19[\%]$ $Min = 0,00[\%]$	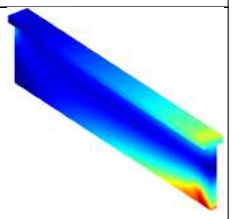 $Max = 0,18[\%]$ $Min = 0,00[\%]$
07	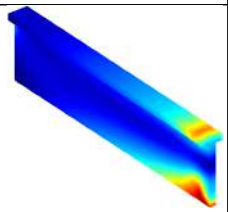 $Max = 0,26[\%]$ $Min = 0,00[\%]$	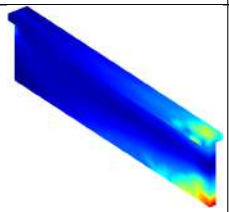 $Max = 0,34[\%]$ $Min = 0,00[\%]$	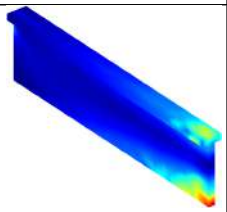 $Max = 0,34[\%]$ $Min = 0,00[\%]$	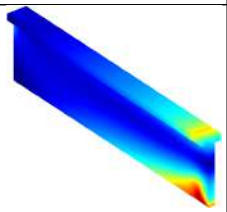 $Max = 0,24[\%]$ $Min = 0,00[\%]$	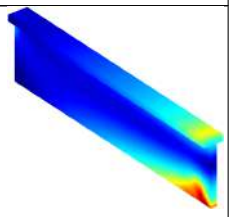 $Max = 0,22[\%]$ $Min = 0,00[\%]$
08	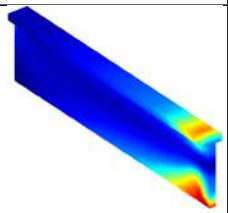 $Max = 0,36[\%]$ $Min = 0,00[\%]$	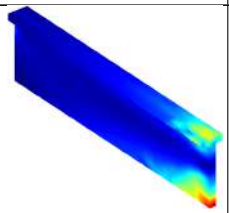 $Max = 0,46[\%]$ $Min = 0,00[\%]$	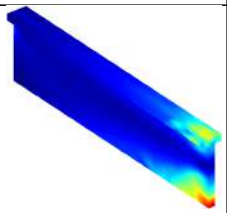 $Max = 0,46[\%]$ $Min = 0,00[\%]$	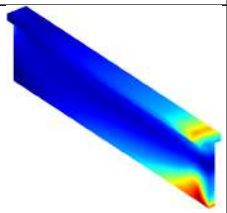 $Max = 0,31[\%]$ $Min = 0,00[\%]$	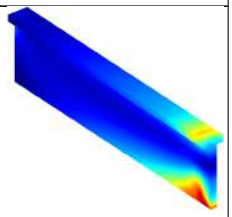 $Max = 0,29[\%]$ $Min = 0,00[\%]$
09	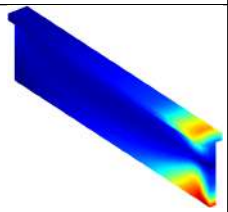 $Max = 0,53[\%]$ $Min = 0,00[\%]$	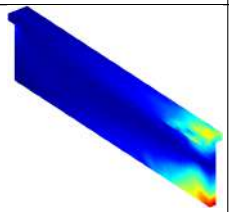 $Max = 0,66[\%]$ $Min = 0,00[\%]$	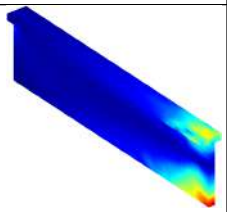 $Max = 0,66[\%]$ $Min = 0,00[\%]$	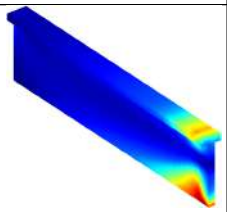 $Max = 0,45[\%]$ $Min = 0,00[\%]$	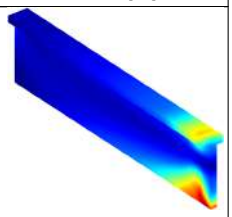 $Max = 0,41[\%]$ $Min = 0,00[\%]$
10	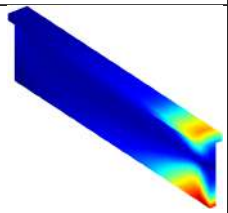 $Max = 0,73[\%]$ $Min = 0,00[\%]$	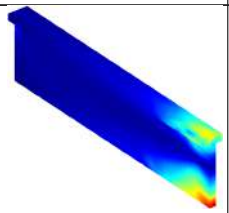 $Max = 0,88[\%]$ $Min = 0,00[\%]$	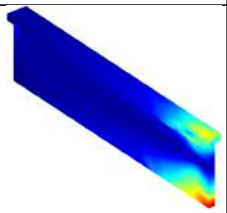 $Max = 0,88[\%]$ $Min = 0,00[\%]$	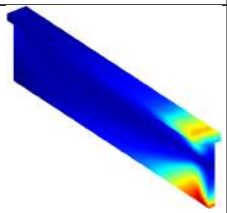 $Max = 0,63[\%]$ $Min = 0,00[\%]$	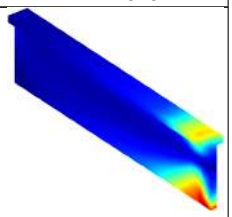 $Max = 0,58[\%]$ $Min = 0,00[\%]$
	 Min Max				

When we analyze the images in table 6.25, we observe that the similarities between the FEM, RPIM, and NNRPIM simulations are much closer than those observed in the I-plate strain results. The most notable and visible difference is in the RPIM

Table 6.26: Percentual strain's difference for the meshless methods simulations compared with the FEM simulation, to the 3D T beam with b=100 [mm]

Increment	RPIM Const.	RPIM Linear	NNRPIM 1º	NNRPIM 2º
01	0.00%	0.00%	0.00%	11.11%
02	9.09%	9.09%	0.00%	9.09%
03	15.38%	15.38%	7.69%	7.69%
04	28.57%	28.57%	0.00%	0.00%
05	43.75%	43.75%	0.00%	0.00%
06	35.00%	35.00%	5.00%	10.00%
07	30.77%	30.77%	7.69%	15.38%
08	27.78%	27.78%	13.89%	19.44%
09	24.53%	24.53%	15.09%	22.64%
10	20.55%	20.55%	13.70%	20.55%

simulations, where the area with the highest strain is located. In terms of percentage divergence, and continuing to consider the FEM method as the reference, we can find the different percentage values in table 6.26.

T-Beam with b=200 [mm]

The next analysis focuses on the T-beam with dimension $b = 200$ mm. The dimensions of this beam are shown in figure 6.34, and the corresponding mesh is presented in figure 6.35.

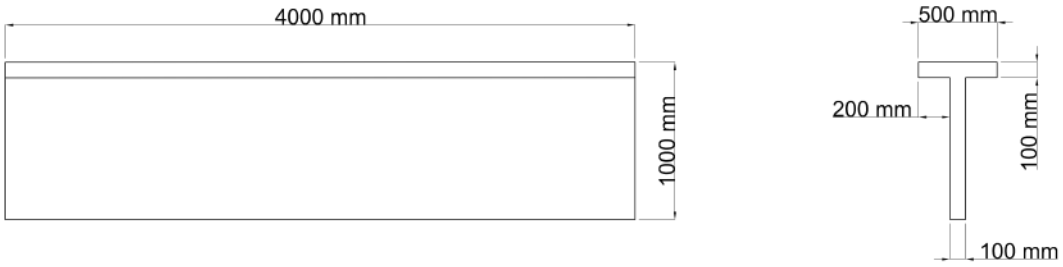

Figure 6.34: T-Beam (b=200 [mm]) Dimensions

The applied force on each iteration to each simulation can be seen in the table 6.27, while the percentual difference can be studied in table 6.28.

Once again, we start by analyzing the von Mises stress for the beam in question, in this case, the T-beam with b=200 mm. In table 6.29, we are capable of studying the stress expansion behavior of the T-beam.

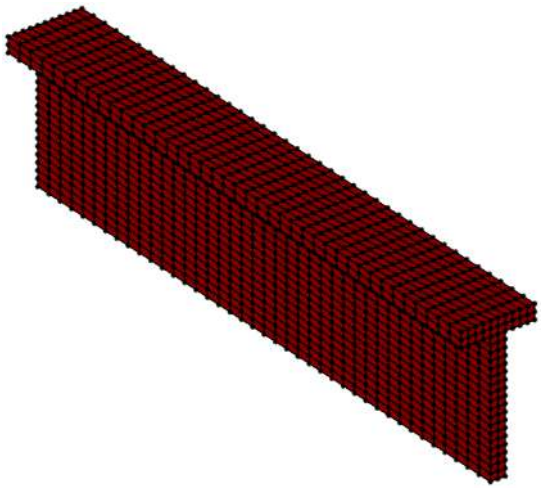

Figure 6.35: T-Beam (b=200 [mm]) Mesh

Table 6.27: Applied force in T-Beam with b=200 [mm]

Iteration	FEM	RPIM (Constante)	RPIM (Linear)	NNRPIM (1º order)	NNRPIM (2º order)
01	1 095,0 [kN]	1 070,2 [kN]	1 070,2 [kN]	1 057,2 [kN]	1 030,9 [kN]
02	1 253,7 [kN]	1 225,4 [kN]	1 225,4 [kN]	1 210,5 [kN]	1 180,4 [kN]
03	1 412,5 [kN]	1 380,5 [kN]	1 380,5 [kN]	1 363,8 [kN]	1 329,9 [kN]
04	1 571,3 [kN]	1 535,7 [kN]	1 535,7 [kN]	1 517,1 [kN]	1 479,3 [kN]
05	1 730,0 [kN]	1 690,9 [kN]	1 690,9 [kN]	1 670,4 [kN]	1 628,8 [kN]
06	1 888,8 [kN]	1 846,1 [kN]	1 846,1 [kN]	1 823,7 [kN]	1 778,3 [kN]
07	2 047,6 [kN]	2 001,3 [kN]	2 001,2 [kN]	1 977,0 [kN]	1 927,8 [kN]
08	2 206,3 [kN]	2 156,4 [kN]	2 156,4 [kN]	2 130,3 [kN]	2 077,2 [kN]
09	2 365,1 [kN]	2 311,6 [kN]	2 311,6 [kN]	2 283,6 [kN]	2 226,7 [kN]
10	2 523,9 [kN]	2 466,8 [kN]	2 466,8 [kN]	2 436,9 [kN]	2 376,2 [kN]

Table 6.28: Percentual force difference for the meshless methods simulations compared with the FEM simulation, for the 3D T-beam with b=200 mm

Increment	RPIM Const.	RPIM Linear	NNRPIM 1º	NNRPIM 2º
01	2.26%	2.26%	3.45%	5.85%
02	2.26%	2.26%	3.45%	5.85%
03	2.27%	2.27%	3.45%	5.85%
04	2.27%	2.27%	3.45%	5.86%
05	2.26%	2.26%	3.45%	5.85%
06	2.26%	2.26%	3.45%	5.85%
07	2.26%	2.27%	3.45%	5.85%
08	2.26%	2.26%	3.44%	5.85%
09	2.26%	2.26%	3.45%	5.85%
10	2.26%	2.26%	3.45%	5.85%

Table 6.29: Von Mises stress contour plot images resulted from the 3D T-beam with b=200 [mm] simulations

	FEM	RPIM Constant	RPIM Linear	NNRPIM 1^{o} Order	NNRPIM 2^{o} Order
01	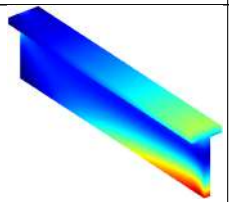 $Max = 193,80[MPa]$ $Min = 0,18[MPa]$	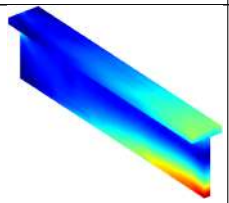 $Max = 199,99[MPa]$ $Min = 1,35[MPa]$	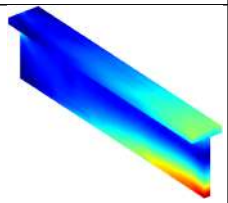 $Max = 199,99[MPa]$ $Min = 1,35[MPa]$	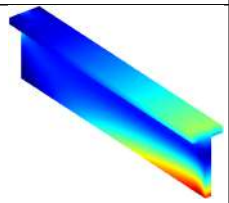 $Max = 193,55[MPa]$ $Min = 0,32[MPa]$	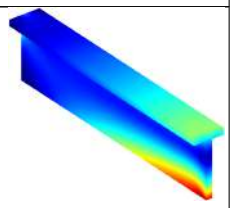 $Max = 186,26[MPa]$ $Min = 0,09[MPa]$
02	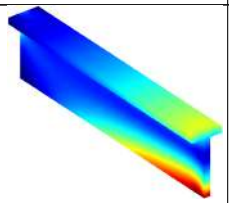 $Max = 202,18[MPa]$ $Min = 0,21[MPa]$	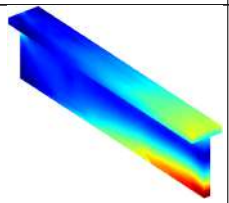 $Max = 203,72[MPa]$ $Min = 1,56[MPa]$	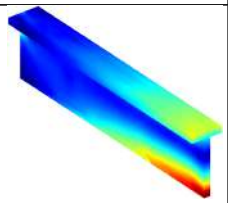 $Max = 203,72[MPa]$ $Min = 1,56[MPa]$	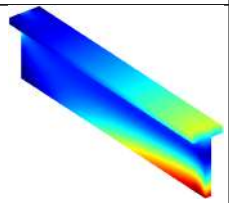 $Max = 201,88[MPa]$ $Min = 0,36[MPa]$	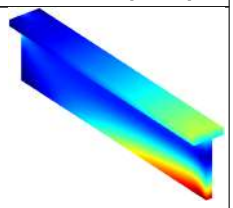 $Max = 200,11[MPa]$ $Min = 0,10[MPa]$
03	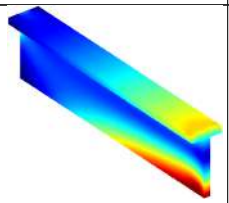 $Max = 205,06[MPa]$ $Min = 0,23[MPa]$	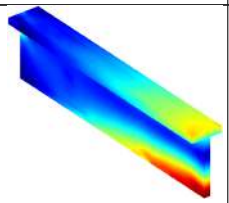 $Max = 209,45[MPa]$ $Min = 1,78[MPa]$	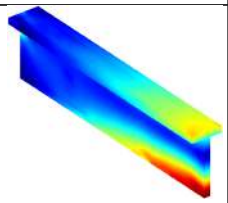 $Max = 209,45[MPa]$ $Min = 1,78[MPa]$	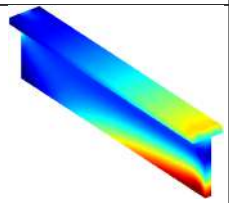 $Max = 203,57[MPa]$ $Min = 0,41[MPa]$	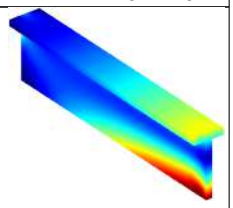 $Max = 202,10[MPa]$ $Min = 0,11[MPa]$
04	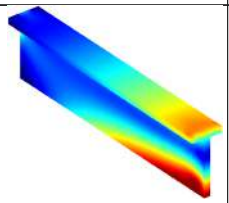 $Max = 207,58[MPa]$ $Min = 0,26[MPa]$	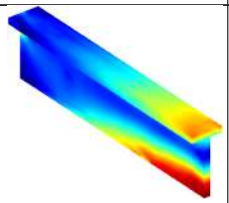 $Max = 211,67[MPa]$ $Min = 1,93[MPa]$	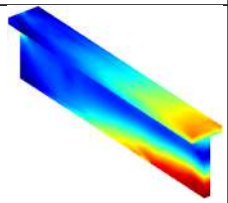 $Max = 211,67[MPa]$ $Min = 1,93[MPa]$	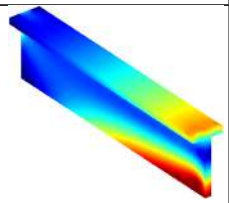 $Max = 206,94[MPa]$ $Min = 0,45[MPa]$	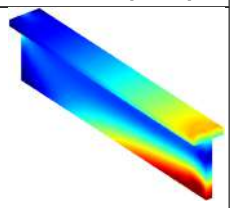 $Max = 205,58[MPa]$ $Min = 0,12[MPa]$
05	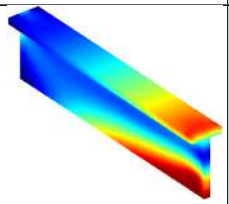 $Max = 210,58[MPa]$ $Min = 0,28[MPa]$	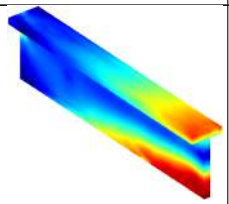 $Max = 217,64[MPa]$ $Min = 2,06[MPa]$	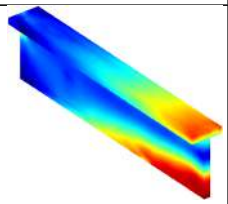 $Max = 217,64[MPa]$ $Min = 2,06[MPa]$	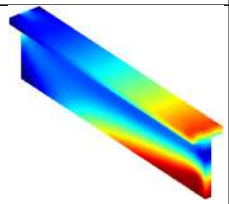 $Max = 209,76[MPa]$ $Min = 0,50[MPa]$	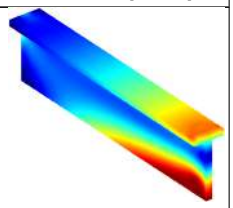 $Max = 208,09[MPa]$ $Min = 0,14[MPa]$

Table 6.29 continued from previous page

	FEM	RPIM Constant	RPIM Linear	NNRPIM 1^{o} Order	NNRPIM 2^{o} Order
06	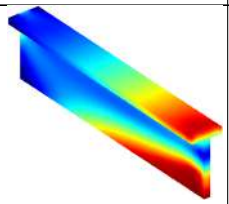 $Max = 214,52[MPa]$ $Min = 0,31[MPa]$	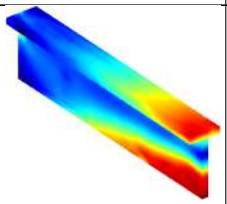 $Max = 222,62[MPa]$ $Min = 2,22[MPa]$	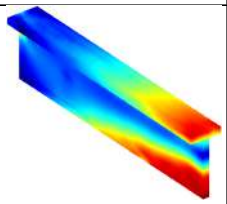 $Max = 222,62[MPa]$ $Min = 2,22[MPa]$	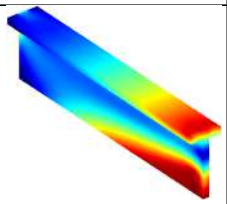 $Max = 213,58[MPa]$ $Min = 0,54[MPa]$	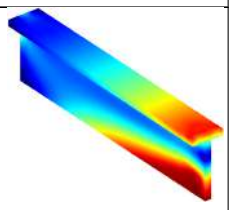 $Max = 211,69[MPa]$ $Min = 0,15[MPa]$
07	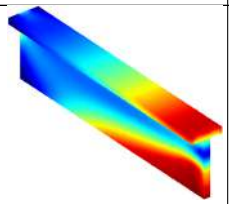 $Max = 219,59[MPa]$ $Min = 0,34[MPa]$	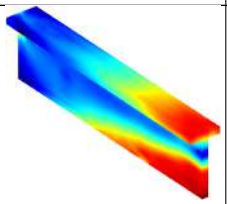 $Max = 230,78[MPa]$ $Min = 2,29[MPa]$	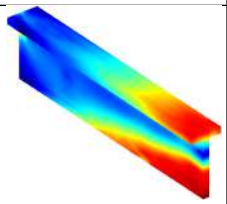 $Max = 230,78[MPa]$ $Min = 2,29[MPa]$	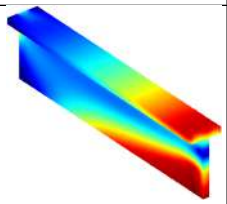 $Max = 218,69[MPa]$ $Min = 0,59[MPa]$	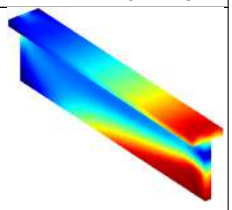 $Max = 216,12[MPa]$ $Min = 0,16[MPa]$
08	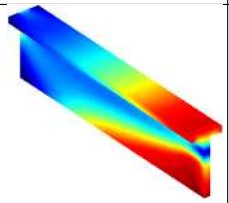 $Max = 230,67[MPa]$ $Min = 0,36[MPa]$	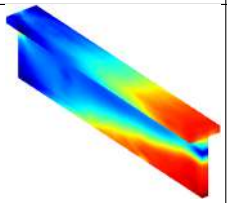 $Max = 244,15[MPa]$ $Min = 2,38[MPa]$	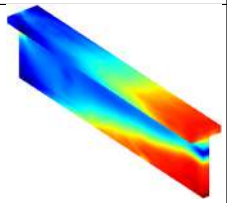 $Max = 244,15[MPa]$ $Min = 2,38[MPa]$	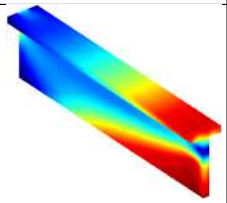 $Max = 226,99[MPa]$ $Min = 0,64[MPa]$	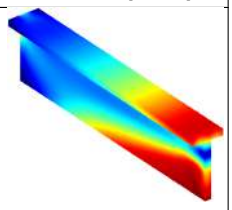 $Max = 223,47[MPa]$ $Min = 0,17[MPa]$
09	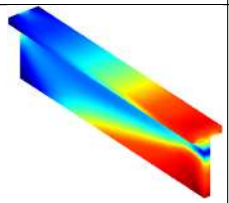 $Max = 248,45[MPa]$ $Min = 0,39[MPa]$	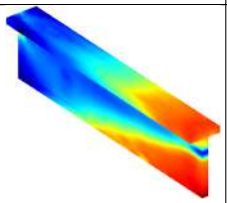 $Max = 266,19[MPa]$ $Min = 2,47[MPa]$	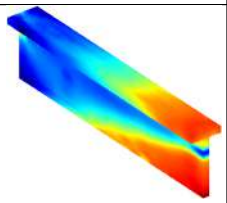 $Max = 266,19[MPa]$ $Min = 2,47[MPa]$	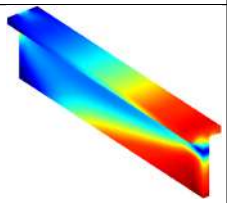 $Max = 243,06[MPa]$ $Min = 0,68[MPa]$	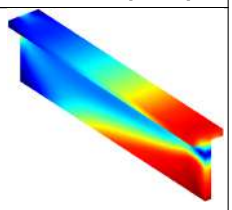 $Max = 236,30[MPa]$ $Min = 0,19[MPa]$
10	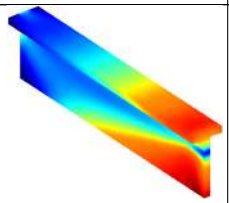 $Max = 272,36[MPa]$ $Min = 0,42[MPa]$	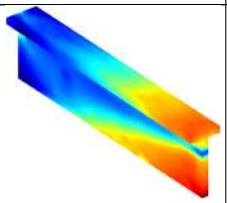 $Max = 294,40[MPa]$ $Min = 2,57[MPa]$	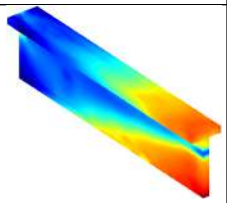 $Max = 294,41[MPa]$ $Min = 2,57[MPa]$	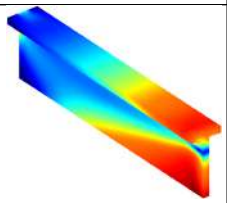 $Max = 265,04[MPa]$ $Min = 0,72[MPa]$	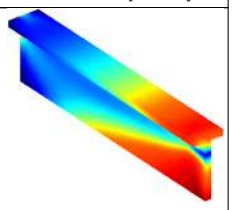 $Max = 256,43[MPa]$ $Min = 0,20[MPa]$
	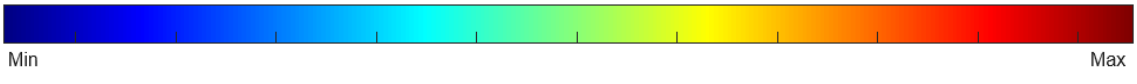 Min Max				

Consistent with the previously analyzed cases, the RPIM simulations shown in table 6.29 exhibit slightly higher stress values. It is important to note that these higher values result from nodal stresses, and the areas with the highest stress values are quite similar across all simulation types. In this case, unlike the previous

Table 6.30: Percentual stress difference for the meshless methods simulations compared with the FEM simulation, for the 3D T-beam with b=200 [mm]

Increment	RPIM Const.	RPIM Linear	NNRPIM 1^{o}	NNRPIM 2^{o}
01	3.19%	3.19%	0.13%	3.89%
02	0.76%	0.76%	0.15%	1.02%
03	2.14%	2.14%	0.73%	1.44%
04	1.97%	1.97%	0.31%	0.96%
05	3.35%	3.35%	0.39%	1.18%
06	3.78%	89.46%	0.44%	1.32%
07	5.10%	5.10%	0.41%	1.58%
08	5.84%	5.84%	1.60%	3.12%
09	7.14%	7.14%	2.17%	4.89%
10	8.09%	8.10%	2.69%	5.85%

analyses, there is only a marginal (and not relevant) difference between the RPIM Constant simulation (294.40 MPa) and the RPIM Linear simulation (294.41 MPa). In the following table 6.30, we can observe the percentual difference between the FEM simulations and the meshless methods simulations (RPIM and NNRPIM) for the maximum von Mises stress values.

The next analysis concerns the plastic strain of the T-beam with $b = 200$ mm. Once again, these images and values are presented in table 6.31.

Table 6.31: Plastic strain contour plot images resulted from the 3D T-beam with b=200 [mm] simulations

	FEM	RPIM Constant	RPIM Linear	NNRPIM 1^{o} Order	NNRPIM 2^{o} Order
01					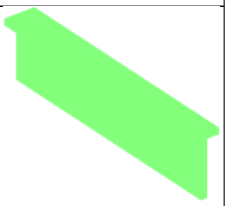
02	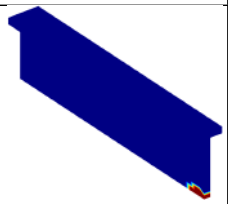	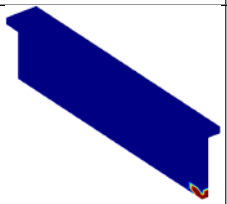	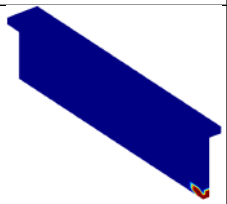	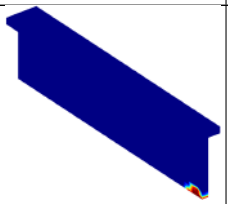	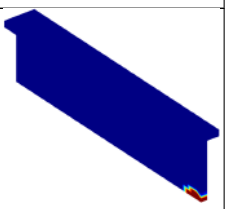
03	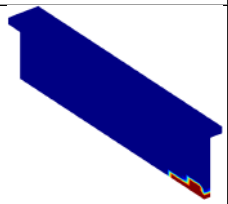	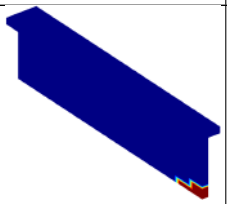	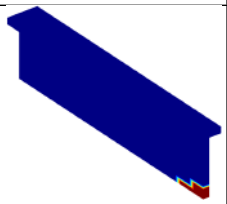	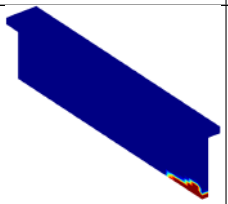	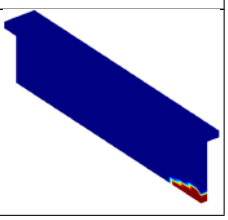

Table 6.31 continued from previous page

	FEM	RPIM Constant	RPIM Linear	NNRPIM 1^{o} Order	NNRPIM 2^{o} Order
04	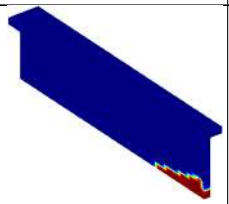	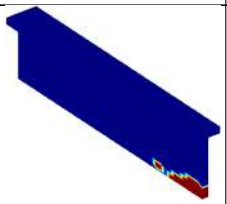	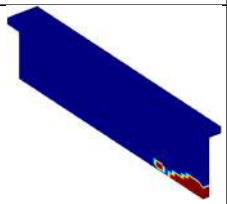	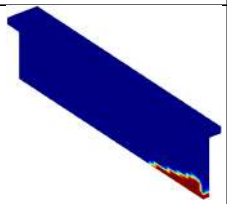	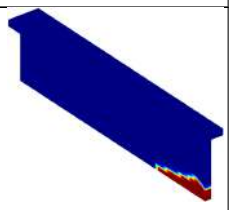
05	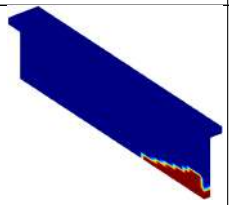	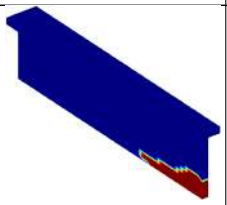	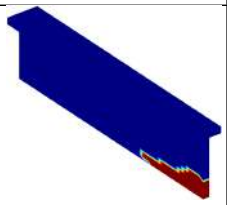	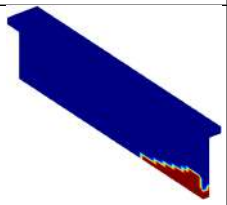	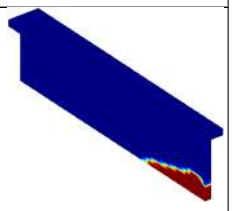
06	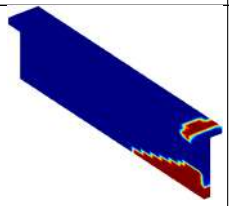	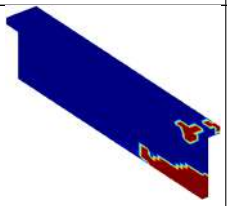	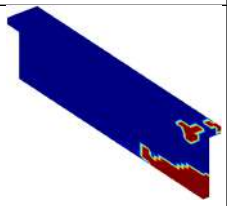	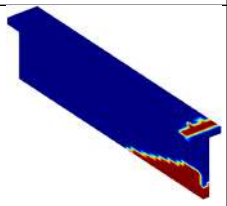	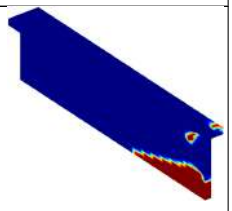
07	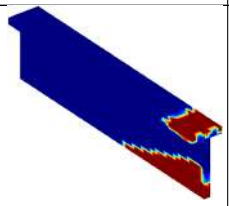	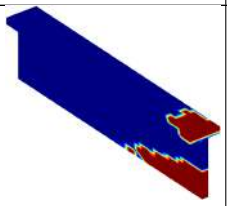	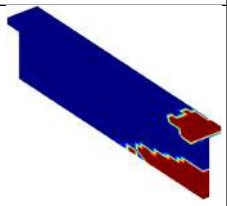	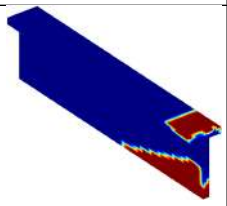	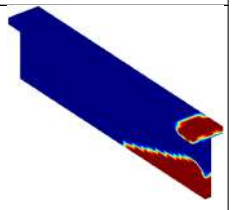
08	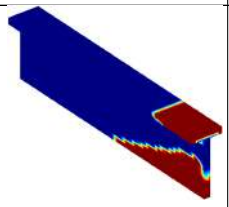	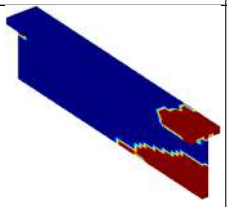	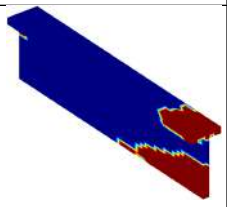	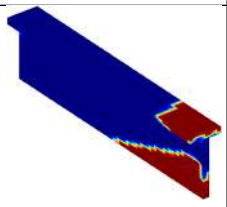	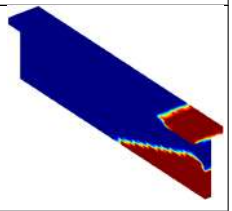
09	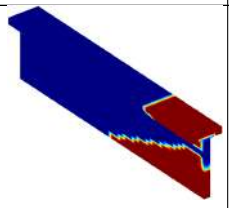	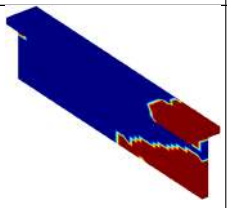	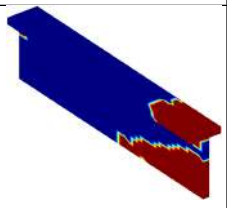	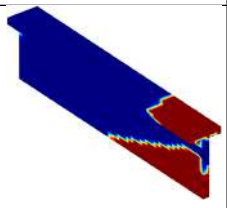	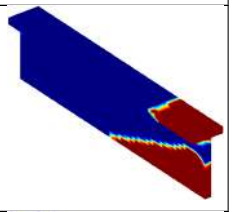
10	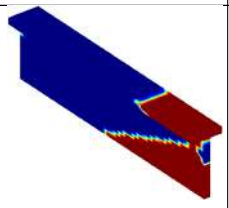	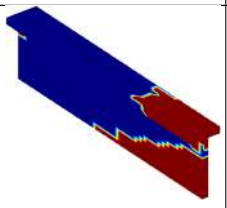	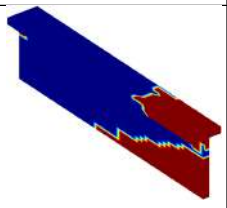	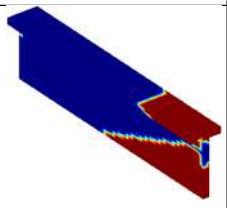	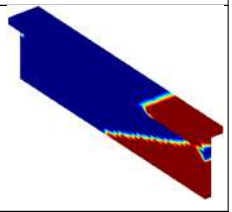

Once again, and keeping the consistency, so far, we can verify that in all the simulations, the plastic strain behaviour is very similar and identical.

To finalise the T beam b=200 analyses, we can observe and study table 6.32, where we will encounter the total strain values and the respective contour plot images.

Table 6.32: Total strain contour plot images resulted from the 3D T-beam with b=200 [mm] simulations

	FEM	RPIM Constant	RPIM Linear	NNRPIM 1^{o} Order	NNRPIM 2^{o} Order
01	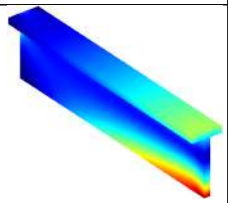 $Max = 0,09[\%]$ $Min = 0,00[\%]$	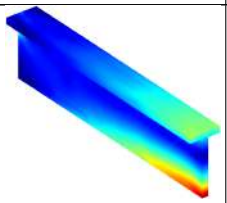 $Max = 0,09[\%]$ $Min = 0,00[\%]$	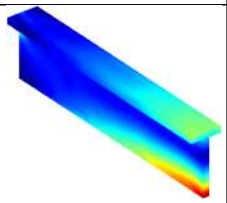 $Max = 0,09[\%]$ $Min = 0,00[\%]$	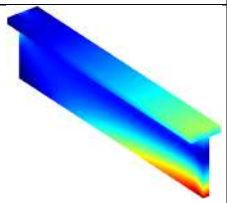 $Max = 0,09[\%]$ $Min = 0,00[\%]$	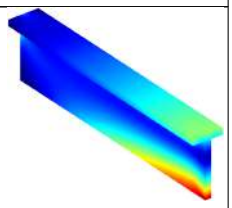 $Max = 0,08[\%]$ $Min = 0,00[\%]$
02	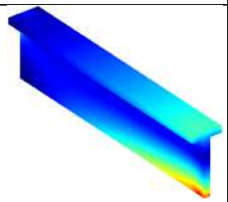 $Max = 0,12[\%]$ $Min = 0,00[\%]$	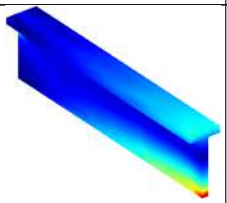 $Max = 0,14[\%]$ $Min = 0,00[\%]$	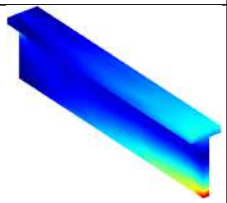 $Max = 0,14[\%]$ $Min = 0,00[\%]$	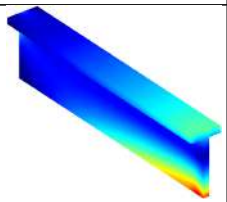 $Max = 0,11[\%]$ $Min = 0,00[\%]$	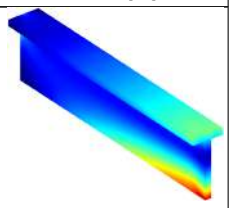 $Max = 0,10[\%]$ $Min = 0,00[\%]$
03	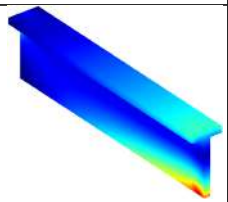 $Max = 0,14[\%]$ $Min = 0,00[\%]$	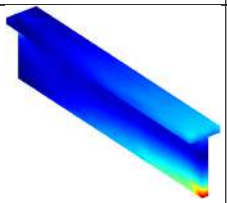 $Max = 0,18[\%]$ $Min = 0,00[\%]$	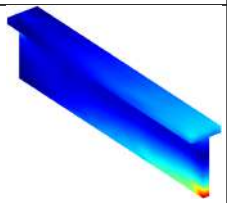 $Max = 0,18[\%]$ $Min = 0,00[\%]$	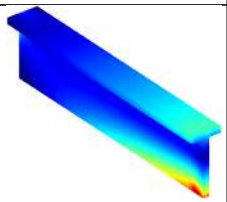 $Max = 0,14[\%]$ $Min = 0,00[\%]$	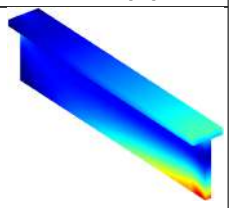 $Max = 0,13[\%]$ $Min = 0,00[\%]$
04	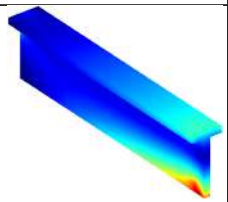 $Max = 0,16[\%]$ $Min = 0,00[\%]$	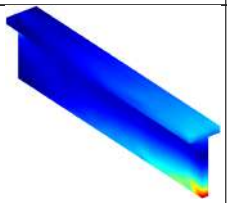 $Max = 0,21[\%]$ $Min = 0,00[\%]$	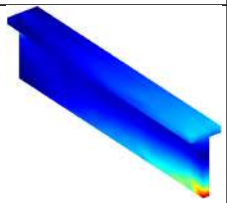 $Max = 0,21[\%]$ $Min = 0,00[\%]$	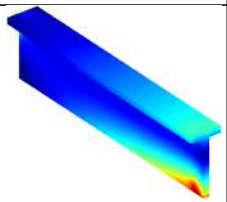 $Max = 0,16[\%]$ $Min = 0,00[\%]$	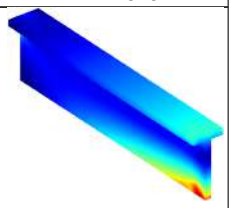 $Max = 0,15[\%]$ $Min = 0,00[\%]$
05	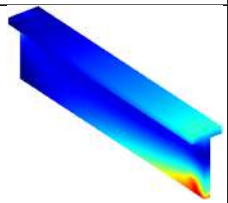 $Max = 0,19[\%]$ $Min = 0,00[\%]$	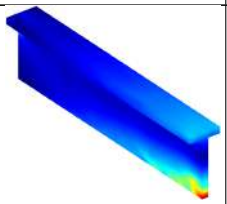 $Max = 0,25[\%]$ $Min = 0,00[\%]$	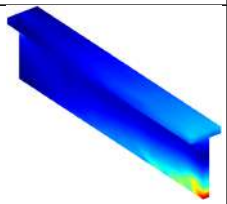 $Max = 0,25[\%]$ $Min = 0,00[\%]$	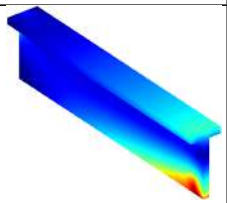 $Max = 0,18[\%]$ $Min = 0,00[\%]$	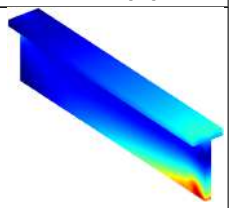 $Max = 0,17[\%]$ $Min = 0,00[\%]$

Table 6.32 continued from previous page

	FEM	RPIM Constant	RPIM Linear	NNRPIM 1^{o} Order	NNRPIM 2^{o} Order
06	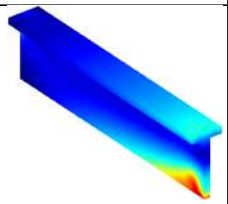 $Max = 0,22[\%]$ $Min = 0,00[\%]$	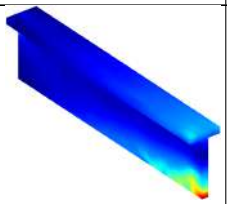 $Max = 0,30[\%]$ $Min = 0,00[\%]$	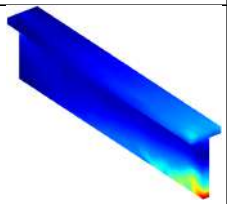 $Max = 0,30[\%]$ $Min = 0,00[\%]$	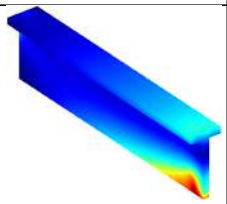 $Max = 0,22[\%]$ $Min = 0,00[\%]$	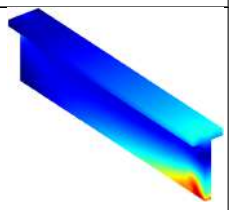 $Max = 0,21[\%]$ $Min = 0,00[\%]$
07	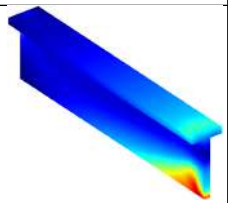 $Max = 0,28[\%]$ $Min = 0,00[\%]$	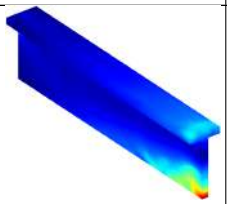 $Max = 0,38[\%]$ $Min = 0,00[\%]$	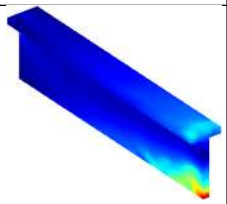 $Max = 0,38[\%]$ $Min = 0,00[\%]$	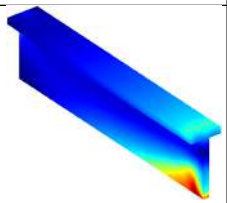 $Max = 0,26[\%]$ $Min = 0,00[\%]$	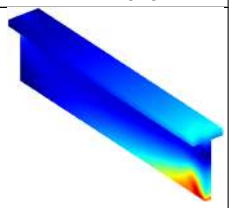 $Max = 0,25[\%]$ $Min = 0,00[\%]$
08	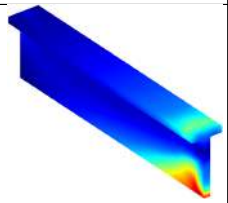 $Max = 0,37[\%]$ $Min = 0,00[\%]$	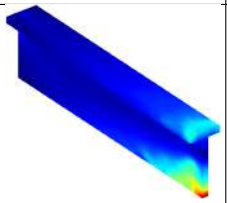 $Max = 0,50[\%]$ $Min = 0,00[\%]$	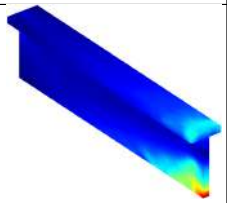 $Max = 0,50[\%]$ $Min = 0,00[\%]$	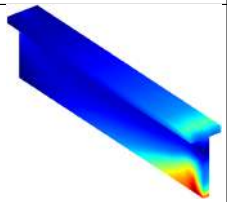 $Max = 0,34[\%]$ $Min = 0,00[\%]$	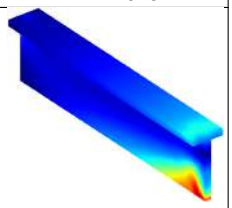 $Max = 0,31[\%]$ $Min = 0,00[\%]$
09	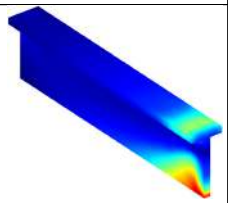 $Max = 0,54[\%]$ $Min = 0,00[\%]$	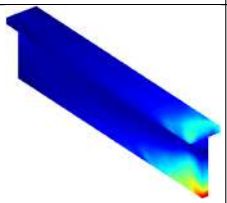 $Max = 0,71[\%]$ $Min = 0,00[\%]$	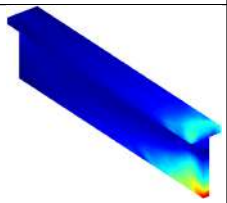 $Max = 0,71[\%]$ $Min = 0,00[\%]$	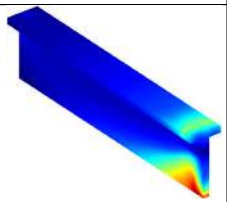 $Max = 0,49[\%]$ $Min = 0,00[\%]$	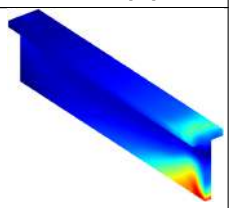 $Max = 0,43[\%]$ $Min = 0,00[\%]$
10	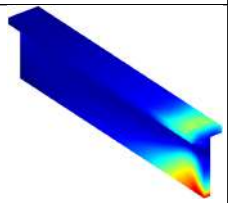 $Max = 0,77[\%]$ $Min = 0,00[\%]$	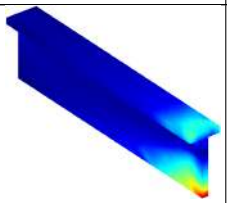 $Max = 0,98[\%]$ $Min = 0,00[\%]$	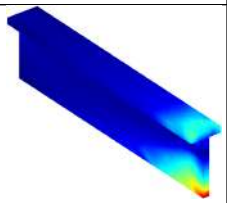 $Max = 0,98[\%]$ $Min = 0,00[\%]$	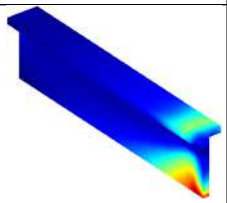 $Max = 0,70[\%]$ $Min = 0,00[\%]$	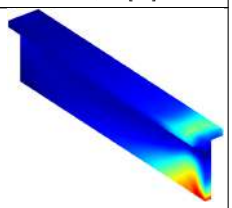 $Max = 0,62[\%]$ $Min = 0,00[\%]$
	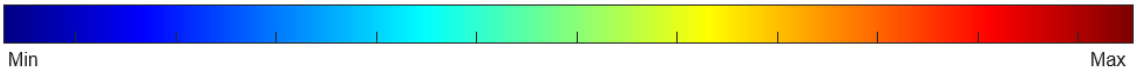 Min Max				

Analyzing the images from each increment, we can verify that they are very similar, with the RPIM simulation images being the most notably distinctive. As in the case of the T-beam with $b = 100mm$, in subchapter 6.3.2, the most visible difference is the smaller area where the highest percentage strain occurs in the RPIM

Table 6.33: Percentual strain's difference for the meshless methods simulations compared with the FEM simulation, for the 3D T-beam with b=200 [mm]

Increment	RPIM Const.	RPIM Linear	NNRPIM 1º	NNRPIM 2º
01	0.00%	0.00%	0.00%	0.00%
02	16.67%	16.67%	8.33%	16.67%
03	28.57%	28.57%	0.00%	7.14%
04	31.25%	31.25%	0.00%	6.25%
05	31.58%	31.58%	5.26%	10.53%
06	36.36%	36.36%	0.00%	4.55%
07	35.71%	35.71%	7.14%	10.71%
08	35.14%	35.14%	8.11%	16.22%
09	31.48%	31.48%	9.26%	20.37%
10	27.27%	27.27%	9.09%	19.48%

simulations. In terms of percentage discrepancy, we can see the percentual strain values in the table 6.33.

T-Beam with b=400 [mm]

To finalize this subchapter's 3D non-linear study, we will analyze the T-beam with $b = 400mm$. As with the other beams already studied, the dimensions of this beam are shown in figure 6.36, and the corresponding mesh is presented in figure 6.37.

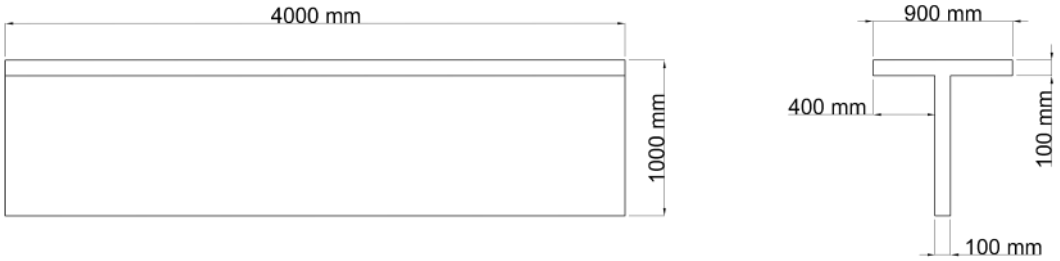

Figure 6.36: T-Beam (b=400 [mm]) Dimensions

The force exerted on each iteration to each simulation can be compared in the table 6.34, and in table 6.35 we can see the percentual difference of the force exerted by each meshless method compared to the industry standard, FEM simulation.

The table 6.36 shows us the values and the expansion behavior from the von Mises stress.

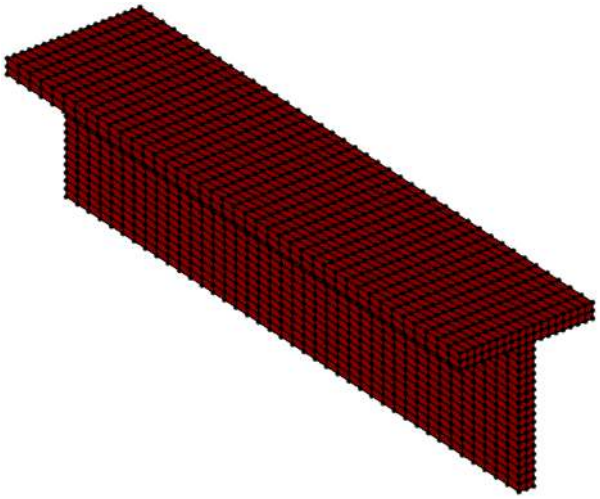

Figure 6.37: T-Beam (b=400 [mm]) Mesh

Table 6.34: Applied force in T-Beam with b=400 [mm]

Iteration	FEM	RPIM (Constante)	RPIM (Linear)	NNRPIM (1º order)	NNRPIM (2º order)
01	1 176,7 [kN]	1 147,3 [kN]	1 147,3 [kN]	1 142,5 [kN]	1 109,6 [kN]
02	1 370,9 [kN]	1 336,7 [kN]	1 336,6 [kN]	1 331,0 [kN]	1 292,6 [kN]
03	1 565,0 [kN]	1 526,0 [kN]	1 526,0 [kN]	1 519,6 [kN]	1 475,7 [kN]
04	1 759,2 [kN]	1 715,3 [kN]	1 715,3 [kN]	1 708,1 [kN]	1 658,8 [kN]
05	1 953,3 [kN]	1 904,6 [kN]	1 904,6 [kN]	1 896,6 [kN]	1 841,9 [kN]
06	2 147,5 [kN]	2 093,9 [kN]	2 093,9 [kN]	2 085,1 [kN]	2 025,0 [kN]
07	2 341,6 [kN]	2 283,2 [kN]	2 283,2 [kN]	2 273,6 [kN]	2 208,0 [kN]
08	2 535,8 [kN]	2 472,5 [kN]	2 472,5 [kN]	2 462,1 [kN]	2 391,1 [kN]
09	2 730,0 [kN]	2 661,8 [kN]	2 661,8 [kN]	2 650,7 [kN]	2 574,2 [kN]
10	2 924,1 [kN]	2 851,2 [kN]	2 851,1 [kN]	2 839,2 [kN]	2 757,3 [kN]

Table 6.35: Percentual force difference for the meshless methods simulations compared with the FEM simulation, for the 3D T-beam with b=400 [mm]

Increment	RPIM Const.	RPIM Linear	NNRPIM 1º	NNRPIM 2º
01	3.33%	3.08%	3.82%	5.56%
02	3.33%	3.08%	3.83%	5.57%
03	3.33%	3.08%	3.82%	5.57%
04	3.34%	3.08%	3.82%	5.56%
05	3.33%	3.08%	3.82%	5.57%
06	3.33%	3.08%	3.83%	5.57%
07	3.33%	3.08%	3.82%	5.56%
08	3.33%	3.08%	3.82%	5.56%
09	3.33%	3.08%	3.82%	5.56%
10	3.33%	3.08%	3.83%	5.57%

Table 6.36: Von Mises stress contour plot images resulted from the 3D T-beam with b=400 [mm] simulations

	FEM	RPIM Constant	RPIM Linear	NNRPIM 1^{o} Order	NNRPIM 2^{o} Order
01	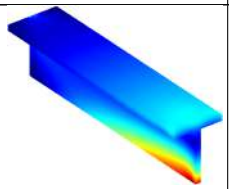 $Max = 192,71[MPa]$ $Min = 0,20[MPa]$	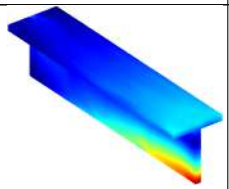 $Max = 199,99[MPa]$ $Min = 1,50[MPa]$	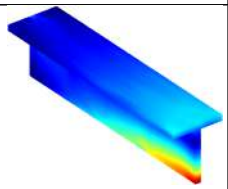 $Max = 199,99[MPa]$ $Min = 1,50[MPa]$	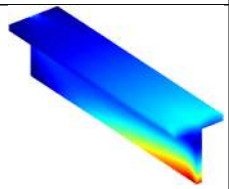 $Max = 193,34[MPa]$ $Min = 0,27[MPa]$	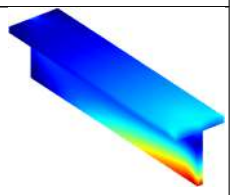 $Max = 185,29[MPa]$ $Min = 0,10[MPa]$
02	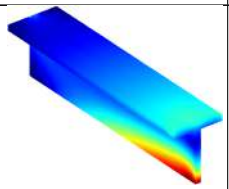 $Max = 202,44[MPa]$ $Min = 0,24[MPa]$	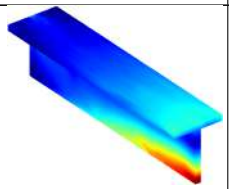 $Max = 204,22[MPa]$ $Min = 1,77[MPa]$	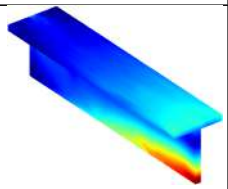 $Max = 204,22[MPa]$ $Min = 1,77[MPa]$	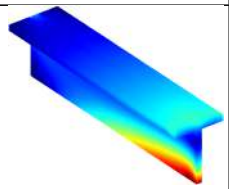 $Max = 202,29[MPa]$ $Min = 0,32[MPa]$	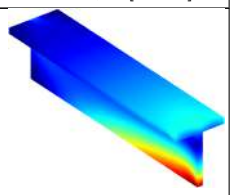 $Max = 200,86[MPa]$ $Min = 0,11[MPa]$
03	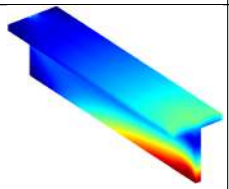 $Max = 205,62[MPa]$ $Min = 0,27[MPa]$	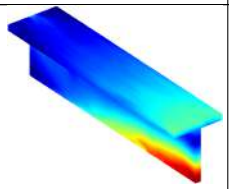 $Max = 212,03[MPa]$ $Min = 2,01[MPa]$	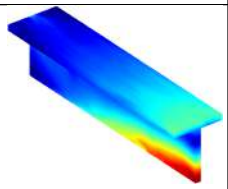 $Max = 212,03[MPa]$ $Min = 2,01[MPa]$	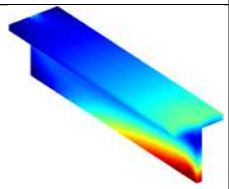 $Max = 204,63[MPa]$ $Min = 0,36[MPa]$	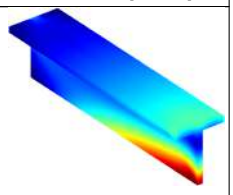 $Max = 202,94[MPa]$ $Min = 0,13[MPa]$
04	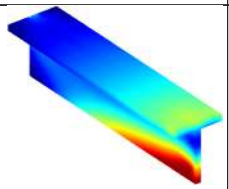 $Max = 209,20[MPa]$ $Min = 0,30[MPa]$	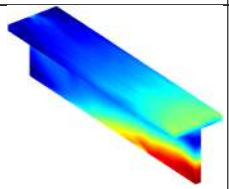 $Max = 215,82[MPa]$ $Min = 2,33[MPa]$	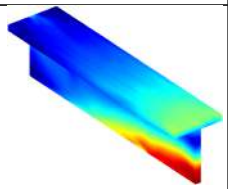 $Max = 215,82[MPa]$ $Min = 2,33[MPa]$	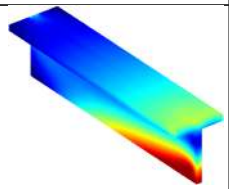 $Max = 208,27[MPa]$ $Min = 0,41[MPa]$	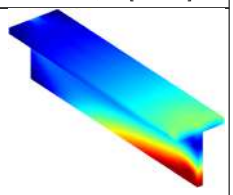 $Max = 206,89[MPa]$ $Min = 0,15[MPa]$
05	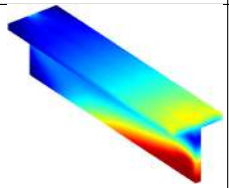 $Max = 213,03[MPa]$ $Min = 0,34[MPa]$	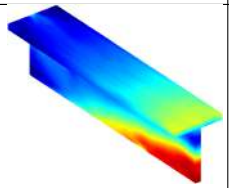 $Max = 222,13[MPa]$ $Min = 2,79[MPa]$	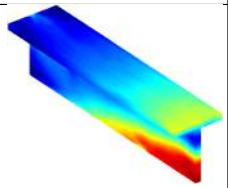 $Max = 222,13[MPa]$ $Min = 2,79[MPa]$	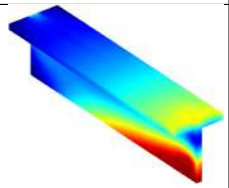 $Max = 212,01[MPa]$ $Min = 0,45[MPa]$	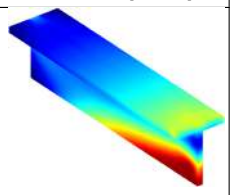 $Max = 210,39[MPa]$ $Min = 0,16[MPa]$
06	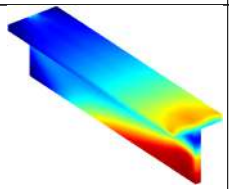 $Max = 218,46[MPa]$ $Min = 0,37[MPa]$	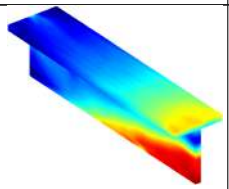 $Max = 228,97[MPa]$ $Min = 3,24[MPa]$	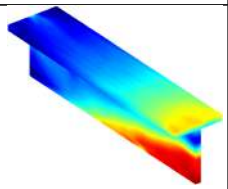 $Max = 228,97[MPa]$ $Min = 3,24[MPa]$	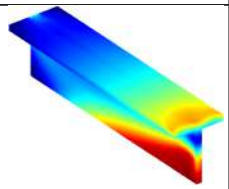 $Max = 217,50[MPa]$ $Min = 0,50[MPa]$	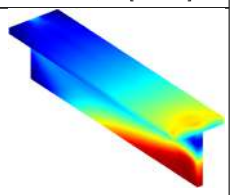 $Max = 215,53[MPa]$ $Min = 0,18[MPa]$

Table 6.36 continued from previous page

	FEM	RPIM Constant	RPIM Linear	NNRPIM 1^{o} Order	NNRPIM 2^{o} Order
07	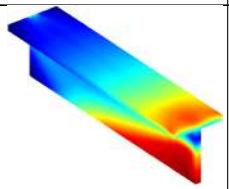 $Max = 226,29[MPa]$ $Min = 0,41[MPa]$	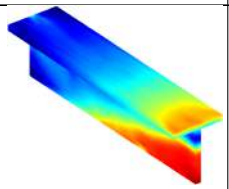 $Max = 241,04[MPa]$ $Min = 3,66[MPa]$	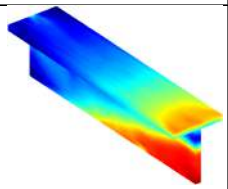 $Max = 241,04[MPa]$ $Min = 3,66[MPa]$	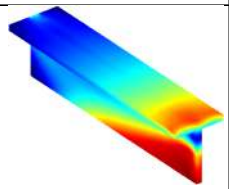 $Max = 225,19[MPa]$ $Min = 0,54[MPa]$	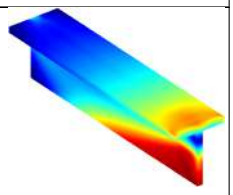 $Max = 222,17[MPa]$ $Min = 0,19[MPa]$
08	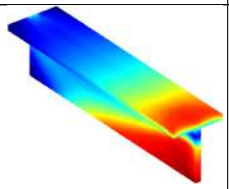 $Max = 236,92[MPa]$ $Min = 0,44[MPa]$	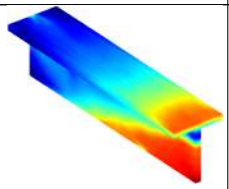 $Max = 254,19[MPa]$ $Min = 4,25[MPa]$	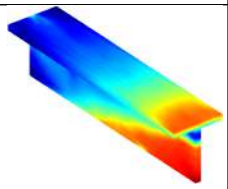 $Max = 254,19[MPa]$ $Min = 4,25[MPa]$	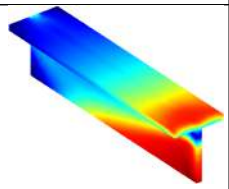 $Max = 236,08[MPa]$ $Min = 0,58[MPa]$	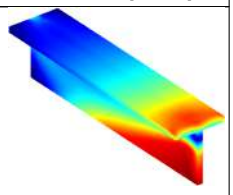 $Max = 231,46[MPa]$ $Min = 0,21[MPa]$
09	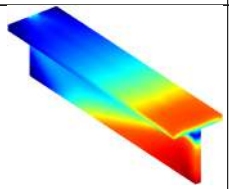 $Max = 253,77[MPa]$ $Min = 0,47[MPa]$	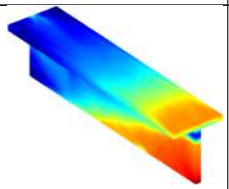 $Max = 277,18[MPa]$ $Min = 4,64[MPa]$	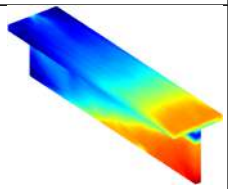 $Max = 277,18[MPa]$ $Min = 4,64[MPa]$	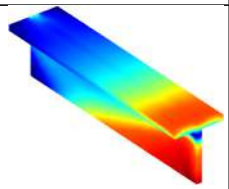 $Max = 252,98[MPa]$ $Min = 0,61[MPa]$	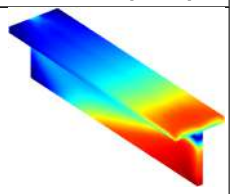 $Max = 245,56[MPa]$ $Min = 0,23[MPa]$
10	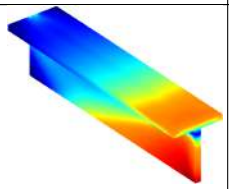 $Max = 275,81[MPa]$ $Min = 0,51[MPa]$	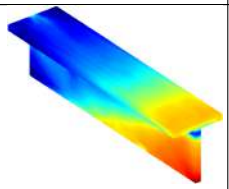 $Max = 302,77[MPa]$ $Min = 5,01[MPa]$	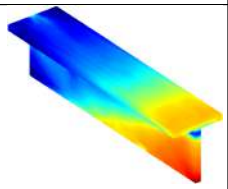 $Max = 302,77[MPa]$ $Min = 5,01[MPa]$	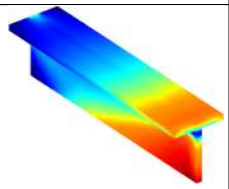 $Max = 275,25[MPa]$ $Min = 0,63[MPa]$	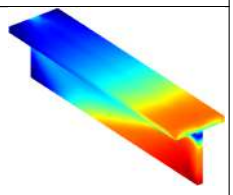 $Max = 265,37[MPa]$ $Min = 0,25[MPa]$
	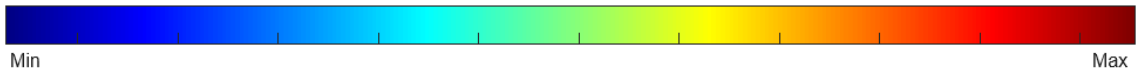				

By analyzing the images in table 6.36, we observe that the beam behavior is very similar across all simulations in this study. As seen in previous examples, it is not surprising that the RPIM simulations yield slightly higher values, which is also reflected by the lighter colors in the high-stress areas. Continuing to consider the FEM as the reference, we can calculate the final percentage difference in maximum stress values between the FEM and the meshless methods simulations. In the following table 6.37 we can observe the percentual difference between the FEM simulations and the meshless methods simulations (RPIM and NNRPIM) for the maximum von Mises stress.

The next analysis concerns the plastic strain of the T-beam in question, which can be observed in the images presented in table 6.38.

Table 6.37: Percentual stress difference for the meshless methods simulations compared with the FEM simulation, for the 3D T-beam with b=400 [mm]

Increment	RPIM Const.	RPIM Linear	NNRPIM 1º	NNRPIM 2º
01	3.78%	3.78%	0.33%	3.85%
02	0.88%	0.88%	0.07%	0.78%
03	3.12%	3.12%	0.48%	1.30%
04	3.16%	3.16%	0.44%	1.10%
05	4.27%	4.27%	0.48%	1.24%
06	4.81%	4.81%	0.44%	1.34%
07	6.52%	6.52%	0.49%	1.82%
08	7.29%	7.29%	0.35%	2.30%
09	9.22%	9.22%	0.31%	3.24%
10	9.77%	9.77%	0.20%	3.79%

Table 6.38: Plastic strain contour plot images resulted from the 3D T-beam with b=400 [mm] simulations

	FEM	RPIM Constant	RPIM Linear	NNRPIM 1º Order	NNRPIM 2º Order
01	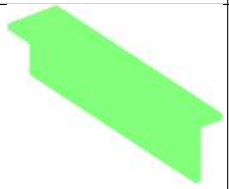	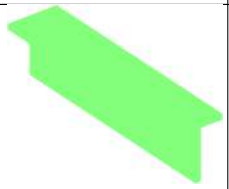	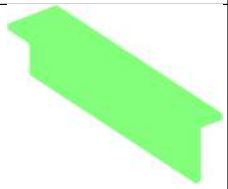	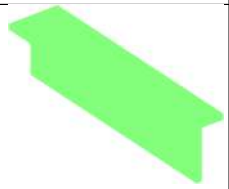	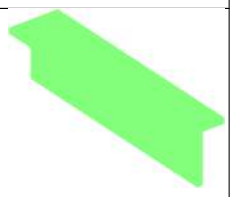
02	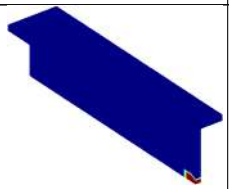	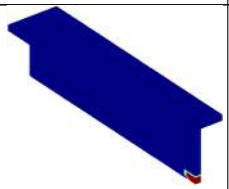	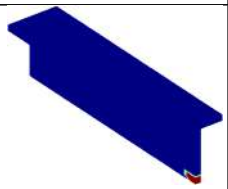	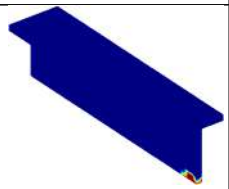	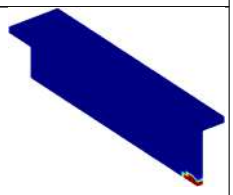
03	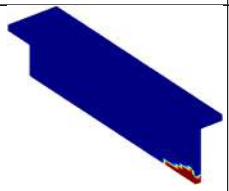	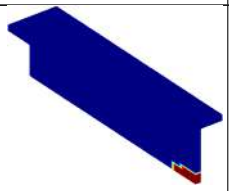	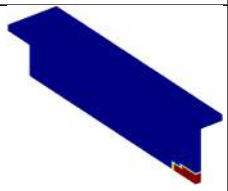	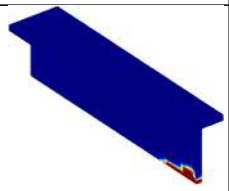	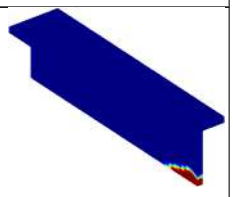
04	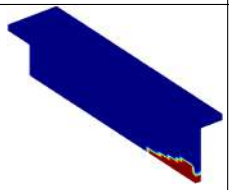	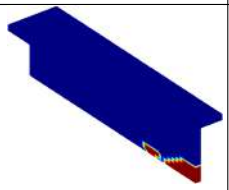	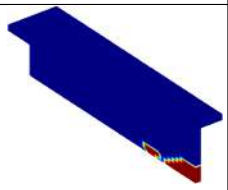	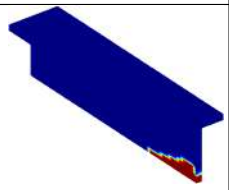	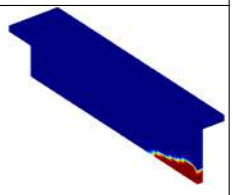
05	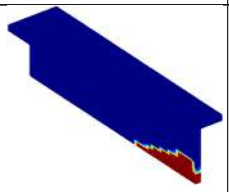	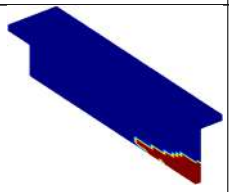	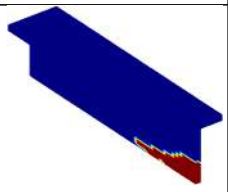	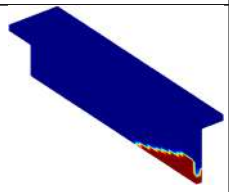	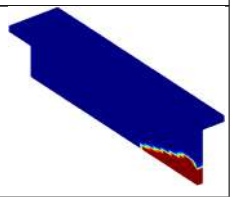

Table 6.38 continued from previous page

	FEM	RPIM Constant	RPIM Linear	NNRPIM 1^{o} Order	NNRPIM 2^{o} Order
06	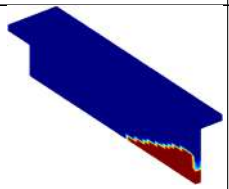	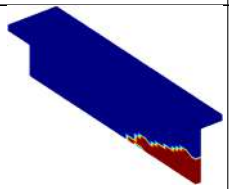	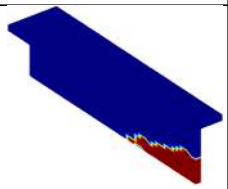	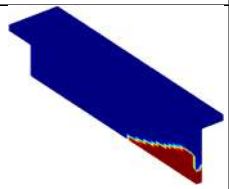	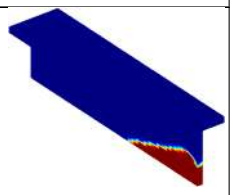
07	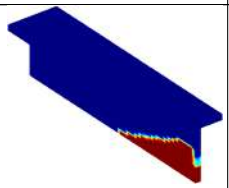	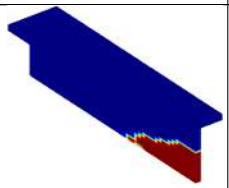	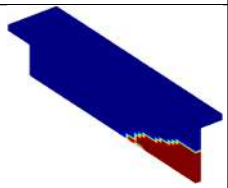	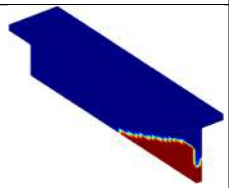	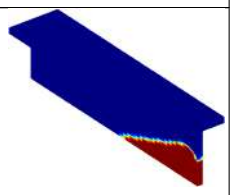
08	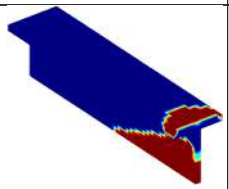	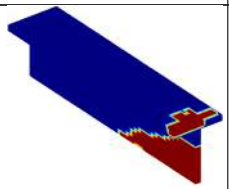	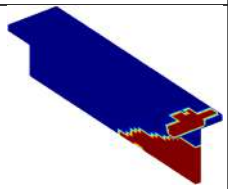	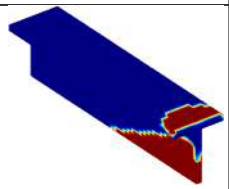	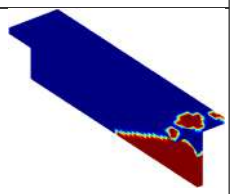
09	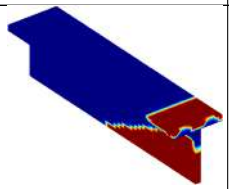	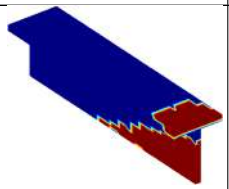	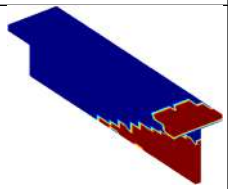	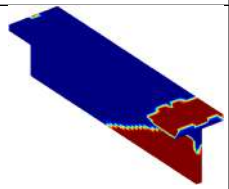	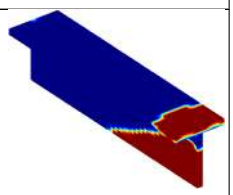
10	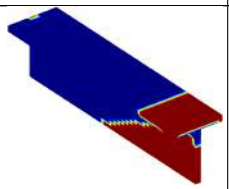	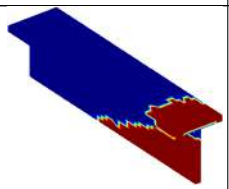	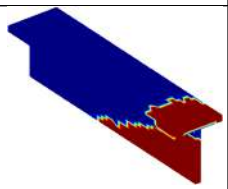	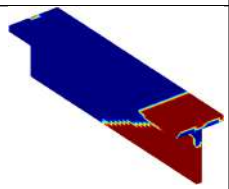	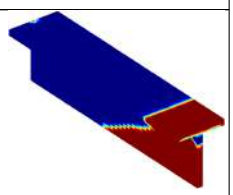

After a careful analysis of the images in table 6.38, we can conclude that the plastic strain is very similar across all simulations, just like in the other studied geometries, so far.

To finalize, we will examine table 6.39, where the strain behavior during the different simulation iterations and their respective values can be observed.

Table 6.39: Total strain contour plot images resulted from the 3D T beam with b=400 [mm] simulations

	FEM	RPIM Constant	RPIM Linear	NNRPIM 1^{o} Order	NNRPIM 2^{o} Order
01	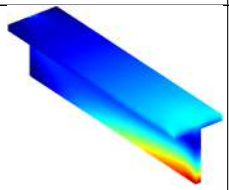 $Max = 0,09[\%]$ $Min = 0,00[\%]$	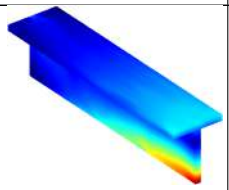 $Max = 0,09[\%]$ $Min = 0,00[\%]$	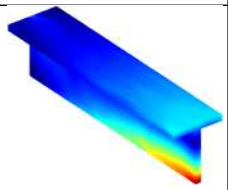 $Max = 0,09[\%]$ $Min = 0,00[\%]$	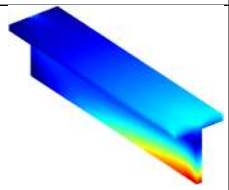 $Max = 0,09[\%]$ $Min = 0,00[\%]$	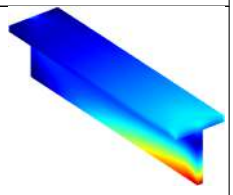 $Max = 0,08[\%]$ $Min = 0,00[\%]$

Table 6.39 continued from previous page

	FEM	RPIM Constant	RPIM Linear	NNRPIM 1^{o} Order	NNRPIM 2^{o} Order
02	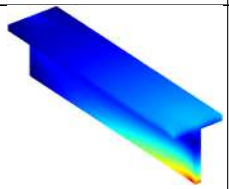 $Max = 0,13[\%]$ $Min = 0,00[\%]$	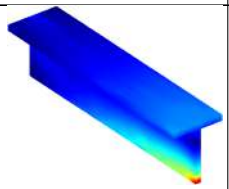 $Max = 0,14[\%]$ $Min = 0,00[\%]$	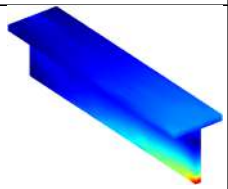 $Max = 0,14[\%]$ $Min = 0,00[\%]$	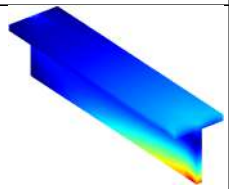 $Max = 0,12[\%]$ $Min = 0,00[\%]$	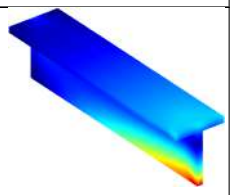 $Max = 0,11[\%]$ $Min = 0,00[\%]$
03	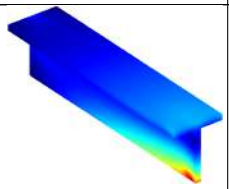 $Max = 0,15[\%]$ $Min = 0,00[\%]$	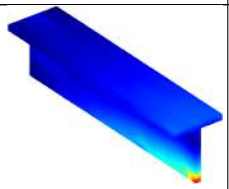 $Max = 0,21[\%]$ $Min = 0,00[\%]$	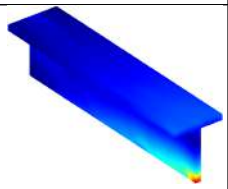 $Max = 0,21[\%]$ $Min = 0,00[\%]$	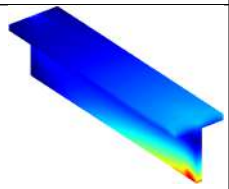 $Max = 0,15[\%]$ $Min = 0,00[\%]$	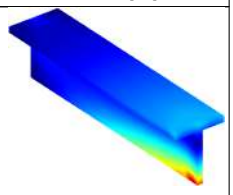 $Max = 0,13[\%]$ $Min = 0,00[\%]$
04	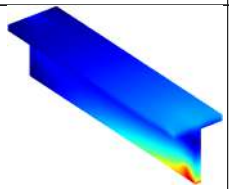 $Max = 0,18[\%]$ $Min = 0,00[\%]$	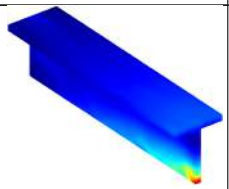 $Max = 0,24[\%]$ $Min = 0,00[\%]$	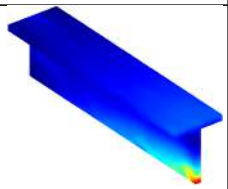 $Max = 0,24[\%]$ $Min = 0,00[\%]$	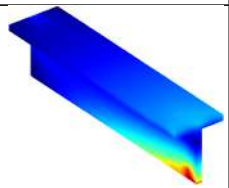 $Max = 0,17[\%]$ $Min = 0,00[\%]$	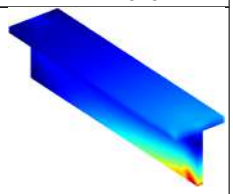 $Max = 0,16[\%]$ $Min = 0,00[\%]$
05	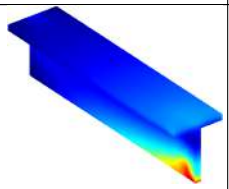 $Max = 0,21[\%]$ $Min = 0,00[\%]$	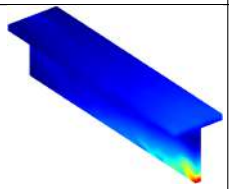 $Max = 0,29[\%]$ $Min = 0,00[\%]$	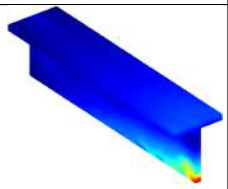 $Max = 0,29[\%]$ $Min = 0,00[\%]$	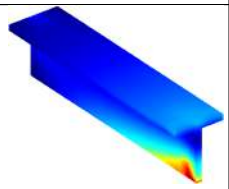 $Max = 0,20[\%]$ $Min = 0,00[\%]$	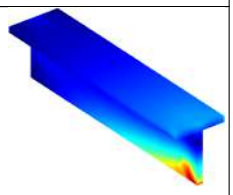 $Max = 0,19[\%]$ $Min = 0,00[\%]$
06	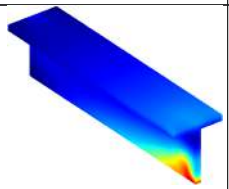 $Max = 0,26[\%]$ $Min = 0,00[\%]$	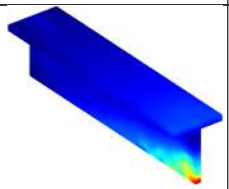 $Max = 0,35[\%]$ $Min = 0,00[\%]$	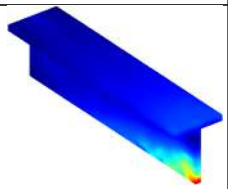 $Max = 0,35[\%]$ $Min = 0,00[\%]$	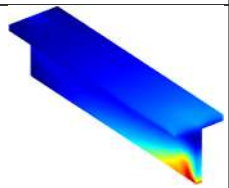 $Max = 0,25[\%]$ $Min = 0,00[\%]$	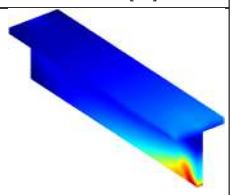 $Max = 0,24[\%]$ $Min = 0,00[\%]$
07	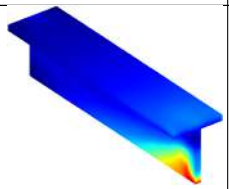 $Max = 0,33[\%]$ $Min = 0,00[\%]$	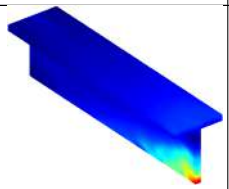 $Max = 0,44[\%]$ $Min = 0,00[\%]$	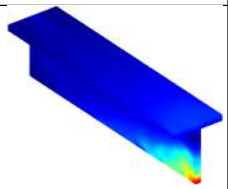 $Max = 0,44[\%]$ $Min = 0,00[\%]$	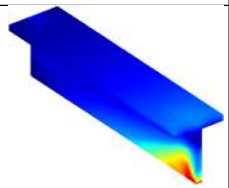 $Max = 0,33[\%]$ $Min = 0,00[\%]$	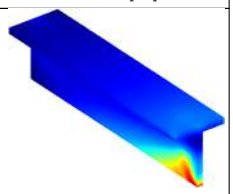 $Max = 0,30[\%]$ $Min = 0,00[\%]$

Table 6.39 continued from previous page

	FEM	RPIM Constant	RPIM Linear	NNRPIM 1^{o} Order	NNRPIM 2^{o} Order
08	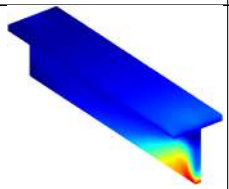 $Max = 0,43[\%]$ $Min = 0,00[\%]$	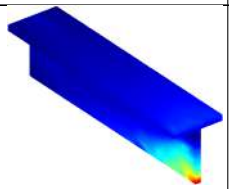 $Max = 0,58[\%]$ $Min = 0,00[\%]$	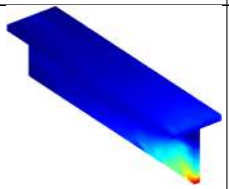 $Max = 0,58[\%]$ $Min = 0,00[\%]$	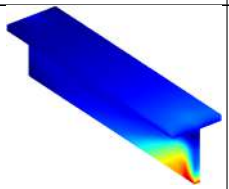 $Max = 0,43[\%]$ $Min = 0,00[\%]$	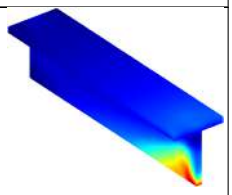 $Max = 0,39[\%]$ $Min = 0,00[\%]$
09	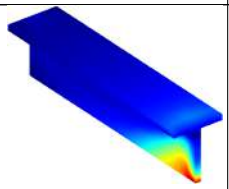 $Max = 0,58[\%]$ $Min = 0,00[\%]$	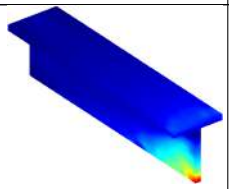 $Max = 0,78[\%]$ $Min = 0,00[\%]$	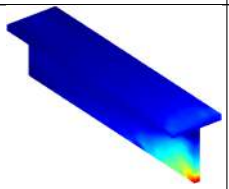 $Max = 0,78[\%]$ $Min = 0,00[\%]$	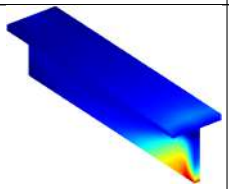 $Max = 0,58[\%]$ $Min = 0,00[\%]$	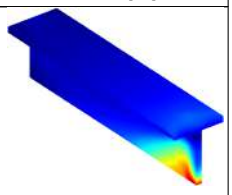 $Max = 0,52[\%]$ $Min = 0,00[\%]$
10	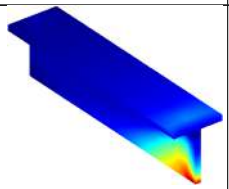 $Max = 0,79[\%]$ $Min = 0,00[\%]$	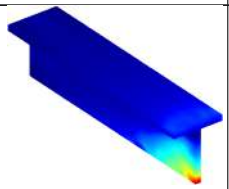 $Max = 1,04[\%]$ $Min = 0,00[\%]$	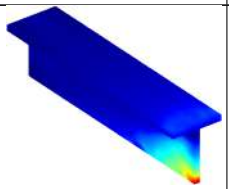 $Max = 1,04[\%]$ $Min = 0,00[\%]$	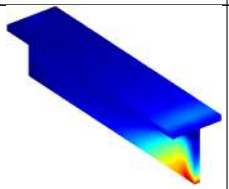 $Max = 0,79[\%]$ $Min = 0,00[\%]$	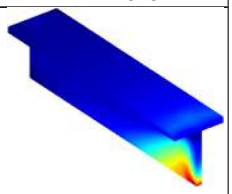 $Max = 0,70[\%]$ $Min = 0,00[\%]$
	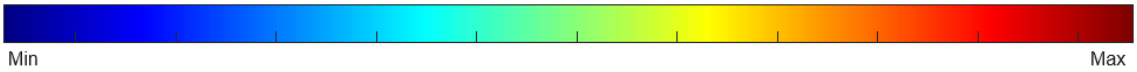				

To finalize this 3D nonlinear study, we carefully evaluate the table 6.39, where we observe that the same conclusions regarding strain from the previous 3D simulations also apply to the T-beam with $b = 400mm$. In the RPIM simulations, the area with a higher strain is smaller, even though the maximum strain value is higher compared to the other methods. Continuing to use FEM simulation as the reference, the table 6.40 shows the percentage difference in strain between the FEM simulation and the other methods.

6.4 2D Simulations

Let us start by analyzing the 2D mesh used in these simulations, which consists of quadrilateral elements. Since all the simulations are in 2D, the number of nodes and elements remains the same for every 2D simulation analyzed: 861 nodes and 800 elements. Figure 6.38 shows the mesh used for the I-plate simulations. Because the T-beam flanges have a different thickness from the webs, it was necessary to divide the mesh into two regions. This is illustrated in figure 6.39, where the red elements represent the T-beam flange and the green area represents the web of the T-beam.

Table 6.40: Percentual strain's difference for the meshless methods simulations compared with the FEM simulation, for the 3D T-beam with b=400 [mm]

Increment	RPIM Const.	RPIM Linear	NNRPIM 1^{o}	NNRPIM 2^{o}
01	0.00%	0.00%	0.00%	11.11%
02	7.69%	7.69%	7.69%	15.38%
03	40.00%	40.00%	0.00%	13.33%
04	33.33%	33.33%	5.56%	11.11%
05	38.10%	38.10%	4.76%	9.52%
06	34.62%	34.62%	3.85%	7.69%
07	33.33%	33.33%	0.00%	0.00%
08	34.88%	34.88%	0.00%	9.30%
09	34.48%	34.48%	0.00%	10.34%
10	31.65%	31.65%	0.00%	11.39%

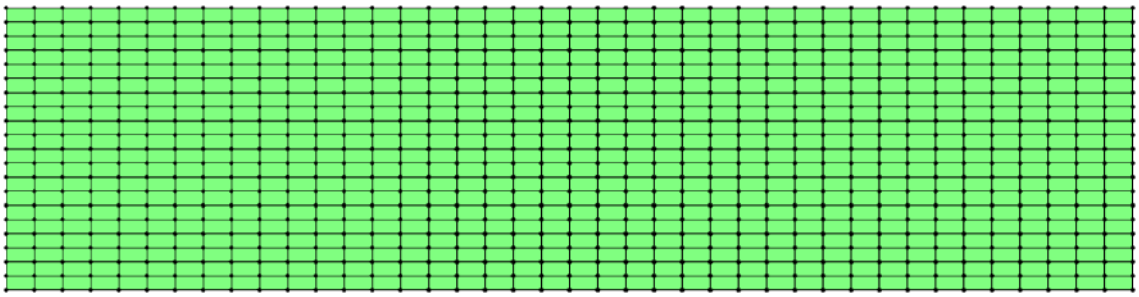

Figure 6.38: I-plate 2D mesh

It is important to note that the elastic limit ratio used in the 2D simulations is the same as that used in the 3D simulations and can be found in table 6.11. The same applies to the material properties and simulation parameters.

6.4.1 I-Plate

We start this 2D study by analyzing the I plate 2D simulation results. The plate dimension is visible in the left view of the image 6.29.

The table 6.41 represents the applied force on each iteration from all the 2D I plate simulations, while the table 6.42 shows us the percentual difference between FEM and meshless methods simulations.

Let's start by analyzing the simulation von Mises stress results present in the table 6.43.

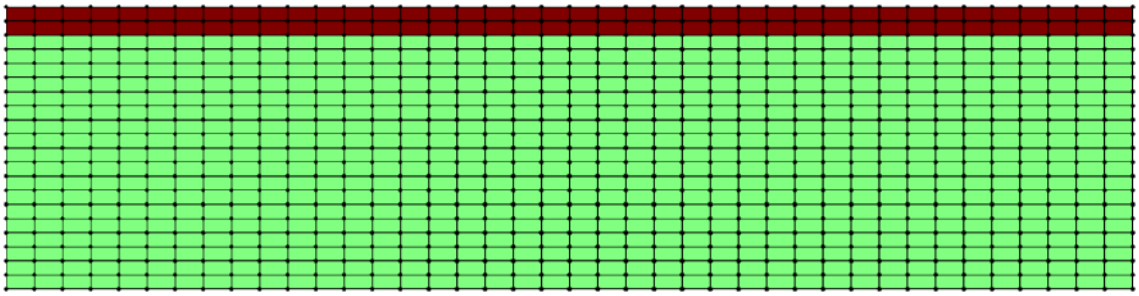

Figure 6.39: T-beam 2D mesh

Table 6.41: Applied force in the 2D I-Plate

Iteration	FEM	RPIM (Constante)	RPIM (Linear)	NNRPIM (1º order)	NNRPIM (2º order)
01	780,3 [kN]	825,4 [kN]	825,4 [kN]	789,0 [kN]	763,9 [kN]
02	838,8 [kN]	887,3 [kN]	887,3 [kN]	848,2 [kN]	821,2 [kN]
03	897,3 [kN]	949,2 [kN]	949,3 [kN]	907,4 [kN]	878,5 [kN]
04	955,8 [kN]	1 011,2 [kN]	1 011,2 [kN]	966,6 [kN]	935,8 [kN]
05	1 014,3 [kN]	1 073,1 [kN]	1 073,1 [kN]	1 025,7 [kN]	993,1 [kN]
06	1 072,8 [kN]	1 135,0 [kN]	1 135,0 [kN]	1 084,9 [kN]	1 050,4 [kN]
07	1 131,4[kN]	1 196,9 [kN]	1 196,9 [kN]	1 144,1 [kN]	1 107,7 [kN]
08	1 189,9 [kN]	1 258,8 [kN]	1 258,8 [kN]	1 203,3 [kN]	1 165,0 [kN]
09	1 248,4 [kN]	1 320,7 [kN]	1 320,7 [kN]	1 262,5 [kN]	1 222,3 [kN]
10	1 306,9 [kN]	1 382,6 [kN]	1 382,6 [kN]	1 321,6 [kN]	1 279,6 [kN]

Table 6.42: Percentual force difference for the meshless methods simulations compared with the FEM simulation, for the 2D I-plate

Increment	RPIM Const.	RPIM Linear	NNRPIM 1º	NNRPIM 2º
01	5.78%	5.78%	1.11%	2.10%
02	5.78%	5.78%	1.12%	2.10%
03	5.78%	5.80%	1.13%	2.10%
04	5.80%	5.80%	1.13%	2.09%
05	5.80%	5.80%	1.12%	2.09%
06	5.80%	5.80%	1.13%	2.09%
07	5.79%	5.79%	1.12%	2.09%
08	5.79%	5.79%	1.13%	2.09%
09	5.79%	5.79%	1.13%	2.09%
10	5.79%	5.79%	1.12%	2.09%

Table 6.43: Von Mises stress images resulted from the 2D I-plate simulations

	FEM	RPIM Constant	RPIM Linear	NNRPIM 1^{o} Order	NNRPIM 2^{o} Order
01	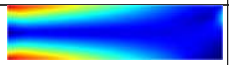 $Max = 197,48[MPa]$ $Min = 0,13[MPa]$	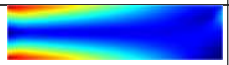 $Max = 199,83[MPa]$ $Min = 0,33[MPa]$	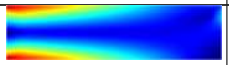 $Max = 199,83[MPa]$ $Min = 0,33[MPa]$	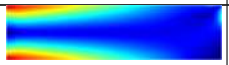 $Max = 197,00[MPa]$ $Min = 0,04[MPa]$	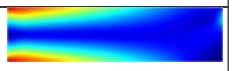 $Max = 191,98[MPa]$ $Min = 0,09[MPa]$
02	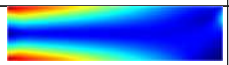 $Max = 199,53[MPa]$ $Min = 0,14[MPa]$	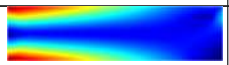 $Max = 201,51[MPa]$ $Min = 0,37[MPa]$	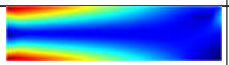 $Max = 201,91[MPa]$ $Min = 0,37[MPa]$	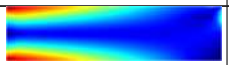 $Max = 200,49[MPa]$ $Min = 0,34[MPa]$	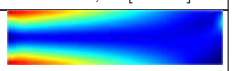 $Max = 198,33[MPa]$ $Min = 0,1[MPa]$
03	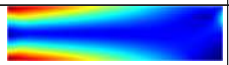 $Max = 201,75[MPa]$ $Min = 0,15[MPa]$	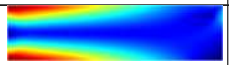 $Max = 202,91[MPa]$ $Min = 0,41[MPa]$	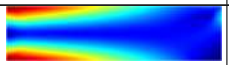 $Max = 202,91[MPa]$ $Min = 0,41[MPa]$	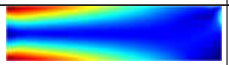 $Max = 201,70[MPa]$ $Min = 0,39[MPa]$	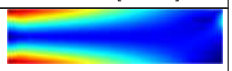 $Max = 201,17[MPa]$ $Min = 0,10[MPa]$
04	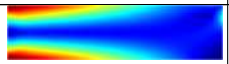 $Max = 203,17[MPa]$ $Min = 0,16[MPa]$	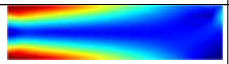 $Max = 204,58[MPa]$ $Min = 0,44[MPa]$	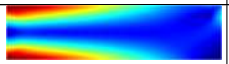 $Max = 204,58[MPa]$ $Min = 0,44[MPa]$	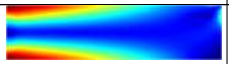 $Max = 202,86[MPa]$ $Min = 0,42[MPa]$	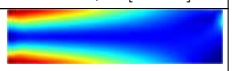 $Max = 202,65[MPa]$ $Min = 0,11[MPa]$
05	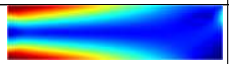 $Max = 204,63[MPa]$ $Min = 0,17[MPa]$	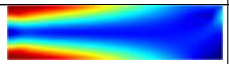 $Max = 207,88[MPa]$ $Min = 0,43[MPa]$	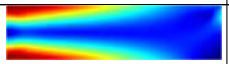 $Max = 207,88[MPa]$ $Min = 0,43[MPa]$	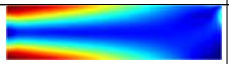 $Max = 204,85[MPa]$ $Min = 0,44[MPa]$	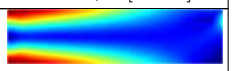 $Max = 205,09[MPa]$ $Min = 0,12[MPa]$
06	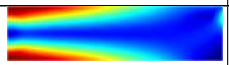 $Max = 206,63[MPa]$ $Min = 0,18[MPa]$	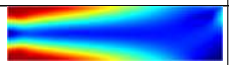 $Max = 210,57[MPa]$ $Min = 0,50[MPa]$	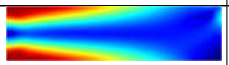 $Max = 210,57[MPa]$ $Min = 0,50[MPa]$	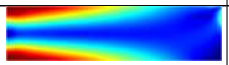 $Max = 206,48[MPa]$ $Min = 0,47[MPa]$	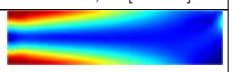 $Max = 206,95[MPa]$ $Min = 0,12[MPa]$
07	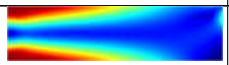 $Max = 209,20[MPa]$ $Min = 0,19[MPa]$	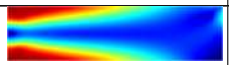 $Max = 213,92[MPa]$ $Min = 0,52[MPa]$	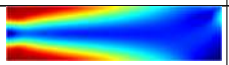 $Max = 213,92[MPa]$ $Min = 0,52[MPa]$	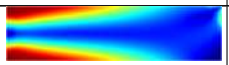 $Max = 208,76[MPa]$ $Min = 0,49[MPa]$	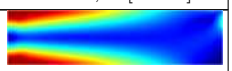 $Max = 209,83[MPa]$ $Min = 0,13[MPa]$
08	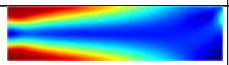 $Max = 211,73[MPa]$ $Min = 0,20[MPa]$	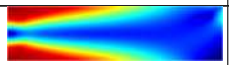 $Max = 218,66[MPa]$ $Min = 0,53[MPa]$	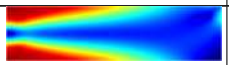 $Max = 218,66[MPa]$ $Min = 0,53[MPa]$	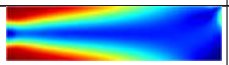 $Max = 212,51[MPa]$ $Min = 0,52[MPa]$	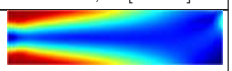 $Max = 212,52[MPa]$ $Min = 0,14[MPa]$
09	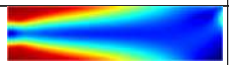 $Max = 215,68[MPa]$ $Min = 0,21[MPa]$	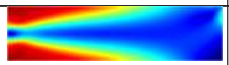 $Max = 223,71[MPa]$ $Min = 0,54[MPa]$	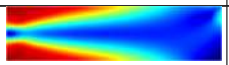 $Max = 223,71[MPa]$ $Min = 0,54[MPa]$	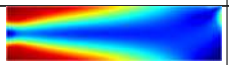 $Max = 217,15[MPa]$ $Min = [MPa]$	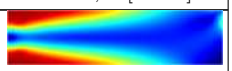 $Max = 215,87[MPa]$ $Min = 0,14[MPa]$
10	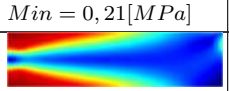 $Max = 221,05[MPa]$ $Min = 0,21[MPa]$	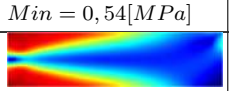 $Max = 232,54[MPa]$ $Min = 0,57[MPa]$	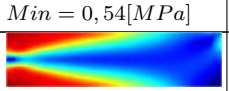 $Max = 232,54[MPa]$ $Min = 0,57[MPa]$	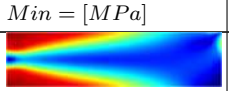 $Max = 223,46[MPa]$ $Min = 0,57[MPa]$	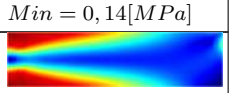 $Max = 220,81[MPa]$ $Min = 0,15[MPa]$
	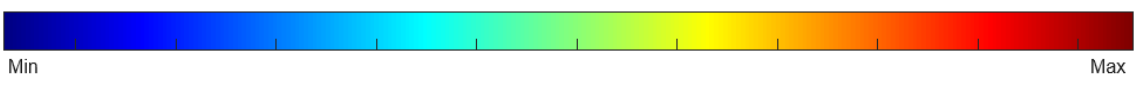 Min Max				

By analyzing the images in table 6.43, we can clearly observe the similarity and closeness among all the simulations performed. As in the 3D simulations, we use

Table 6.44: Percentual stress difference for the meshless methods simulations compared with the FEM simulation, for the 2D I-plate

Increment	RPIM Const.	RPIM Linear	NNRPIM 1^{o}	NNRPIM 2^{o}
01	1.19%	1.19%	0.24%	2.79%
02	0.99%	1.19%	0.48%	0.60%
03	0.57%	0.57%	0.02%	0.29%
04	0.69%	0.69%	0.15%	0.26%
05	1.59%	1.59%	0.11%	0.22%
06	1.91%	1.91%	0.07%	0.15%
07	2.26%	2.26%	0.21%	0.30%
08	3.27%	3.27%	0.37%	0.37%
09	3.72%	3.72%	0.68%	0.09%
10	5.20%	5.20%	1.09%	0.11%

the FEM simulations as the reference, where the table 6.44 shows us the percentual difference between the FEM and meshless methods.

After the von Mises stress analysis, we proceed to the plastic strain study, which can be observed in table 6.45.

Table 6.45: Plastic strain contour plot images resulted from the 2D I-plate simulations

	FEM	RPIM Constant	RPIM Linear	NNRPIM 1^{o} Order	NNRPIM 2^{o} Order
01					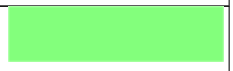
02					
03					
04					
05					
06					
07					
08					
09					
10	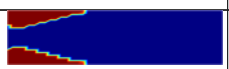				

After evaluating table 6.45, it is clear that the images are very similar, making it extremely difficult to distinguish differences between the corresponding results.

This demonstrates that the simulations are highly consistent and equivalent across all methods.

To finalize the 2D I-plate study, let us analyze the total strain by observing and comparing the images and values presented in table 6.46.

Table 6.46: Total strain contour plot images resulted from the 2D I-plate simulations

	FEM	RPIM Constant	RPIM Linear	NNRPIM 1^{o} Order	NNRPIM 2^{o} Order
01	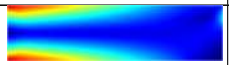 $Max = 0,08[\%]$ $Min = 0,00[\%]$	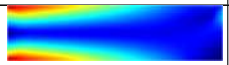 $Max = 0,08[\%]$ $Min = 0,00[\%]$	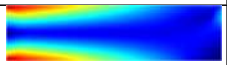 $Max = 0,08[\%]$ $Min = 0,00[\%]$	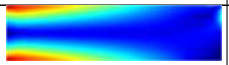 $Max = 0,08[\%]$ $Min = 0,00[\%]$	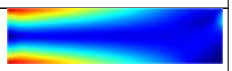 $Max = 0,08[\%]$ $Min = 0,00[\%]$
02	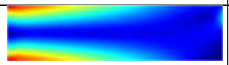 $Max = 0,09[\%]$ $Min = 0,00[\%]$	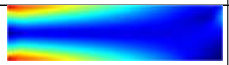 $Max = 0,10[\%]$ $Min = 0,00[\%]$	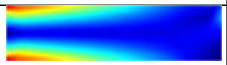 $Max = 0,10[\%]$ $Min = 0,00[\%]$	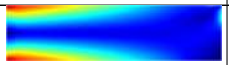 $Max = 0,09[\%]$ $Min = 0,00[\%]$	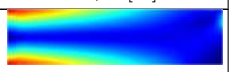 $Max = 0,09[\%]$ $Min = 0,00[\%]$
03	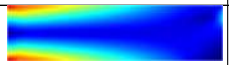 $Max = 0,10[\%]$ $Min = 0,00[\%]$	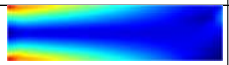 $Max = 0,11[\%]$ $Min = 0,00[\%]$	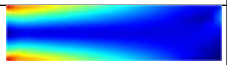 $Max = 0,11[\%]$ $Min = 0,00[\%]$	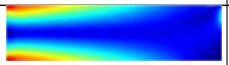 $Max = 0,10[\%]$ $Min = 0,00[\%]$	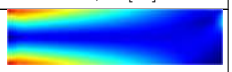 $Max = 0,11[\%]$ $Min = 0,00[\%]$
04	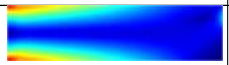 $Max = 0,11[\%]$ $Min = 0,00[\%]$	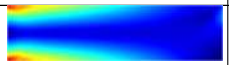 $Max = 0,13[\%]$ $Min = 0,00[\%]$	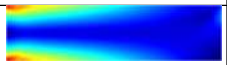 $Max = 0,13[\%]$ $Min = 0,00[\%]$	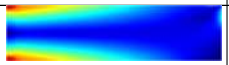 $Max = 0,11[\%]$ $Min = 0,00[\%]$	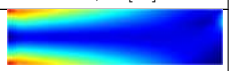 $Max = 0,13[\%]$ $Min = 0,00[\%]$
05	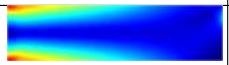 $Max = 0,13[\%]$ $Min = 0,00[\%]$	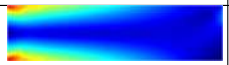 $Max = 0,14[\%]$ $Min = 0,00[\%]$	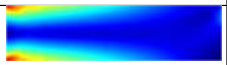 $Max = 0,14[\%]$ $Min = 0,00[\%]$	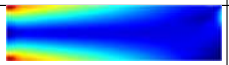 $Max = 0,12[\%]$ $Min = 0,00[\%]$	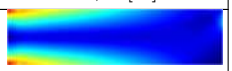 $Max = 0,14[\%]$ $Min = 0,00[\%]$
06	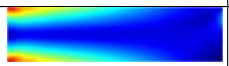 $Max = 0,14[\%]$ $Min = 0,00[\%]$	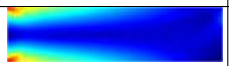 $Max = 0,17[\%]$ $Min = 0,00[\%]$	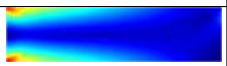 $Max = 0,17[\%]$ $Min = 0,00[\%]$	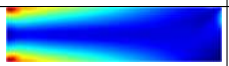 $Max = 0,14[\%]$ $Min = 0,00[\%]$	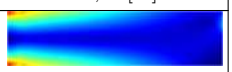 $Max = 0,15[\%]$ $Min = 0,00[\%]$
07	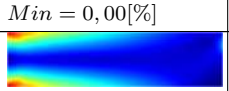 $Max = 0,16[\%]$ $Min = 0,00[\%]$	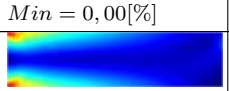 $Max = 0,20[\%]$ $Min = 0,00[\%]$	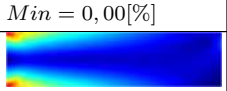 $Max = 0,20[\%]$ $Min = 0,00[\%]$	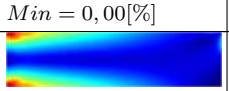 $Max = 0,16[\%]$ $Min = 0,00[\%]$	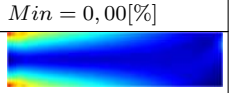 $Max = 0,17[\%]$ $Min = 0,00[\%]$
08	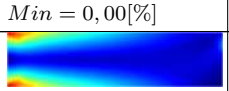 $Max = 0,18[\%]$ $Min = 0,00[\%]$	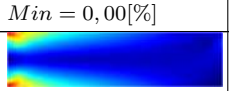 $Max = 0,23[\%]$ $Min = 0,00[\%]$	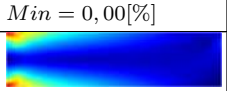 $Max = 0,23[\%]$ $Min = 0,00[\%]$	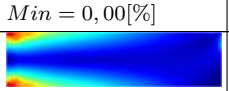 $Max = 0,18[\%]$ $Min = 0,00[\%]$	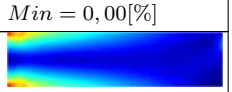 $Max = 0,22[\%]$ $Min = 0,00[\%]$
09	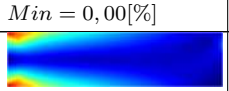 $Max = 0,21[\%]$ $Min = 0,00[\%]$	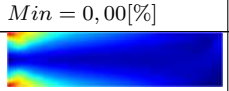 $Max = 0,28[\%]$ $Min = 0,00[\%]$	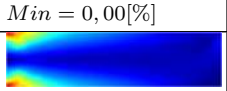 $Max = 0,28[\%]$ $Min = 0,00[\%]$	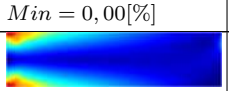 $Max = 0,22[\%]$ $Min = 0,00[\%]$	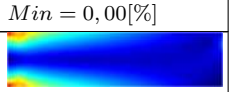 $Max = 0,33[\%]$ $Min = 0,00[\%]$
10	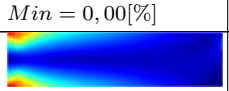 $Max = 0,25[\%]$ $Min = 0,00[\%]$	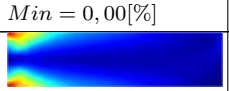 $Max = 0,34[\%]$ $Min = 0,00[\%]$	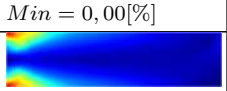 $Max = 0,34[\%]$ $Min = 0,00[\%]$	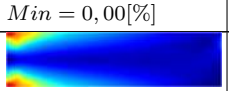 $Max = 0,27[\%]$ $Min = 0,00[\%]$	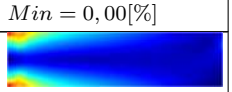 $Max = 0,67[\%]$ $Min = 0,00[\%]$

Table 6.47: Percentual strain's difference for the meshless methods simulations compared with the FEM simulation, for the 2D I-plate

Increment	RPIM Const.	RPIM Linear	NNRPIM 1º	NNRPIM 2º
01	0.00%	0.00%	0.00%	0.00%
02	11.11%	11.11%	0.00%	0.00%
03	10.00%	10.00%	0.00%	10.00%
04	18.18%	18.18%	0.00%	18.18%
05	7.69%	7.69%	7.69%	7.69%
06	21.43%	21.43%	0.00%	7.14%
07	25.00%	25.00%	0.00%	6.25%
08	27.78%	27.78%	0.00%	22.22%
09	33.33%	33.33%	4.76%	57.14%
10	36.00%	36.00%	8.00%	168.00%

Table 6.46 continued from previous page

	FEM	RPIM Constant	RPIM Linear	NNRPIM 1º Order	NNRPIM 2º Order
					
	Min Max				

As with the von Mises analysis, in this case, the similarities between all the corresponding images are undeniable and clear throughout all iterations. Once again, we can observe the percentual difference in table 6.47.

6.4.2 T-Beams

As previously outlined, the 2D T-beam simulations required different thicknesses for the two regions shown in figure 6.39. This division allows us to assign different thicknesses to the web and the flange of the T-beams. Table 6.48 presents the thickness values for the flanges of the T-beams, while the web thickness is 100 mm for all cases.

Table 6.48: T-beam flange thickness

	T Beam (b=100 [mm])	T Beam (b=200 [mm])	T Beam (b=400 [mm])
Thickness [mm]	300	500	900

T-Beam with b=100 [mm]

We begin the 2D T-beam studies with the analysis of the T-beam with $b = 100mm$. Tables 6.49 and 6.50 show us the force applied in each iteration for all the simulations performed and the percentual values difference with the FEM method being the standard one, while table 6.51 presents the von Mises stress values and corresponding images for this case.

Table 6.49: Applied force in 2D T-Beam with b=100 [mm]

Iteration	FEM	RPIM (Constante)	RPIM (Linear)	NNRPIM (1º order)	NNRPIM (2º order)
01	919,8 [kN]	975,3 [kN]	975,3 [kN]	936,6 [kN]	757,4 [kN]
02	1 034,7 [kN]	1 097,2 [kN]	1 097,2 [kN]	1 053,6 [kN]	867,2 [kN]
03	1 149,7 [kN]	1 219,2 [kN]	1 219,2 [kN]	1 170,7 [kN]	977,0 [kN]
04	1 264,7[kN]	1 341,1 [kN]	1 341,1 [kN]	1 287,8 [kN]	1 086,8 [kN]
05	1 379,7 [kN]	1 463,0 [kN]	1 463,0 [kN]	1 404,8 [kN]	1 196,6 [kN]
06	1 494,6 [kN]	1 584,9 [kN]	1 584,9 [kN]	1 521,9 [kN]	1 306,5 [kN]
07	1 609,6[kN]	1 706,8 [kN]	1 706,8 [kN]	1 639,0 [kN]	1 416,3 [kN]
08	1 724,6 [kN]	1 828,7 [kN]	1 828,7 [kN]	1 756,0 [kN]	1 526,1 [kN]
09	1 839,5 [kN]	1 950,7 [kN]	1 950,7 [kN]	1 873,1 [kN]	1 635,9 [kN]
10	1 954,5 [kN]	2 072,6 [kN]	2 072,6 [kN]	1 990,2 [kN]	1 745,7 [kN]

Table 6.50: Percentual force difference for the meshless methods simulations compared with the FEM simulation, for the 2D T-beam with b=100 [mm]

Increment	RPIM Const.	RPIM Linear	NNRPIM 1º	NNRPIM 2º
01	6.03%	6.03%	1.83%	17.66%
02	6.04%	6.05%	1.83%	16.19%
03	6.05%	6.05%	1.83%	15.02%
04	6.04%	6.04%	1.83%	14.07%
05	6.04%	6.04%	1.82%	13.27%
06	6.04%	6.04%	1.83%	12.59%
07	6.04%	6.04%	1.83%	12.01%
08	6.04%	6.04%	1.82%	11.51%
09	6.05%	6.05%	1.83%	11.07%
10	6.04%	6.04%	1.83%	10.68%

Table 6.51: Von Mises stress contour plots images resulted from the 2D T beam with b=100 [mm] simulations

	FEM	RPIM Constant	RPIM Linear	NNRPIM 1^{o} Order	NNRPIM 2^{o} Order
01	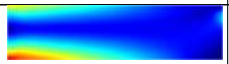 $Max = 194,82[\%]$ $Min = 0,16[MPa]$	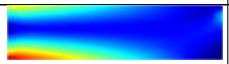 $Max = 199,99[MPa]$ $Min = 1,13[MPa]$	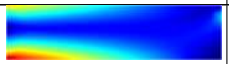 $Max = 199,99[MPa]$ $Min = 1,13[MPa]$	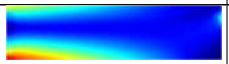 $Max = 193,11[MPa]$ $Min = 0,38[MPa]$	 $Max = 187,23[MPa]$ $Min = 0,08[MPa]$
02	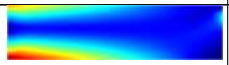 $Max = 201,29[MPa]$ $Min = 0,18[MPa]$	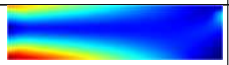 $Max = 203,01[MPa]$ $Min = 1,30[MPa]$	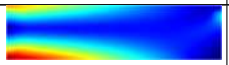 $Max = 203,01[MPa]$ $Min = 1,30[MPa]$	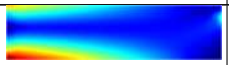 $Max = 201,26[MPa]$ $Min = 0,42[MPa]$	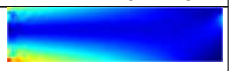 $Max = 199,28[MPa]$ $Min = 0,09[MPa]$
03	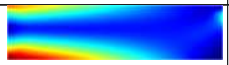 $Max = 202,70[MPa]$ $Min = 0,20[MPa]$	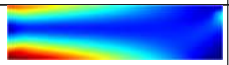 $Max = 205,08[MPa]$ $Min = 1,50[MPa]$	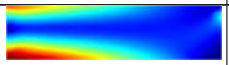 $Max = 205,08[MPa]$ $Min = 1,50[MPa]$	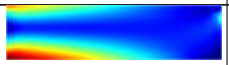 $Max = 202,76[MPa]$ $Min = 0,47[MPa]$	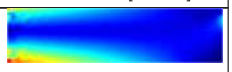 $Max = 201,74[MPa]$ $Min = 0,10[MPa]$
04	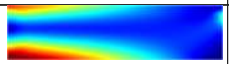 $Max = 205,34[MPa]$ $Min = 0,22[MPa]$	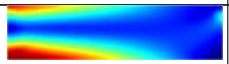 $Max = 208,97[MPa]$ $Min = 1,58[MPa]$	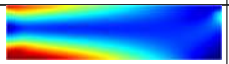 $Max = 208,97[MPa]$ $Min =, 1,58[MPa]$	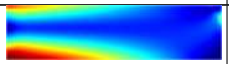 $Max = 205,34[MPa]$ $Min = 0,52[MPa]$	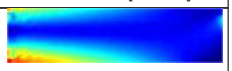 $Max = 204,20[MPa]$ $Min = 0,11[MPa]$
05	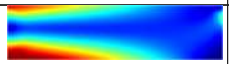 $Max = 207,78[MPa]$ $Min = 0,24[MPa]$	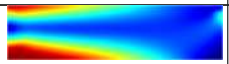 $Max = 213,47[MPa]$ $Min = 1,74[MPa]$	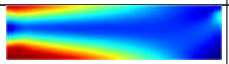 $Max = 213,47[MPa]$ $Min = 1,74[MPa]$	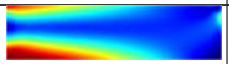 $Max = 207,74[MPa]$ $Min = 0,56[MPa]$	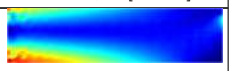 $Max = 206,31[MPa]$ $Min = 0,12[MPa]$
06	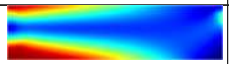 $Max = 211,39[MPa]$ $Min = 0,26[MPa]$	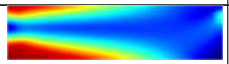 $Max = 219,11[MPa]$ $Min = 1,94[MPa]$	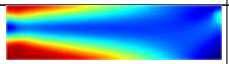 $Max = 219,11[MPa]$ $Min = 1,94[MPa]$	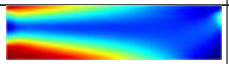 $Max = 210,79[MPa]$ $Min = 0,61[MPa]$	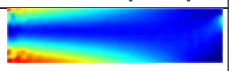 $Max = 209,16[MPa]$ $Min = 0,13[MPa]$
07	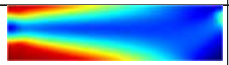 $Max = 217,86[MPa]$ $Min = 0,28[MPa]$	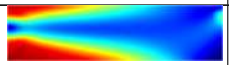 $Max = 226,17[MPa]$ $Min = 2,16[MPa]$	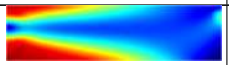 $Max = 226,17[MPa]$ $Min = 2,16[MPa]$	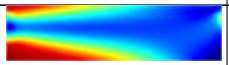 $Max = 216,02[MPa]$ $Min = 0,66[MPa]$	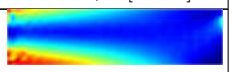 $Max = 213,41[MPa]$ $Min = 0,14[MPa]$
08	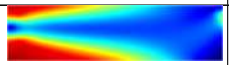 $Max = 228,65[MPa]$ $Min = 0,29[MPa]$	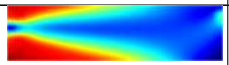 $Max = 240,57[MPa]$ $Min = 2,20[MPa]$	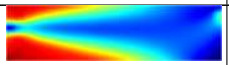 $Max = 240,57[MPa]$ $Min = 2,20[MPa]$	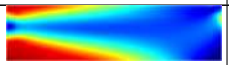 $Max = 224,34[MPa]$ $Min = 0,70[MPa]$	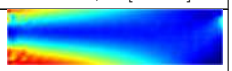 $Max = 220,91[MPa]$ $Min = 0,14[MPa]$
09	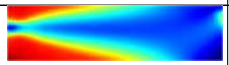 $Max = 246,16[MPa]$ $Min = 0,31[MPa]$	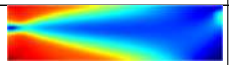 $Max = 260,41[MPa]$ $Min = 2,32[MPa]$	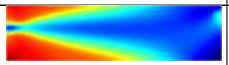 $Max = 260,41[MPa]$ $Min = 2,32[MPa]$	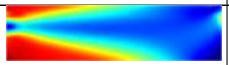 $Max = 238,10[MPa]$ $Min = 0,75[MPa]$	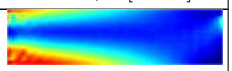 $Max = 233,78[MPa]$ $Min = 0,15[MPa]$
10	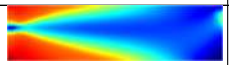 $Max = 266,74[MPa]$ $Min = 0,33[MPa]$	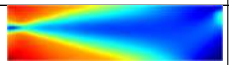 $Max = 283,47[MPa]$ $Min = 2,54[MPa]$	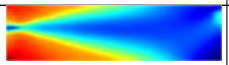 $Max = 283,47[MPa]$ $Min = 2,54[MPa]$	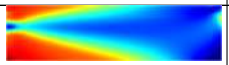 $Max = 257,20[MPa]$ $Min = 0,79[MPa]$	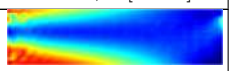 $Max = 252,06[MPa]$ $Min = 0,16[MPa]$
					

v

Table 6.52: Percentual stress difference for the meshless methods simulations compared with the FEM simulation, for the 2D T beam with b=100 [mm]

Increment	RPIM Const.	RPIM Linear	NNRPIM 1º	NNRPIM 2º
01	2.65%	2.65%	0.88%	3.90%
02	0.85%	0.85%	0.01%	1.00%
03	1.17%	1.17%	0.03%	0.47%
04	1.77%	1.77%	0.00%	0.56%
05	2.74%	2.74%	0.02%	0.71%
06	3.65%	3.65%	0.28%	1.05%
07	3.81%	3.81%	0.84%	2.04%
08	5.21%	5.21%	1.88%	3.39%
09	5.79%	5.79%	3.27%	5.03%
10	6.27%	6.27%	3.58%	5.50%

By comparing the images present in table 6.43 we can visualize continuous similarity, being it once again, very difficult to find differences between the equivalent images throughout all the simulations, except for the NNRPIM of second order, where we find a slightly distorted image, with the area of heights stress (red zone) being smaller than the images obtained in the other simulations. The percentual difference between the maximum stress values can be visualized in table 6.52.

The next analysis is the plastic strain, and the respective images required for the study analysis are in table 6.53.

Let us now proceed to the analysis of the plastic strain in the 2D T-beam simulations, with the corresponding images and values presented in table 6.53.

Table 6.53: Plastic strain contour plots images resulted from the 2D T-beam with b=100 [mm] simulations

	FEM	RPIM Constant	RPIM Linear	NNRPIM 1º Order	NNRPIM 2º Order
01					
02					
03					
04					
05					
06					
07	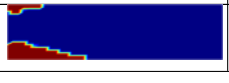	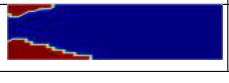	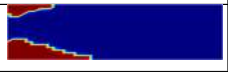		

Table 6.53 continued from previous page

	FEM	RPIM Constant	RPIM Linear	NNRPIM 1^{o} Order	NNRPIM 2^{o} Order
08					
09	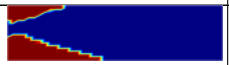				
10	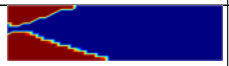			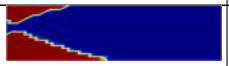	

In this table 6.53, we can observe that the NNRPIM simulation with the second degree of neighborhood is the one that differs most from the other simulation types, presenting us with a considerably smaller plastic deformed area.

Let us now analyze table 6.54, which contains the strain images and values, to finalize the 2D simulations for the T-beam with $b = 100mm$.

Table 6.54: Total strain contour plot images resulted from the 2D T-beam with b=100 [mm] simulations

	FEM	RPIM Constant	RPIM Linear	NNRPIM 1^{o} Order	NNRPIM 2^{o} Order
01	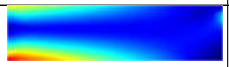 $Max = 0,09[\%]$ $Min = 0,00[\%]$	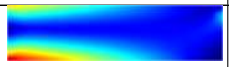 $Max = 0,09[\%]$ $Min = 0,00[\%]$	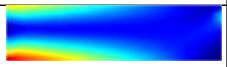 $Max = 0,09[\%]$ $Min = 0,00[\%]$	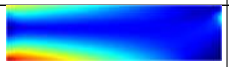 $Max = 0,09[\%]$ $Min = 0,00[\%]$	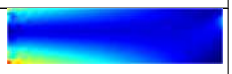 $Max = 0,08[\%]$ $Min = 0,00[\%]$
02	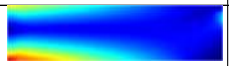 $Max = 0,11[\%]$ $Min = 0,00[\%]$	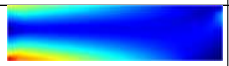 $Max = 0,12[\%]$ $Min = 0,00[\%]$	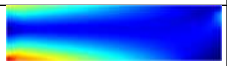 $Max = 0,12[\%]$ $Min = 0,00[\%]$	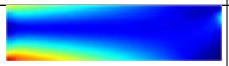 $Max = 0,11[\%]$ $Min = 0,00[\%]$	 $Max = 0,10[\%]$ $Min = 0,00[\%]$
03	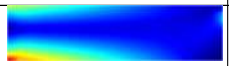 $Max = 0,13[\%]$ $Min = 0,00[\%]$	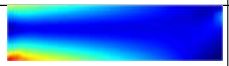 $Max = 0,15[\%]$ $Min = 0,00[\%]$	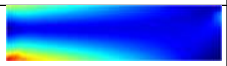 $Max = 0,15[\%]$ $Min = 0,00[\%]$	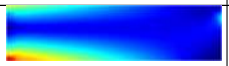 $Max = 0,12[\%]$ $Min = 0,00[\%]$	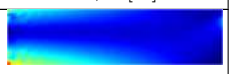 $Max = 0,12[\%]$ $Min = 0,00[\%]$
04	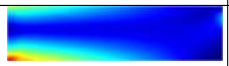 $Max = 0,14[\%]$ $Min = 0,00[\%]$	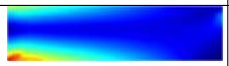 $Max = 0,18[\%]$ $Min = 0,00[\%]$	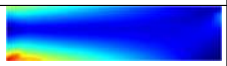 $Max = 0,18[\%]$ $Min = 0,00[\%]$	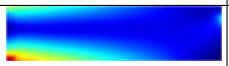 $Max = 0,14[\%]$ $Min = 0,00[\%]$	 $Max = 0,14[\%]$ $Min = 0,00[\%]$
05	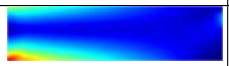 $Max = 0,16[\%]$ $Min = 0,00[\%]$	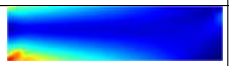 $Max = 0,23[\%]$ $Min = 0,00[\%]$	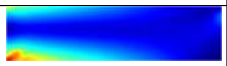 $Max = 0,23[\%]$ $Min = 0,00[\%]$	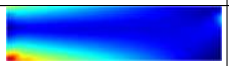 $Max = 0,16[\%]$ $Min = 0,00[\%]$	 $Max = 0,16[\%]$ $Min = 0,00[\%]$
06	 $Max = 0,20[\%]$ $Min = 0,00[\%]$	 $Max = 0,27[\%]$ $Min = 0,00[\%]$	 $Max = 0,27[\%]$ $Min = 0,00[\%]$	 $Max = 0,19[\%]$ $Min = 0,00[\%]$	 $Max = 0,18[\%]$ $Min = 0,00[\%]$
07	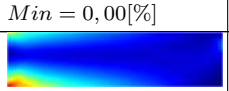 $Max = 0,26[\%]$ $Min = 0,00[\%]$	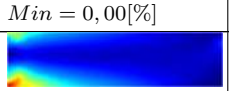 $Max = 0,34[\%]$ $Min = 0,00[\%]$	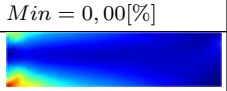 $Max = 0,34[\%]$ $Min = 0,00[\%]$	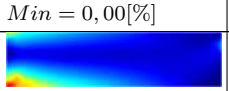 $Max = 0,24[\%]$ $Min = 0,00[\%]$	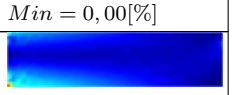 $Max = 0,22[\%]$ $Min = 0,00[\%]$

Table 6.55: Percentual strain's difference for the meshless methods simulations compared with the FEM simulation, for the 2D T-beam with b=100 [mm]

Increment	RPIM Const.	RPIM Linear	NNRPIM 1º	NNRPIM 2º
01	0.00%	0.00%	0.00%	11.11%
02	9.09%	9.09%	0.00%	9.09%
03	15.38%	15.38%	7.69%	7.69%
04	28.57%	28.57%	0.00%	0.00%
05	43.75%	43.75%	0.00%	0.00%
06	35.00%	35.00%	5.00%	10.00%
07	30.77%	30.77%	7.69%	15.38%
08	27.78%	27.78%	13.89%	19.44%
09	24.53%	24.53%	15.09%	22.64%
10	20.55%	20.55%	13.70%	20.55%

Table 6.54 continued from previous page

	FEM	RPIM Constant	RPIM Linear	NNRPIM 1º Order	NNRPIM 2º Order
08	 $Max = 0,36[\%]$ $Min = 0,00[\%]$	 $Max = 0,46[\%]$ $Min = 0,00[\%]$	 $Max = 0,46[\%]$ $Min = 0,00[\%]$	 $Max = 0,31[\%]$ $Min = 0,00[\%]$	 $Max = 0,29[\%]$ $Min = 0,00[\%]$
09	 $Max = 0,53[\%]$ $Min = 0,00[\%]$	 $Max = 0,66[\%]$ $Min = 0,00[\%]$	 $Max0,66[\%]$ $Min = 0,00[\%]$	 $Max = 0,45[\%]$ $Min = 0,00[\%]$	 $Max = 0,41[\%]$ $Min = 0,00[\%]$
10	 $Max = 0,73[\%]$ $Min = 0,00[\%]$	 $Max = 0,88[\%]$ $Min = 0,00[\%]$	 $Max = 0,88[\%]$ $Min = 0,00[\%]$	 $Max = 0,63[\%]$ $Min = 0,00[\%]$	 $Max = 0,58[\%]$ $Min = 0,00[\%]$
	 Min Max				

Once again, we can observe that the NNRPIM simulation, with the second degree of neighborhood, is the one that offers a more distinct contour plot image, resulting in a smaller strain area. The table 6.55 shows us the percentual difference between the FEM simulation results with the meshless methods.

T-Beam with b=200 mm

To begin the 2D simulations of the T-beam with $b = 200mm$, we will first analyze the forces applied in each simulation, as shown in table 6.56, and the respective percentual difference between the FEM method and the others can be studied in table 6.57. Afterward, we will study the von Mises stress images and values presented in table 6.58.

Table 6.56: Applied force in 2D T-Beam with b=200 [mm]

Iteration	FEM	RPIM (Constante)	RPIM (Linear)	NNRPIM (1º order)	NNRPIM (2º order)
01	993,1 [kN]	1 054,5 [kN]	1 054,5 [kN]	1 005,9 [kN]	757,4 [kN]
02	1 137,1 [kN]	1 207,4 [kN]	1 207,4 [kN]	1 151,8 [kN]	867,2 [kN]
03	1 281,1 [kN]	1 360,3 [kN]	1 360,3 [kN]	1 297,7 [kN]	977,0 [kN]
04	1 425,1[kN]	1 513,2 [kN]	1 513,2 [kN]	1 443,5 [kN]	1 086,8 [kN]
05	1 569,1 [kN]	1 666,1 [kN]	1 666,1 [kN]	1 589,4 [kN]	1 196,6 [kN]
06	1 713,1 [kN]	1 819,0 [kN]	1 819,0 [kN]	1 735,2 [kN]	1 306,5 [kN]
07	1 857,1[kN]	1 971,9 [kN]	1 971,9 [kN]	1 881,1 [kN]	1 416,3 [kN]
08	2 001,1 [kN]	2 124,8 [kN]	2 124,8 [kN]	2 027,0 [kN]	1 526,1 [kN]
09	2 145,1 [kN]	2 277,7 [kN]	2 277,7 [kN]	2 172,8 [kN]	1 635,9 [kN]
10	2 289,1 [kN]	2 430,6 [kN]	2 430,6 [kN]	2 318,7 [kN]	1 745,7 [kN]

Table 6.57: Percentual force difference for the meshless methods simulations compared with the FEM simulation, for the 2D T-beam with b=200 [mm]

Increment	RPIM Const.	RPIM Linear	NNRPIM 1º	NNRPIM 2º
01	6.18%	6.18%	1.29%	23.73%
02	6.18%	6.18%	1.29%	23.74%
03	6.18%	6.18%	1.30%	23.74%
04	6.18%	6.18%	1.29%	23.74%
05	6.18%	6.18%	1.29%	23.74%
06	6.18%	6.18%	1.29%	23.73%
07	6.18%	6.18%	1.29%	23.74%
08	6.18%	6.18%	1.29%	23.74%
09	6.18%	6.18%	1.29%	23.74%
10	6.18%	6.18%	1.29%	23.74%

Table 6.58: Von Mises stress contour plot images resulted from the 2D T-beam with b=200 [mm] simulations

	FEM	RPIM Constant	RPIM Linear	NNRPIM 1^{o} Order	NNRPIM 2^{o} Order
01	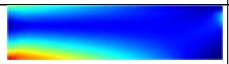 $Max = 197,49[MPa]$ $Min = 0,18[MPa]$	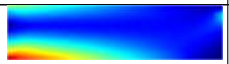 $Max = 199,83[MPa]$ $Min = 0,23[MPa]$	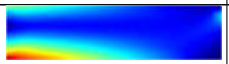 $Max = 199,83[MPa]$ $Min = 0,23[MPa]$	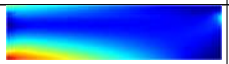 $Max = 196,92[MPa]$ $Min = 0,51[MPa]$	 $Max = 192,31[MPa]$ $Min = 0,32[MPa]$
02	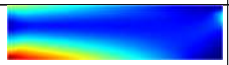 $Max = 201,00[MPa]$ $Min = 0,20[MPa]$	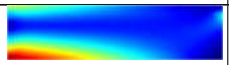 $Max = 203,95[MPa]$ $Min = 0,27[MPa]$	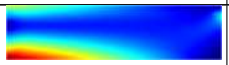 $Max = 203,95[MPa]$ $Min = 0,27[MPa]$	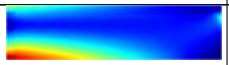 $Max = 201,14[MPa]$ $Min = 0,58[MPa]$	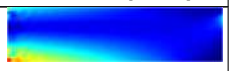 $Max = 198,85[MPa]$ $Min = 0,37[MPa]$
03	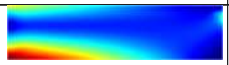 $Max = 204,12[MPa]$ $Min = 0,23[MPa]$	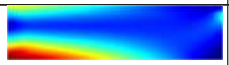 $Max = 206,70[MPa]$ $Min = 0,34[MPa]$	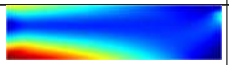 $Max = 206,70[MPa]$ $Min = 0,34[MPa]$	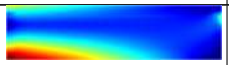 $Max = 203,62[MPa]$ $Min = 0,65[MPa]$	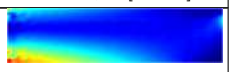 $Max = 202,36[MPa]$ $Min = 0,42[MPa]$
04	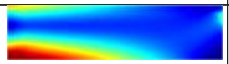 $Max = 206,34[MPa]$ $Min = 0,25[MPa]$	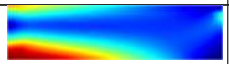 $Max = 210,43[MPa]$ $Min = 0,38[MPa]$	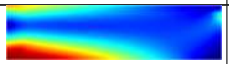 $Max = 210,43[MPa]$ $Min = 0,38[MPa]$	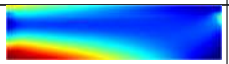 $Max = 207,77[MPa]$ $Min = 0,73[MPa]$	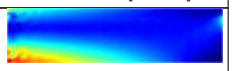 $Max = 205,33[MPa]$ $Min = 0,47[MPa]$
05	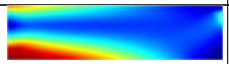 $Max = 211,47[MPa]$ $Min = 0,28[MPa]$	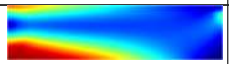 $Max = 215,40[MPa]$ $Min = 0,43[MPa]$	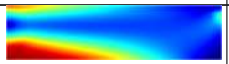 $Max = 215,40[MPa]$ $Min = 0,43[MPa]$	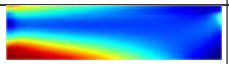 $Max = 210,37[MPa]$ $Min = 0,80[MPa]$	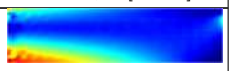 $Max = 210,38[MPa]$ $Min = 0,52[MPa]$
06	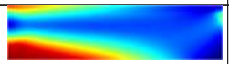 $Max = 214,43[MPa]$ $Min = 0,30[MPa]$	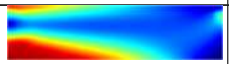 $Max = 219,67[MPa]$ $Min = 0,60[MPa]$	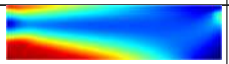 $Max = 219,67[MPa]$ $Min = 0,60[MPa]$	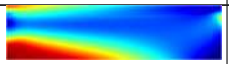 $Max = 215,23[MPa]$ $Min = 0,87[MPa]$	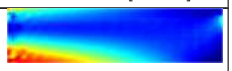 $Max = 214,79[MPa]$ $Min = 0,57[MPa]$
07	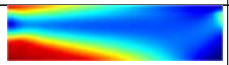 $Max = 221,09[MPa]$ $Min = 0,33[MPa]$	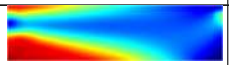 $Max = 227,86[MPa]$ $Min = 0,59[MPa]$	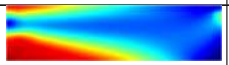 $Max = 227,86[MPa]$ $Min = 0,59[MPa]$	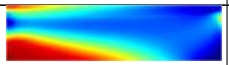 $Max = 220,98[MPa]$ $Min = 0,95[MPa]$	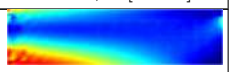 $Max = 220,24[MPa]$ $Min = 0,64[MPa]$
08	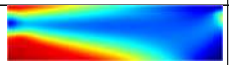 $Max = 228,18[MPa]$ $Min = 0,35[MPa]$	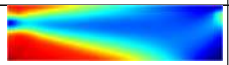 $Max = 240,54[MPa]$ $Min = 0,80[MPa]$	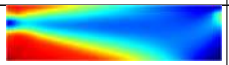 $Max = 240,54[MPa]$ $Min = 0,80[MPa]$	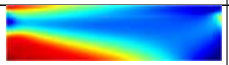 $Max = 229,00[MPa]$ $Min = 1,02[MPa]$	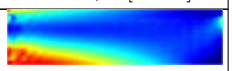 $Max = 227,36[MPa]$ $Min = 0,70[MPa]$
09	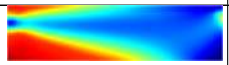 $Max = 242,45[MPa]$ $Min = 0,38[MPa]$	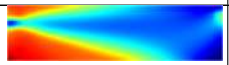 $Max = 261,55[MPa]$ $Min = 0,93[MPa]$	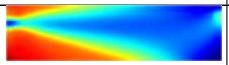 $Max = 261,55[MPa]$ $Min = 0,93[MPa]$	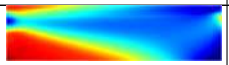 $Max = 241,60[MPa]$ $Min = 1,09[MPa]$	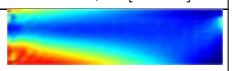 $Max = 234,21[MPa]$ $Min = 0,79[MPa]$
10	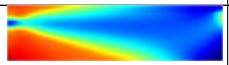 $Max = 265,40[MPa]$ $Min = 0,40[MPa]$	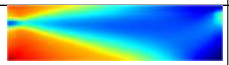 $Max = 289,67[MPa]$ $Min = 1,00[MPa]$	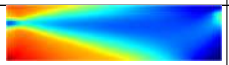 $Max = 289,67[MPa]$ $Min = 1,00[MPa]$	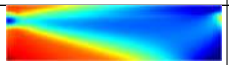 $Max = 259,95[MPa]$ $Min = 1,17[MPa]$	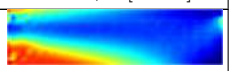 $Max = 242,11[MPa]$ $Min = 0,89[MPa]$

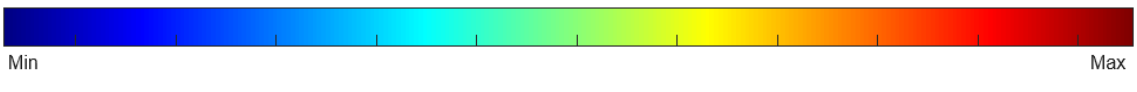

Once more, the visual similarities are vast, with the exception being the NNRPIM (of second order), where the stress contour plot images show a smaller area subjected

Table 6.59: Percentual stress difference for the meshless methods simulations compared with the FEM simulation, for the 2D T-beam with b=200 [mm]

Increment	RPIM Const.	RPIM Linear	NNRPIM 1º	NNRPIM 2º
01	1.18%	1.18%	0.29%	2.62%
02	1.47%	1.47%	0.07%	1.07%
03	1.26%	1.26%	0.24%	0.86%
04	1.98%	1.98%	0.69%	0.49%
05	1.86%	1.86%	0.52%	0.52%
06	2.44%	2.44%	0.37%	0.17%
07	3.06%	3.06%	0.05%	0.38%
08	5.42%	5.42%	0.36%	0.36%
09	7.88%	7.88%	0.35%	3.40%
10	9.14%	9.14%	2.05%	8.78%

to the values closer to maximum stress. In table 6.59 we can see the percentual comparative difference values from the standard method (FEM), to the meshless methods.

The table 6.60 shows us the images required to make an analysis of the plastic strain behavior in the 2D simulations for the T-beam with b=200 mm.

Table 6.60: Plastic strain contour plot images resulted from the 2D T-beam with b=200 [mm] simulations

	FEM	RPIM Constant	RPIM Linear	NNRPIM 1º Order	NNRPIM 2º Order
01					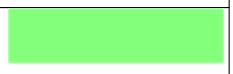
02					
03					
04					
05					
06		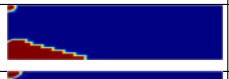	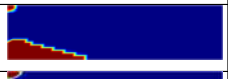		
07				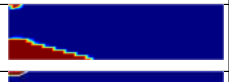	
08					
09	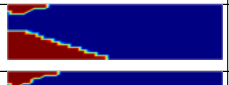			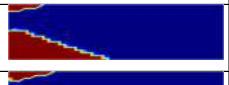	
10	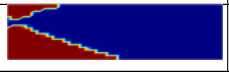	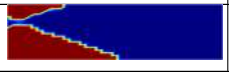	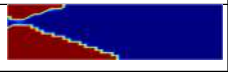	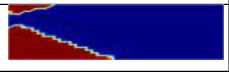	

Analyzing the images presented in table 6.60 we can observe that the NNRPIM with a second degree of neighborhood presents a considerably less plastic deformed area than the others four simulation cases, we can also observe that the NNRPIM with the first degree of neighborhood is very closely matched visually with the FEM and RPIM methods, but is possible to observe that it too have a little less plastic deformed area.

To conclude the 2D study for the T-beam with $b = 200mm$, let us analyze the table 6.61, which presents the strain images and values for the different simulations and iterations.

Table 6.61: Total strain contour plot images resulted from the 2D T-beam with b=200 [mm] simulations

	FEM	RPIM Constant	RPIM Linear	NNRPIM 1^{o} Order	NNRPIM 2^{o} Order
01	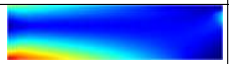 $Max = 0,08[\%]$ $Min = 0,00[\%]$	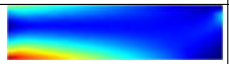 $Max = 0,08[\%]$ $Min = 0,00[\%]$	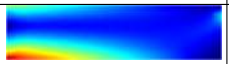 $Max = 0,08[\%]$ $Min = 0,00[\%]$	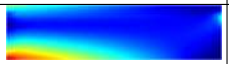 $Max = 0,08[\%]$ $Min = 0,00[\%]$	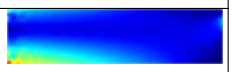 $Max = 0,08[\%]$ $Min = 0,00[\%]$
02	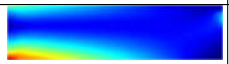 $Max = 0,10[\%]$ $Min = 0,00[\%]$	 $Max = 0,13[\%]$ $Min = 0,00[\%]$	 $Max = 0,13[\%]$ $Min = 0,00[\%]$	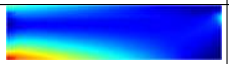 $Max = 0,10[\%]$ $Min = 0,00[\%]$	 $Max = 0,10[\%]$ $Min = 0,00[\%]$
03	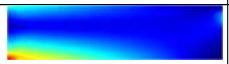 $Max = 0,12[\%]$ $Min = 0,00[\%]$	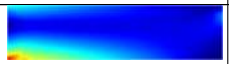 $Max = 0,15[\%]$ $Min = 0,00[\%]$	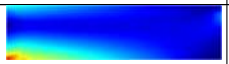 $Max = 0,15[\%]$ $Min = 0,00[\%]$	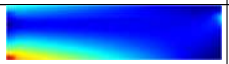 $Max = 0,12[\%]$ $Min = 0,00[\%]$	 $Max = 0,12[\%]$ $Min = 0,00[\%]$
04	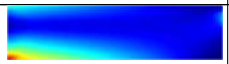 $Max = 0,15[\%]$ $Min = 0,00[\%]$	 $Max = 0,17[\%]$ $Min = 0,00[\%]$	 $Max = 0,17[\%]$ $Min = 0,00[\%]$	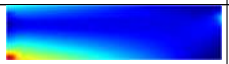 $Max = 0,15[\%]$ $Min = 0,00[\%]$	 $Max = 0,14[\%]$ $Min = 0,00[\%]$
05	 $Max = 0,17[\%]$ $Min = 0,00[\%]$	 $Max = 0,21[\%]$ $Min = 0,00[\%]$	 $Max = 0,21[\%]$ $Min = 0,00[\%]$	 $Max = 0,17[\%]$ $Min = 0,00[\%]$	 $Max = 0,17[\%]$ $Min = 0,00[\%]$
06	 $Max = 0,20[\%]$ $Min = 0,00[\%]$	 $Max = 0,25[\%]$ $Min = 0,00[\%]$	 $Max = 0,25[\%]$ $Min = 0,00[\%]$	 $Max = 0,21[\%]$ $Min = 0,00[\%]$	 $Max = 0,21[\%]$ $Min = 0,00[\%]$
07	 $Max = 0,24[\%]$ $Min = 0,00[\%]$	 $Max = 0,31[\%]$ $Min = 0,00[\%]$	 $Max = 0,31[\%]$ $Min = 0,00[\%]$	 $Max = 0,25[\%]$ $Min = 0,00[\%]$	 $Max = 0,25[\%]$ $Min = 0,00[\%]$
08	 $Max = 0,30[\%]$ $Min = 0,00[\%]$	 $Max = 0,40[\%]$ $Min = 0,00[\%]$	 $Max = 0,40[\%]$ $Min = 0,00[\%]$	 $Max = 0,31[\%]$ $Min = 0,00[\%]$	 $Max = 0,29[\%]$ $Min = 0,00[\%]$

Table 6.62: Percentual strain's difference for the meshless methods simulations compared with the FEM simulation, for the 2D T-beam with b=200 [mm]

Increment	RPIM Const.	RPIM Linear	NNRPIM 1º	NNRPIM 2º
01	0.00%	0.00%	0.00%	0.00%
02	30.00%	30.00%	0.00%	0.00%
03	25.00%	25.00%	0.00%	0.00%
04	13.33%	13.33%	0.00%	6.67%
05	23.53%	23.53%	0.00%	0.00%
06	25.00%	25.00%	5.00%	5.00%
07	29.17%	29.17%	4.17%	4.17%
08	33.33%	33.33%	3.33%	3.33%
09	42.50%	42.50%	2.50%	15.00%
10	40.35%	40.35%	3.51%	31.58%

Table 6.61 continued from previous page

	FEM	RPIM Constant	RPIM Linear	NNRPIM 1º Order	NNRPIM 2º Order
09	 $Max = 0,40[\%]$ $Min = 0,00[\%]$	 $Max = 0,57[\%]$ $Min = 0,00[\%]$	 $Max = 0,57[\%]$ $Min = 0,00[\%]$	 $Max = 0,41[\%]$ $Min = 0,00[\%]$	 $Max = 0,34[\%]$ $Min = 0,00[\%]$
10	 $Max = 0,57[\%]$ $Min = 0,00[\%]$	 $Max = 0,80[\%]$ $Min = 0,00[\%]$	 $Max = 0,80[\%]$ $Min = 0,00[\%]$	 $Max = 0,55[\%]$ $Min = 0,00[\%]$	 $Max = 0,39[\%]$ $Min = 0,00[\%]$

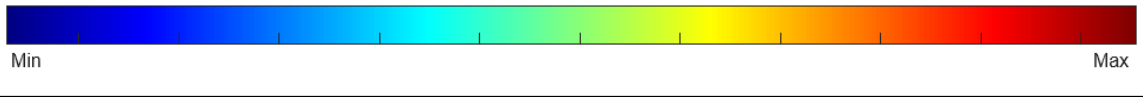

Just like in the previous 2D simulations, in the NNRPIM simulation with the second order of neighborhood, the results distance themselves from the other simulations' results, as is possible to observe in the table 6.62.

T-Beam with b=400 [mm]

In order to complete the studies of the different 2D non-linear deformations, it is necessary to analyze the results of the 2D simulations for the T beam with b=400 mm. Before starting to analyze the results, let's divert your attention to table 6.63 and 6.64, where we can study and compare the applied force through each iteration's simulation and its respective differential percentile values, respectively. The first study will be about the von Mises stress, and the respective values and images are present in table 6.65.

Table 6.63: Applied force in 2D T Beam with b=400 [mm]

Iteration	FEM	RPIM (Constante)	RPIM (Linear)	NNRPIM (1º order)	NNRPIM (2º order)
01	1 070,2 [kN]	1 137,5 [kN]	1 137,5 [kN]	937,4 [kN]	818,9 [kN]
02	1 246,8 [kN]	1 325,2 [kN]	1 325,2 [kN]	1 092,1 [kN]	954,0 [kN]
03	1 423,4 [kN]	1 512,9 [kN]	1 512,9 [kN]	1 246,7 [kN]	1 089,1 [kN]
04	1 600,0 [kN]	1 700,5 [kN]	1 700,5 [kN]	1 401,4 [kN]	1 224,2 [kN]
05	1 776,6 [kN]	1 888,2 [kN]	1 888,2 [kN]	1 556,1 [kN]	1 359,3 [kN]
06	1 953,2 [kN]	2 075,9 [kN]	2 075,9 [kN]	1 710,7 [kN]	1 494,5 [kN]
07	2 129,8[kN]	2 263,6 [kN]	2 263,6 [kN]	1 865,4 [kN]	1 629,6 [kN]
08	2 306,3 [kN]	2 451,3 [kN]	2 451,3 [kN]	2 020,1 [kN]	1 764,7 [kN]
09	2 482,9 [kN]	2 639,0 [kN]	2 639,0 [kN]	2 174,7 [kN]	1 899,8 [kN]
10	2 659,5 [kN]	2 826,6 [kN]	2 826,6 [kN]	2 329,4 [kN]	2 034,9 [kN]

Table 6.64: Percentual force difference for the meshless methods simulations compared with the FEM simulation, for the 2D T beam with b=400 [mm]

Increment	RPIM Const.	RPIM Linear	NNRPIM 1º	NNRPIM 2º
01	6.29%	6.29%	12.41%	23.48%
02	6.29%	6.29%	12.41%	23.48%
03	6.29%	6.29%	12.41%	23.49%
04	6.28%	6.28%	12.41%	23.49%
05	6.28%	6.28%	12.41%	23.49%
06	6.28%	6.28%	12.42%	23.48%
07	6.28%	6.28%	12.41%	23.49%
08	6.29%	6.29%	12.41%	23.48%
09	6.29%	6.29%	12.41%	23.48%
10	6.28%	6.28%	12.41%	23.49%

Table 6.65: Von Mises stress contour plot images resulted from the 2D T-beam with b=400 [mm] simulations

	FEM	RPIM Constant	RPIM Linear	NNRPIM 1^{o} Order	NNRPIM 2^{o} Order
01	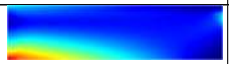 $Max = 197,49[MPa]$ $Min = 0,20[MPa]$	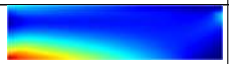 $Max = 199,83[MPa]$ $Min = 0,16[MPa]$	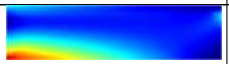 $Max = 199,83[MPa]$ $Min = 0,16[MPa]$	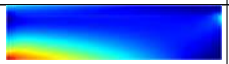 $Max = 196,88[MPa]$ $Min = 0,37[MPa]$	 $Max = 192,43[MPa]$ $Min = 0,25[MPa]$
02	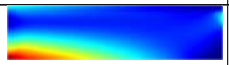 $Max = 201,31[MPa]$ $Min = 0,24[MPa]$	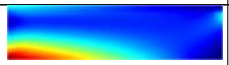 $Max = 204,96[MPa]$ $Min = 0,23[MPa]$	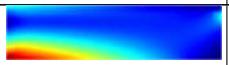 $Max = 204,96[MPa]$ $Min = 0,23[MPa]$	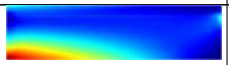 $Max = 201,44[MPa]$ $Min = 0,43[MPa]$	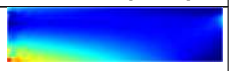 $Max = 199,30[MPa]$ $Min = 0,29[MPa]$
03	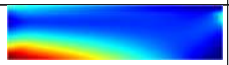 $Max = 206,00[MPa]$ $Min = 0,27[MPa]$	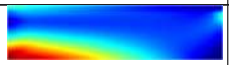 $Max = 211,43[MPa]$ $Min = 0,25[MPa]$	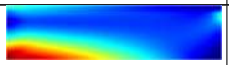 $Max = 211,43[MPa]$ $Min = 0,25[MPa]$	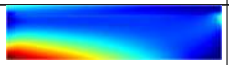 $Max = 204,73[MPa]$ $Min = 0,49[MPa]$	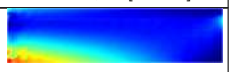 $Max = 203,59[MPa]$ $Min = 0,33[MPa]$
04	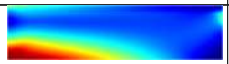 $Max = 209,77[MPa]$ $Min = 0,30[MPa]$	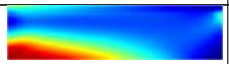 $Max = 214,32[MPa]$ $Min = 0,28[MPa]$	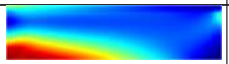 $Max = 214,32[MPa]$ $Min = 0,28[MPa]$	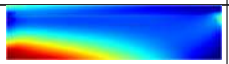 $Max = 210,15[MPa]$ $Min = 0,56[MPa]$	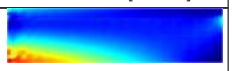 $Max = 206,70[MPa]$ $Min = 0,38[MPa]$
05	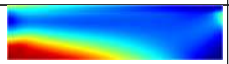 $Max = 215,43[MPa]$ $Min = 0,34[MPa]$	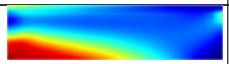 $Max = 222,11[MPa]$ $Min = 0,33[MPa]$	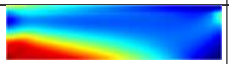 $Max = 222,11[MPa]$ $Min = 0,33[MPa]$	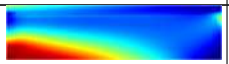 $Max = 213,10[MPa]$ $Min = 0,62[MPa]$	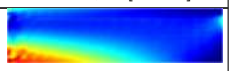 $Max = 213,32[MPa]$ $Min = 0,42[MPa]$
06	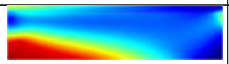 $Max = 221,14[MPa]$ $Min = 0,37[MPa]$	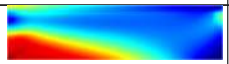 $Max = 228,91[MPa]$ $Min = 0,42[MPa]$	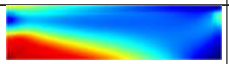 $Max = 228,91[MPa]$ $Min = 0,42[MPa]$	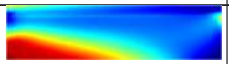 $Max = 220,98[MPa]$ $Min = 0,68[MPa]$	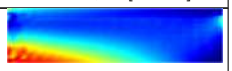 $Max = 217,87[MPa]$ $Min = 0,47[MPa]$
07	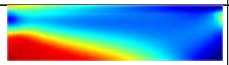 $Max = 228,98[MPa]$ $Min = 0,40[MPa]$	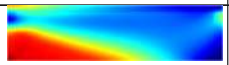 $Max = 238,68[MPa]$ $Min = 0,45[MPa]$	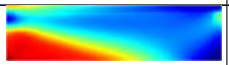 $Max = 238,91[MPa]$ $Min = 0,42[MPa]$	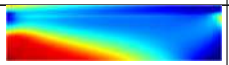 $Max = 228,26[MPa]$ $Min = 0,74[MPa]$	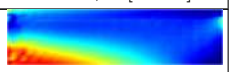 $Max = 226,29[MPa]$ $Min = 0,54[MPa]$
08	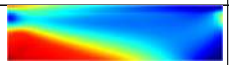 $Max = 239,55[MPa]$ $Min = 0,44[MPa]$	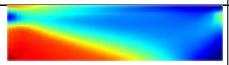 $Max = 251,23[MPa]$ $Min = 0,56[MPa]$	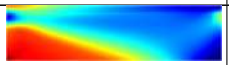 $Max = 251,23[MPa]$ $Min = 0,56[MPa]$	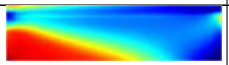 $Max = 240,88[MPa]$ $Min = 0,80[MPa]$	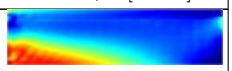 $Max = 233,59[MPa]$ $Min = 0,61[MPa]$
09	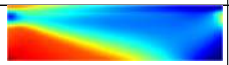 $Max = 253,97[MPa]$ $Min = 0,47[MPa]$	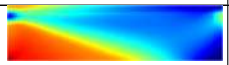 $Max = 272,40[MPa]$ $Min = 0,54[MPa]$	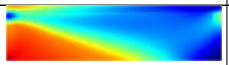 $Max = 272,40[MPa]$ $Min = 0,54[MPa]$	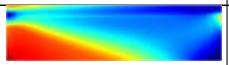 $Max = 256,58[MPa]$ $Min = 0,86[MPa]$	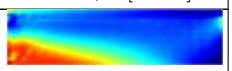 $Max = 242,38[MPa]$ $Min = 0,69[MPa]$
10	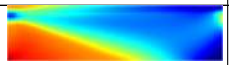 $Max = 275,52[MPa]$ $Min = 0,50[MPa]$	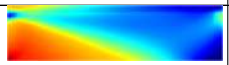 $Max = 297,96[MPa]$ $Min = 1,01[MPa]$	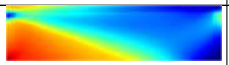 $Max = 297,96[MPa]$ $Min = 1,01[MPa]$	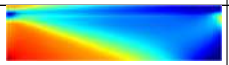 $Max = 280,88[MPa]$ $Min = 0,92[MPa]$	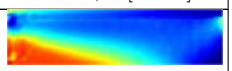 $Max = 250,86[MPa]$ $Min = 0,81[MPa]$
	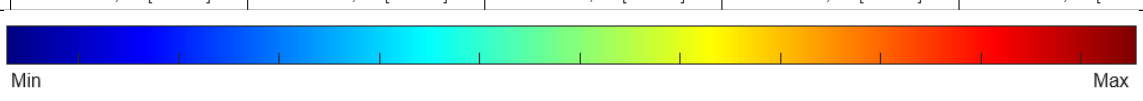				

By carefully observing table 6.65, we can notice that the NNRPIM (with a second degree of neighborhood) gives us, once again, a smaller area subjected to the higher

simulated stress values.

The table 6.66 shows us the plastic strain behavior resulting from the 2D simulations of the T-beam with b=400 mm.

Table 6.66: Plastic strain contour plot images resulted from the 2D T beam with b=400 [mm] simulations

	FEM	RPIM Constant	RPIM Linear	NNRPIM 1^{o} Order	NNRPIM 2^{o} Order
01					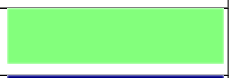
02					
03					
04					
05					
06		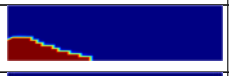	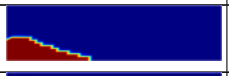		
07	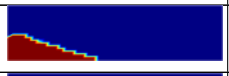	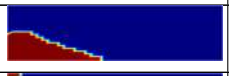		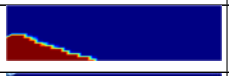	
08	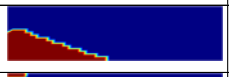	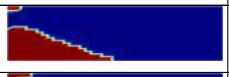	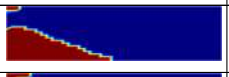	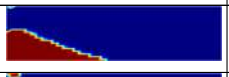	
09	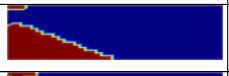	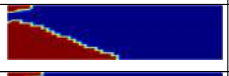	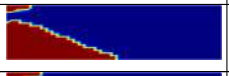	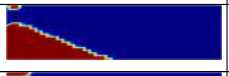	
10	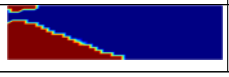	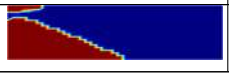	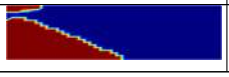	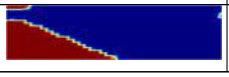	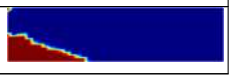

As has been the norm in this study, the NNRPIM (with a second degree of neighborhood) presents us with a smaller plastic deformation area than its respective counterparts.

The last table in the analysis, in these simulations in 2D, is the table 6.67 and it shows us the values and images from the total strain to the T beam with b=400 mm.

Table 6.67: Total strain contour plot images resulted from the 2D T-beam with b=400 [mm] simulations

	FEM	RPIM Constant	RPIM Linear	NNRPIM 1^{o} Order	NNRPIM 2^{o} Order
01	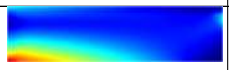	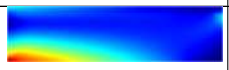	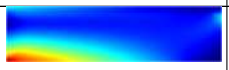	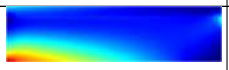	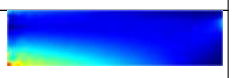
	$Max = 0,08[\%]$ $Min = 0,00[\%]$	$Max = 0,08[\%]$ $Min = 0,00[\%]$	$Max = 0,08[\%]$ $Min = 0,00[\%]$	$Max = 0,08[\%]$ $Min = 0,00[\%]$	$Max = 0,08[\%]$ $Min = 0,00[\%]$

Table 6.67 continued from previous page

	FEM	RPIM Constant	RPIM Linear	NNRPIM 1^{o} Order	NNRPIM 2^{o} Order
02	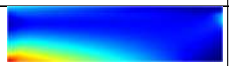 $Max = 0,10[\%]$ $Min = 0,00[\%]$	 $Max = 0,15[\%]$ $Min = 0,00[\%]$	 $Max = 0,15[\%]$ $Min = 0,00[\%]$	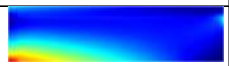 $Max = 0,10[\%]$ $Min = 0,00[\%]$	 $Max = 0,10[\%]$ $Min = 0,00[\%]$
03	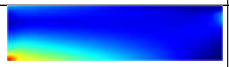 $Max = 0,14[\%]$ $Min = 0,00[\%]$	 $Max = 0,18[\%]$ $Min = 0,00[\%]$	 $Max = 0,18[\%]$ $Min = 0,00[\%]$	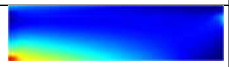 $Max = 0,13[\%]$ $Min = 0,00[\%]$	 $Max = 0,12[\%]$ $Min = 0,00[\%]$
04	 $Max = 0,17[\%]$ $Min = 0,00[\%]$	 $Max = 0,22[\%]$ $Min = 0,00[\%]$	 $Max = 0,22[\%]$ $Min = 0,00[\%]$	 $Max = 0,17[\%]$ $Min = 0,00[\%]$	 $Max = 0,15[\%]$ $Min = 0,00[\%]$
05	 $Max = 0,20[\%]$ $Min = 0,00[\%]$	 $Max = 0,27[\%]$ $Min = 0,00[\%]$	 $Max = 0,27[\%]$ $Min = 0,00[\%]$	 $Max = 0,20[\%]$ $Min = 0,00[\%]$	 $Max = 0,19[\%]$ $Min = 0,00[\%]$
06	 $Max = 0,25[\%]$ $Min = 0,00[\%]$	 $Max = 0,32[\%]$ $Min = 0,00[\%]$	 $Max = 0,32[\%]$ $Min = 0,00[\%]$	 $Max = 0,25[\%]$ $Min = 0,00[\%]$	 $Max = 0,24[\%]$ $Min = 0,00[\%]$
07	 $Max = 0,30[\%]$ $Min = 0,00[\%]$	 $Max = 0,40[\%]$ $Min = 0,00[\%]$	 $Max = 0,40[\%]$ $Min = 0,00[\%]$	 $Max = 0,31[\%]$ $Min = 0,00[\%]$	 $Max = 0,28[\%]$ $Min = 0,00[\%]$
08	 $Max = 0,38[\%]$ $Min = 0,00[\%]$	 $Max = 0,51[\%]$ $Min = 0,00[\%]$	 $Max = 0,51[\%]$ $Min = 0,00[\%]$	 $Max = 0,40[\%]$ $Min = 0,00[\%]$	 $Max = 0,33[\%]$ $Min = 0,00[\%]$
09	 $Max = 0,49[\%]$ $Min = 0,00[\%]$	 $Max = 0,67[\%]$ $Min = 0,00[\%]$	 $Max = 0,67[\%]$ $Min = 0,00[\%]$	 $Max = 0,53[\%]$ $Min = 0,00[\%]$	 $Max = 0,39[\%]$ $Min = 0,00[\%]$
10	 $Max = 0,65[\%]$ $Min = 0,00[\%]$	 $Max = 0,89[\%]$ $Min = 0,00[\%]$	 $Max = 0,89[\%]$ $Min = 0,00[\%]$	 $Max = 0,70[\%]$ $Min = 0,00[\%]$	 $Max = 0,45[\%]$ $Min = 0,00[\%]$
	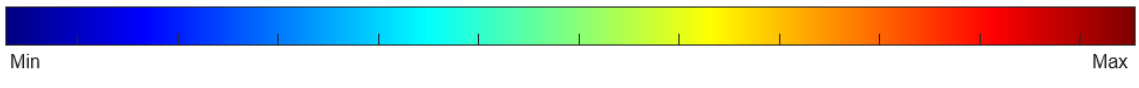 Min Max				

To end the T beam with b=400 mm contour plot image observation and analysis, we can examine table 6.67, where it is noticeable that the NNRPIM (with a second degree of neighborhood) presents us with a shorter area subjected to the higher simulated strain values. Table 6.68 presents the percentual values of the result's difference between the standard and the non-standard simulation methods.

Table 6.68: Percentual strain's difference for the meshless methods simulations compared with the FEM simulation, for the 2D T-beam with b=400 [mm]

Increment	RPIM Const.	RPIM Linear	NNRPIM 1º	NNRPIM 2º
01	0.00%	0.00%	0.00%	0.00%
02	50.00%	50.00%	0.00%	0.00%
03	28.57%	28.57%	7.14%	14.29%
04	29.41%	29.41%	0.00%	11.76%
05	35.00%	35.00%	0.00%	5.00%
06	28.00%	28.00%	0.00%	4.00%
07	33.33%	33.33%	3.33%	6.67%
08	34.21%	34.21%	5.26%	13.16%
09	37.96%	36.73%	8.16%	20.41%
10	36.92%	36.92%	7.69%	30.77%

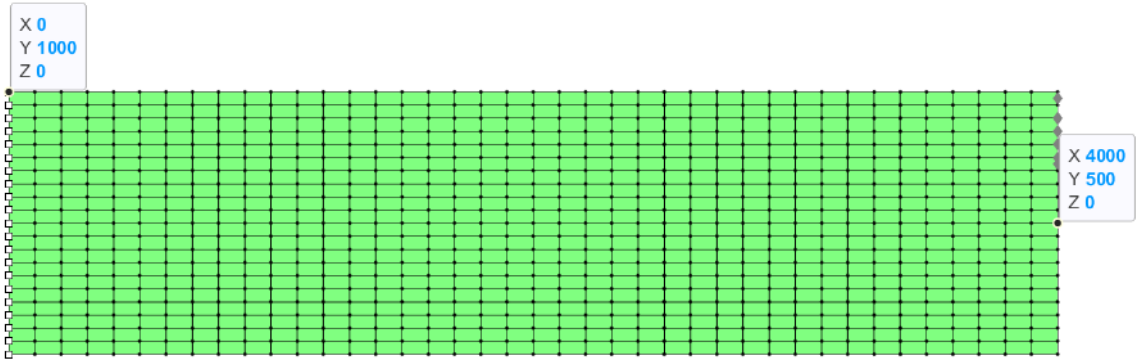

Figure 6.40: Points of location on the 2D I-plate

6.5 Comparative 2D and 3D Analysis

After a careful analysis of the previous subchapter, we are ready to compare the 2D results with the 3D across the different types of simulated sections. Let's start with the I plate comparison. To compare the 2D and 3D simulations, we will analyze the stress, strain, and plastic strain from point A and the deflection of point B. Point A is the top fixed point with the 3D coordinates (0, 0, 1000) and the 2D coordinates (0, 1000), where it is expected to visualize the max stress, strain, and plastic strain. Point B is the midpoint of the section opposite to the fixed section where the displacement is bigger, with the 3D coordinates of (0, 4000, 500) and the 2D coordinates (4000, 500). These points' locations can be seen in the figure 6.40 and 6.41.

6.5.1 I-Plate

The figures 6.42 and 6.43 show the respective force versus stress graphics from the 2D and 3D I-plates simulations, in point A, where it is easy to observe the different behavior from the 5 different simulations for the 2D and 3D studies. It is possible to visualize the similar results produced by all the 2D simulations in the graphic

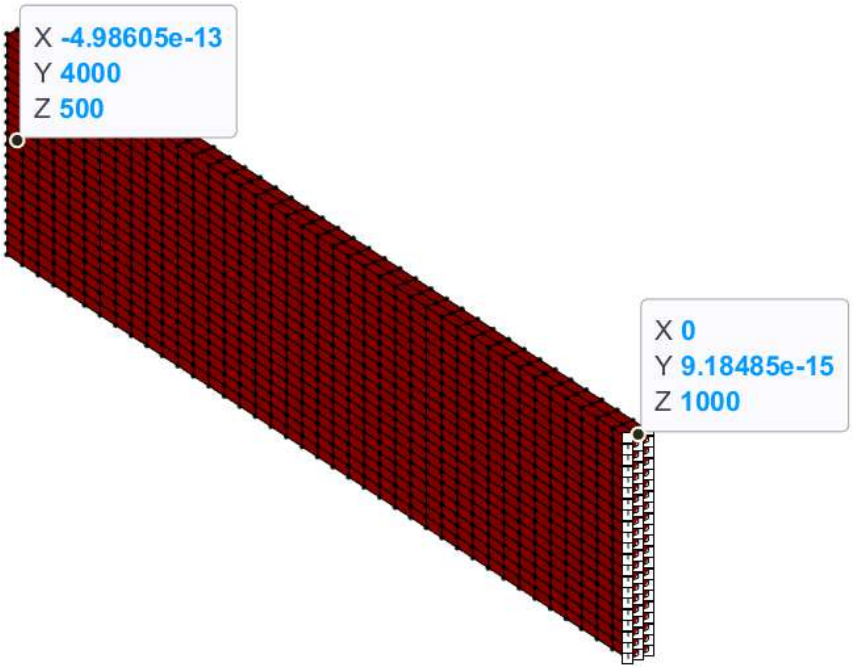

Figure 6.41: Points of location on the 3D I-plate

from the figure 6.42. The graphic in question shows us that the simulations almost completely overlap each other, with the biggest visible difference being that the RPIM simulations (with NNRPIM parameters) present higher values of stress and force. Despite the large values, the curve elaborated by all the involved simulations presents no significant difference. Analyzing now the figure 6.43, which contains the force vs stress graphic from the 3D simulations, at point A, it is very clear that the curve behavior is, in general, very different from the 2D simulation. The RPIM simulations present a curve very different, in behavioral terms, from the rest of the 3D simulations, but with more observable resemblances to the 2D simulations. Another visual conclusion is the fact that the 3D RPIM simulations with NNRPIM parameters give us higher force and stress values, just like in the 2D simulations. It's important to highlight that when a simulation gives us a greater force than another one, it's just an indicator that the yield force is bigger, and therefore, according to the simulated method results, the plate can hold more load without entering a state of plasticity.

By analyzing figure 6.44, we can observe the overlapping of the different 2D and 3D force versus stress curves from all the simulations, in point A of the I-plate. As it is possible to observe in the graphic in question, the 3D simulations produce slightly higger force values than the respective counterparts simulations in 2D, and in the inverse way, the stress values are slightly lower. In all the overlapping graphics presented in this subchapter, it will be possible to observe the RPIM simulations with the RPIM parameters, and in this way, with the help of visual aids, understand the reason for this study's dismissal.

Analyzing now the strain with the graphics in the figures 6.45 and 6.46 for the graphics force versus strain in 2D and 3D respectively is possible to observe that the

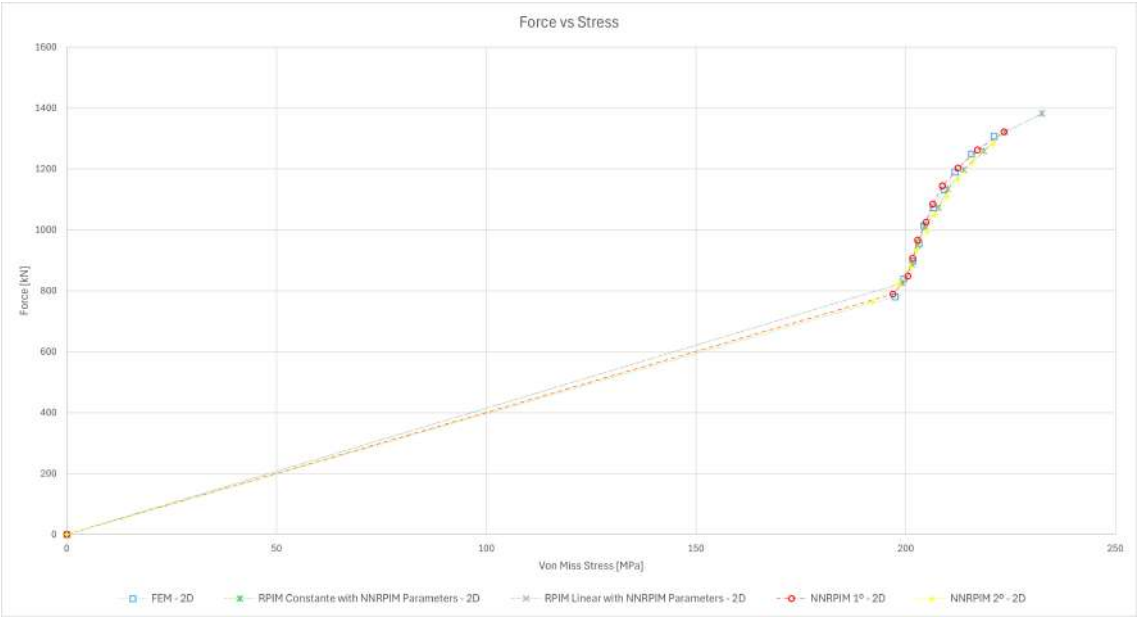

Figure 6.42: Graphic Force versus Stress of the I-plate's 2D simulations in point A

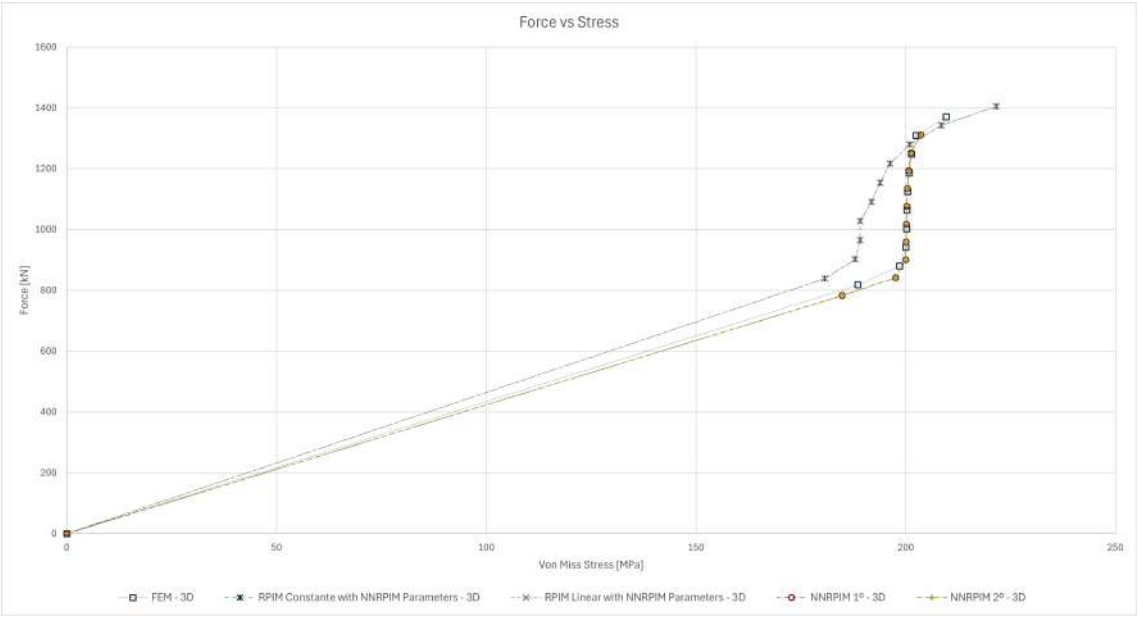

Figure 6.43: Graphic Force versus Stress of the I-plate's 3D simulations in point A

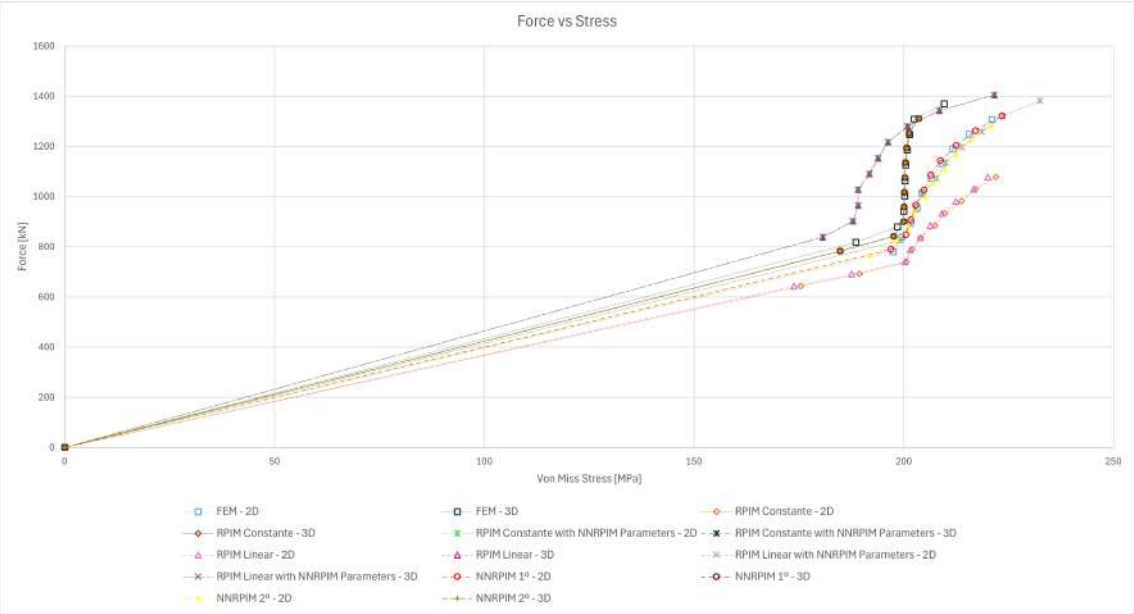

Figure 6.44: Graphic Force versus Stress of the I-plate's simulations in point A

curves involve are relatively close to each other, with the exception of the RPIM, with linear base, simulation with NNRPIM parameters, that has a step behavior and not a curve, in the 3D results. This step behavior tends to happen due to numerical problems and higher concentrated shear stress.

When the 2 graphics overlap each other, just like in the figure 6.47, it is possible to see that the strain values are considerably bigger in the 3D simulations than the respective counterparts in the 2D simulations. In this overlapping graphic figure, the discrepancy between the 2D RPIM studies with the normal RPIM parameters compared to all the others simulations.

Finally, to conclude the point A analysis, we will observe the plastic strain of the present point. The graphics existing in images 6.48 and 6.49 are the 2D and 3D representations of the respective simulations. The simulation's behavior, in regards to the plastic strain conduct, is extremely similar on an optical level, and that means that the plastic strain in question has a well-defined curve behaviour, while the 3D results present a similar step behaviour, in the same simulations, compared to the strain study.

The figure 6.50 presents us with the overlapping 2D and 3D graphics with the RPIM (with RPIM parameters) simulations added. By analysing the image, it's possible to conclude that in point A, the plastic strain is bigger in the 3D results than in the 2D, just like in the strain examination, as expected.

To finalize now the I-plate study, we will observe and study the results for the displacement in point B. By comparing the figures 6.51 and 6.52, which are the graphics for the 2D simulations and the 3D simulations, it's evident that the 3D simulations present slightly higher values of displacement.

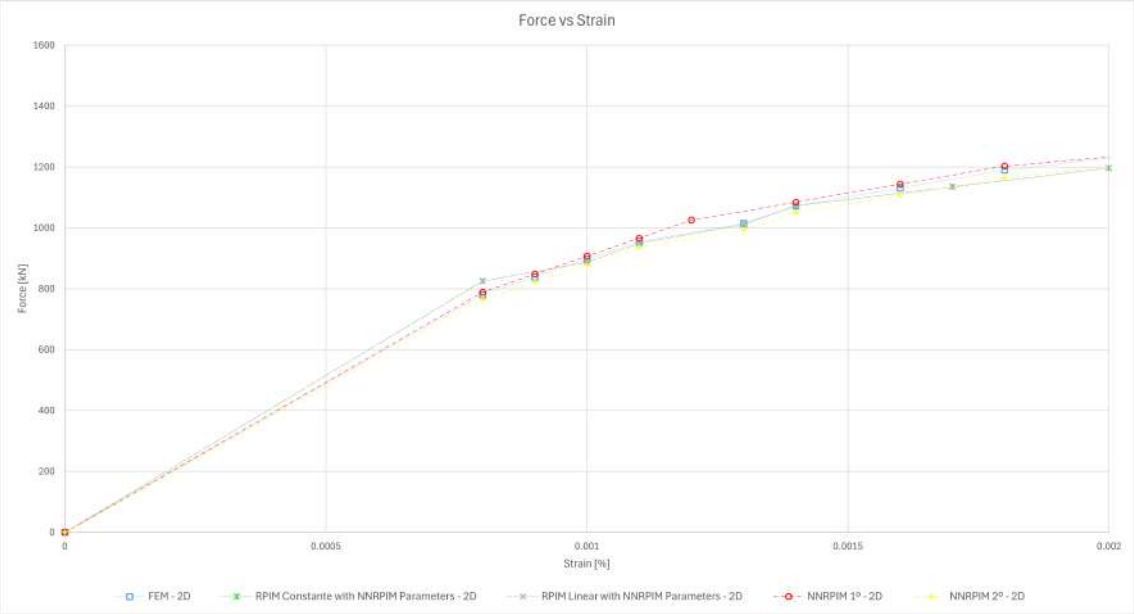

Figure 6.45: Graphic Force versus Strain of the I-plate's 2D simulations in point A

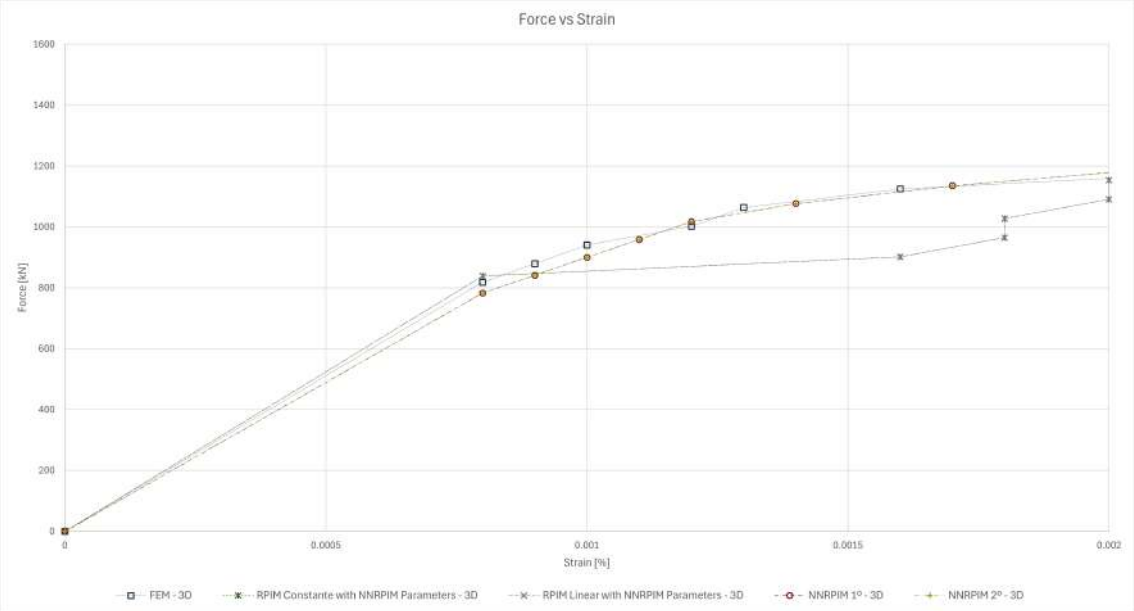

Figure 6.46: Graphic Force versus Strain of the I-plate's 3D simulations in point A

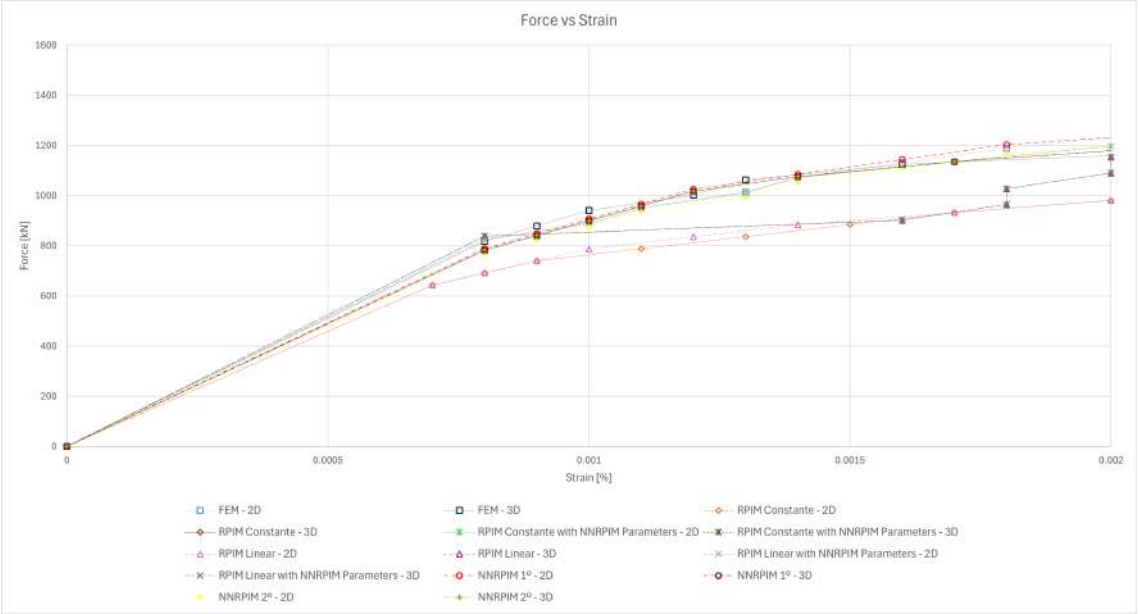

Figure 6.47: Graphic Force versus Strain of the I-plate's simulations in point A

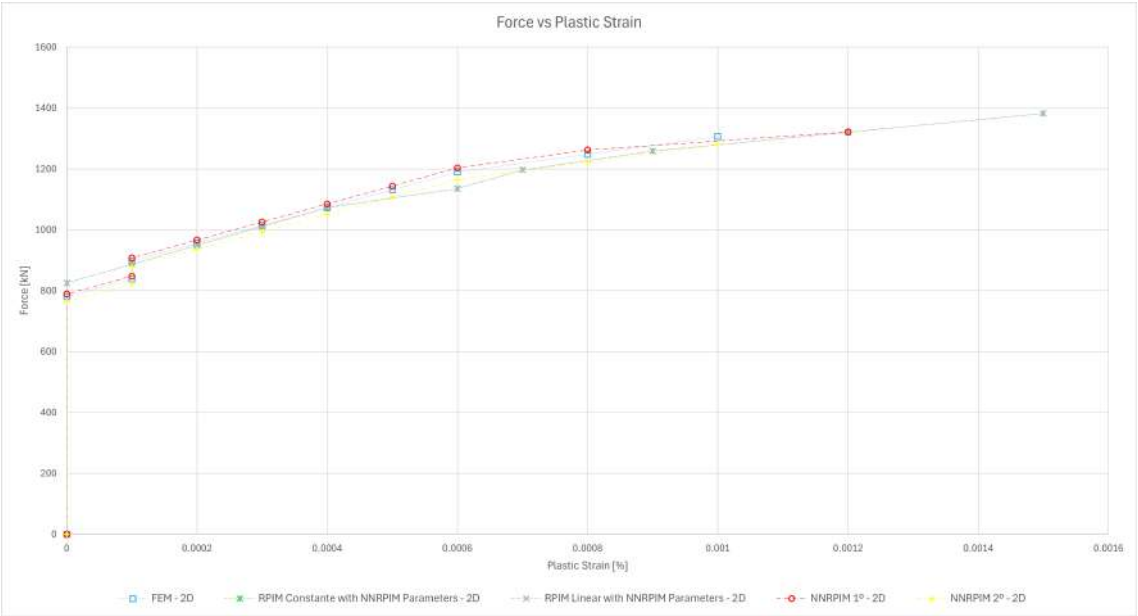

Figure 6.48: Graphic Force versus Plastic Strain of the I-plate's 2D simulations in point A

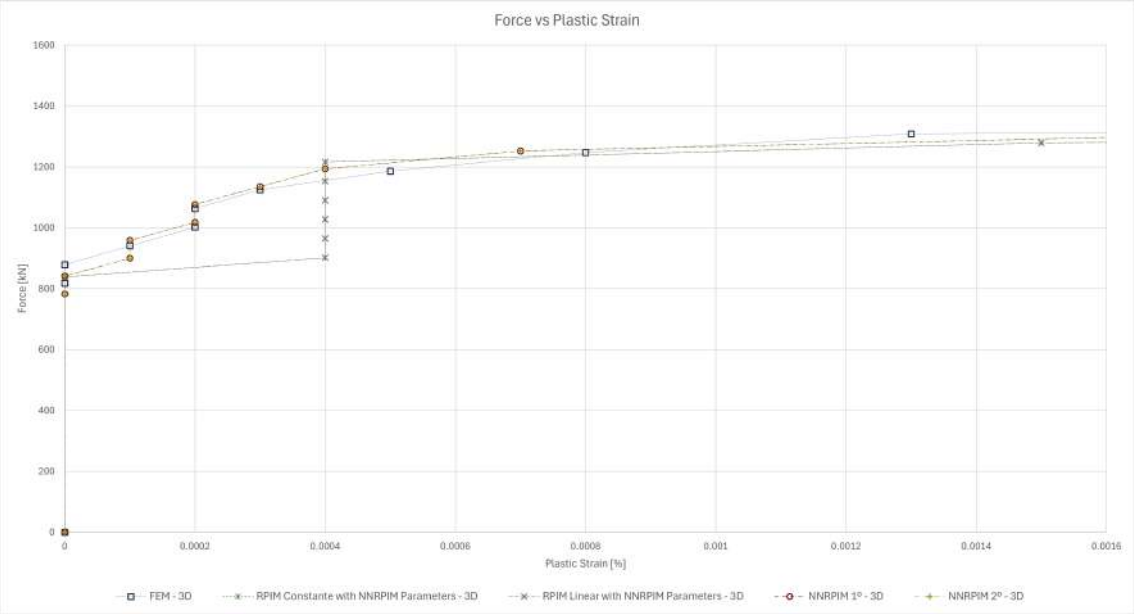

Figure 6.49: Graphic Force versus Plastic Strain of the I-plate's 3D simulations in point A

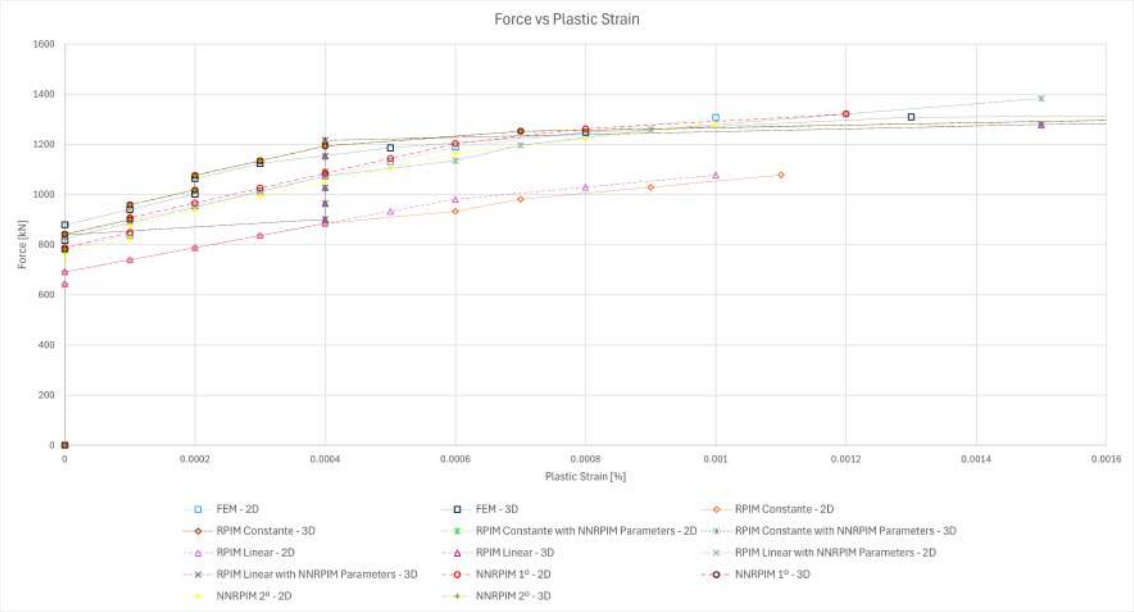

Figure 6.50: Graphic Force versus Plastic Strain of the I-plate's simulations in point A

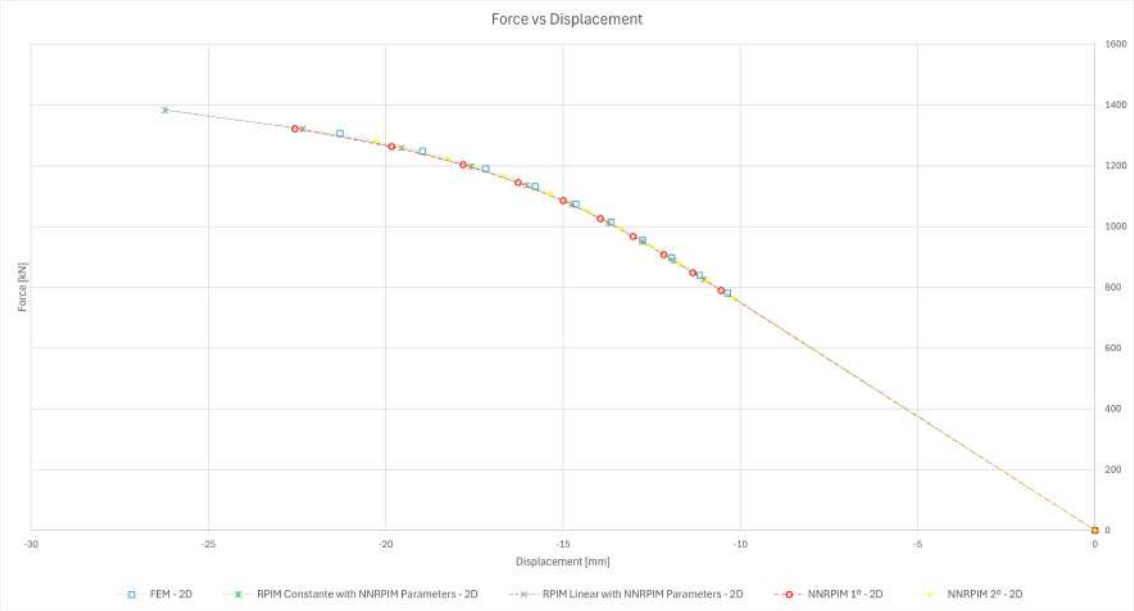

Figure 6.51: Graphic Force versus Displacement of the I-plate's 2D simulations in point B

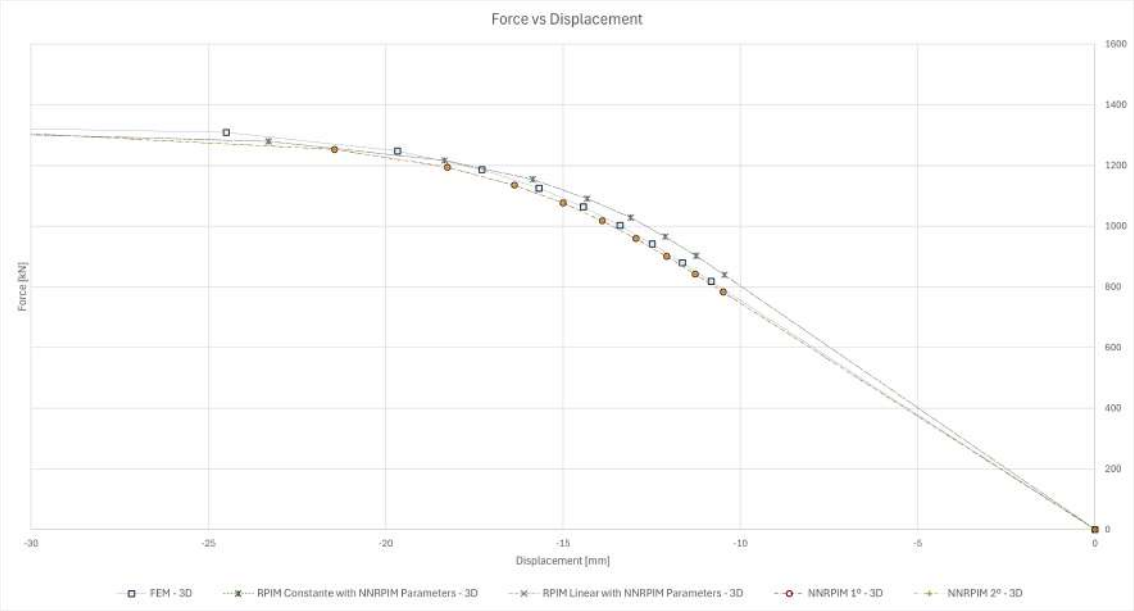

Figure 6.52: Graphic Force versus Displacement of the I-plate's 3D simulations in point B

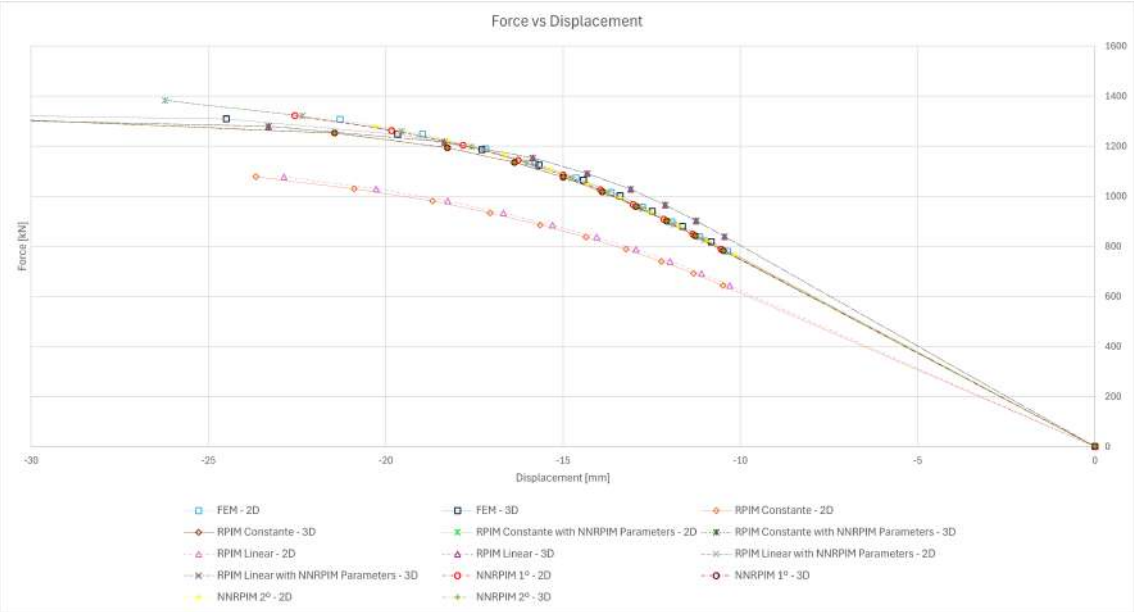

Figure 6.53: Graphic Force versus Displacement of the I-plate's simulations in point B

Table 6.69: Percentual force difference for the I-plate 2D and 3D results

Increment	FEM	RPIM Const.	RPIM Linear	NNRPIM 1º	NNRPIM 2º
01	4.61%	1.61%	1.61%	0.79%	2.41%
02	4.61%	1.62%	1.62%	0.79%	2.41%
03	4.61%	1.62%	1.61%	0.79%	2.41%
04	4.61%	1.61%	1.61%	0.80%	2.41%
05	4.62%	1.60%	1.60%	0.79%	2.41%
06	4.61%	1.61%	1.61%	0.79%	2.41%
07	4.61%	1.61%	1.61%	0.80%	2.41%
08	4.61%	1.61%	1.61%	0.80%	2.40%
09	4.61%	1.61%	1.61%	0.80%	2.40%
10	4.61%	1.61%	1.61%	0.79%	2.40%

In the figure 6.53 we can see the overlapping from the 2D and 3D graphics, where it's possible to see the different displacement and force values from the RPIM simulations with RPIM parameters, and it is possible to verify that even with the slightly higher 3D values, the overlapping is undeniable.

In tables 6.69, 6.70 and, 6.71 show us the percentual difference between the 3D and 2D results of force, stress in point A, and strain in point A, respectively, this values were previously examined in subchapters 6.3.1 and 6.4.1.

In these tables, we can observe that the percentual difference between the 2D and 3D results remains roughly stable between iterations, with the NNRPIM method of first order showing the lowest difference indicating a very precise approximation between the 2D and 3D results, while the FEM method as gives us the biggest

Table 6.70: Percentual stress difference for the I plate 2D and 3D results

Increment	FEM	RPIM Const.	RPIM Linear	NNRPIM 1º	NNRPIM 2º
01	2.98%	2.21%	2.21%	3.79%	1.28%
02	0.16%	0.58%	0.77%	0.39%	0.69%
03	0.69%	1.14%	1.14%	0.75%	0.49%
04	1.30%	1.67%	1.67%	1.22%	1.12%
05	1.90%	3.05%	3.05%	2.15%	2.27%
06	2.80%	4.11%	4.11%	2.92%	3.14%
07	3.99%	4.92%	4.92%	3.92%	4.41%
08	4.86%	5.75%	5.75%	5.48%	5.48%
09	6.12%	3.48%	3.48%	7.27%	6.72%
10	5.13%	0.64%	0.64%	8.85%	7.76%

Table 6.71: Percentual strain difference for the I plate 2D and 3D results

Increment	FEM	RPIM Const.	RPIM Linear	NNRPIM 1º	NNRPIM 2º
01	0.00%	0.00%	0.00%	0.00%	0.00%
02	0.00%	75.61%	75.61%	0.00%	0.00%
03	44.44%	74.42%	74.42%	9.09%	0.00%
04	38.89%	71.11%	71.11%	15.38%	0.00%
05	31.58%	69.57%	69.57%	14.29%	0.00%
06	30.00%	80.23%	80.23%	6.67%	0.00%
07	36.00%	80.00%	80.00%	5.88%	0.00%
08	51.35%	82.84%	82.84%	18.18%	0.00%
09	54.35%	90.31%	90.31%	33.33%	0.00%
10	85.47%	90.68%	90.68%	59.70%	0.00%

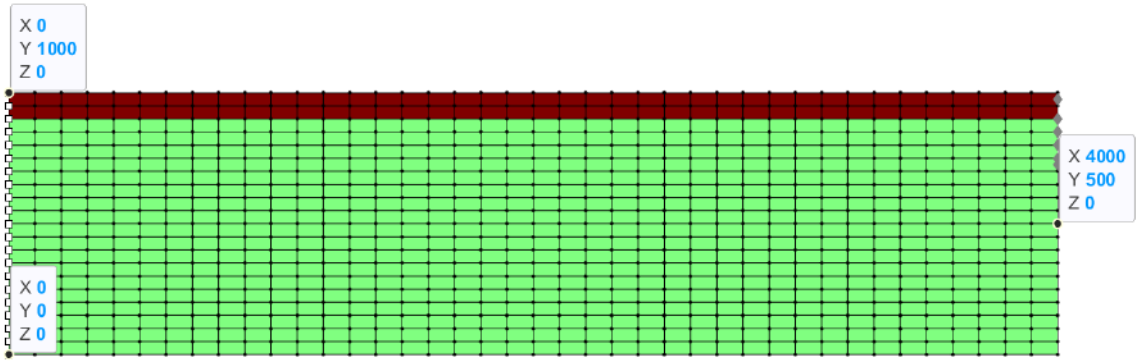

Figure 6.54: Points' location on the 2D T-beams

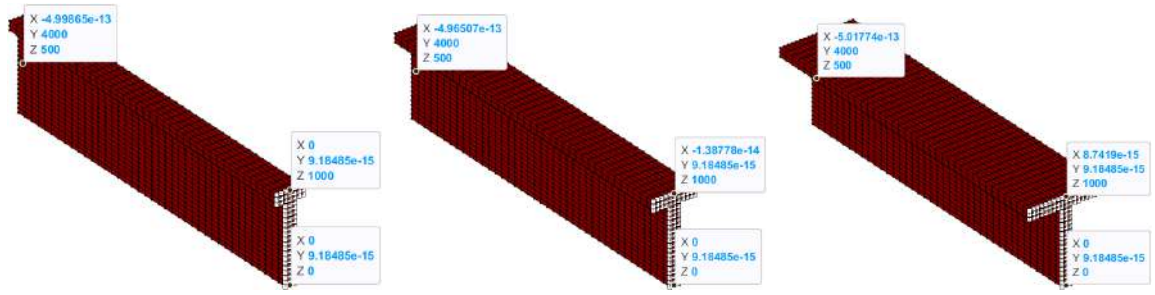

Figure 6.55: Points' location on the 3D T-beams, from left to right, T-beam with b=100 [mm], T-beam with b=200 [mm], and T-beam with b=400 [mm]

difference between the used methods, indicating a slightly higher discrepancy between the 2D and the 3D results. The stress values present us with more instability between iterations with the NNRPIM and FEM methods', giving us more linear behaviors in the RPIM methods, with a more unpredictable percentage value. The strain percentual values are much higher, and therefore give us a greater deviation for all the methods except one, the NNRPIM of the second order ended up giving us a striking null percentual value.

6.5.2 T-Beams

To analyze the T-beams we will study 3 points, being, points A, B, and C, where point A is located at the (0, 0, 1000) coordinate for the 3D studies and (0, 1000) to the 2D studies, point B at the (0, 0, 0) and (0, 0) to the 3D and 2D studies respectively, and finally point C located at (0, 500, 4000) to the 3D studies and (500, 4000) to the 2D studies. Figures 6.54 and 6.55 show us the 2D and 3D points locations, respectively.

T-Beam with b=100 [mm]

Let's start by analyzing point A. If we look at figures 6.56 and 6.57, we can observe the force versus stress graphs from the 2D and 3D simulations, respectively. In all simulations, the curves exhibit the same behavior, indicating that there are no significant discrepancies between the results presented. This consistency suggests that both the 2D and 3D models are capturing the mechanical response at point A

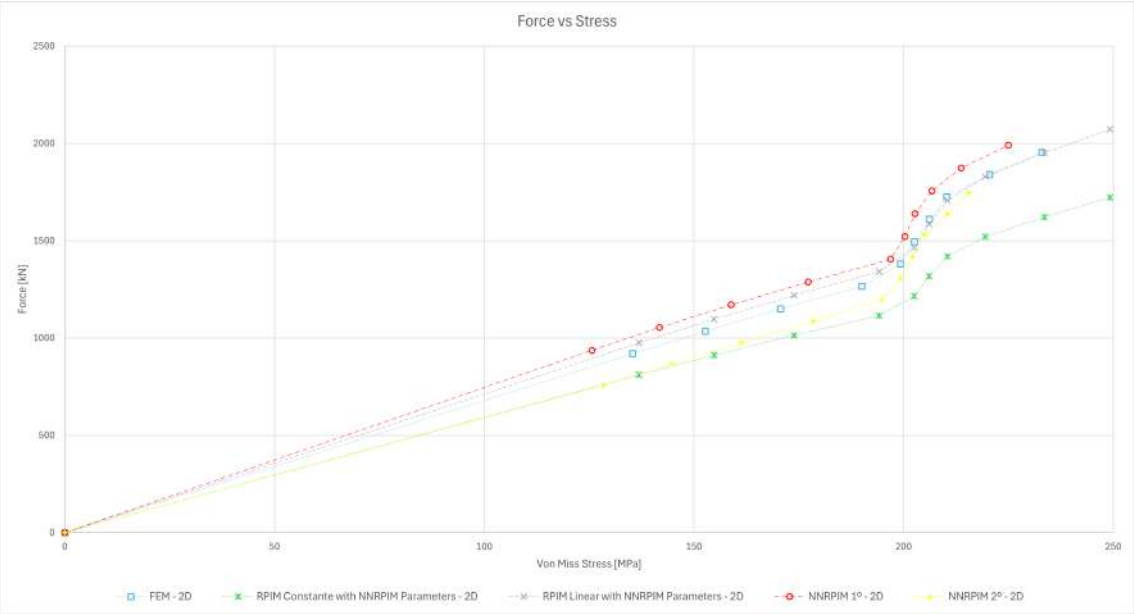

Figure 6.56: Graphic Force vs Stress of the T-beam with b=100 [mm] from 2D simulations in point A

in a similar manner, thereby validating the reliability of the simulation approaches for this specific point. The most notable difference is the fact that the 3D RPIM simulations presented us with a slightly inferior curve, as is possible to observe in figure 6.57.

It is clear that the results from the simulations are very similar, as can be observed in figure 6.58 by the overlapping of the 2D and 3D graphs. As shown in previous simulations, the 3D models yield slightly higher force values but slightly lower stress values compared to the 2D models. It is also interesting to note the difference between the 3D RPIM simulations (with specific RPIM parameters) and all the other simulations. By examining the overlapping graphs, it is evident that these particular 3D simulations exhibit significantly lower values, making them unreliable.

Turning our attention to figures 6.59 and 6.60, we observe the 2D and 3D plots of force versus strain at point A. Once again, the results are highly consistent across the simulations, with both the numerical values and the overall curve behavior showing no significant differences.

The next graphic, shown in figure 6.61 presents an overlap of the 2D and 3D simulation results previously displayed in figures 6.59 and 6.60. The comparison reveals that the 2D and 3D simulations exhibit a very close match. In contrast, all RRPIM simulations (using RPIM parameters) yield noticeably lower strain by force values than the aforementioned simulations. Notably, the 3D RPIM simulations (with RPIM parameters) are highly disproportionate, displaying extremely low values in comparison to the other cases.

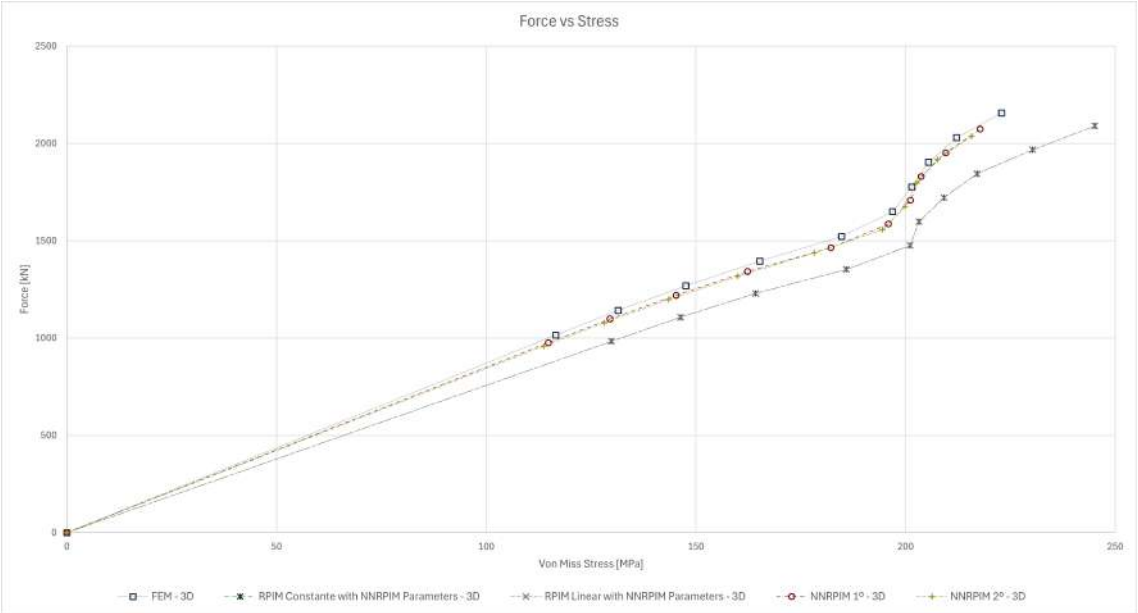

Figure 6.57: Graphic Force versus Stress of the T-beam with b=100 [mm] from 3D simulations in point A

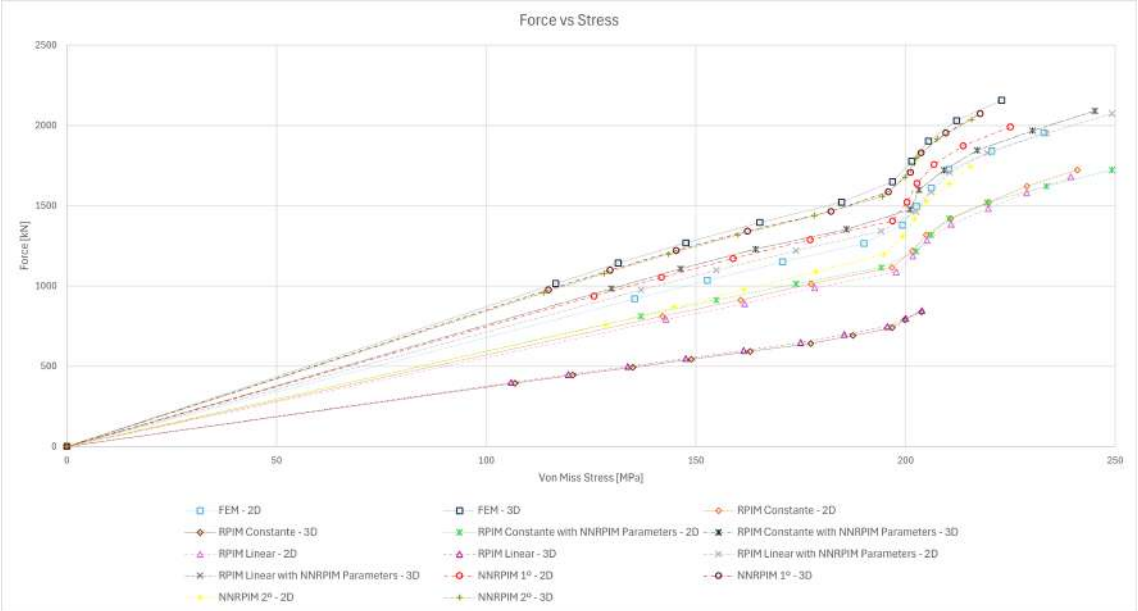

Figure 6.58: Graphic Force versus Stress of the T-beam with b=100 [mm] from simulations in point A

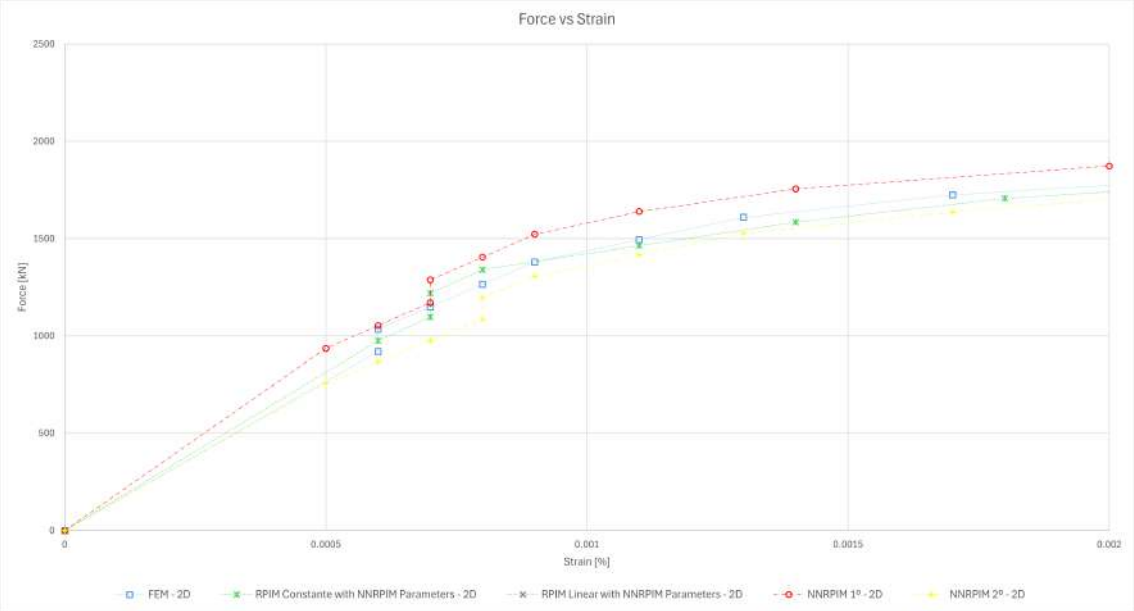

Figure 6.59: Graphic Force versus Strain of the T-beam with b=100 [mm] from 2D simulations in point A

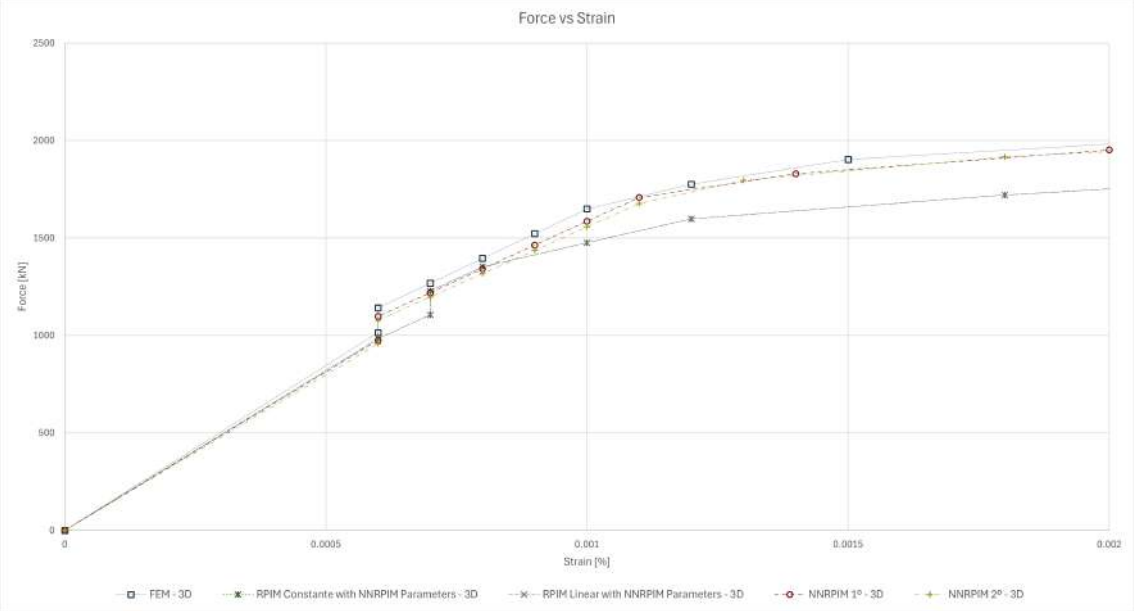

Figure 6.60: Graphic Force vs Strain of the T-beam with b=100 [mm] from 3D simulations in point A

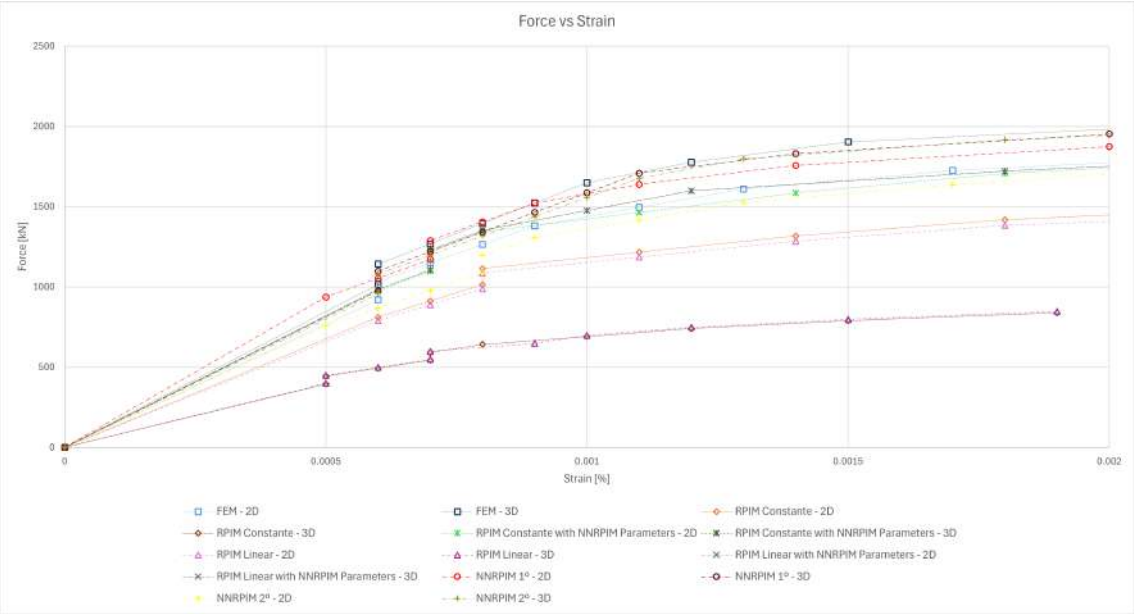

Figure 6.61: Graphic Force vs Strain of the T-beam with b=100 [mm] from simulations in point A

Finally, to conclude the analysis of point A, we examine the force versus plastic strain relationship. In figures 6.62 and 6.63, the force versus plastic strain values for the two-dimensional and three-dimensional cases are presented, respectively. Similar to the force versus strain results, it can be observed that the simulations for both dimensions closely match at the same point, further validating the consistency of the results.

Diverting our attention now to figure 6.64, which shows us the overlapping graphic present in figures 6.62 and 6.63, we can just like in the strain analysis, observe that the 2D and 3D simulations present behaviors closely match, with the RPIM (with RPIM parameters) being the already normal exception, with values lower comparatively to the other simulations, and in the 3D case, these values are very low in comparison.

Let's now move on to the point B analyses. If we look at figures 6.65 and 6.66, we can observe the force versus stress graphics from the 2D and 3D simulations, respectively. In all the simulations, the curves present the same behavior, which means that there are no relevant discrepancies between the presented results.

It's clear that the results from the simulations are very similar, which can be observed in figure 6.67 with the overlapping of the 2D and 3D graphics. As the previous simulations show us, the 3D results present us with slightly higher force values but slightly lower stress values. It is also interesting to realize the difference between the 3D RPIM simulations (with RPIM parameters) and all the other simulations. By looking at the overlapping graphic, it is clear that the 3D simulations in question present us with very low values, but funnily enough, with a higher stiffness.

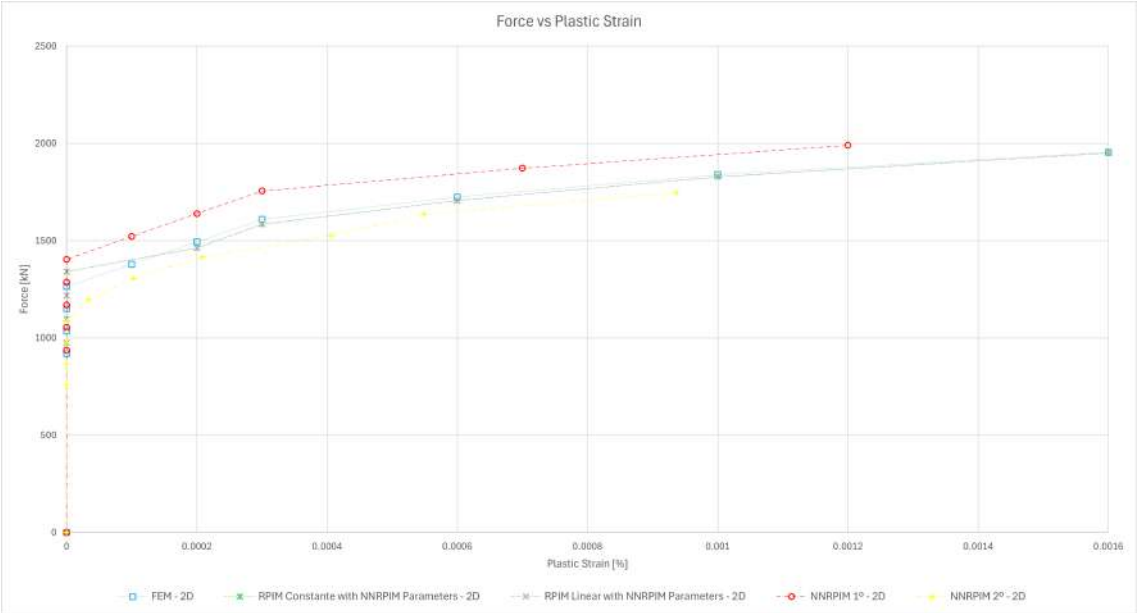

Figure 6.62: Graphic Force versus Plastic Strain of the T-beam with b=100 [mm] from 2D simulations in point A

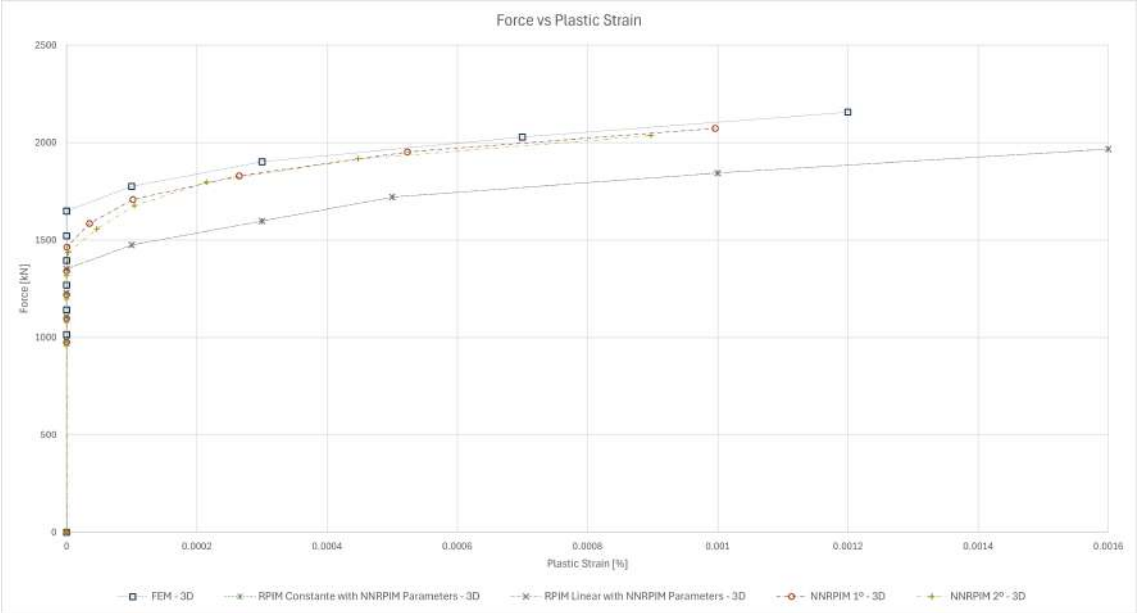

Figure 6.63: Graphic Force versus Plastic Strain of the T-beam with b=100 [mm] from 3D simulations in point A

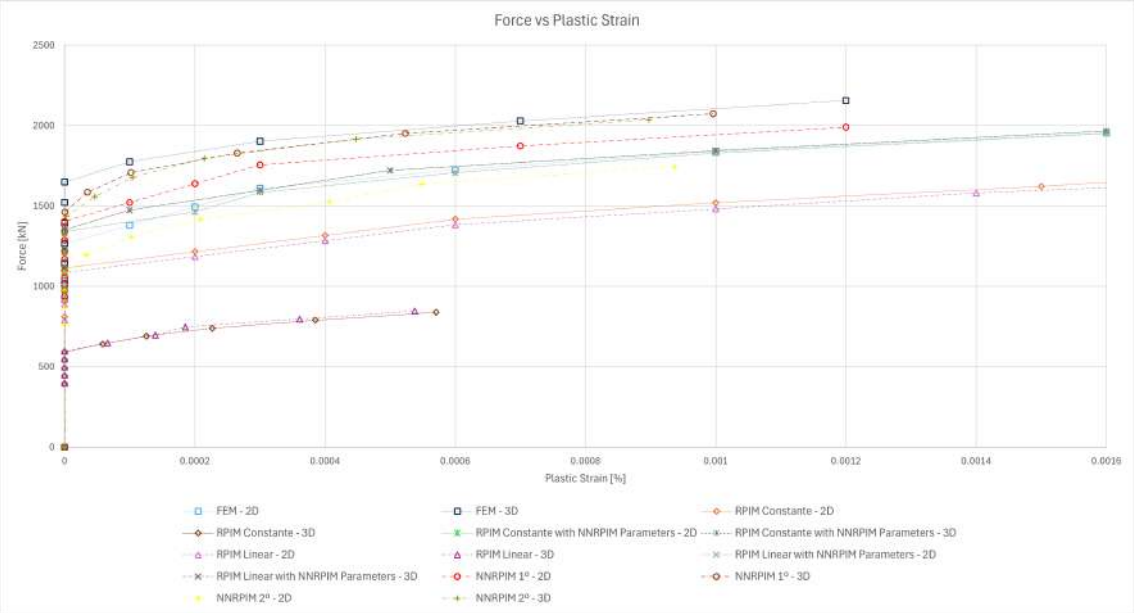

Figure 6.64: Graphic Force versus Plastic Strain of the T-beam with b=100 [mm] from simulations in point A

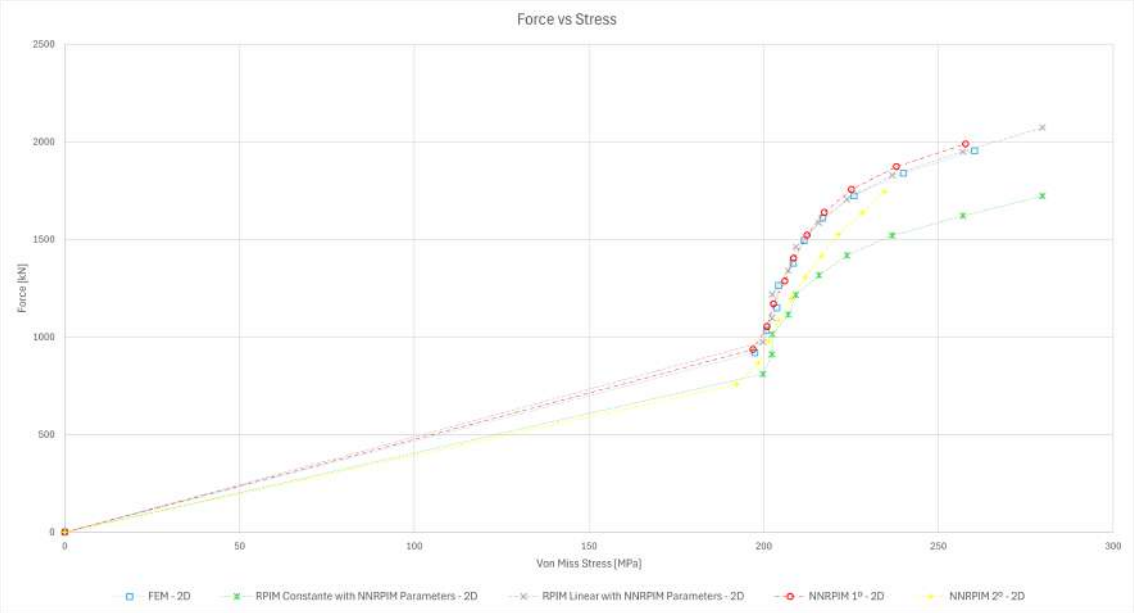

Figure 6.65: Graphic Force versus Stress of the T-beam with b=100 [mm] from 2D simulations in point B

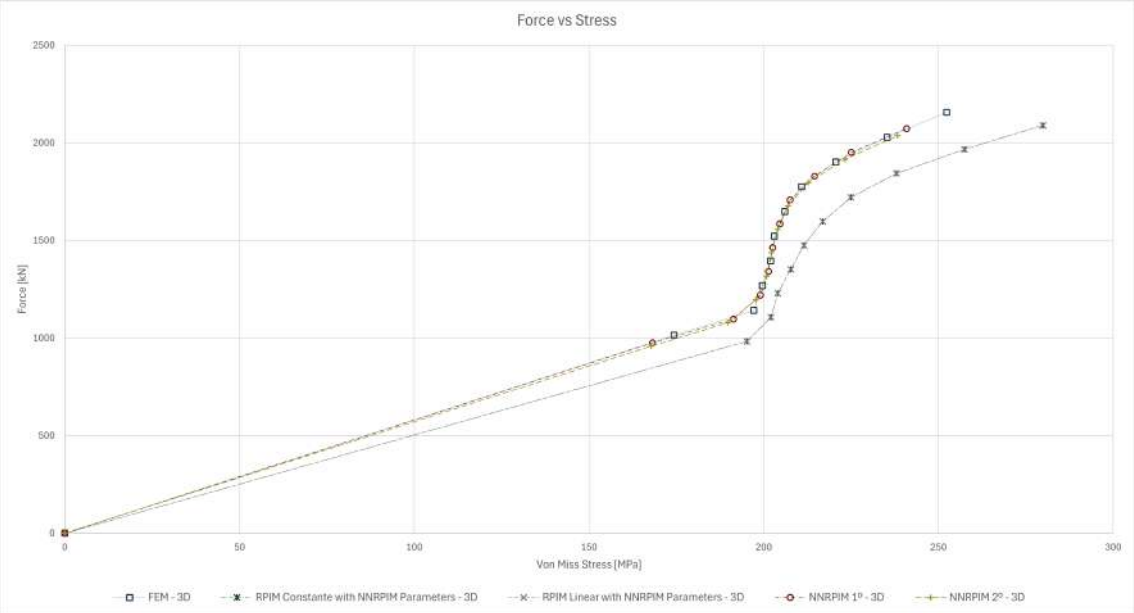

Figure 6.66: Graphic Force versus Stress of the T-beam with b=100 [mm] from 3D simulations in point B

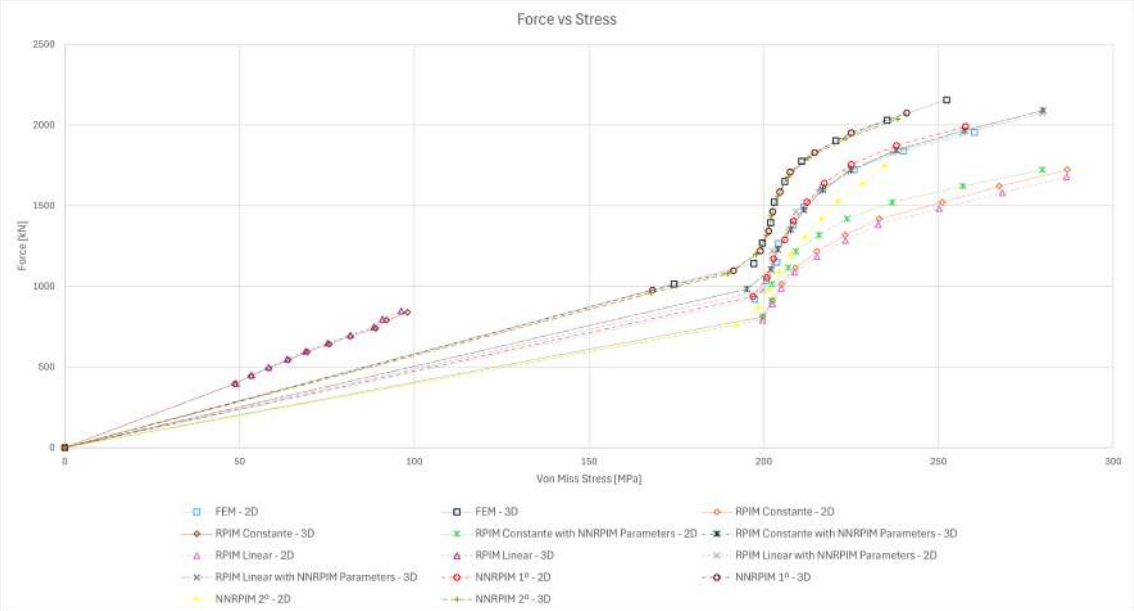

Figure 6.67: Graphic Force versus Stress of the T-beam with b=100 [mm] from simulations in point B

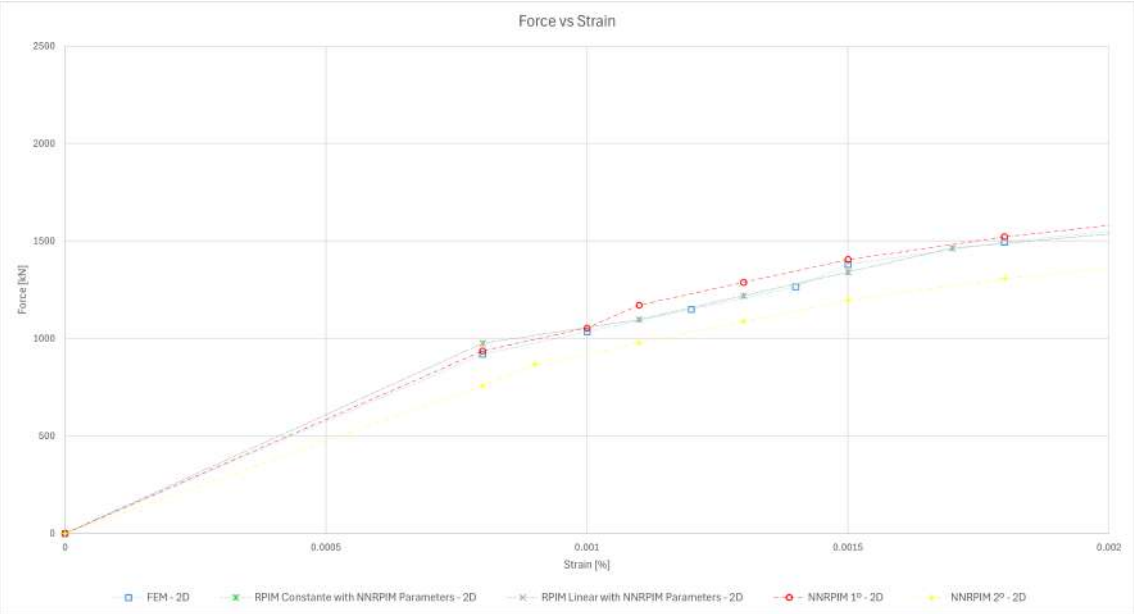

Figure 6.68: Graphic Force versus Strain of the T-beam with b=100 [mm] from 2D simulations in point B

If we move our attention to figures 6.68 and 6.69 we can observe the 2D and 3D graphics for the force versus strain, on point B. Once again, the results presented are very similar between simulations. The values and curve behavior presented show no relevant difference.

The next graphic can be observed in figure 6.70. This graphic is the overlapping graphic between the 2D and 3D simulations previously shown in figure 6.68 and 6.69. The considered 2D and 3D simulations present a very close match. On the other hand, all the RRPIM simulations (with RPIM parameters) present us with values lower in terms of strain by force than the considered simulations. The 3D RPIM simulations (with RPIM parameters) are completely disproportional and have extremely low values in comparison.

Finally, to end the point B analysis, we need to analyze the force versus plastic strain. In figures 6.71 and 6.72, we can observe the force versus plastic strain graphic from 2 dimensions and 3 dimensions, respectively. Just like in the force versus strain, for the same point, it is possible to conclude that the simulations very closely match.

Diverting our attention now to figure 6.73, which shows us the overlapping graphic present in figures 6.71 and 6.72. We can, just like in the strain analysis, observe that the 2D and 3D simulations present behaviors that closely match. With the RPIM (with RPIM parameters) being the already normal exception, with values lower compared to the other simulations. In the 3D case, these values are much lower in comparison.

To finalize the T-beam with b=100 mm study, let's divert our attention to point C, where the study will be about the displacement presented. Figure 6.74 shows us the

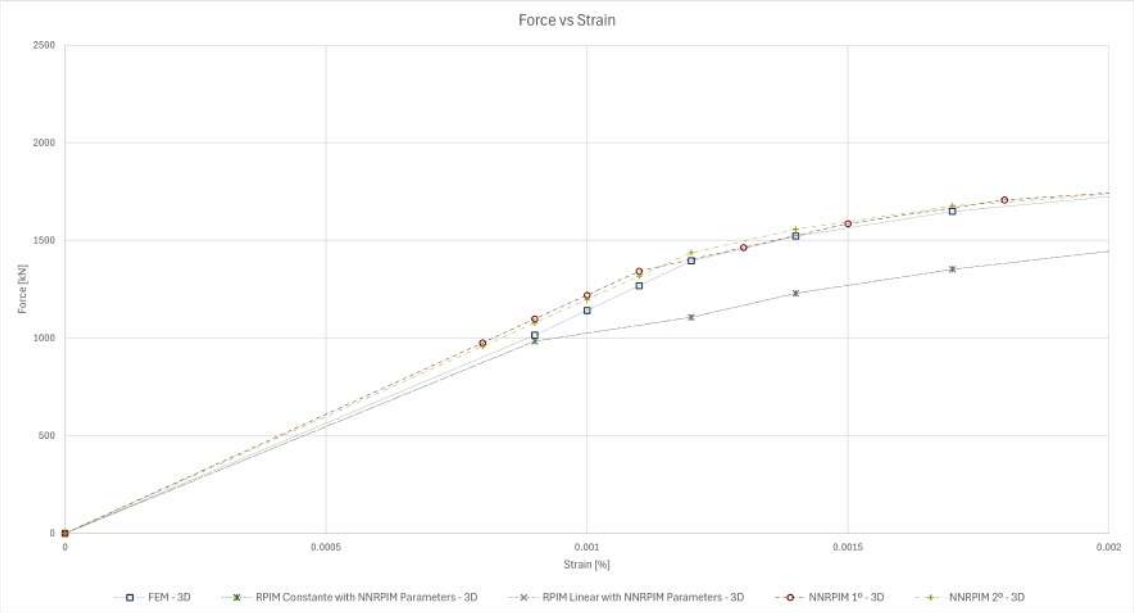

Figure 6.69: Graphic Force versus Strain of the T-beam with b=100 [mm] from 3D simulations in point B

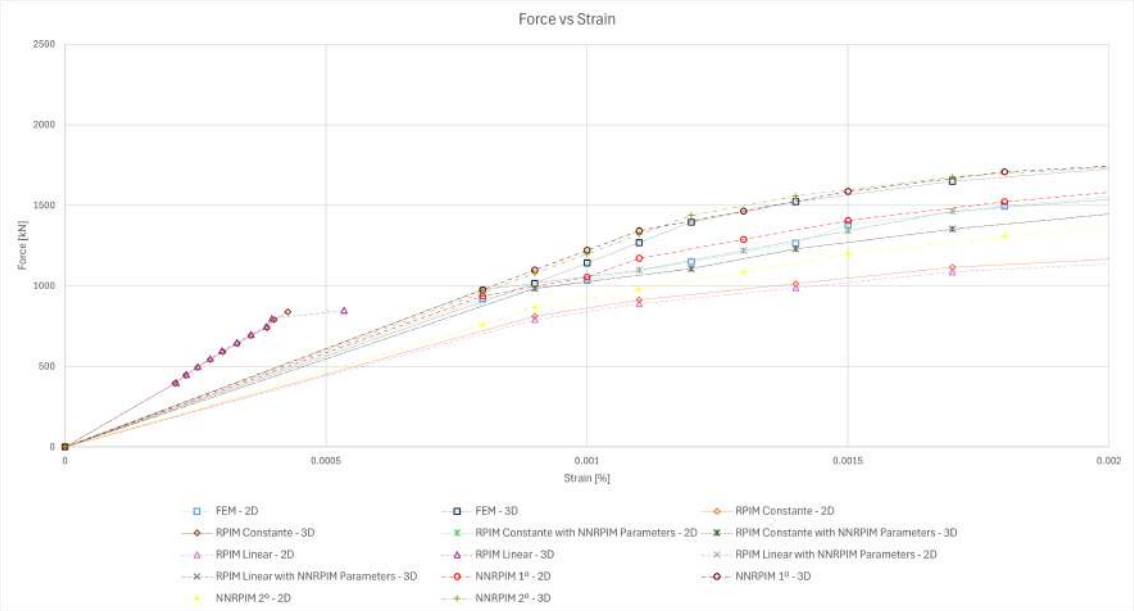

Figure 6.70: Graphic Force versus Strain of the T-beam with b=100 [mm] from simulations in point B

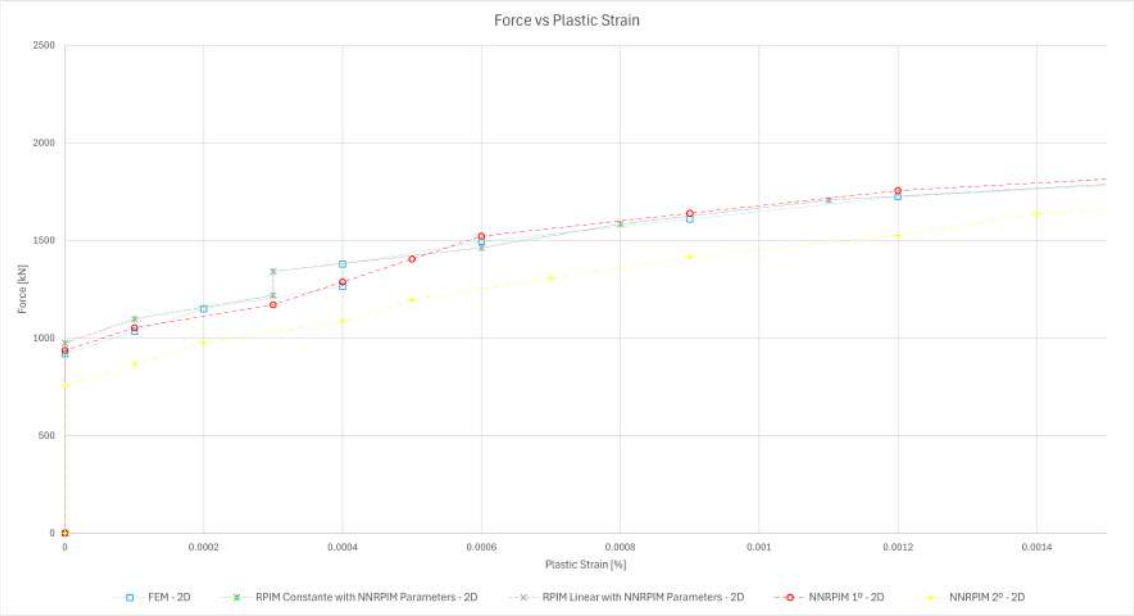

Figure 6.71: Graphic Force versus Plastic Strain of the T-beam with b=100 [mm] from 2D simulations in point B

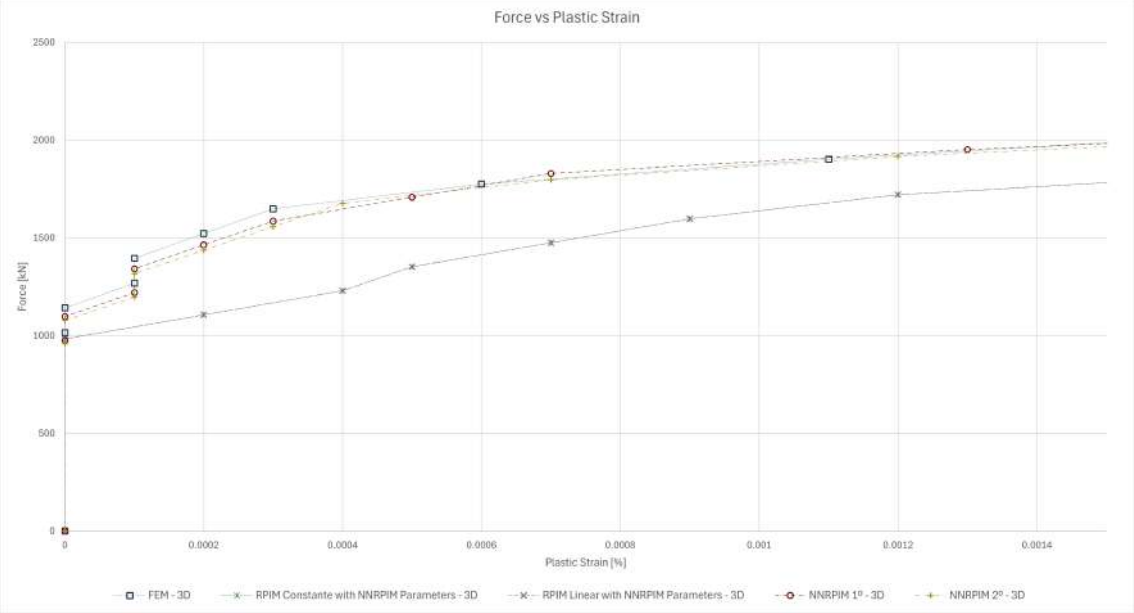

Figure 6.72: Graphic Force versus Plastic Strain of the T-beam with b=100 [mm] from 3D simulations in point B

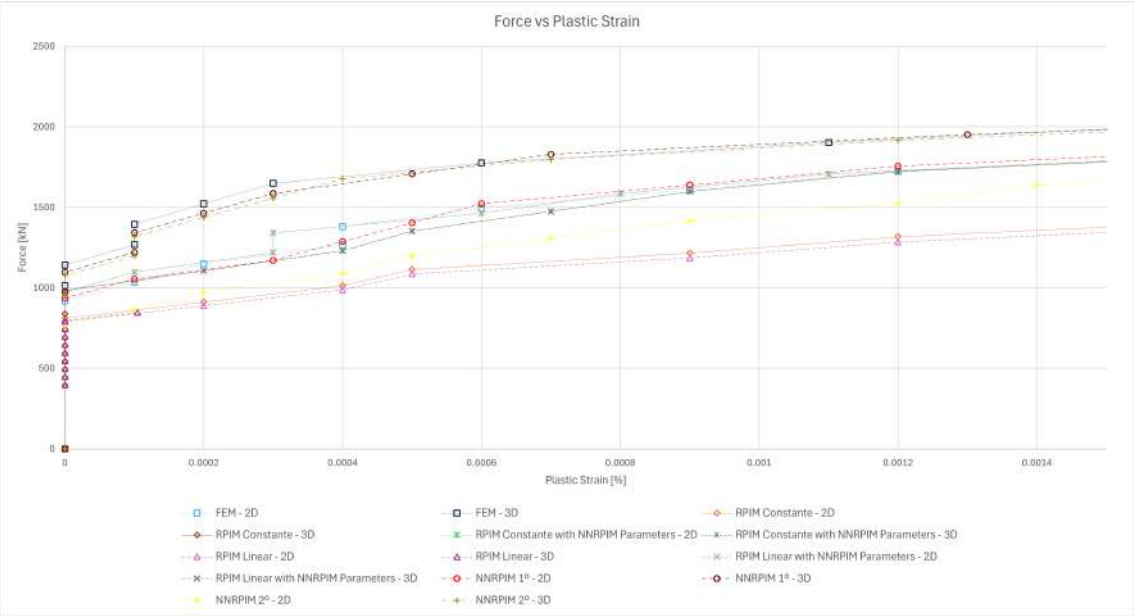

Figure 6.73: Graphic Force versus Plastic Strain of the T-beam with b=100 [mm] from simulations in point B

displacement from the 2D simulations, while figure 6.75 shows us the displacement from the 3D simulation. The simulations present us with values and curve behavior very similar, except for the 2D NNRPIM of the second order; however, it was close enough to almost overlap with the other' curves' simulations. So, that means that the NNRPIM in question isn't considered a bad result or an unreliable one, quite the opposite.

The overlapping graphic for the force versus displacement can be seen in figure 6.76, where the difference, already noted, of the NNRPIM simulation of the second order is more noticeable. This simulation in question presents us with a plastic deformation sooner than the rest of the simulations. However, the curve behavior isn't very different from the rest of the considered simulations. In fact, it is visible that the curve from the 2D NNRPIM of the second order presents signs of conversion to the other simulation. As normal, in this study, the RPIM (with RPIM parameters) presents notorious and visible differences.

In tables 6.72, 6.73, and, 6.74 show us the percentual difference between the values obtained in the 2D vs. 3D simulations, regarding the applied force, stress, and strain from the maximum and minimum values, from each simulation, present in the subchapters 6.3.2 and 6.4.2, that belong to the T-beam with b=100 [mm].

In terms of force difference, the FEM method keeps giving us a higher percentual difference while the RPIM methods' values are very closely matched; however, the highest percentual values belong to the NNRPIM method with the second degree of neighborhood. For the beam in T with b=100 mm, the percentage difference values in stress and strain are null, giving us a strong feeling of reliability.

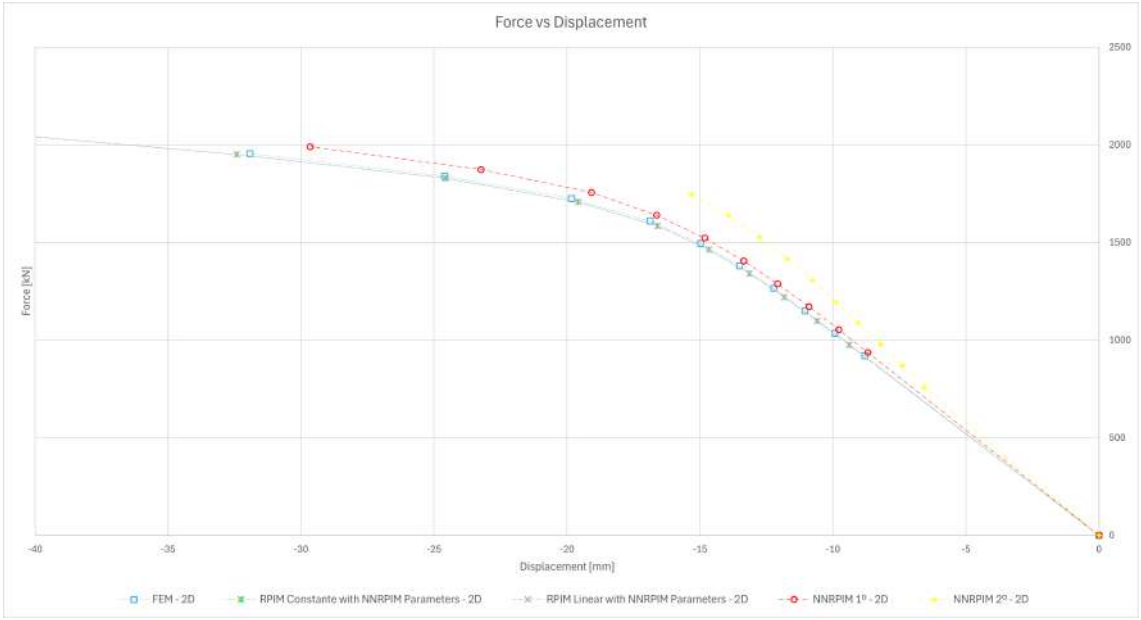

Figure 6.74: Graphic Force versus Displacement of the T-beam with b=100 [mm] from 2D simulations in point C

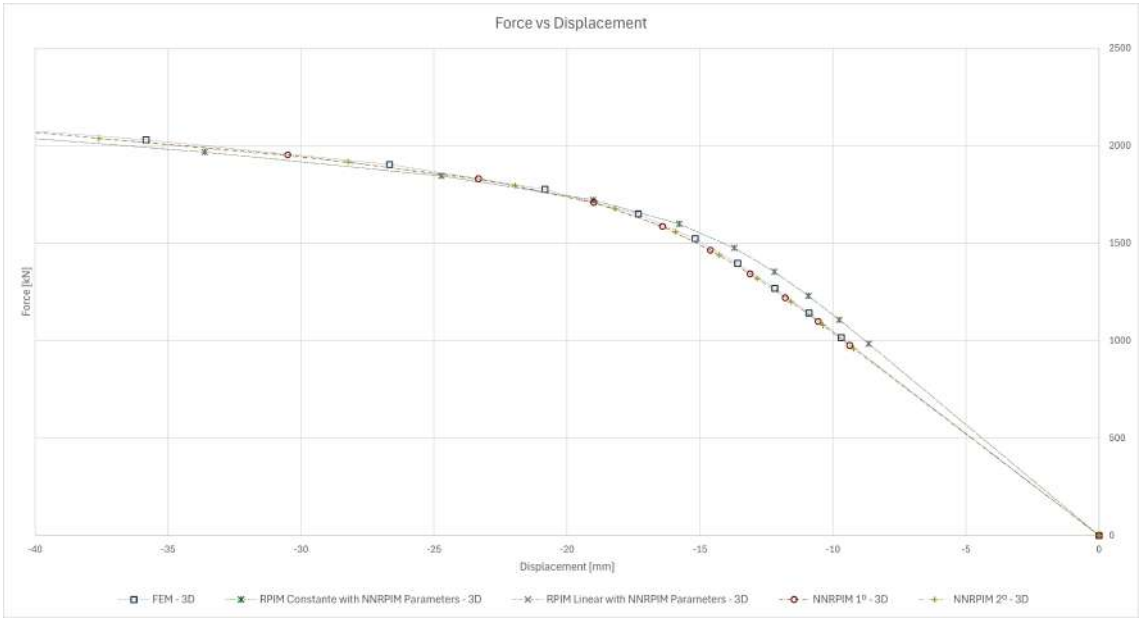

Figure 6.75: Graphic Force versus Displacement of the T-beam with b=100 [mm] from 3D simulations in point C

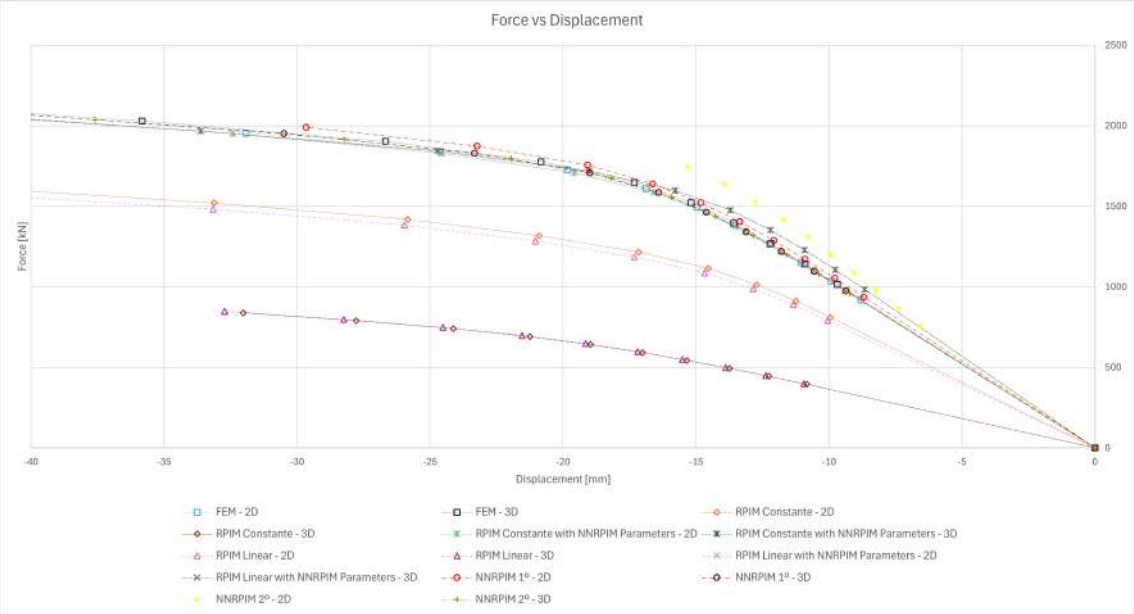

Figure 6.76: Graphic Force versus Displacement of the T-beam with b=100 [mm] from simulations in point C

Table 6.72: Percentual force difference for the T-beam (with b=100 [mm]]) 2D and 3D results

Increment	FEM	RPIM Const.	RPIM Linear	NNRPIM 1º	NNRPIM 2º
01	9.34%	0.82%	0.82%	4.02%	20.96%
02	9.36%	0.82%	0.81%	4.03%	19.55%
03	9.35%	0.81%	0.81%	4.03%	18.43%
04	9.35%	0.82%	0.81%	4.02%	17.51%
05	9.34%	0.82%	0.82%	4.02%	16.74%
06	9.35%	0.82%	0.82%	4.02%	16.09%
07	9.35%	0.82%	0.82%	4.02%	15.54%
08	9.35%	0.82%	0.81%	4.03%	15.06%
09	9.35%	0.82%	0.81%	4.03%	14.63%
10	9.35%	0.82%	0.82%	4.02%	14.26%

Table 6.73: Percentual stress difference for the T-beam (with b=100 [mm]]) 2D and 3D results

Increment	FEM	RPIM Const.	RPIM Linear	NNRPIM 1º	NNRPIM 2º
01	0.00%	0.00%	0.00%	0.00%	0.00%
02	0.00%	0.00%	0.00%	0.00%	0.00%
03	0.00%	0.00%	0.00%	0.00%	0.00%
04	0.00%	0.00%	0.00%	0.00%	0.00%
05	0.00%	0.00%	0.00%	0.00%	0.00%
06	0.00%	0.00%	0.00%	0.00%	0.00%
07	0.00%	0.00%	0.00%	0.00%	0.00%
08	0.00%	0.00%	0.00%	0.00%	0.00%
09	0.00%	0.00%	0.00%	0.00%	0.00%
10	0.00%	0.00%	0.00%	0.00%	0.00%

Table 6.74: Percentual strain difference for the T-beam (with b=100 [mm]) 2D and 3D results

Increment	FEM	RPIM Const.	RPIM Linear	NNRPIM 1º	NNRPIM 2º
01	0.00%	0.00%	0.00%	0.00%	0.00%
02	0.00%	0.00%	0.00%	0.00%	0.00%
03	0.00%	0.00%	0.00%	0.00%	0.00%
04	0.00%	0.00%	0.00%	0.00%	0.00%
05	0.00%	0.00%	0.00%	0.00%	0.00%
06	0.00%	0.00%	0.00%	0.00%	0.00%
07	0.00%	0.00%	0.00%	0.00%	0.00%
08	0.00%	0.00%	0.00%	0.00%	0.00%
09	0.00%	0.00%	0.00%	0.00%	0.00%
10	0.00%	0.00%	0.00%	0.00%	0.00%

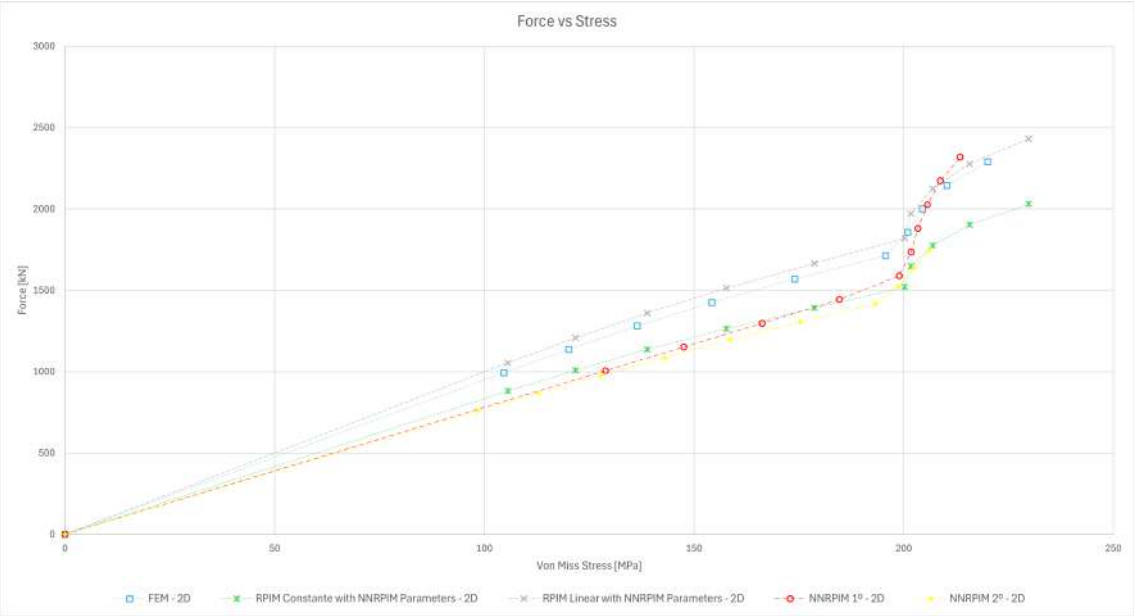

Figure 6.77: Graphic Force versus Stress of the T-beam with b=200 [mm] from 2D simulations in point A

T-Beam with b=200 [mm]

We initiate this study with point A, once again. By turning our attencion at figures 6.77 and 6.78, we can study the force versus stress graphics from the 2D and 3D simulations, respectively. Just like in the previous T-beam, the results' curves present the same behavior, which implies that there are no applicable discrepancies between the offered results.

It's evident that the results from the simulations are very identical, which can be noticed in figure 6.79 with the overlapping of the 2D and 3D graphics. In previous simulations, we were led to the conclusion that the 3D results present us with slightly higher force values but slightly lower stress values, and once again, this tendency is repeated. Once more, it's interesting to realize the difference between the 3D RPIM simulations (with RPIM parameters) and all the further simulations. By looking at the overlapping graphic, it is apparent that the 3D simulations, from the RPIM methods, deliver very low values.

Looking now to figures 6.80 and 6.81, we can watch the 2D and 3D graphics for the force versus strain, on point A. The results presented are very alike between simulations, with results in values and curve behavior showing no relevant distinction.

The next graphic can be studied in figure 6.82. The graphic in question is the overlapping graphic between the 2D and 3D simulations shown before, in figures 6.80 and 6.81. The assessed 2D and 3D simulations give a very close match; on the other hand, all the RRPIM simulations (with RPIM parameters) present us with values lower in terms of strain by force than the evaluated simulations, with the 3D

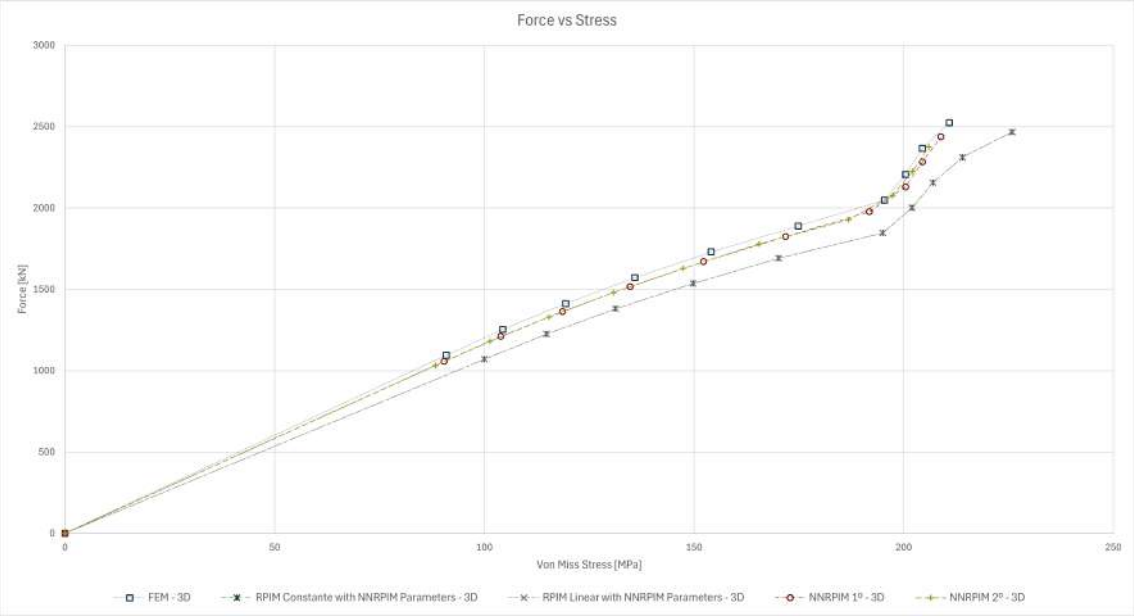

Figure 6.78: Graphic Force versus Stress of the T-beam with b=200 [mm] from 3D simulations in point A

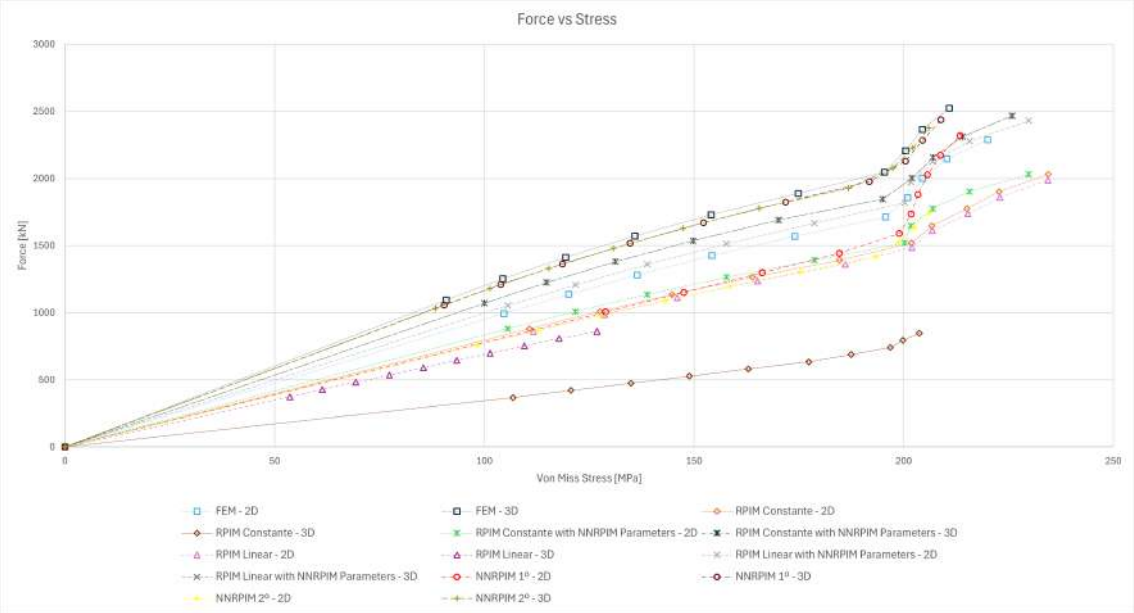

Figure 6.79: Graphic Force versus Stress of the T-beam with b=200 [mm] from simulations in point A

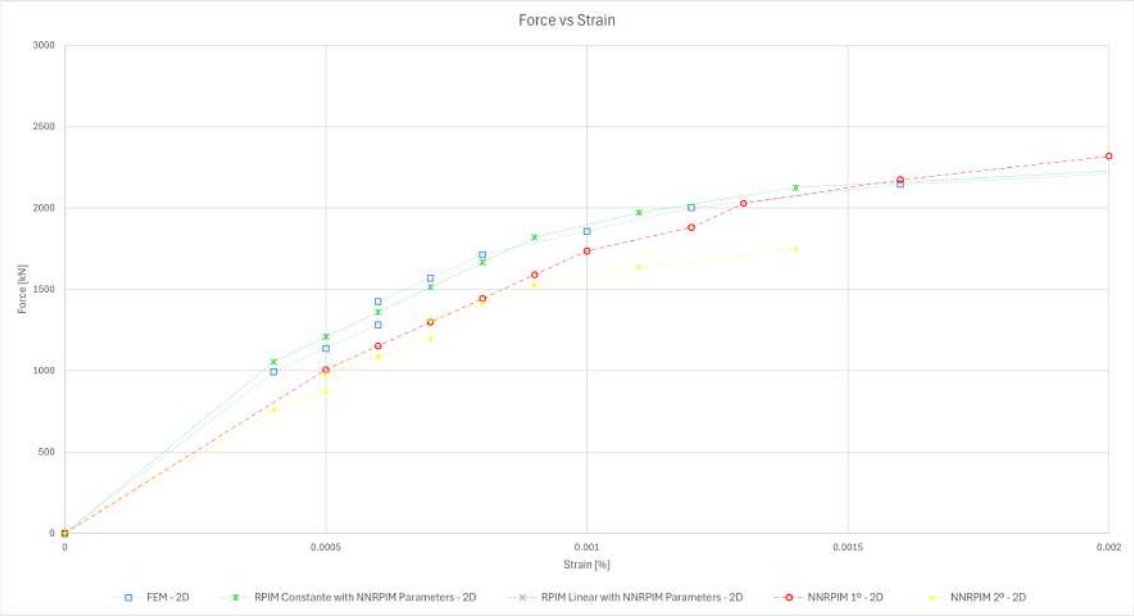

Figure 6.80: Graphic Force versus Strain of the T-beam with b=200 [mm] from 2D simulations in point A

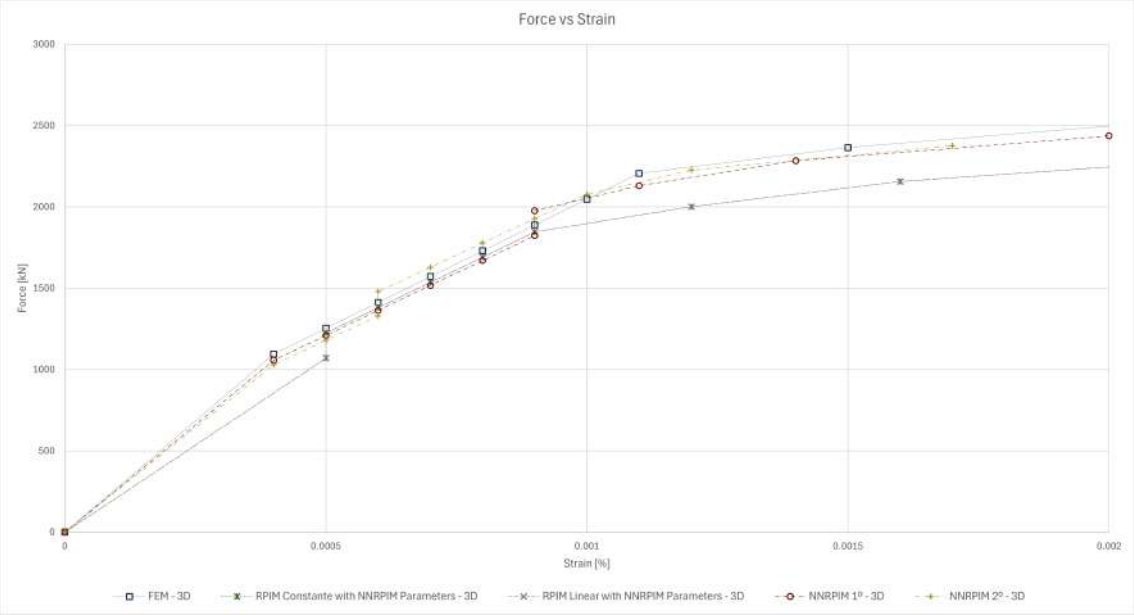

Figure 6.81: Graphic Force versus Strain of the T-beam with b=200 [mm] from 3D simulations in point A

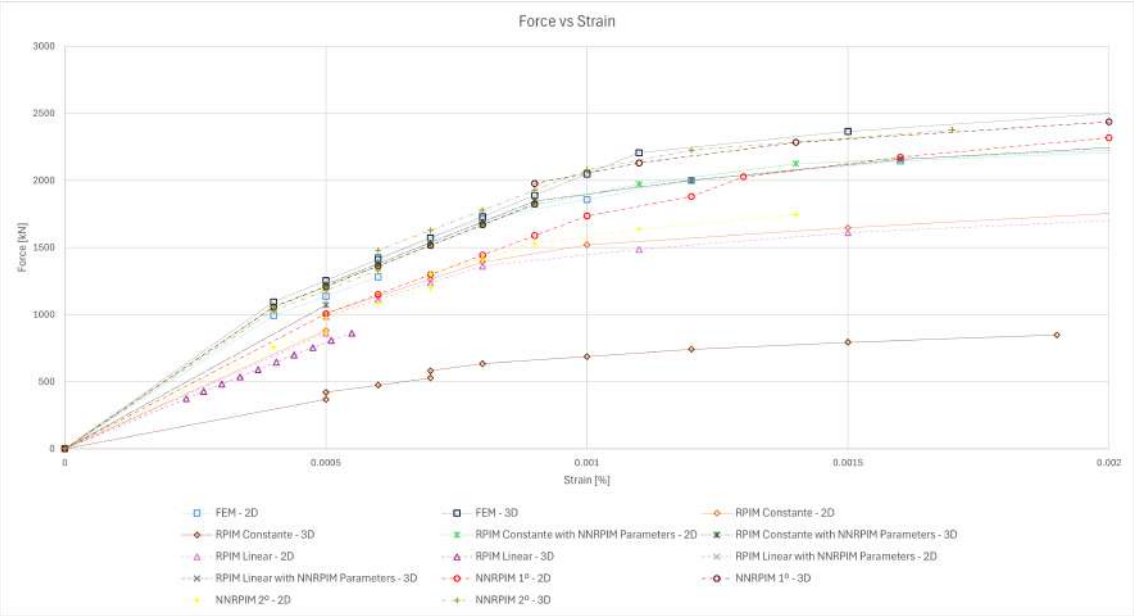

Figure 6.82: Graphic Force versus Strain of the T-beam with b=200 [mm] from simulations in point A

RPIM simulations (with RPIM parameters) being fully disproportional and with overly inferior values in comparison.

To conclude the point A analysis, we need to examine the force versus plastic strain. In figures 6.83 and 6.84, we can observe the force versus plastic strain graphic from 2 dimensions and 3 dimensions, respectively. Like in the force versus strain, it's possible to conclude that the simulations are nearly matched.

Redirecting our attention now to figure 6.85, which shows us the overlapping graphic from figures 6.83 and 6.84, we can just like in the strain analysis, observe that the 2D and 3D simulations conduct itself with closely match behaviors, with the RPIM (with RPIM parameters) being the already expected exception, with values lower comparatively to the different simulations, and in the 3D case these values are significantly low in comparison.

Now we can initiate the point B analysis. If we examine figures 6.86 and 6.87 we can examine the force vs stress graphics from the 2D and 3D simulations, respectively. All the simulations present us with curves that show the same behavior, which means that there are no pertinent dissimilarities between the presented results.

It's apparent that the results obtained in the simulations are significantly comparable, which can be observed in figure 6.88 with the overlapping of the 2D and 3D graphics. Just like in the last simulations, the 3D presents us with a little higher force values but narrowly inferior stress values. It is also intriguing to realize the discrepancy between the 3D RPIM simulations (with RPIM parameters) and all the other simulations. By examining the overlapping graphic, it's unmistakable that the

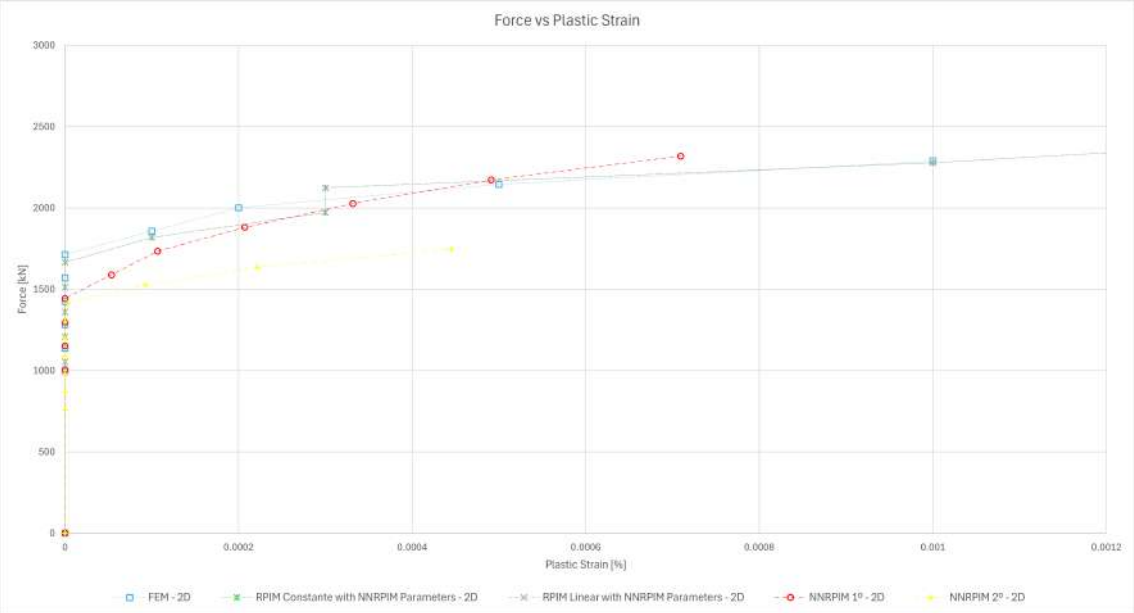

Figure 6.83: Graphic Force versus Plastic Strain of the T-beam with b=200 [mm] from 2D simulations in point A

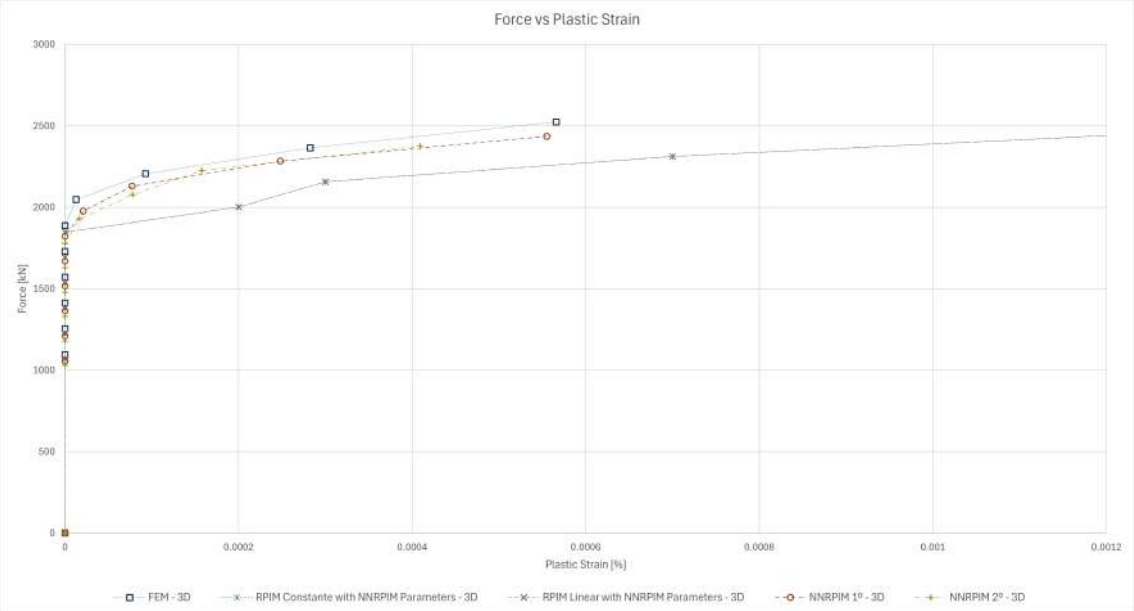

Figure 6.84: Graphic Force versus Plastic Strain of the T-beam with b=200 [mm] from 3D simulations in point A

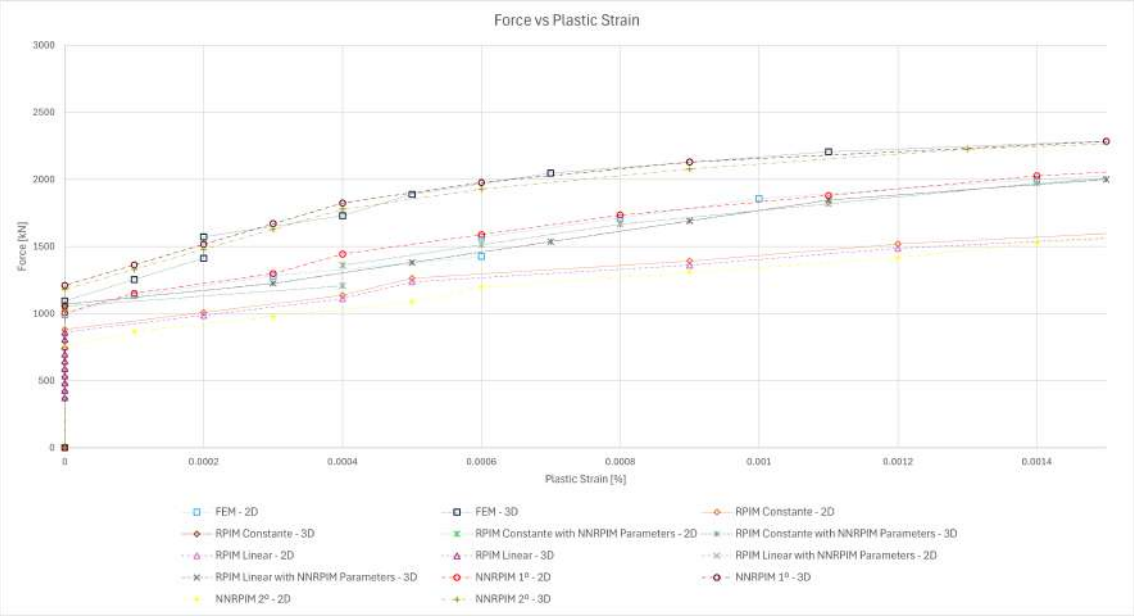

Figure 6.85: Graphic Force versus Plastic Strain of the T-beam with b=200 [mm] from simulations in point A

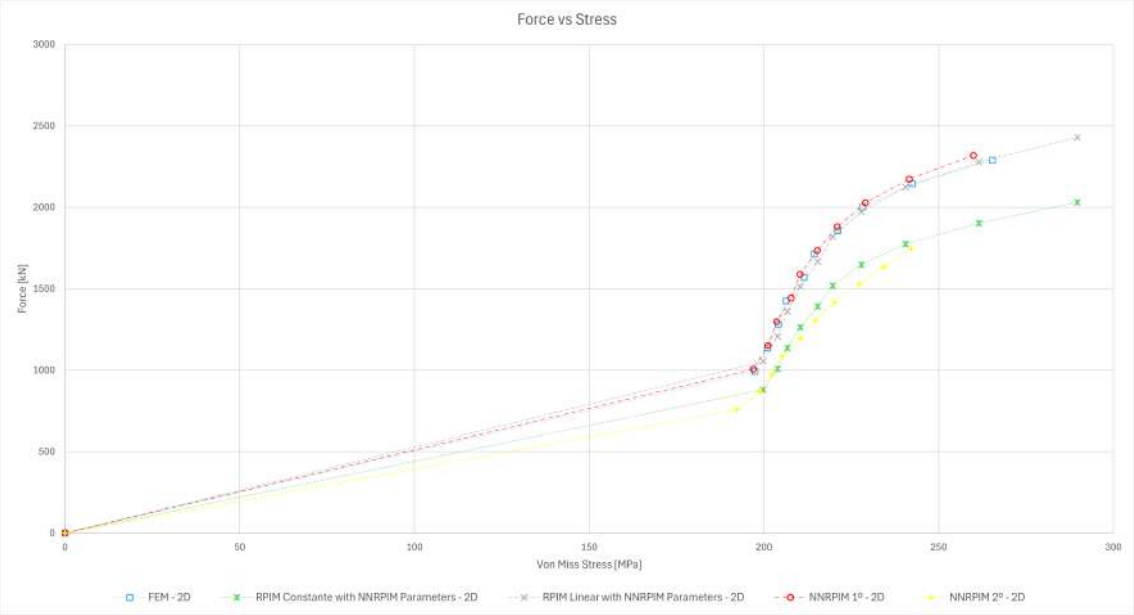

Figure 6.86: Graphic Force versus Stress of the T-beam with b=200 [mm] from 2D simulations in point B

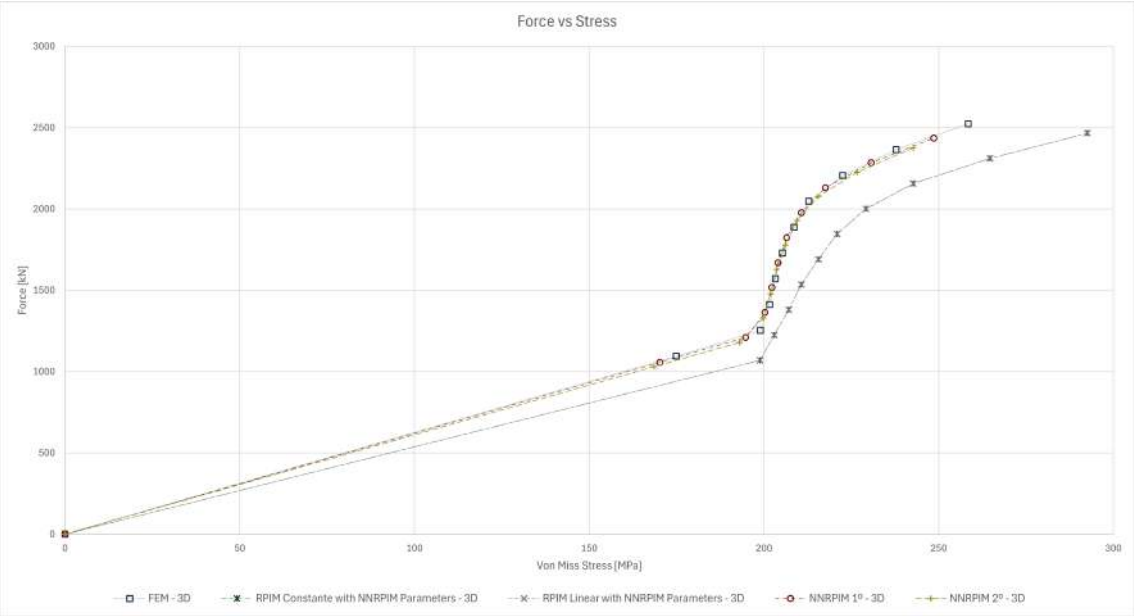

Figure 6.87: Graphic Force versus Stress of the T-beam with b=200 [mm] from 3D simulations in point B

3D simulations in question (mentioned RPIM simulations) present us with very low values.

Moving our attention, now, to figures 6.89 and 6.90 we can see the 2D and 3D graphics for the force versus strain, on point B. Similarly, the results given are very comparable between simulations, with the curve behavior presenting no relevant difference, just like the simulation values.

The next graphic can be observed in figure 6.91. This graphic is the overlapping graphic between the 2D and 3D simulations previously shown in figures 6.89 and 6.90. The considered 2D and 3D simulations present a very close match; on the other hand, all the RRPIM simulations (with RPIM parameters) present us with values lower in terms of strain by force than the considered simulations, with the 3D RPIM simulations (with RPIM parameters) being completely disproportional and with extremely low values in comparison.

To end the point B analysis, we need to investigate the force versus plastic strain. In figures 6.92 and 6.93, we can observe the force versus plastic strain graphic from 2 dimensions and 3 dimensions, respectively. Just like in the force versus strain, for this point, it's possible to conclude that the simulations are identical and closely match.

Redirecting our engagement now to figure 6.94, which shows us the overlapping graphic represented in figures 6.92 and 6.93, we can observe, just like in the strain analysis, that the 2D and 3D simulations present behaviors match closely, with the RPIM (with RPIM parameters) being the already expected exception, again, with

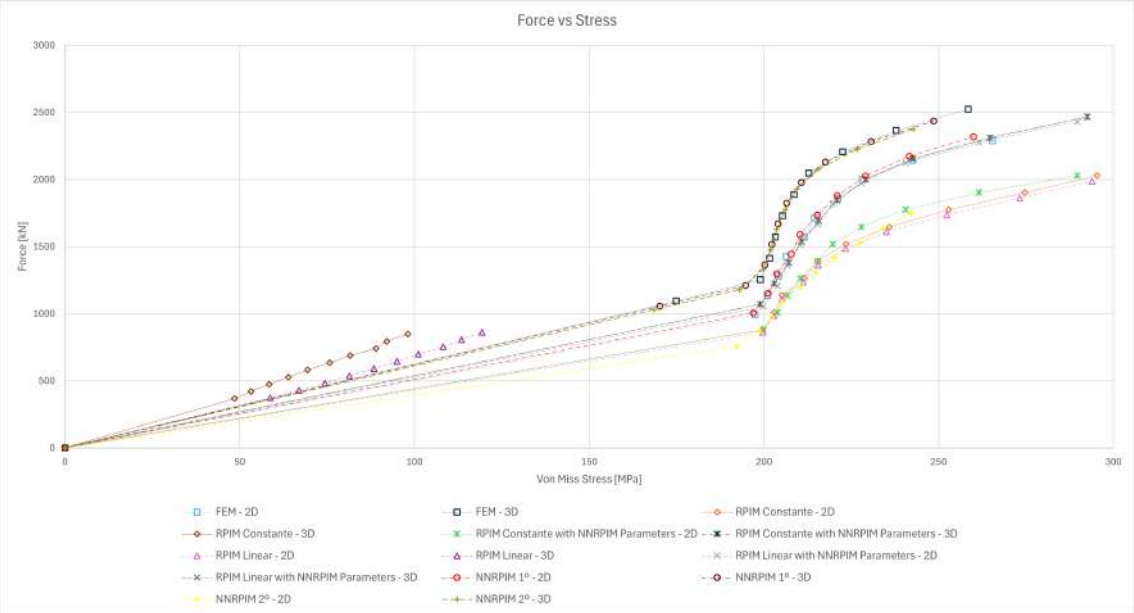

Figure 6.88: Graphic Force versus Stress of the T-beam with b=200 [mm] from simulations in point B

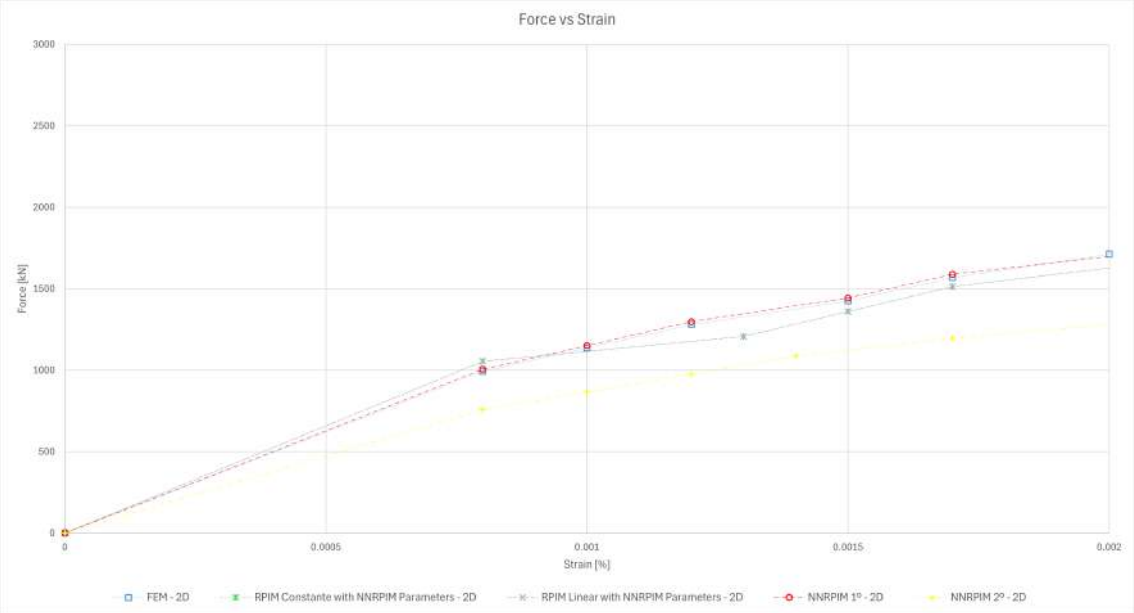

Figure 6.89: Graphic Force versus Strain of the T-beam with b=200 [mm] from 2D simulations in point B

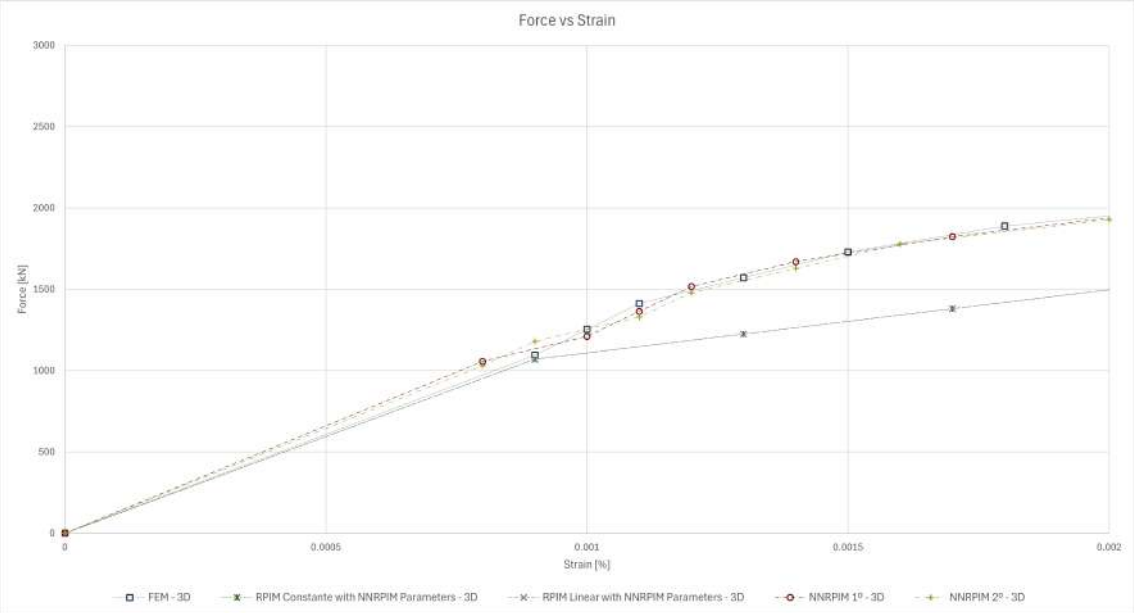

Figure 6.90: Graphic Force versus Strain of the T-beam with b=200 [mm] from 3D simulations in point B

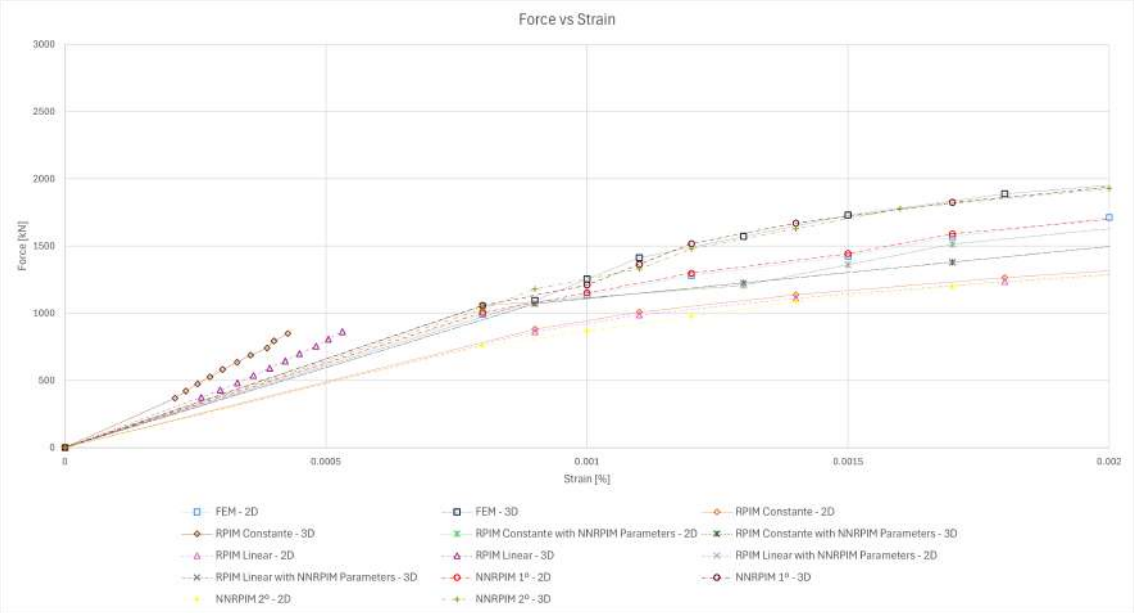

Figure 6.91: Graphic Force versus Strain of the T-beam with b=200 [mm] from simulations in point B

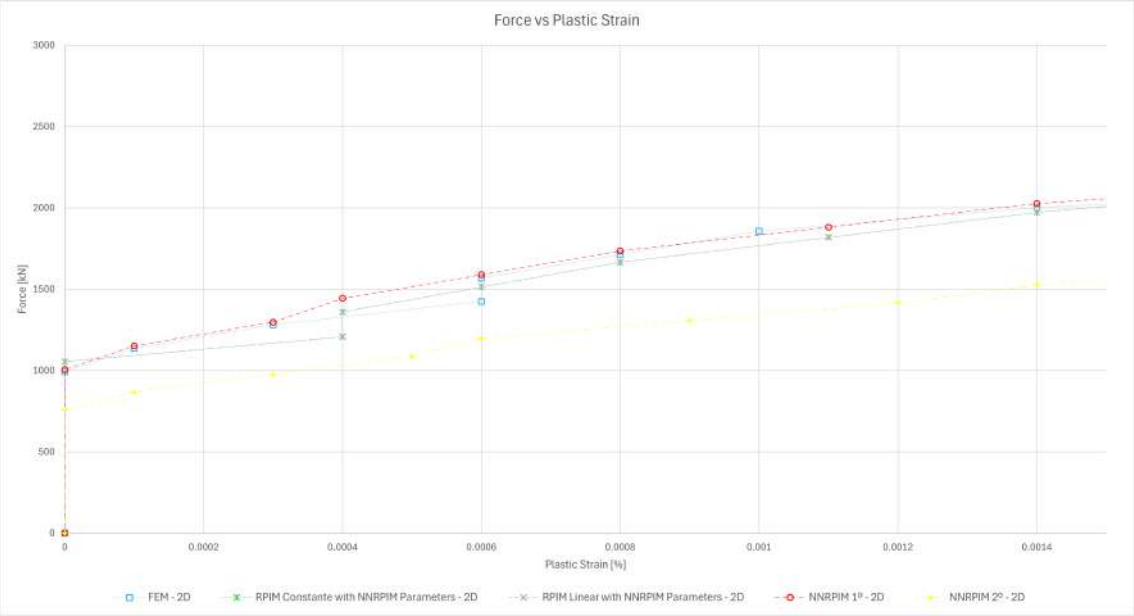

Figure 6.92: Graphic Force versus Plastic Strain of the T-beam with b=200 [mm] from 2D simulations in point B

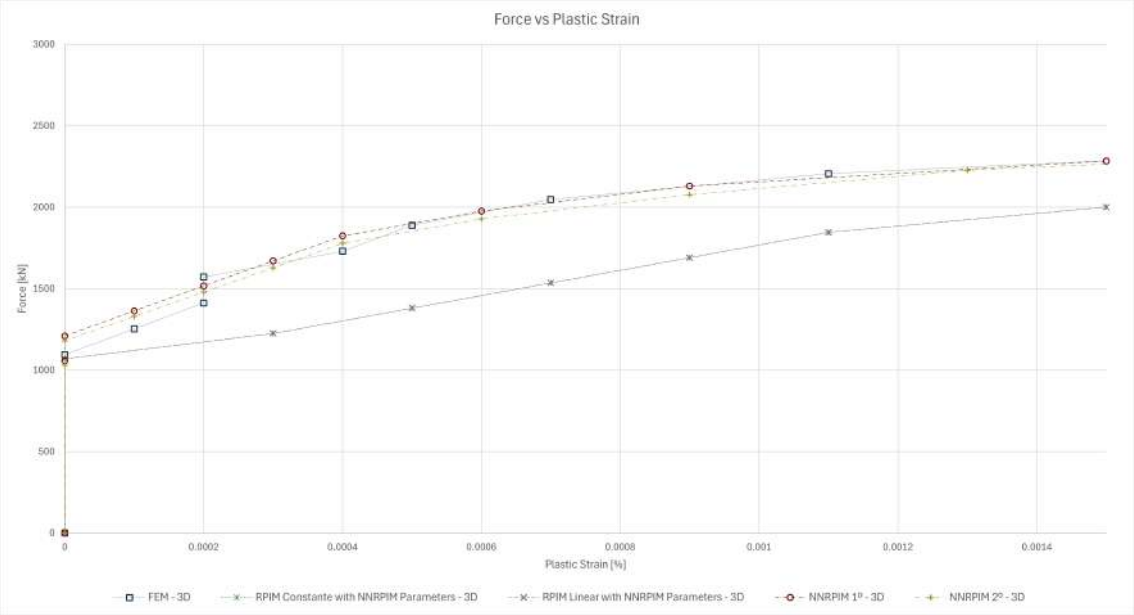

Figure 6.93: Graphic Force versus Plastic Strain of the T-beam with b=200 [mm] from 3D simulations in point B

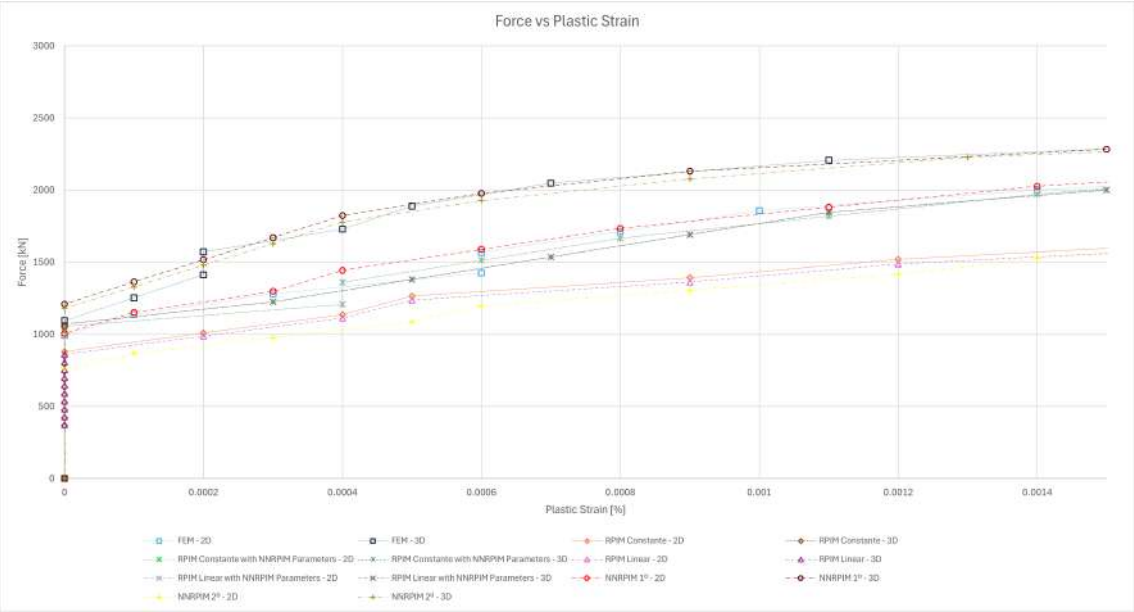

Figure 6.94: Graphic Force versus Plastic Strain of the T-beam with b=200 [mm] from simulations in point B

values more inferior comparatively to the other simulations, and in the 3D case these values are extremely lower in comparison.

To formally complete the T-beam with b=200 mm analysis, let's focus our attention on point C, where the study will be about the displacement. Figure 6.95 demonstrates to us the displacement from the 2D simulations, while figure 6.96 indicates to us the displacement from the 3D simulation. The simulations delivered values and curve behavior very similarly, as has been the norm in this study.

The overlapping graphic for the force versus displacement can be witnessed in figure 6.97, once again, it is possible to calculate, by analising, the graphic, that the 2D and 3D displacement simulated values are extremely match between all the simulatations, except for the RPIM simulation (with RPIm parameters). As normal, in this study, the RPIM (with RPIM parameters) presents notorious and perceptible dissimilarities.

The following tables 6.75, 6.76, and 6.77 present us the different percentual values from the variables of force, maximum stress, and maximum strain, from the 2D simulations to the 3D simulations.

The force difference values show us that all the simulations maintain a constant deviation, with the RPIM methods giving us the lesser percentual difference while the NNRPIM of the second order gives us the bigger one, which is not surprising after the analysis previously done. The stress percentual variation gives us low percentual values; however, these percentual values are not constant or linear; instead, they fluctuate in an unpredictable way. Just like in the previous cases, the strain

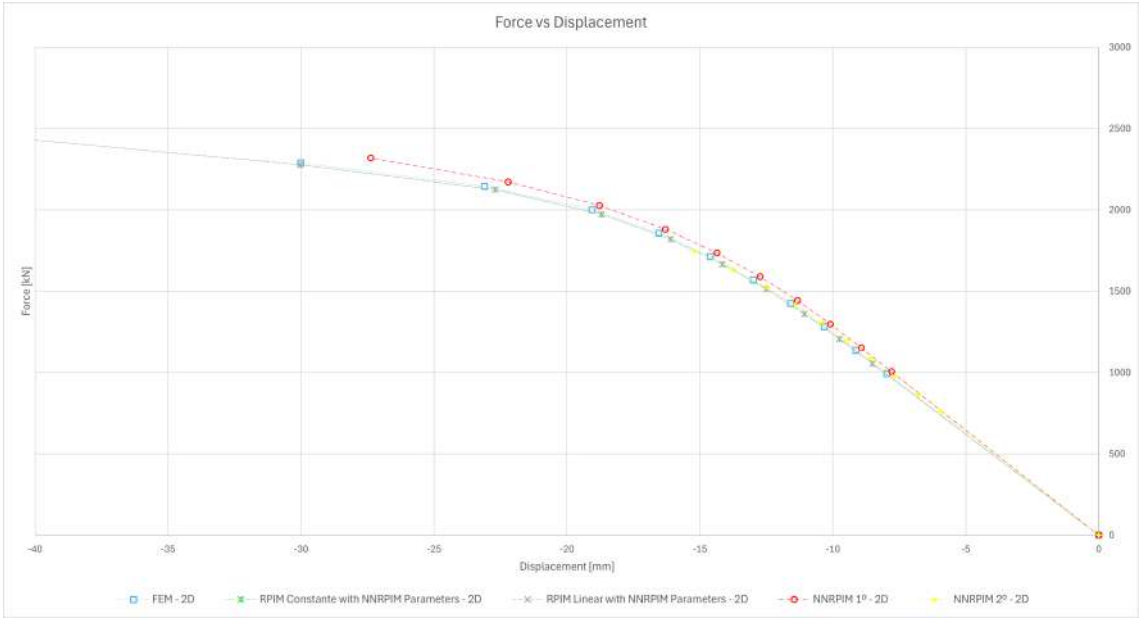

Figure 6.95: Graphic Force versus Displacement of the T-beam with b=200 [mm] from 2D simulations in point C

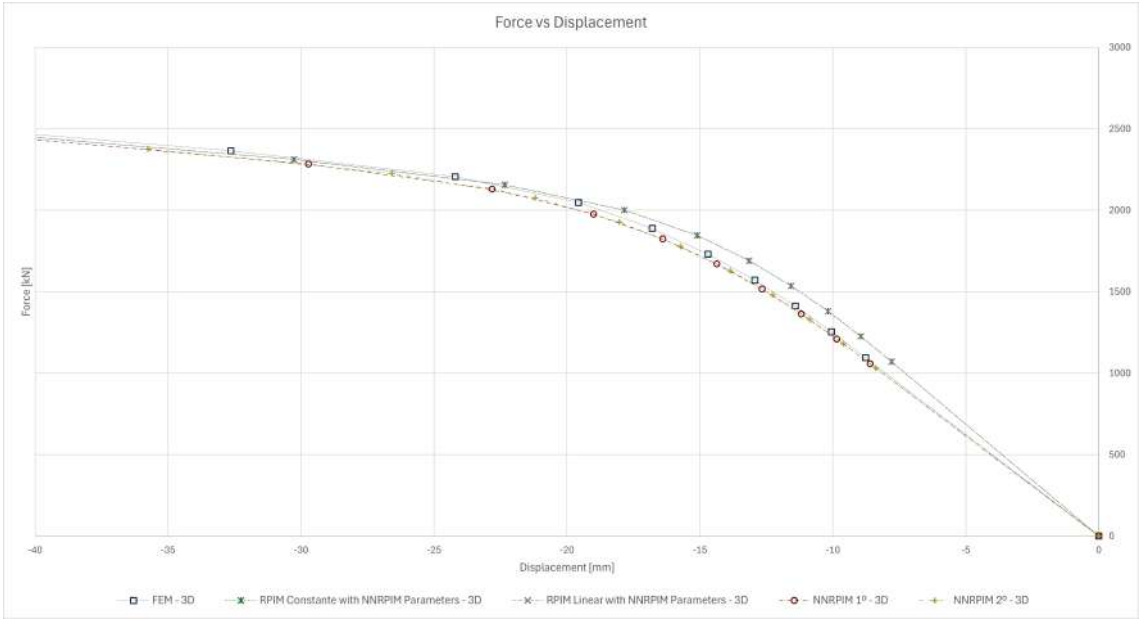

Figure 6.96: Graphic Force versus Displacement of the T-beam with b=200 [mm] from 3D simulations in point C

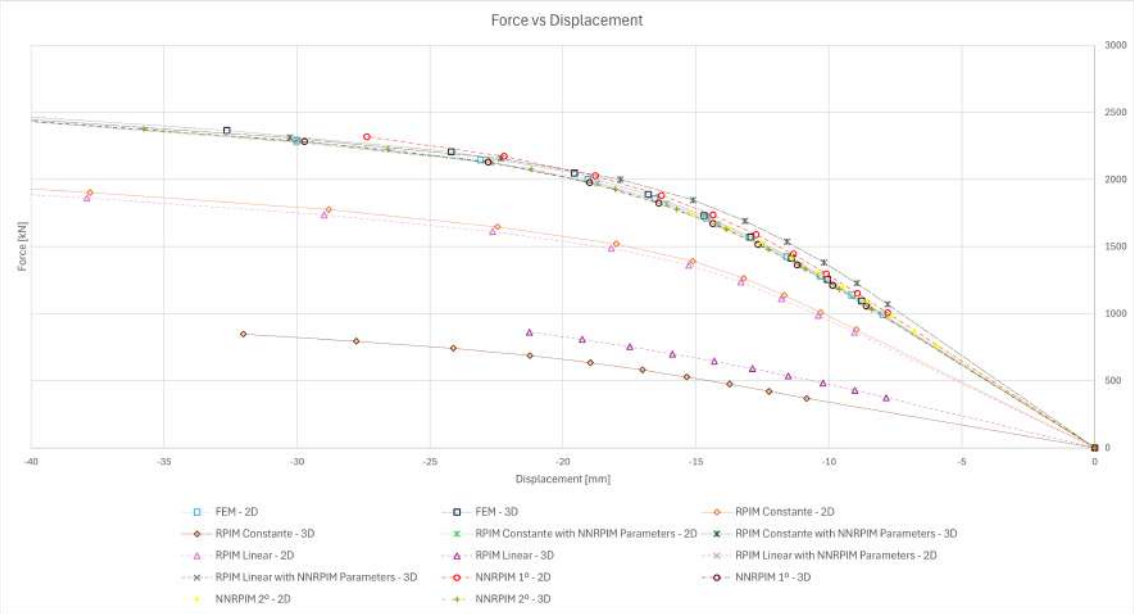

Figure 6.97: Graphic Force versus Displacement of the T-beam with b=200 [mm] from simulations in point C

Table 6.75: Percentual force difference for the T-beam (with b=200 [mm]) 2D and 3D results

Increment	FEM	RPIM Const.	RPIM Linear	NNRPIM 1º	NNRPIM 2º
01	9.31%	1.47%	1.47%	4.85%	26.53%
02	9.30%	1.47%	1.47%	4.85%	26.53%
03	9.30%	1.46%	1.46%	4.85%	26.54%
04	9.30%	1.47%	1.47%	4.85%	26.53%
05	9.30%	1.47%	1.47%	4.85%	26.53%
06	9.30%	1.47%	1.47%	4.85%	26.53%
07	9.30%	1.47%	1.46%	4.85%	26.53%
08	9.30%	1.47%	1.47%	4.85%	26.53%
09	9.30%	1.47%	1.47%	4.85%	26.53%
10	9.30%	1.47%	1.47%	4.85%	26.53%

Table 6.76: Percentual stress difference for the T-beam (with b=200 [mm]) 2D and 3D results

Interation	FEM	RPIM Const.	RPIM Linear	NNRPIM 1º	NNRPIM 2º
01	1.87%	0.08%	0.08%	1.71%	3.15%
02	0.58%	0.11%	0.11%	0.37%	0.63%
03	0.46%	1.31%	1.31%	0.02%	0.13%
04	0.60%	0.59%	0.59%	0.40%	0.12%
05	0.42%	1.03%	1.03%	0.29%	1.09%
06	0.04%	1.33%	1.33%	0.77%	1.44%
07	0.68%	1.27%	1.27%	1.04%	1.87%
08	1.08%	1.48%	1.48%	0.88%	1.71%
09	2.41%	1.74%	1.74%	0.60%	0.88%
10	2.56%	1.61%	1.61%	1.92%	5.58%

Table 6.77: Percentual strain difference for the T-beam (with b=200 [mm]) 2D and 3D results

Interation	FEM	RPIM Const.	RPIM Linear	NNRPIM 1º	NNRPIM 2º
01	11.11%	11.11%	11.11%	11.11%	11.11%
02	16.67%	7.14%	7.14%	9.09%	0.00%
03	14.29%	16.67%	16.67%	14.29%	7.69%
04	6.25%	19.05%	19.05%	6.25%	6.67%
05	10.53%	16.00%	16.00%	5.56%	0.00%
06	9.09%	16.67%	16.67%	4.55%	0.00%
07	14.29%	18.42%	18.42%	3.85%	0.00%
08	18.92%	20.00%	20.00%	8.82%	6.45%
09	25.93%	19.72%	19.72%	16.33%	20.93%
10	25.97%	18.37%	18.37%	21.43%	37.10%

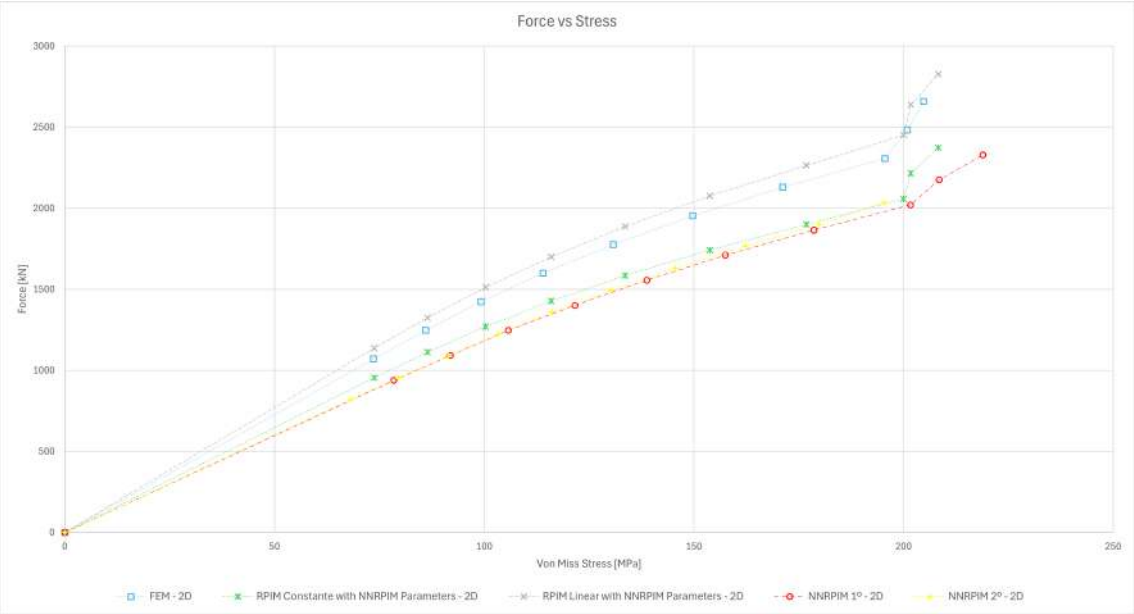

Figure 6.98: Graphic Force versus Stress of the T-beam with b=400 [mm] from 2D simulations in point A

percentual difference is considerably bigger, having the same unpredictable behavior described in the stress percentual values analysis.

T-Beam with b=400 [mm]

In this subchapter, we can start by moving our attention to figures 6.98 and 6.99, where we can observe the 2D and 3D graphics for the force versus strain, on point A. Once again, the results presented are very similar between simulations, where the values and curve behavior presented show no relevant difference.

The next graphic can be observed in figure 6.100. This graphic is the overlapping graphic between the 2D and 3D simulations previously shown in figures 6.98 and 6.99. The considered 2D and 3D simulations present a very close match; on the other hand, all the RRPIM simulations (with RPIM parameters) present us with values lower in terms of strain by force than the considered simulations, with the 3D RPIM simulations (with RPIM parameters) being completely disproportional and with extremely low values in comparison.

By looking at the figures 6.101 and 6.102, we can now observe the 2D and 3D results in the graphic force versus strain, respectively. In the overlapping graphic 6.103, from the two previous ones mentioned, we can visualize an intense similarity, with the NNRPIM simulations from the 2D mesh being the small exception. These two simulations presented us with a higher strain with less applied force. Another small detail that is perceptible is the fact that the 2D simulations present us with a slightly different curve behavior, these being more pronounced and initiating earlier.

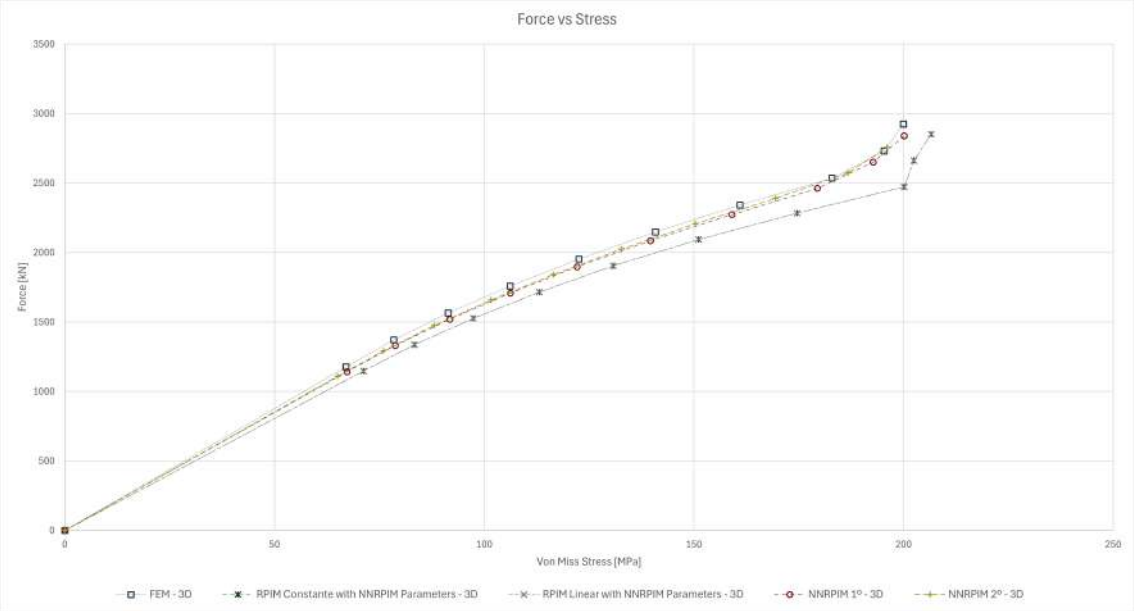

Figure 6.99: Graphic Force versus Stress of the T-beam with b=400 [mm] from 3D simulations in point A

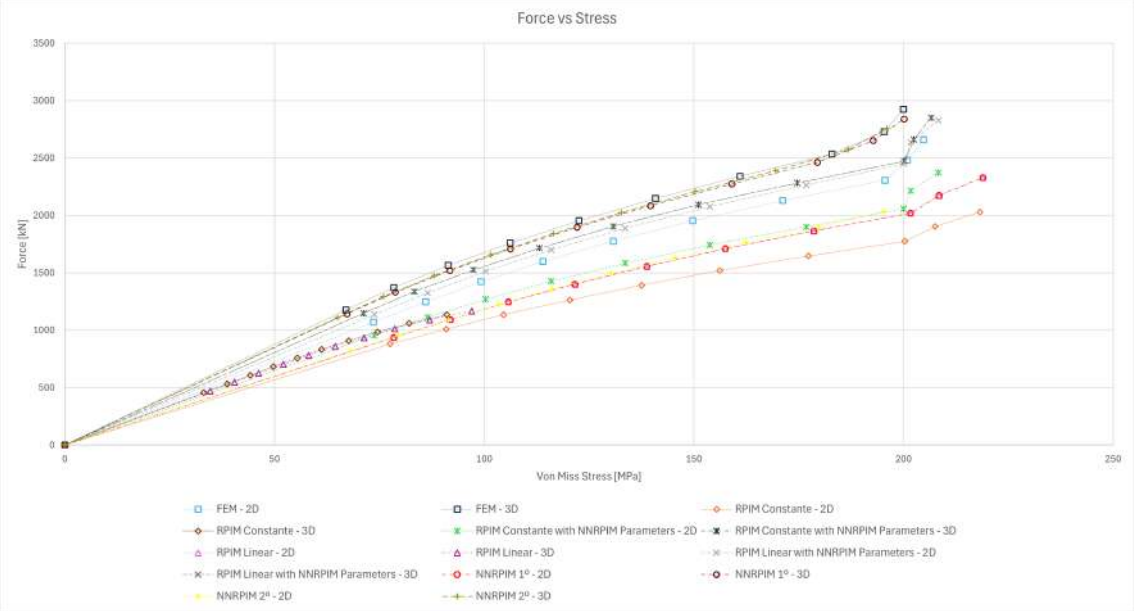

Figure 6.100: Graphic Force versus Stress of the T-beam with b=400 [mm] from simulations in point A

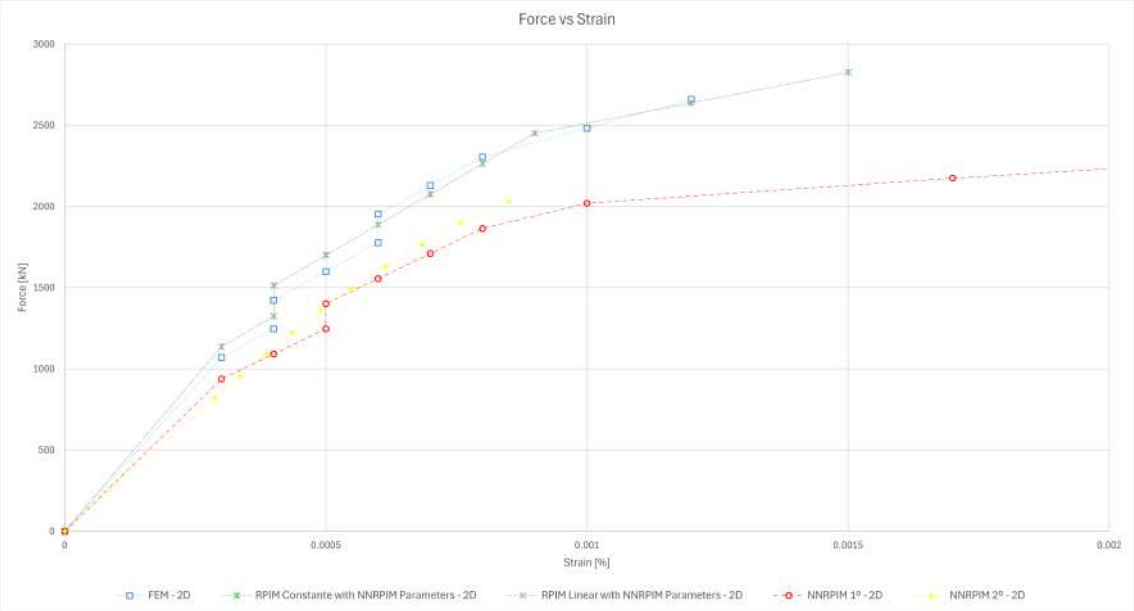

Figure 6.101: Graphic Force versus Strain of the T-beam with b=400 [mm] from 2D simulations in point A

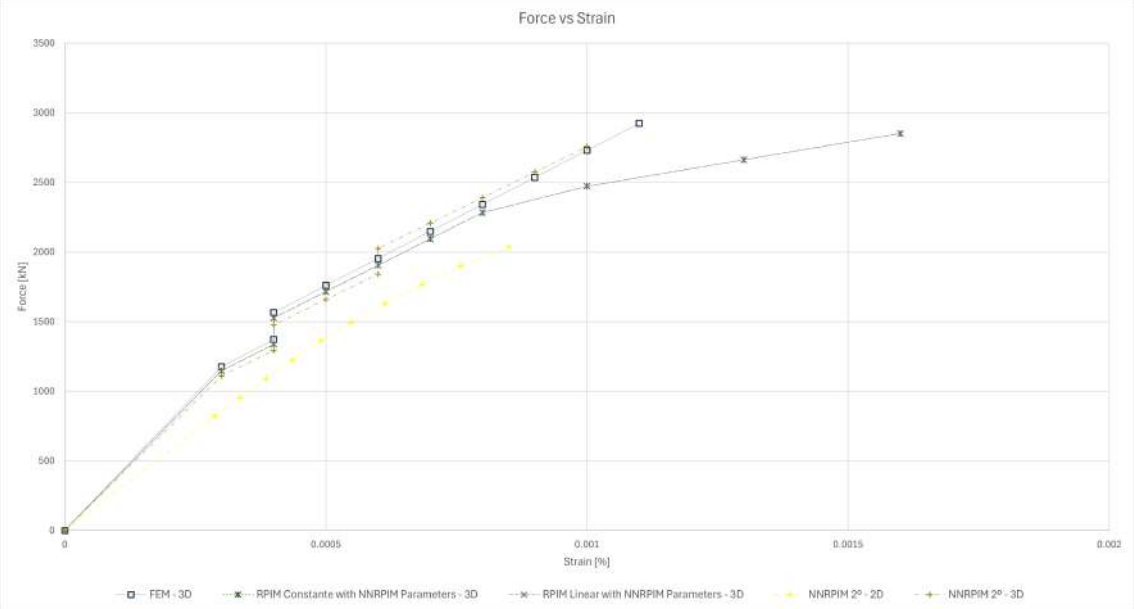

Figure 6.102: Graphic Force versus Strain of the T-beam with b=400 [mm] from 3D simulations in point A

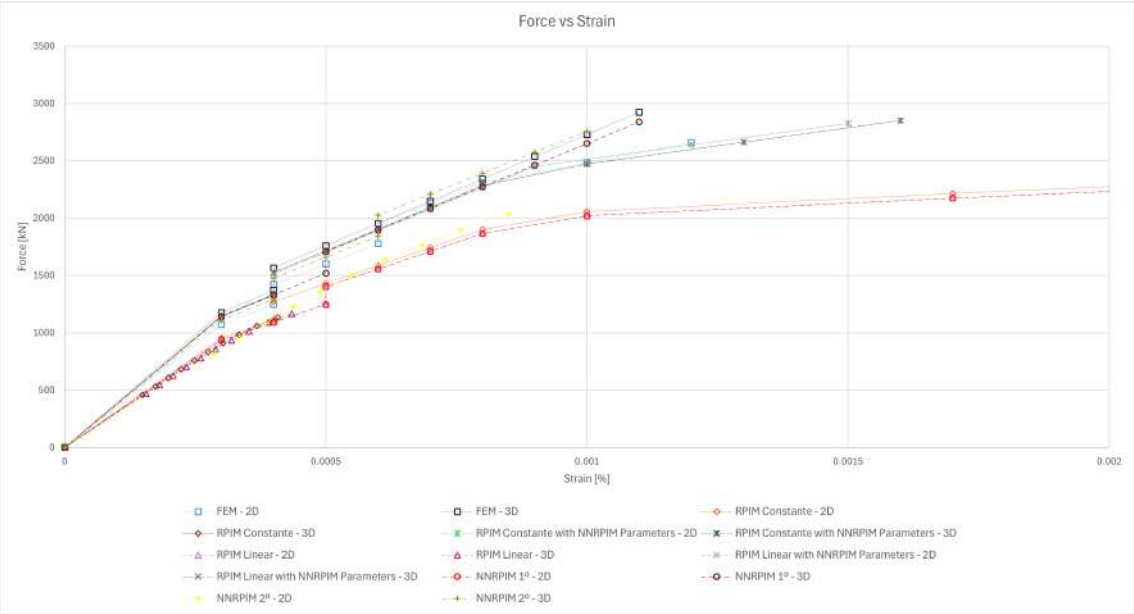

Figure 6.103: Graphic Force versus Strain of the T-beam with b=400 [mm] from simulations in point A

Finally, to end the point A analysis, we need to analyze the force versus plastic strain. In figures 6.104 and 6.105, we can observe the force versus plastic strain graphic from 2 dimensions and 3 dimensions, respectively. Just like in the force versus strain, for the same point, it is possible to conclude that the simulations are very closely matched.

Diverting our attention now to figure 6.106, which delivers us the overlapping graphic from figures 6.104 and 6.105. Just like in the strain analysis, we can observe that the 2D and 3D simulations present behaviors considerably similar, with the RPIM (with RPIM parameters) being the exception expected, with values inferior comparatively to the other simulations, being extremely low in the 3D case, by comparison.

Let's now start analyzing point B. If we look at figures 6.107 and 6.108 we can investigate the force versus stress graphics from the 2D and 3D simulations, respectively. In all simulation methods present in this study, the curves present the same behavior, which implies that there are no relevant discrepancies between the offered results.

It is clear that the results from the simulations are very similar, and that can be observed in figure 6.109 with the overlapping of the 2D and 3D graphics. As the previous simulations show us, the 3D model presents us with slightly higher force values but slightly lower stress values, and this norm is respected in the T beam with b=400 mm. We can again analyze the difference between the 3D RPIM simulations with RPIM parameters and all the other simulations, by examining the overlapping graphic, it's clear that the 3D simulations in question present us with very low values.

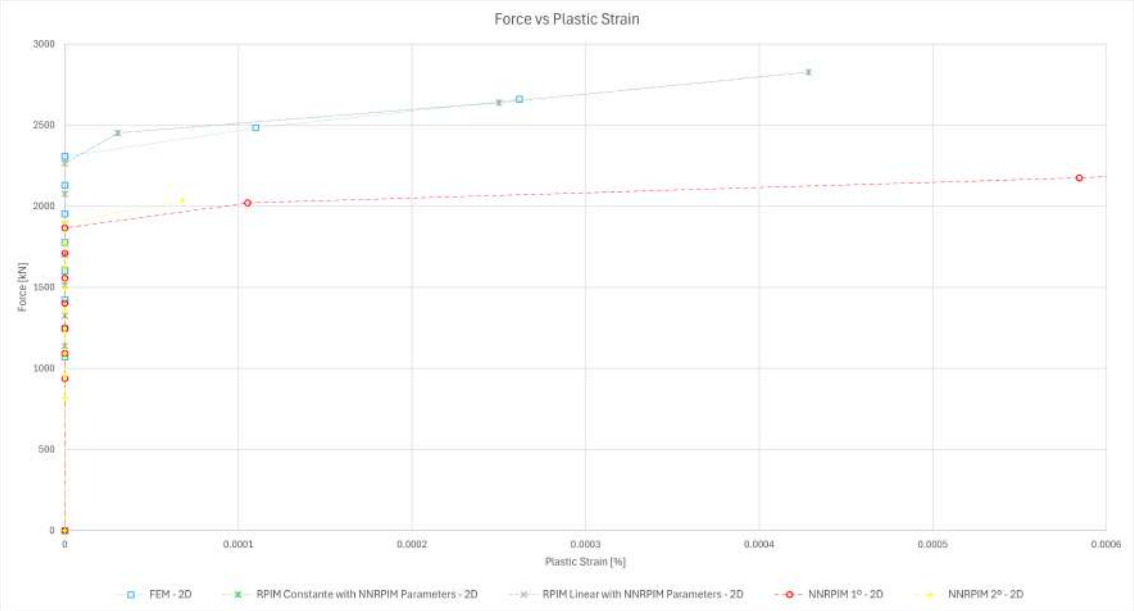

Figure 6.104: Graphic Force versus Plastic Strain of the T-beam with b=400 [mm] from 2D simulations in point A

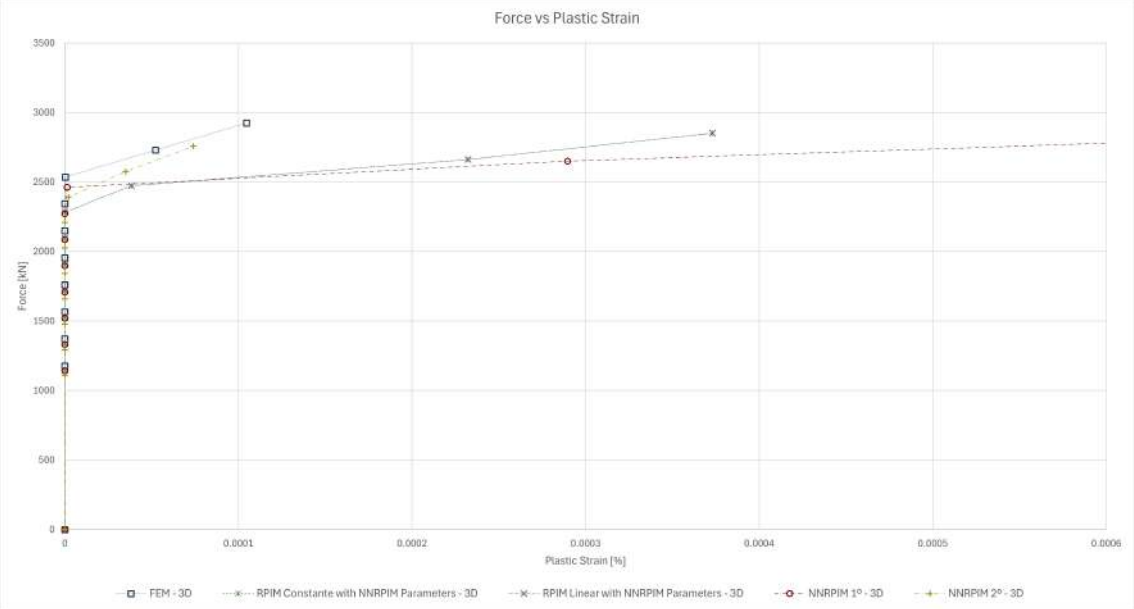

Figure 6.105: Graphic Force versus Plastic Strain of the T-beam with b=400 [mm] from 3D simulations in point A

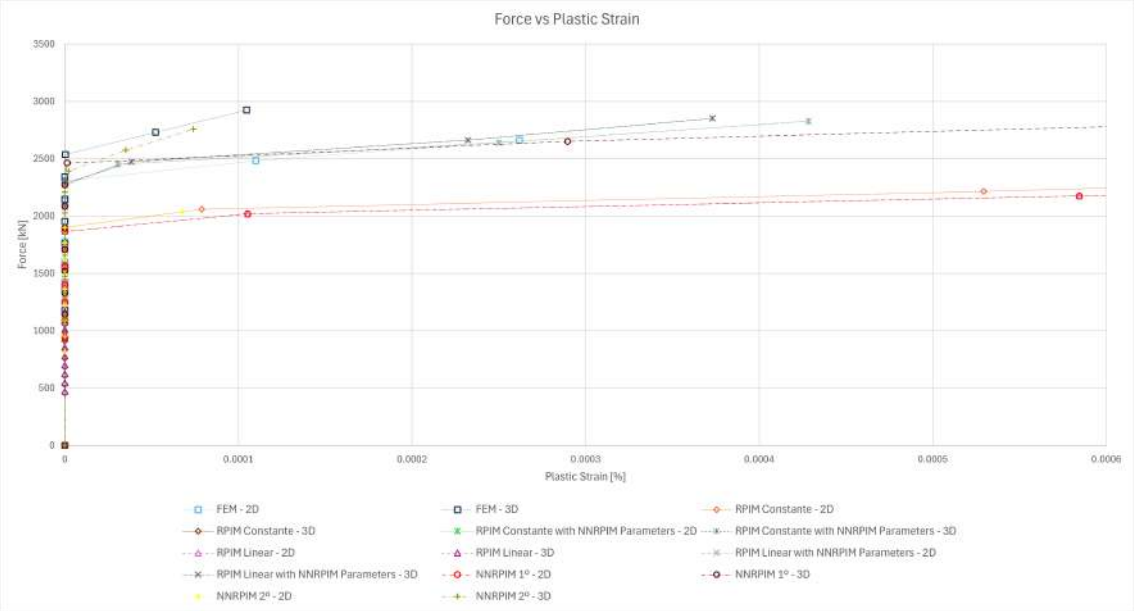

Figure 6.106: Graphic Force versus Plastic Strain of the T-beam with b=400 [mm] from simulations in point A

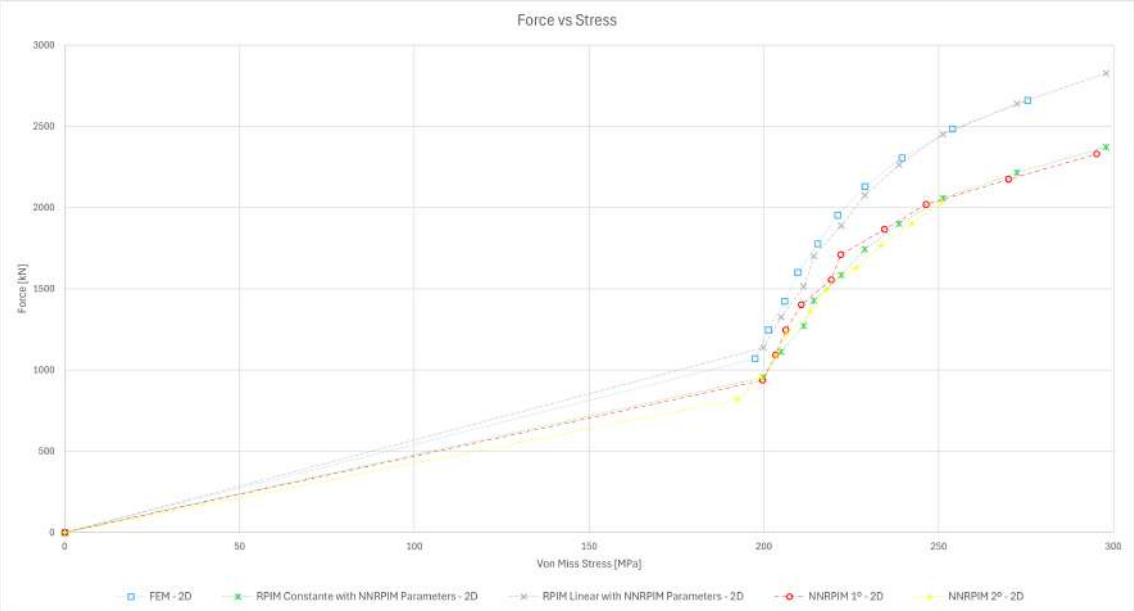

Figure 6.107: Graphic Force versus Stress of the T-beam with b=400 [mm] from 2D simulations in point B

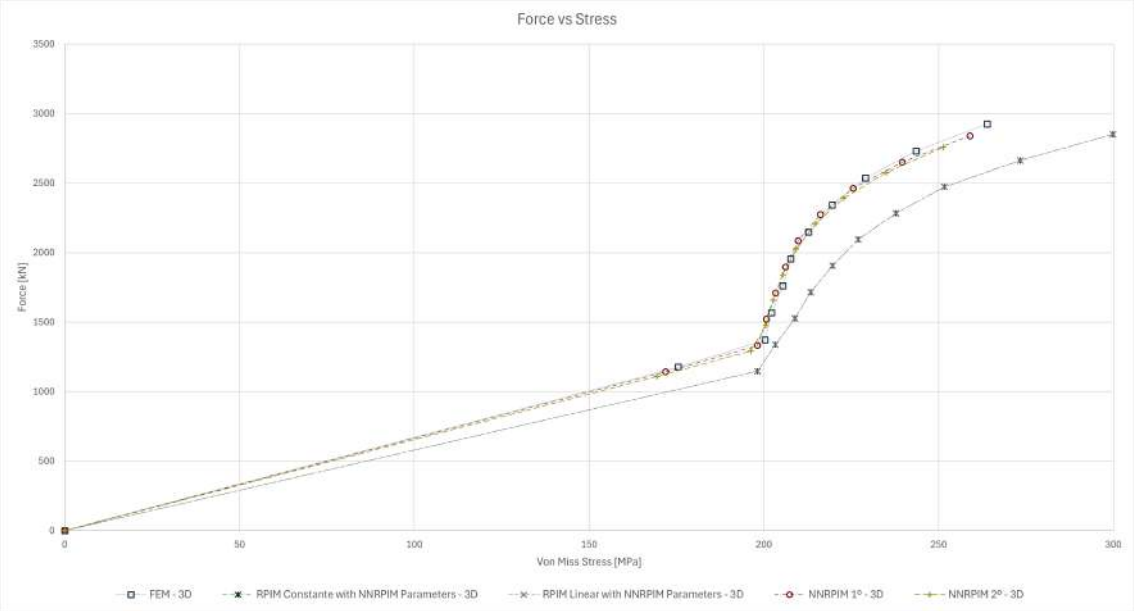

Figure 6.108: Graphic Force versus Stress of the T-beam with b=400 [mm] from 3D simulations in point B

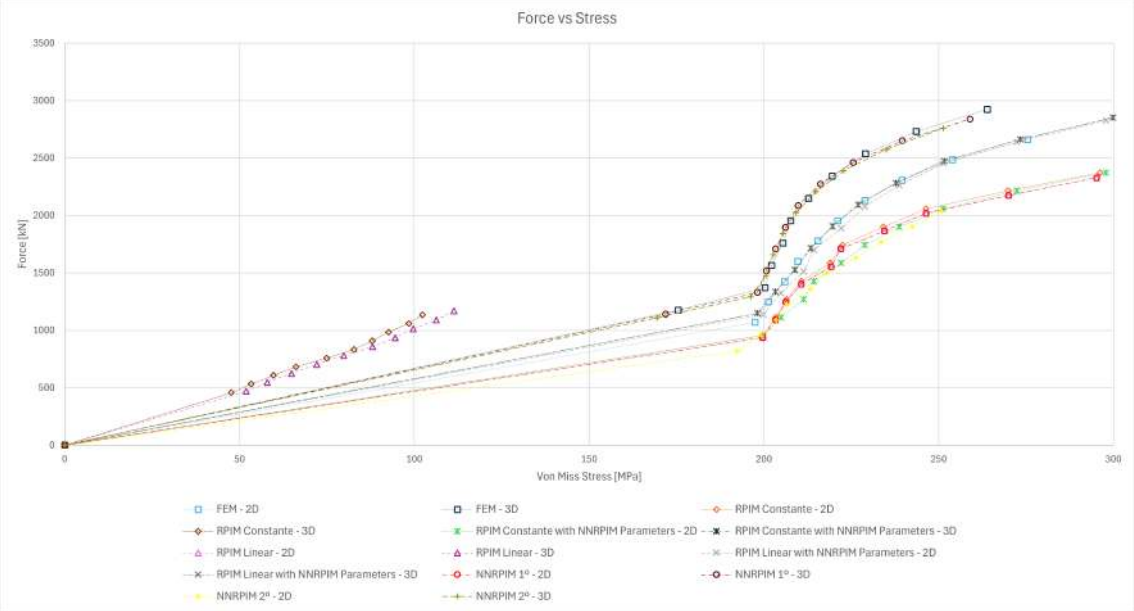

Figure 6.109: Graphic Force versus Stress of the T-beam with b=400 [mm] from simulations in point B

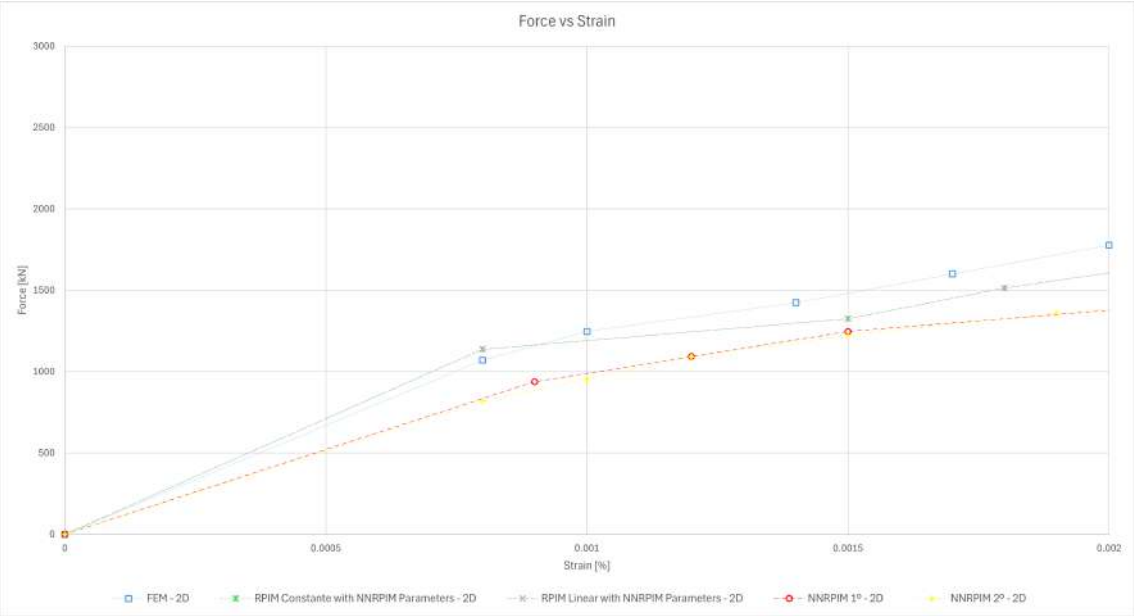

Figure 6.110: Graphic Force versus Strain of the T-beam with b=400 [mm] from 2D simulations in point B

If we deviate our attention to figures 6.110 and 6.111 we can watch the 2D and 3D graphics for the force versus strain, on point B. Once again, the results presented are very similar between simulations, where the values and curve behavior presented show no relevant distinction.

The next graphic can be observed in figure 6.112. This graphic is the overlapping graphic between the 2D and 3D simulations previously shown in figures 6.110 and 6.111, respectively. The considered 2D and 3D simulations present a very close match, on the other hand, all the RRPIM simulations (with RPIM parameters) present us with lower values in terms of strain by force than the assumed simulations, with the 3D RPIM simulations (with RPIM parameters) being fully disproportional and with exorbitantly low values in comparison.

To finally end the point B analysis, we need to analyze the force versus plastic strain. In figures 6.104 and 6.105 we can see the force versus plastic strain graphic from 2 dimensions and 3 dimensions, respectively. Just like in the force versus strain, for the same point, it's possible to deduce that the simulations are very closely fitting.

Diverting our attention now to figure 6.106, which delivers us the overlapping graphic present in figures 6.104 and 6.105, we can just like in the strain analysis, observe that the 2D and 3D simulations present behaviors closely match, with the RPIM (with RPIM parameters) being the expected exception, with values lower comparatively to the other simulations, and comparatively the 3D case values are very low.

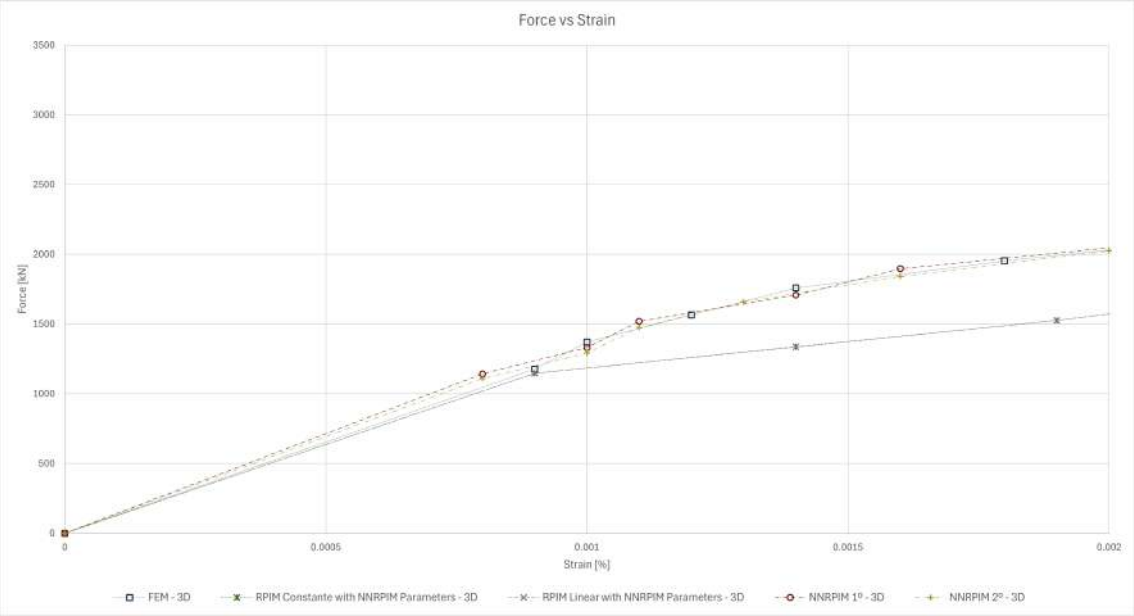

Figure 6.111: Graphic Force versus Strain of the T-beam with b=400 [mm] from 3D simulations in point B

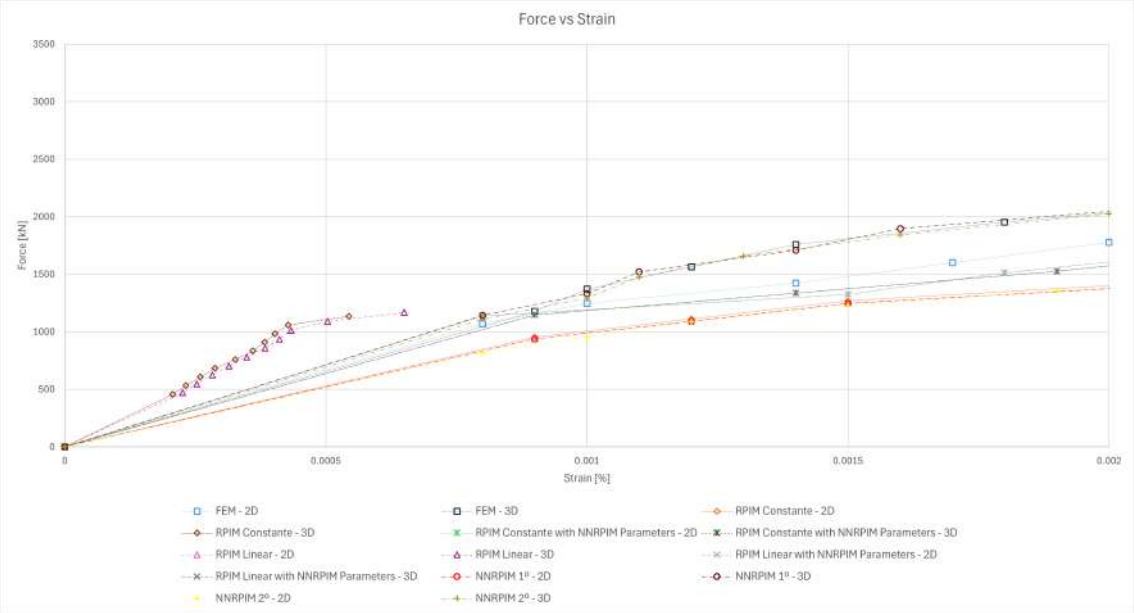

Figure 6.112: Graphic Force versus Strain of the T-beam with b=400 [mm] from simulations in point B

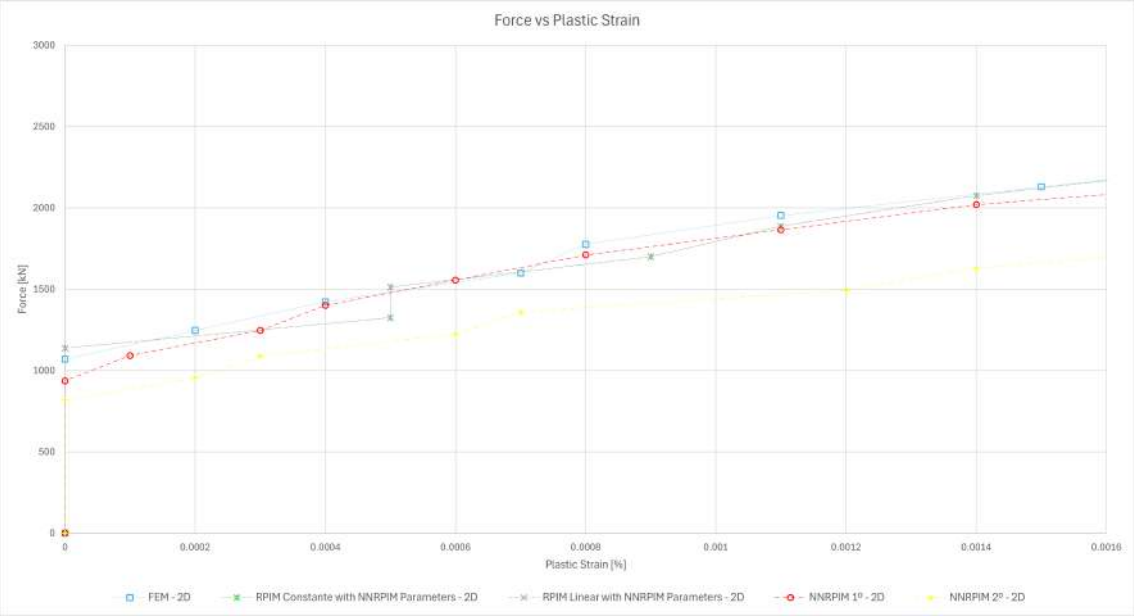

Figure 6.113: Graphic Force versus Plastic Strain of the T-beam with b=400 [mm] from 2D simulations in point B

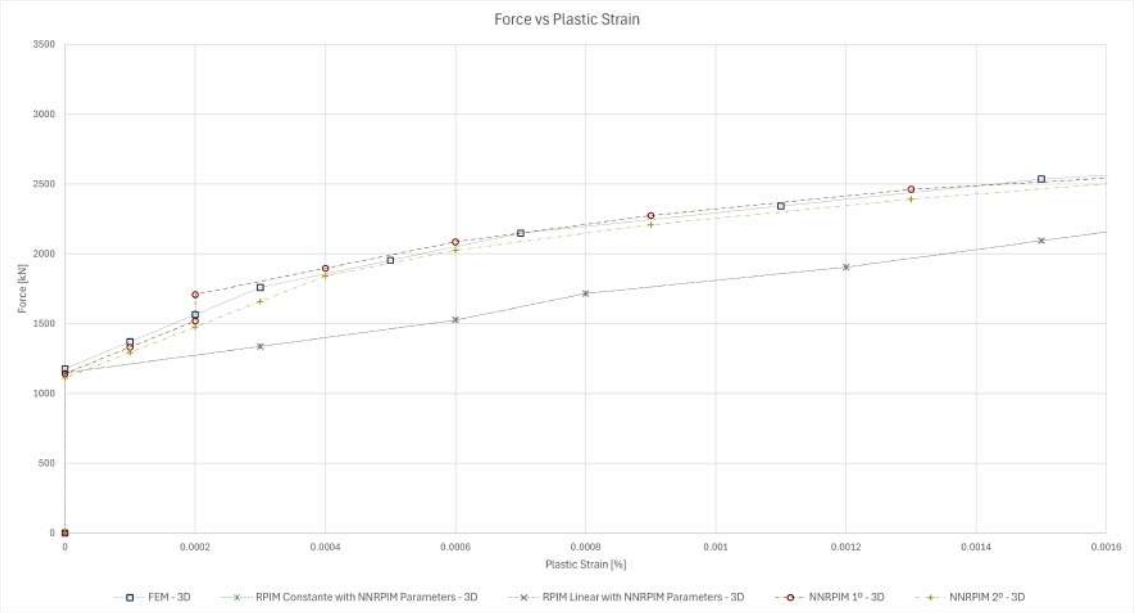

Figure 6.114: Graphic Force versus Plastic Strain of the T-beam with b=400 [mm] from 3D simulations in point B

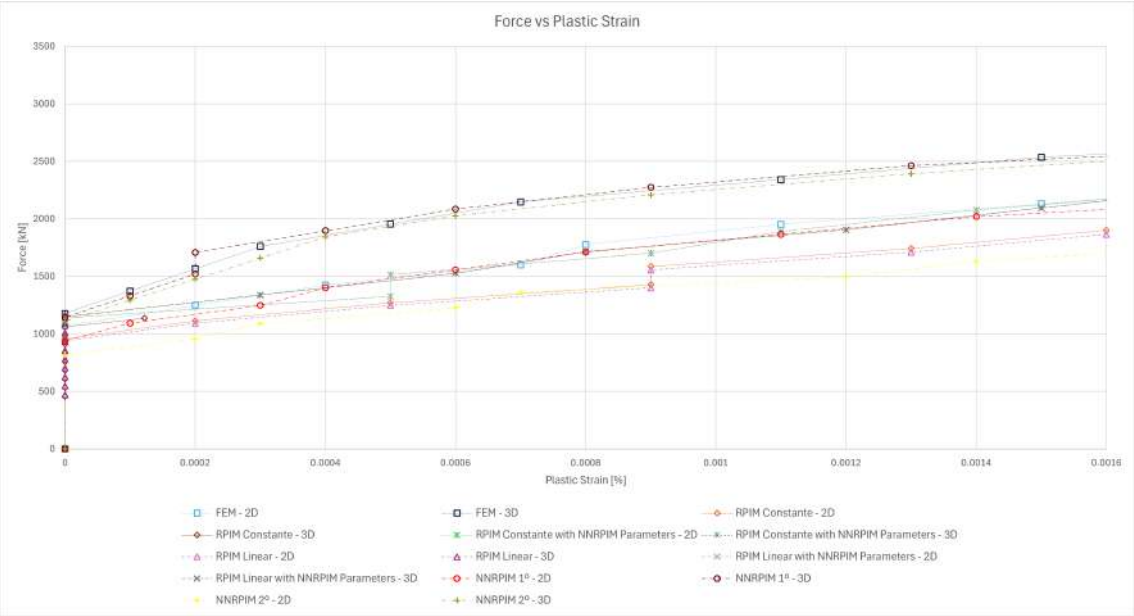

Figure 6.115: Graphic Force versus Plastic Strain of the T-beam with b=400 [mm] from simulations in point B

To terminate the T-beam with b=400 mm study, let's focus our attention on point C, where the study will be about the displacement presented. Figure 6.116 shows us the displacement from the 2D simulations, while figure 6.117 shows us the displacement from the 3D simulations. The simulations give us values and curve behavior very identical to each other, excluding the 2D NNRPIM of the first order.

The overlapping graphic for the force versus displacement can be witnessed in figure 6.118, where the dissimilarity, already cited, of the NNRPIM simulation of first order is more comprehensive. This simulation's curve behavior isn't very different from the rest of the considered simulation, in fact, it's visible that the 2D NNRPIM of the first order curve presents us with indications of conversion to the other simulation. As normal, in this study, the RPIM (with RPIM parameters) presents notorious and perceptible disparities.

To finalize the T-beam studies, we can now observe the tables 6.78, 6.79, and 6.80, which give us the percentual difference between the 2D and 3D applied force, maximum stress, and maximum strain, respectively.

The force difference percentual values reveal a consistency with all the simulation methods, with the RPIM methods being the ones that present the lowest difference value and the NNRPIM methods the highest ones. The stress keeps delivering low percentual difference values that don't show any resemblance with constancy or with linearity. The unpredictability can be found in the strain percentual values as well; however, the difference is that these are much larger than the stress percentual values.

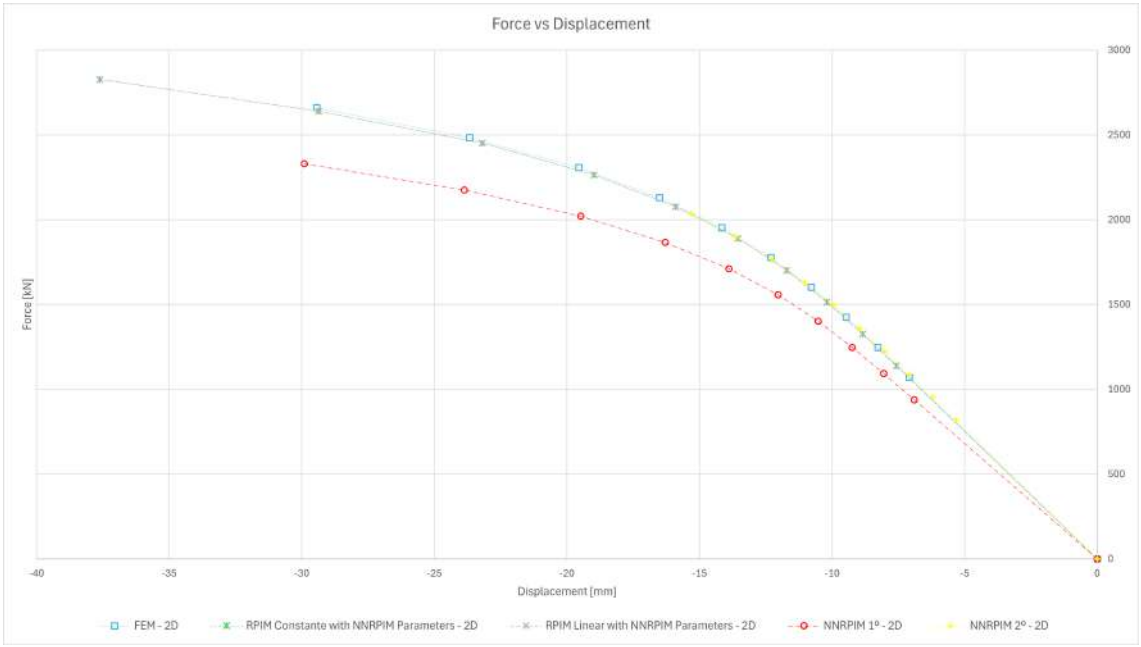

Figure 6.116: Graphic Force versus Displacement of the T-beam with b=400 [mm] from 2D simulations in point C

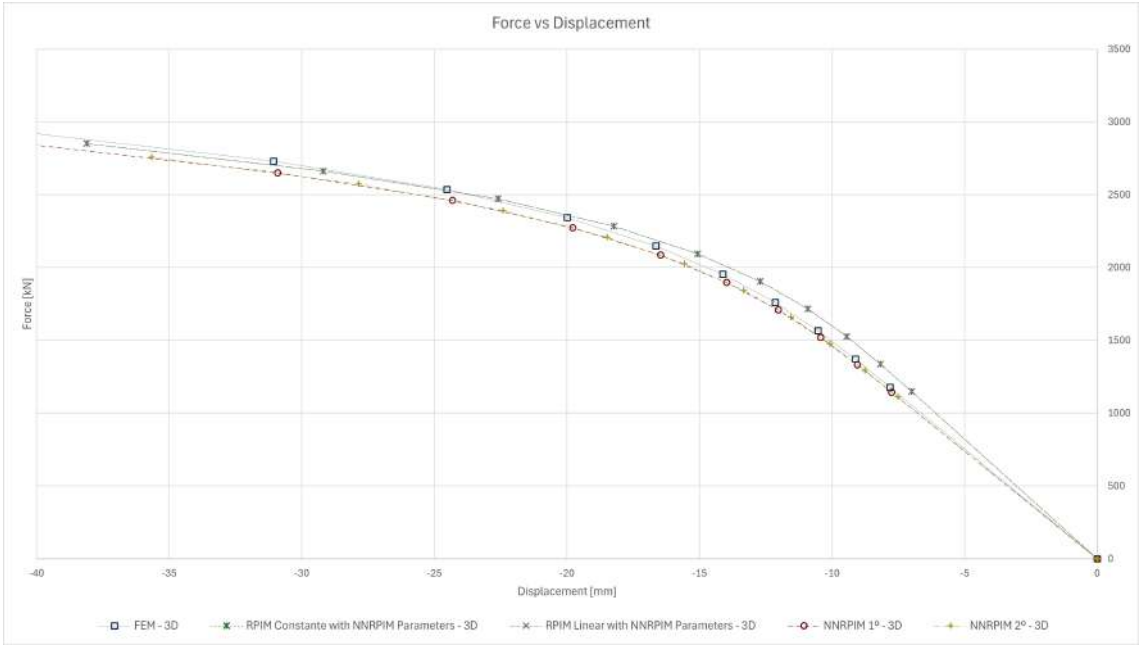

Figure 6.117: Graphic Force versus Displacement of the T-beam with b=400 [mm] from 3D simulations in point C

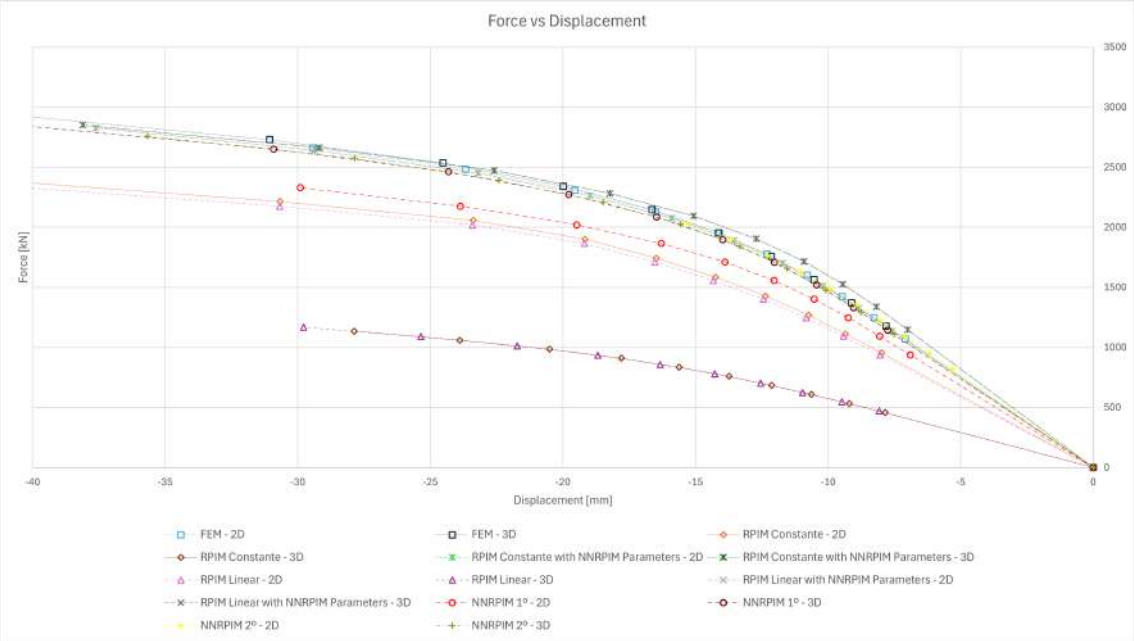

Figure 6.118: Graphic Force versus Displacement of the T-beam with b=400 [mm] from simulations in point C

Table 6.78: Percentual force difference for the T-beam (with b=400 [mm]) 2D and 3D results

Increment	FEM	RPIM Const.	RPIM Linear	NNRPIM 1º	NNRPIM 2º
01	9.05%	0.00%	0.85%	17.95%	26.20%
02	9.05%	0.00%	0.85%	17.95%	26.20%
03	9.05%	0.00%	0.86%	17.96%	26.20%
04	9.05%	0.00%	0.86%	17.96%	26.20%
05	9.05%	0.00%	0.86%	17.95%	26.20%
06	9.05%	0.00%	0.86%	17.96%	26.20%
07	9.05%	0.00%	0.86%	17.95%	26.20%
08	9.05%	0.00%	0.86%	17.95%	26.20%
09	9.05%	0.00%	0.86%	17.96%	26.20%
10	9.05%	0.00%	0.86%	17.96%	26.20%

Table 6.79: Percentual stress difference for the T-beam (with b=400 [mm]) 2D and 3D results

Increment	FEM	RPIM Const.	RPIM Linear	NNRPIM 1º	NNRPIM 2º
01	2.42%	0.08%	0.08%	1.80%	3.71%
02	0.54%	0.36%	0.36%	0.42%	0.78%
03	0.18%	0.28%	0.28%	0.05%	0.32%
04	0.27%	0.70%	0.70%	0.89%	0.09%
05	1.11%	0.01%	0.01%	0.51%	1.37%
06	1.21%	0.03%	0.03%	1.57%	1.07%
07	1.17%	0.98%	0.98%	1.34%	1.82%
08	1.10%	1.16%	1.16%	1.99%	0.91%
09	0.08%	1.72%	1.72%	1.40%	1.29%
10	0.11%	1.59%	1.59%	2.00%	5.47%

Table 6.80: Percentual strain difference for the T-beam (with b=400 [mm]) 2D and 3D results

Increment	FEM	RPIM Const.	RPIM Linear	NNRPIM 1º	NNRPIM 2º
01	11.11%	11.11%	11.11%	11.11%	0.00%
02	23.08%	6.67%	6.67%	16.67%	9.09%
03	6.67%	14.29%	14.29%	13.33%	7.69%
04	5.56%	8.33%	8.33%	0.00%	6.25%
05	4.76%	6.90%	6.90%	0.00%	0.00%
06	3.85%	8.57%	8.57%	0.00%	0.00%
07	9.09%	9.09%	9.09%	6.06%	15.15%
08	11.63%	12.07%	12.07%	6.98%	15.38%
09	15.52%	13.33%	14.10%	8.62%	25.00%
10	17.72%	14.42%	14.42%	11.39%	35.71%

6.5.3 RPIM Simulations with RPIM Parameters

As we saw in this chapter, the RPIM simulations with RPIM parameters didn't present the proper expected results. The images presented in figures 6.44 to 6.118 give us the obtained results from the simulations. During the analysis of all the graphics and images presented in subchapters 6.5.1 and 6.5.2, we can affirm that the simulations in question are inaccurate and that it is possible to conclude in several force versus stress graphics. In these graphics, we can see that the linear behavior doesn't present us with the same stiffness as the rest of the simulations. For these reasons, the rule was implemented that for all RRPIM simulations the parameters values used will be with the NNRPIM parameters values. This implementation will affect the simulations executed in the next two chapters 7 and 8.

6.5.4 2D versus 3D Comparative Conclusions

During the subchapter 6.2, it was evident that the 2D simulations presented us with very similar behaviors on the different points and mechanical property values in the analysis, comparable with the 3D simulations. Normally, the 3D force results tend to be slightly higher; inversely, the stress, strain, and plastic deformation tend to be a little inferior when compared to the results of 2D simulations. In the percentual difference tables, we could see that the NNRPIM method of the first order and the RPIM methods present us, in most cases, with a small difference between the 2D and 3D results, suggesting a very consolidated approximation. The FEM method shows us a percentage difference between the 2D and 3D simulations, considerably higher; however, the NNRPIM method with the second degree of the neighborhood is the one that presents the biggest difference between the 2D and 3D studies.

With this examination, we can conclude that the 2D simulations are very precise and very close to the 3D simulations' results, which indicates that their results can be trusted as if it was 3D results. Because of the 3D and 2D extreme similarities, we will continue the rest of the work with 2D simulations for the next structures still to be analyzed.

6.6 Conclusions

In this chapter, we analyze several beams of nonlinear deformation, with multiple simulation types, to show the reliability of the meshless methods' RPIM and NNRPIM. To validate the results, we also use the FEM method, to work, as a standard solution.

The first nonlinear case study was Cook's Membrane in subchapter 6.1, an industry standard problem for the nonlinear studies, where we saw the different behavior that the algorithms KT0, KT1, and KT-ALL have on the same problem. For this membrane study, we confirm that the KT0 algorithms produced less accurate/realistic solutions, while the KT-ALL returned results with a more exact/realistic solution. This conclusion confirms the claim that the KT-ALL algorithm is the more reliable one, while the KT0 is considered the less precise.

During the 2D and 3D comparative analysis, we could observe that the subchapters 6.2, 6.3, 6.4, and 6.5 are an integral part of this process, being a very significant part of this chapter. The 2D simulations proved that they are extremely similar to the 3D simulations in terms of curve trajectories, applied loads, and stress behavior, with the strain, deformations, and plastic strain variables presenting a bigger discrepancy than the other mentioned variables. More specifically, we could conclude that the force values from the 2D simulations are slightly inferior to the ones presented by the 3D simulations, with the strain, plastic strain, and deformation being the inverse, which means that the 2D solutions' values are slightly larger than the 3D simulations' results. When we compare the 2D results with the 3D ones, we can conclude that the RPIM and NNRPIM (of the first order) methods are the ones that offer the smallest percentual difference in most cases, surpassing the FEM methods, on this particular point. Thus, once again, we can confirm that the 2D simulations are reliable and trustworthy, providing us with values, results, and behaviors remarkably similar to those of the 3D simulations.

7 Elastoplasticity Analysis of a Portic

In this chapter, a portic structure will be analysed using the same numerical methods as in previous sections. To achieve this goal, we will select a structure from the literature and reproduce the simulation, aiming to obtain the same results in the linear phase as those reported.

7.1 Portic Structure

The selected structure is described in the literature paper titled "*Large Deformation Elastic-plastic Analysis of Space Frames*" by Reza Abbasnia and Aslam Kassimali.[5] In this paper, the structure undergoes a nonlinear simulation using the Newton-Raphson algorithm, with a force-based formulation method. This means that the nonlinear aspect of the simulation presented in the paper will differ from the nonlinear simulations performed with the FEMAS software, where the simulations are conducted using FEM, RPIM, and NNRPIM methods, being the meshless methods ones calculated with a weak-base formulation.

Figure 7.1 shows the chosen structure, which is made from a cross-section shaped like a circle. This geometric form poses an interesting challenge in FEMAS: in a 2D simulation, we can assign a constant thickness, but not a thickness determined by a function, which would be necessary to simulate a true circular cross-section. To address this issue, we divide the circular shape into as many parts as possible, approximating it with rectangular shapes that together simulate a circular cross-section, as shown in figure 7.3. For this particular problem, it was decided that the cross-section should be divided into 10 separate sections.

Figure 7.2 displays the simulated structure produced in FEMAS, with 7513 nodes and 6820 square elements, which represents half of the chosen structure shown in figure 7.1. The reason for the noted structure to be half is that the e value will be 0, allowing us to apply the symmetry structure's rule.[5] Figure 7.1 also provides information regarding the material properties and the dimensions of the structure; however, as we can see, these dimensions and properties do not conform to the international system.[5] The following table 7.1 shows the conversion of all dimensions and properties to the international system.

Now we can begin defining the rectangular thicknesses to use in the FEMAS program for the simulations. Table 7.2 presents the thickness values assigned in FEMAS to achieve an area similar to the original circular cross-section, while figure 7.3 helps us visualize the differences between the cross-sections. As in previous simulations, we will use the NNRPIM parameters in the RPIM simulations. The goal of this chapter is to validate FEMAS and confirm its viability, rather than to

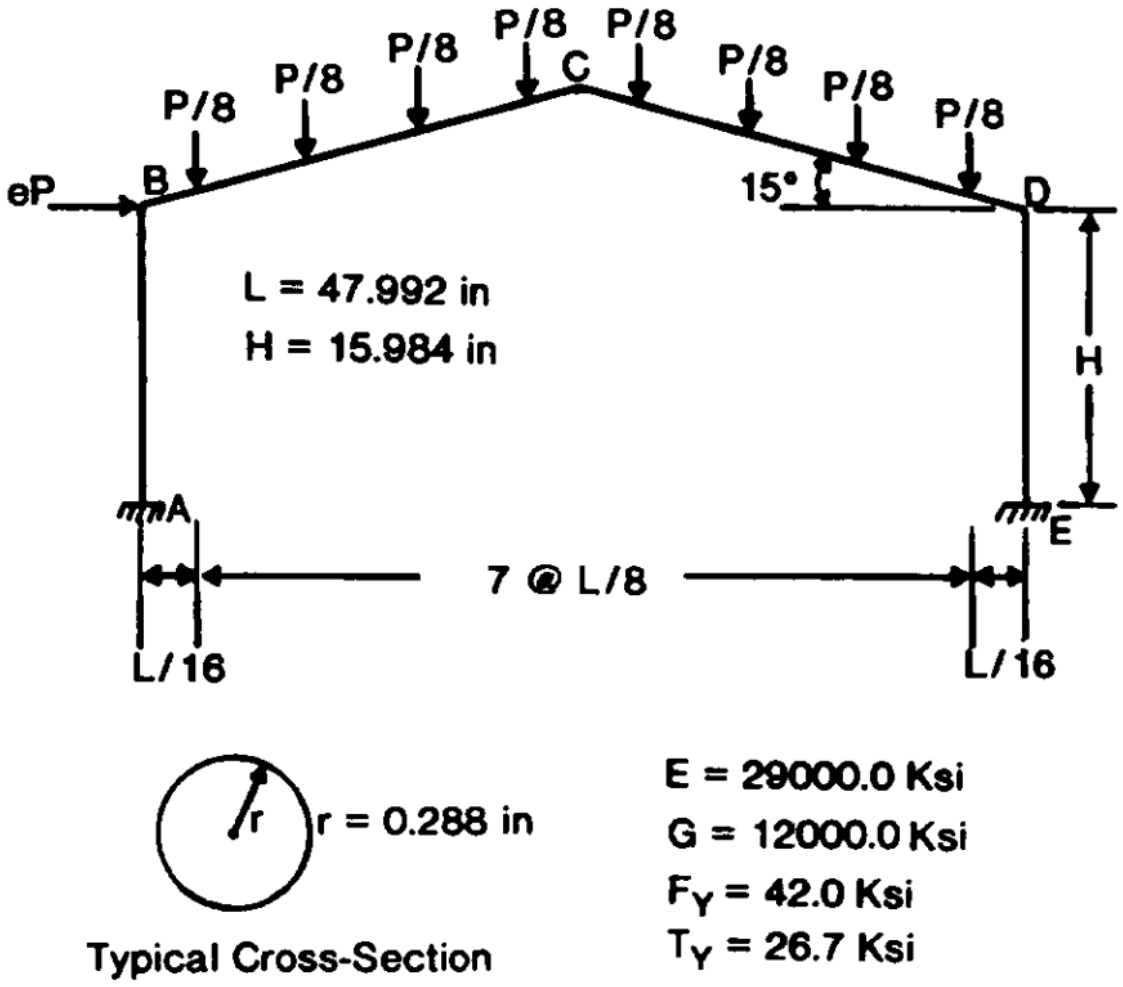

Figure 7.1: Choosen confirmation strucuture [5]

Table 7.1: Variables' problem conversion to the standard international system 7.1

Variables	Original Problem Values	International System Conversion
E - Young's modulus	29 000.0 [Ksi]	199 947 961 502 [Pa]
G - Second polar moment of area	12 000.0 [Ksi]	82 737 087 518 [Pa]
F_y - Yield strength	42.0 [Ksi]	289 579 806.36 [Pa]
r - Radio	0.288 [in]	7.3152 [mm]
L - Structure length	47.992 [in]	406 [mm]
H - Column height	15.984 [in]	1 219 [mm]

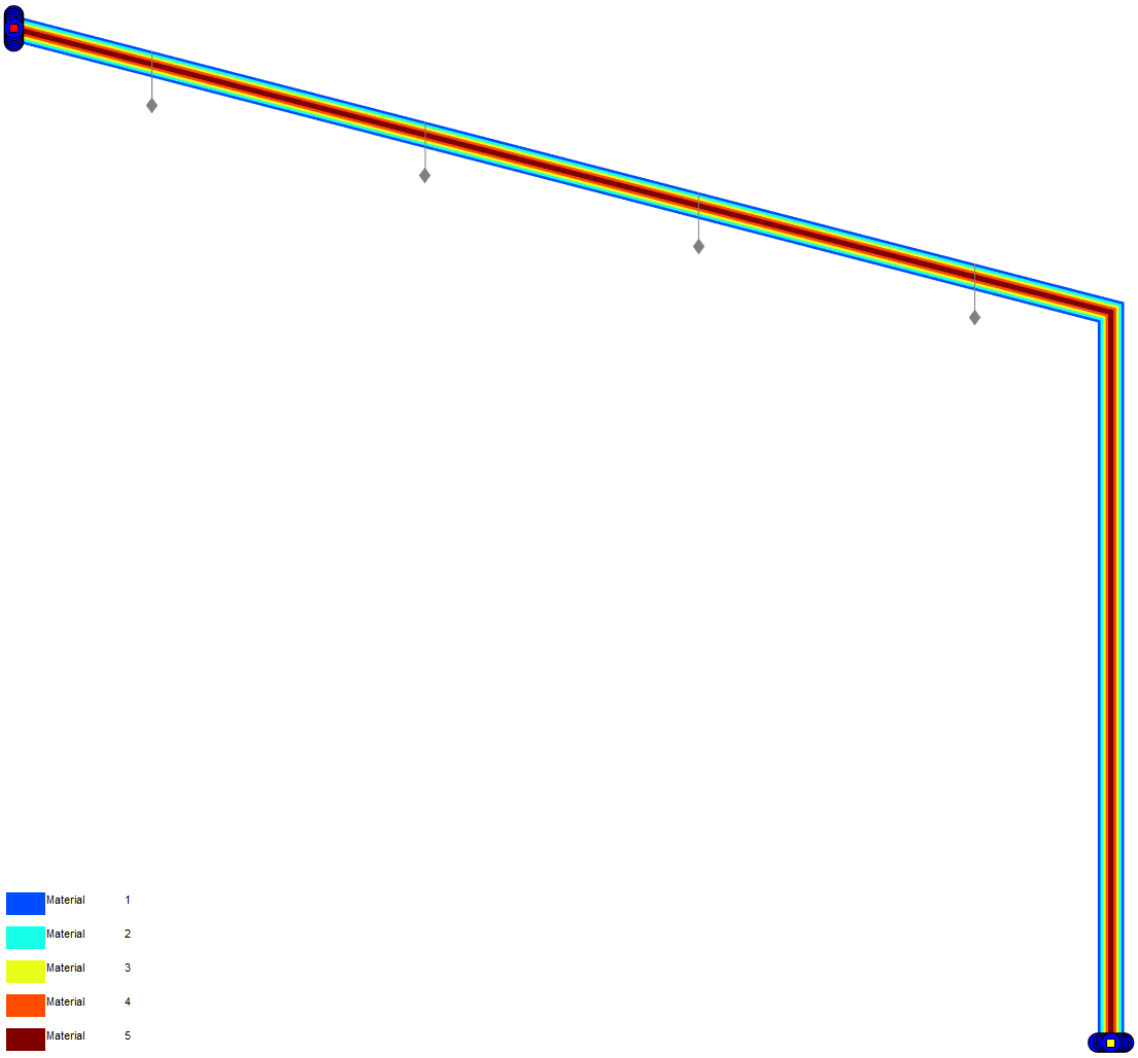

Figure 7.2: Structure in the FEMAS software

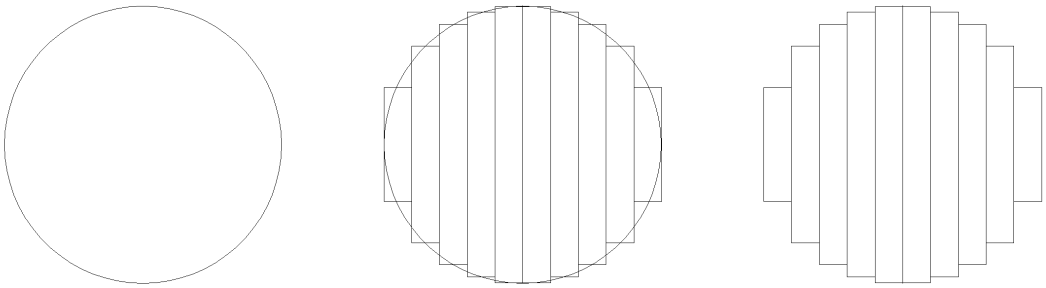

Figure 7.3: Cross-sections from the confirmation structure

Table 7.2: Thickness by FEMAS patch

Patch	Femas Thickness
1 - Dark Blue	5.9801mm
2 - Ligth Blue	10.3798 mm
3 - Yellow	12.6322 mm
4 - Orange	13.928 mm
5 - Bronw	14.5319 mm

compare results across different simulation types and methods. Therefore, we will only conduct simulations using FEM, RPIM with a constant base, and NNRPIM with a second degree of neighborhood.

For the FEMAS simulations to function as expected, we need to verify that the area of the modified cross-section is comparable to that of the original circular cross-section. The following equations, 7.1 and 7.2, illustrate the areas of the two cross-sections under discussion. As we can see, the areas of the two cross-sections are essentially the same; in fact, the difference is insignificant.

$$A_{Circular} = \pi \times r^2 = \pi \times 7.3152^2 = 168.1134[mm^2] \tag{7.1}$$

$$\begin{aligned} A_{\text{Rectangulars}} &= 2 \times (A_{\text{Patch 1}} + A_{\text{Patch 2}} + A_{\text{Patch 3}} + A_{\text{Patch 4}} + A_{\text{Patch 5}}) \\ &= 2 \times \text{Width}_{\text{Single Rectangle}} \times \\ &(\text{Thickness}_1 + \text{Thickness}_2 + \text{Thickness}_3 + \text{Thickness}_4 + \text{Thickness}_5) \\ &= 2 \times \frac{7.3152}{5} \times (5.9801 + 10.3798 + 12.6322 + 13.928 + 14.5319) \\ &= 168.1091 \text{ mm}^2 \end{aligned} \tag{7.2}$$

Figure 7.4 shows the original graph from the results obtained in the literature paper and indicates the deflection that occurred at joint C (see figure 7.1 for the location of point C). As shown, there are four types of results in the same graph, but we will focus only on the experimental result, which corresponds to the symmetric

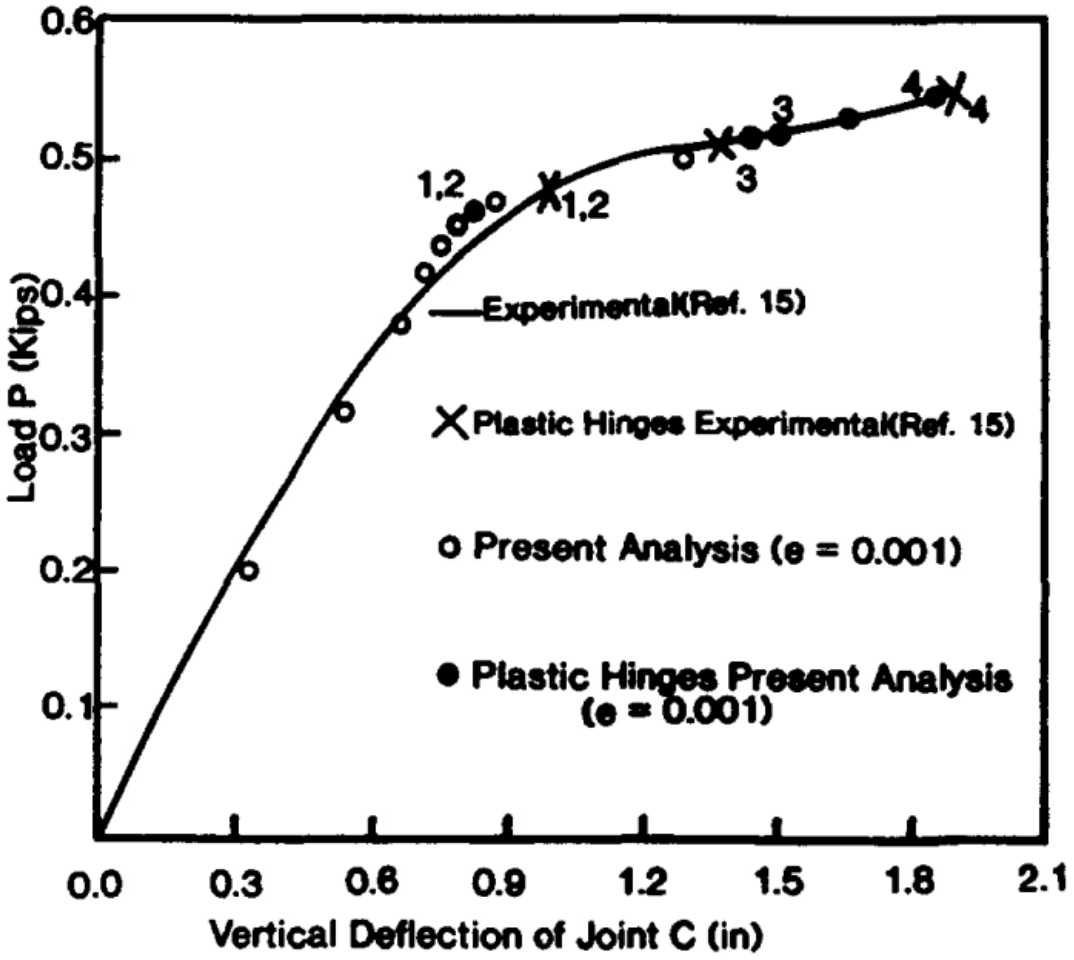

Figure 7.4: Article original graphic [5]

structure; in other words, we will concentrate our attention on the line present in the graph. The next graph, presented in figure 7.5, displays the results obtained from the FEMAS simulations alongside the experimental results from the previous graph (line). As we can see, the linear portion of the FEMAS simulation is extremely close to the comparative results. This allows us to validate and ensure that the FEMAS software provides correct and viable results.

7.2 Conclusions

In this chapter, our focus is to prove that the software in use, FEMAS, is reliable and accurate for mechanical simulations. For this study, we encountered an interesting obstacle; the structure being compared has a circular profile, and that means that to replicate the geometric form as much as possible, and maintain the necessary profile properties, we were forced to divide the circular sections into several rectangular segments. This way, we were capable of simulating the structure and obtaining verification of the expected results.

The successful linear results replication proved that the software FEMAS, in use, is accurate, trustworthy, and reliable, confirming in this way its validity. This val-

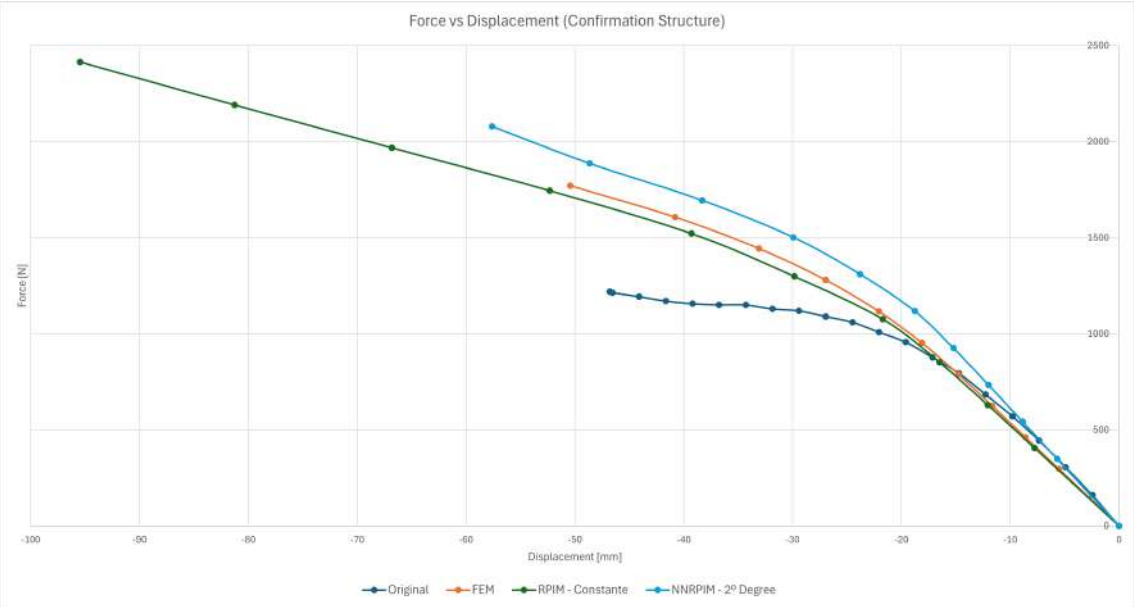

Figure 7.5: Comparative graphic from the FEMAS simulations

idation provides confidence in the work and results elaborated in this work, giving us positive results not just in the FEM method but in the RPIM and NNRPIM methods as well.

8 Frame Structure Analysis

Let us now analyze the final structure studied in this dissertation, for which four different simulations were performed with varying dimensions. This structure is composed of IPN beams and HEB columns, with the four configurations having the dimensions indicated in table 8.1.

8.1 Frame Structure

Figure 8.1 shows the geometry of these structures, with the positions of points A to H visible. For these studies, we will focus on points A, B, D, F, and H. In the first two points (A and B), we will study the stress involved, in point D, we will analyze the plastic strain, and in the two final points (F and H), we will focus on displacement. The material characteristics assumed are 200 MPa for the yield stress, 200 GPa for the Young's modulus, 20 GPa for the tangent modulus, and 0.3 for the Poisson's coefficient. For this last study, we used the FEM, RPIM with a constant base (with NNRPIM parameters), and NNRPIM with first and second degree of neighborhood simulations. These simulation methods were chosen because they present us with the best results, as analyzed in the chapter 6. For all four structures examinations, we used a square mesh with the numbers of nodes and elements visible in the table 8.2, as we can observe, the number of nodes and elements change, this increment is due to the distortion occurring in the column/beam connection as we can observe in the figures 8.2 and 8.3. The locations of the points in analysis in this particular study are present in the following table 8.3. As we can analyze, there are some small differences in the points' locations, which are due to the change in dimensions of the HEB and the IPN laminated profiles; however, the locations of the points difference are so small that it is considered irrelevant, and that allows us to say that the points in question are the same geometrically.

By carefully analyzing figure 8.4, we can see the different mesh groups and their respective locations in the structure in the analysis. As stated earlier, the structural columns are from HEB steel profiles, and the beams are from IPN steel profiles. In figure 8.5 we can visualize the different steel profile geometries, as well as their design variables. Table 8.4 presents the different mesh group thicknesses considered and

Table 8.1: Dimensions for the different sizes of the structure

Structures	IPN dimensions	HEB dimensions
First	IPN 280	HEB 200
Second	IPN 320	HEB 220
Third	IPN 360	HEB 240
Fourth	IPN 400	HEB 260

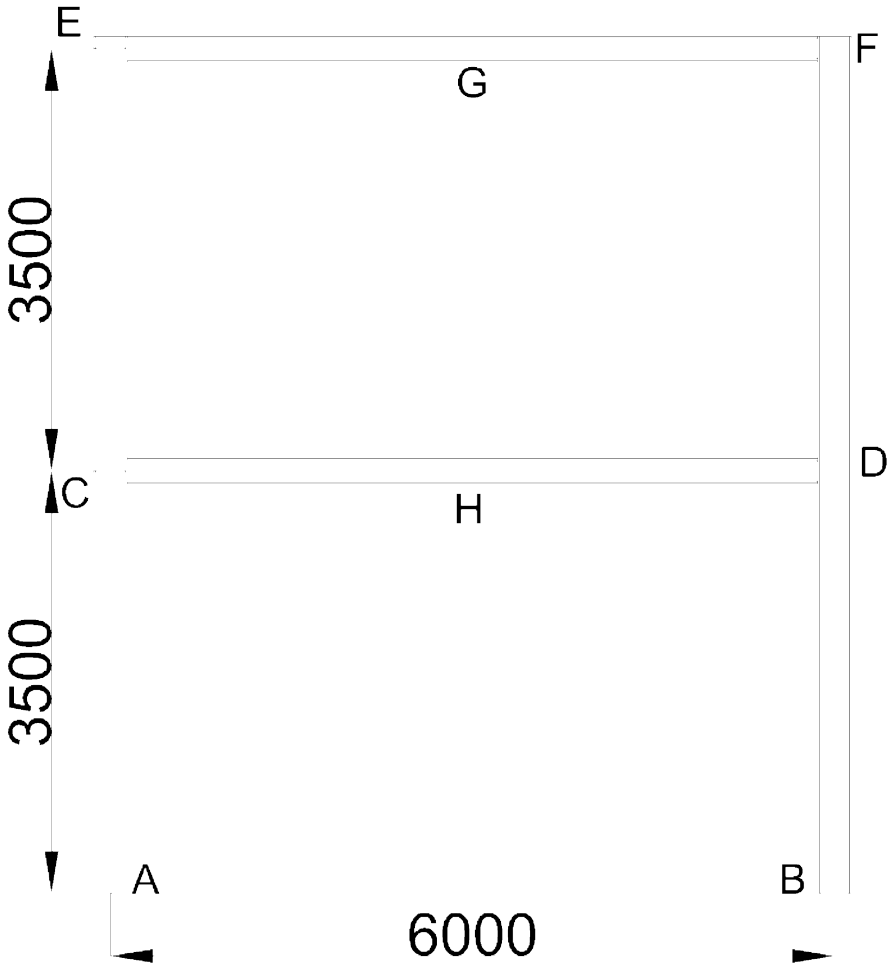

Figure 8.1: Final structure dimensions

Table 8.2: Number of nodes and square elements from the final structures in the analysis

Structures	Nodes' Number	Elements' Number
IPN 280 with HEB 200	8 960	8 064
IPN 320 with HEB 220	9 728	8 836
IPN 360 with HEB 240	10 112	9 222
IPN 400 with HEB 260	10 480	9 592

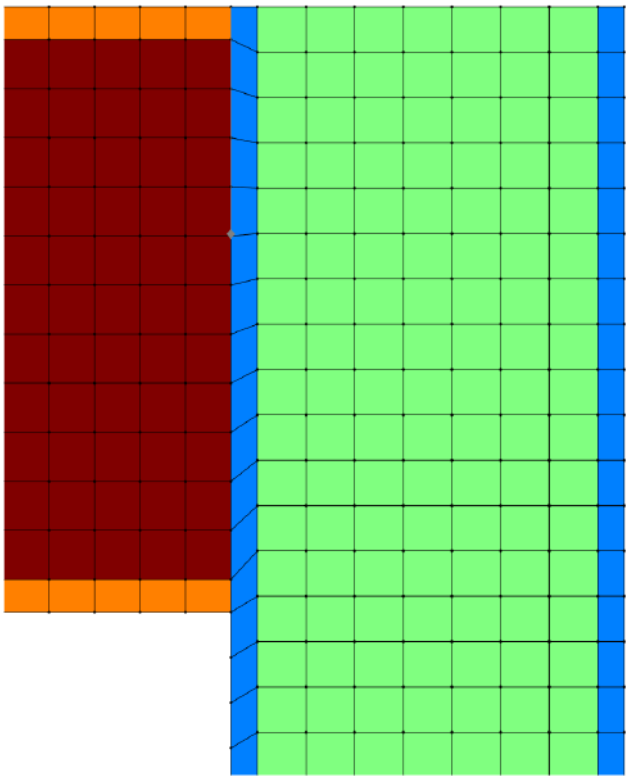

Figure 8.2: Mesh distortion from the upper beam with the column

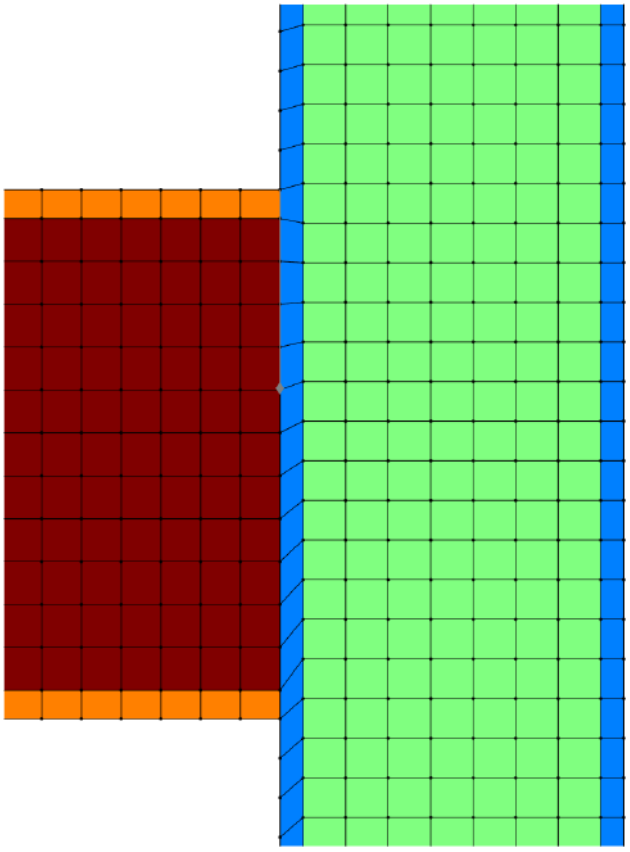

Figure 8.3: Mesh distortion from the lower beam with the column

Table 8.3: Points A, B, D, F, and H locations, in millimeters, to the different structures, in a 2D plan

Structure Type	Points A		Points B		Points D		Points F		Points H	
	x	y	x	y	x	y	x	y	x	y
First	100	29.8347	6100	29.99608	6012.1429	3745.098	6012.1429	7490.1961	3015.0259	3767.8286
Second	110	30.1681	6110	30.0392	6013.5714	3754.902	6013.5714	7509.8039	3014.9223	3734.1444
Third	120	30	6120	30.1176	6014.7143	3764.7059	6014.7143	7499.2941	3014.9741	3750
Fourth	130	29.8319	6130	29.9611	6016.0714	3745.1362	6016.0714	7520.2335	3015.0262	3766.2182

Table 8.4: 2D mesh groups thickness to the frame structure analysis

Structures	Group 1 (variable b from HEB)	Group 2 (variable e from HEB)	Group 3 (variable b from INP)	Group 4 (variable e from INP)
First structure (HEB200 with INP280)	200 [mm]	9 [mm]	119 [mm]	10.1 [mm]
Second structure (HEB220 with INP320)	220 [mm]	9 [mm]	131 [mm]	11.5 [mm]
Third structure (HEB240 with INP360)	240 [mm]	10 [mm]	143 [mm]	13 [mm]
Fourth structure (HEB260 with INP400)	260 [mm]	10 [mm]	155 [mm]	14.4 [mm]

the laminated profile dimensions.

Figure 8.4 shows us not just the square mesh groups but the structure with the applied forces and their respective locations. As we can observe, the structure is subjected to a vertical and horizontal load; the vertical load is a constant distributed force, applied in the two beams, in the negative direction, while the horizontal load is applied in the left column, in a positive direction, at the two beams' neutral line height. The total horizontal applied force value is equal to 10% of the total vertical load value.

8.2 Structure Analysis

As discussed earlier, in this chapter, we will study the von Mises stress, displacement, and plastic strain. To better understand the behavior of the four structures, the following figures from (8.6 at 8.25) provide visual context. In these figures we will visualize the FEM, RPIM, and NNRPIM methods' results.

Let us now analyze the results obtained, starting from point A.

8.2.1 Point A

As outlined in the previous section, in the point A study, we will focus on the stress endured and calculated from the different simulation methods.

Frame Structure HEB200 with IPN280

The graphic of the first structure to point A is shown in figure 8.6, where it's possible to see that the NNRPIM results don't offer the same stiffness value as the FEM and RPIM results. The RPIM result, even though it has the same stiffness as the FEM result, enters the nonlinear state much sooner and by the end of the simulation, presents us with values much closer to the NNRPIM results' values.

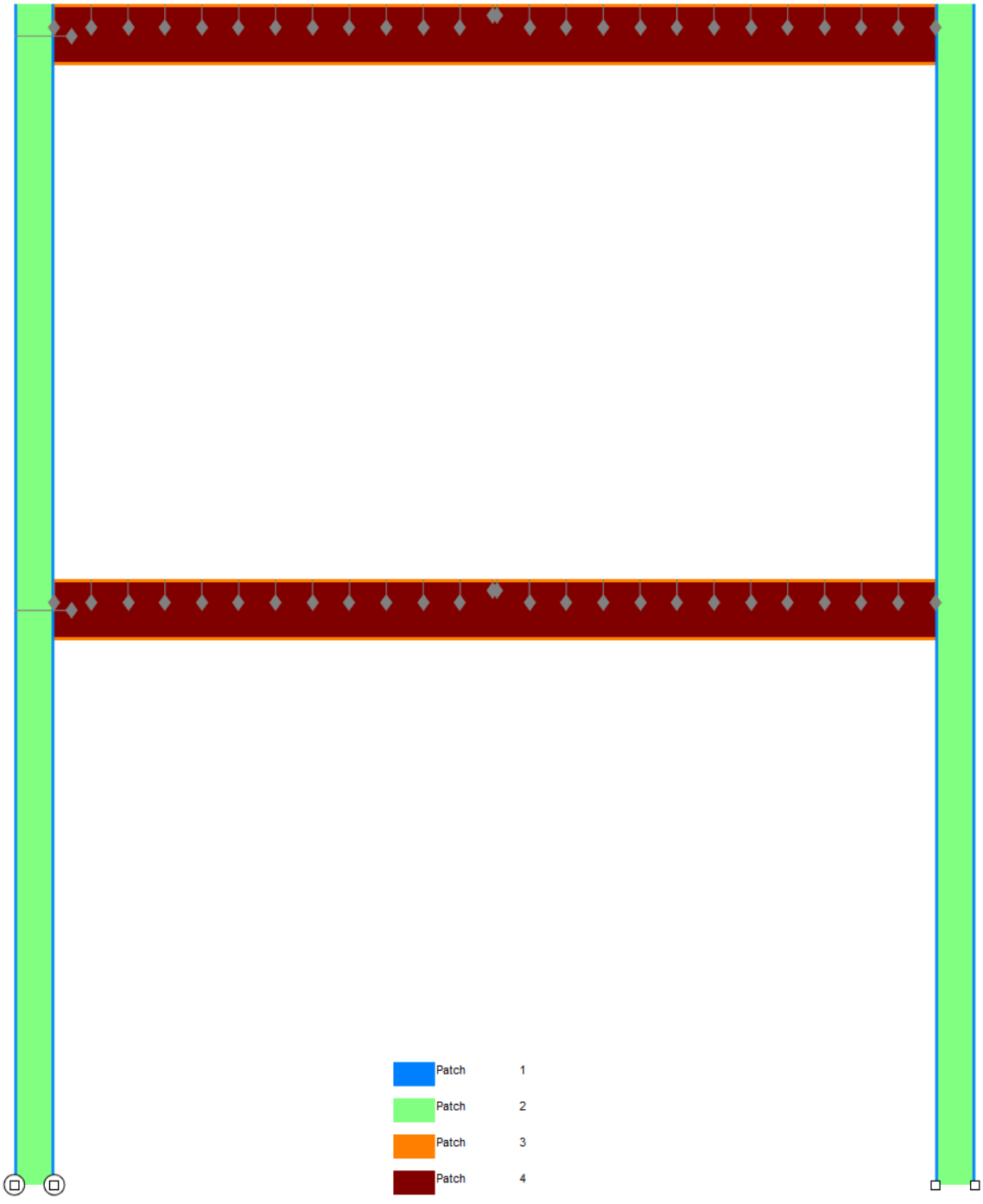

Figure 8.4: Mesh groups from the final structure

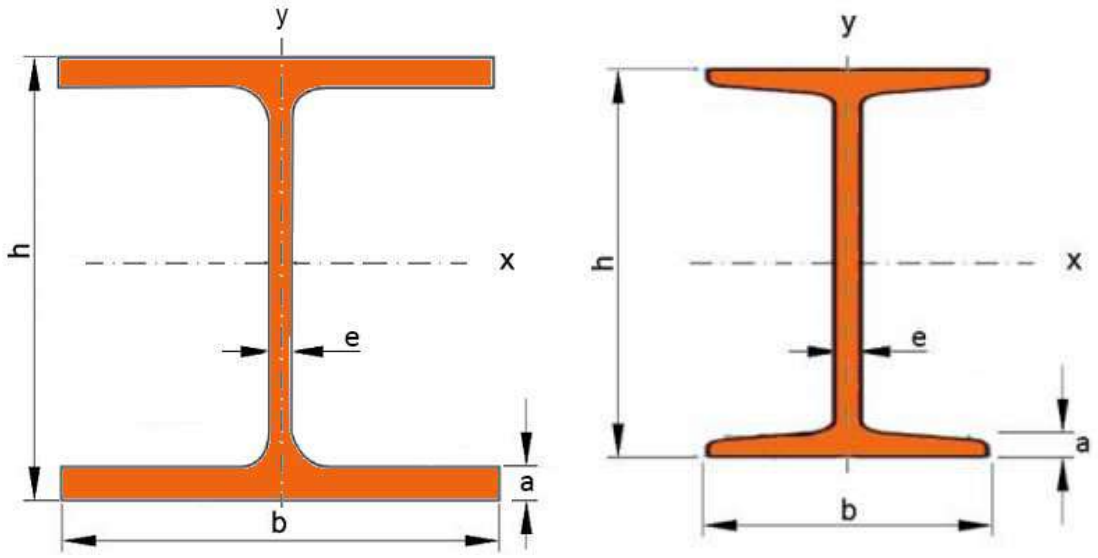

Figure 8.5: Steel profiles HEB and IPN geometry form and their variables dimensions, respectively[6, 7]

However, the bigger problem with the results is indeed the lack of overlap in the linearity state, for the meshless methods compared with FEM.

Frame Structure HEB220 with IPN320

In point A from the second structure, we can see a complete overlap from the FEM and RPIM simulations' results. In the case of the NNRPIM simulations, we see that these two behaviors are significantly different from the 2 previously mentioned methods, having a stiffness difference, and because of that, not even overlapping in the linear state of the simulations, with the FEM results. This can be observed in figure 8.7, where the simulations' results were put on a graphic.

Frame Structure HEB240 with IPN360

Figure 8.8 presents us with the third structure results, where it's possible to scrutinize the results in question. The FEM simulation's result is very close to the RPIM simulation's result, particularly in the first stage of the simulation, showing an overlap between these two methods' results. The fact that the RPIM result presented itself as an overlap of the FEM result gives us the confidence to believe it and have confidence in its validity, unlike the NNRPIM values, which presented a different stiffness. It's worth mentioning that the two NNRPIM curves are overlapping each other.

Frame Structure HEB260 with IPN400

To finalize the point A analysis, we need to turn our attention to figure 8.9, where it's possible to see the stress versus force graphic in the fourth structure. In this fourth structure, we can observe a resemblance between the NNRPIM simulation results and the FEM simulation results. The difference in the last point A analysis is

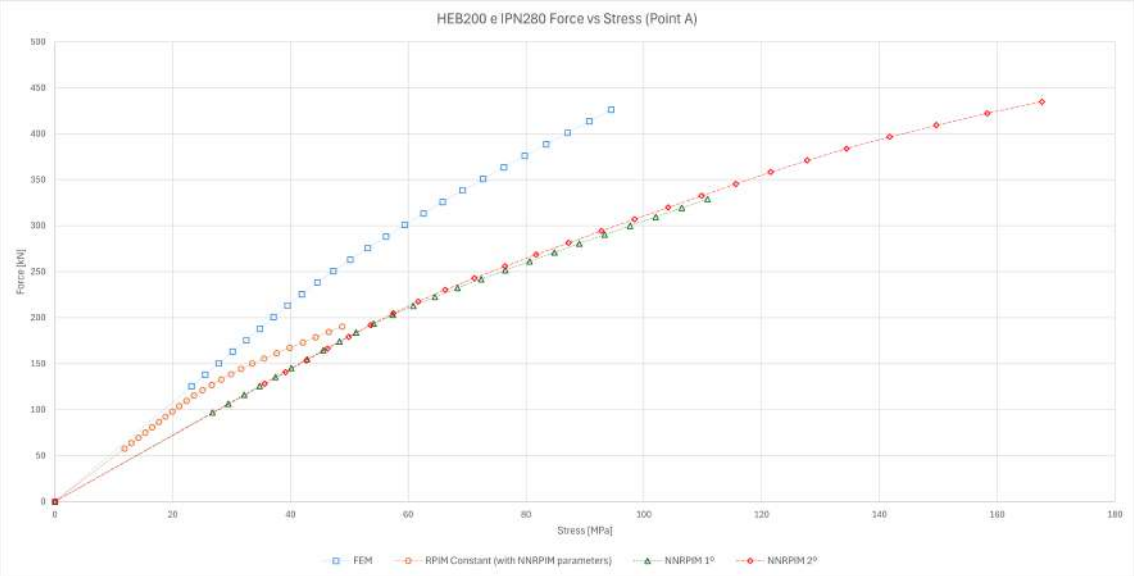

Figure 8.6: Graphic from point A of the first structure (HEB200 with IPN280), with the stress results

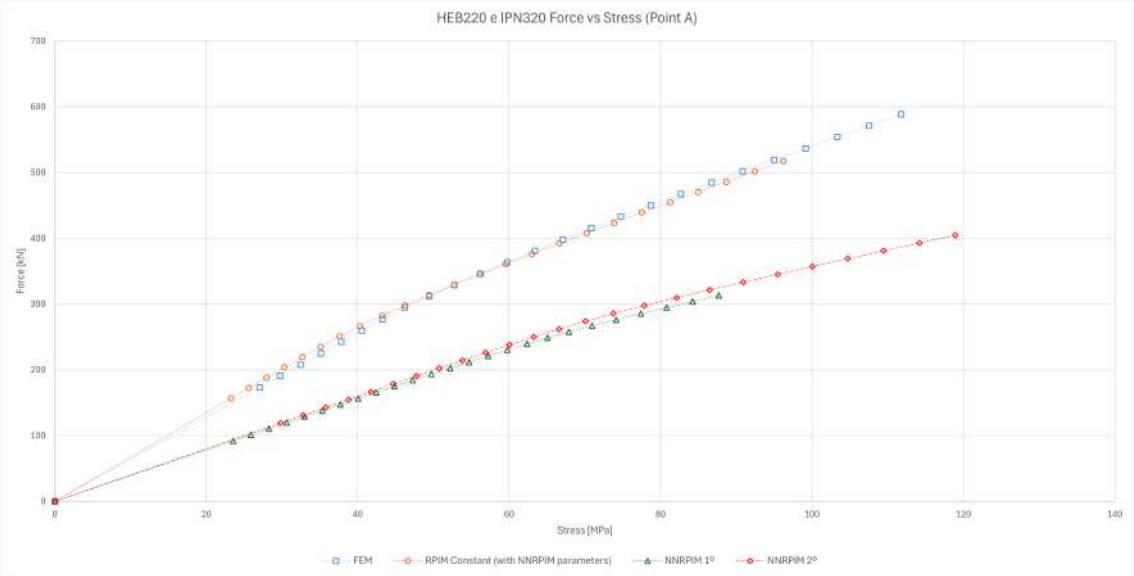

Figure 8.7: Graphic from point A of the second structure (HEB220 with IPN320), with the stress results

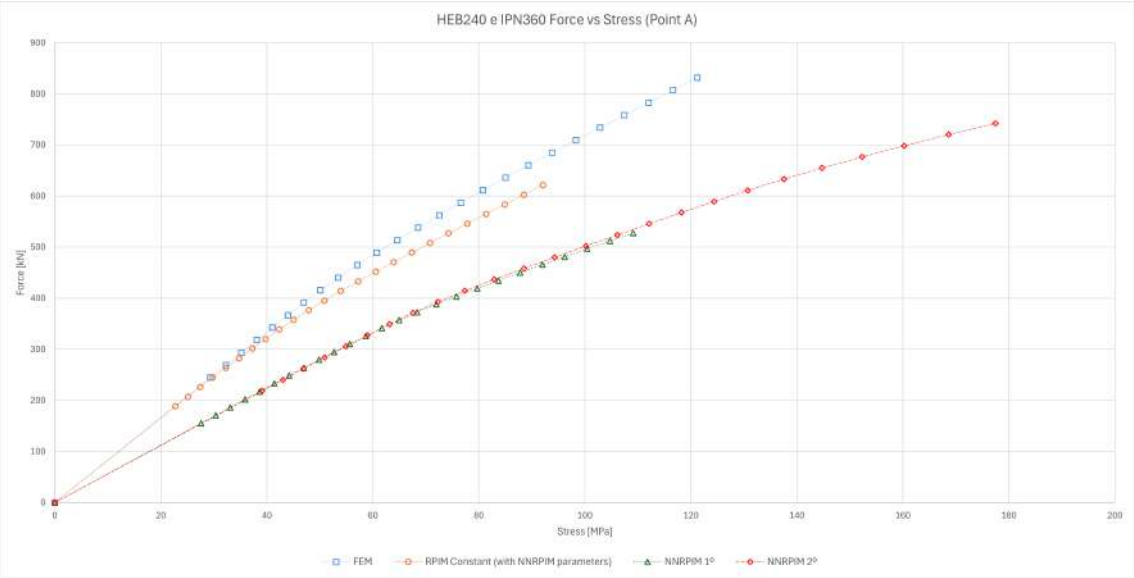

Figure 8.8: Graphic from point A of the third structure (HEB240 with IPN360), with the stress results

that the meshless methods' roles are reversed, which implies that the NNRPIM simulations have a very matched linear state with the FEM simulation, while the RPIM simulations offer an extremely high stiffness, making it significantly unreliable.

8.2.2 Point B

In the point B study, we will keep examining the stress computed during the different simulation methods.

Frame Structure HEB200 with IPN280

First, we can start by analyzing the first structure point B, and for that, we can see the simulations' methods results in figure 8.10. By continuing to analyze FEM as the industry standard, we conclude that for point B of the first structure, none of the meshless methods' simulations produce desirable results. The NNRPIM results overlap with each other, but they are considerably far from the FEM result, presenting even a stiffness considerably smaller. In the RPIM method case, we can see that, unlike the NNRPIM methods, the stiffness is higher than the FEM one, and the RPIM curve is also considerably far from the FEM one, not conceding an overlap.

Frame Structure HEB220 with IPN320

In the second structure analysis, presented in figure 8.11, we see that the results are more encouraging, with overlapping in the methods' FEM and RPIM. These two results are a perfect example of what is expected to overlap between any two methods. The NNRPIM methods offered us results that differ significantly from the other two, and as a consequence, diverge from the industry standard. It's possible

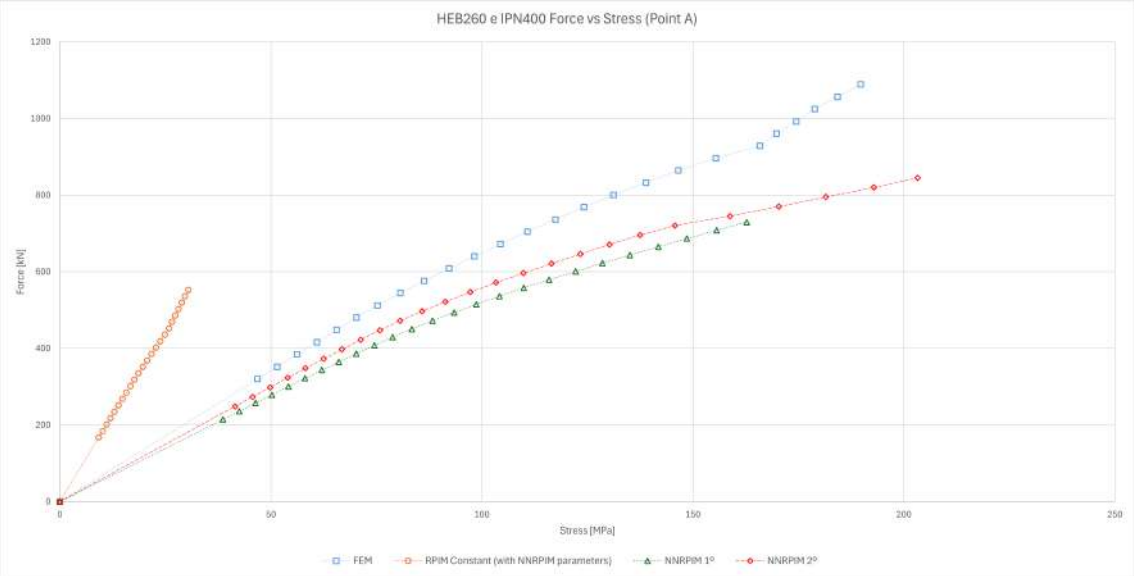

Figure 8.9: Graphic from point A of the fourth structure (HEB260 with IPN400), with the stress results

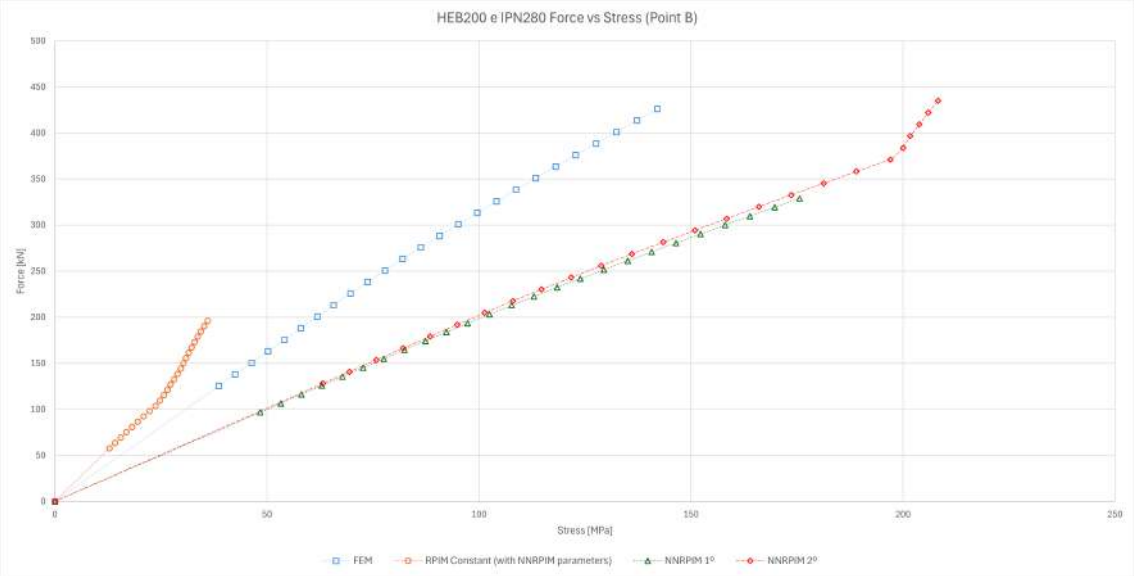

Figure 8.10: Graphic from point B of the first structure (HEB200 with IPN280), with the stress results

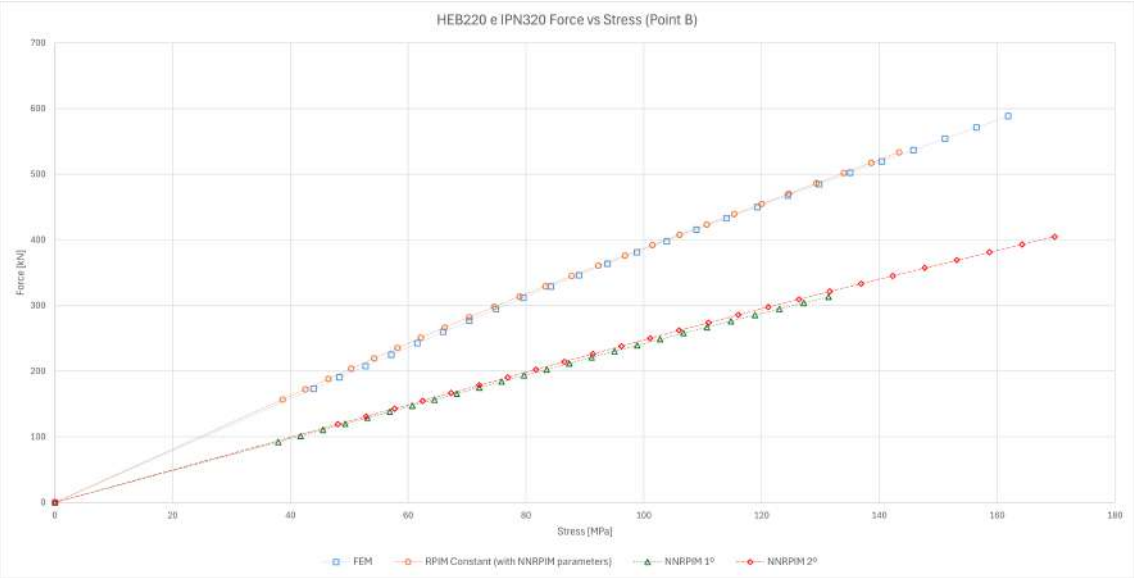

Figure 8.11: Graphic from point B of the second structure (HEB220 with IPN320), with the stress results

to observe that the stiffness is quite lower in comparison to the FEM and RPIM methods' stiffness.

Frame Structure HEB240 with IPN360

For the third structure, the results' conclusion achieved is the same as that achieved in the results from point B of the second structure, and it's easy to understand why when we observe the figure 8.12. We can observe an overlap between the FEM and RPIM simulation results, and we can see a considerable difference between the NNRPIM simulation results and the FEM and RPIM simulation results with the same differentiation characteristics.

Frame Structure HEB260 with IPN400

To finally finish the point B study, let's focus our attention on figure 8.13, where we can scrutinize the fourth structure results from point B. This fourth structure presents us with a different behavior in general. By keeping the FEM simulation as the industry standard, we can conclude that the NNRPIM methods offer a great improvement, being now much closer to the FEM method, almost generating an overlapping. On the contrary direction, we find that the fourth structure RPIM results are the worst, by having an exuberantly higher stiffness, completely discrediting the RPIM result.

8.2.3 Point D

At point D, we will proceed with the plastic strain analysis. The following figures, from 8.14 until 8.17, correspond to the force versus plastic strain graphic, from the first through fourth structures, respectively. A quick glance at these graphs shows that all the results are linear, exactly as expected.

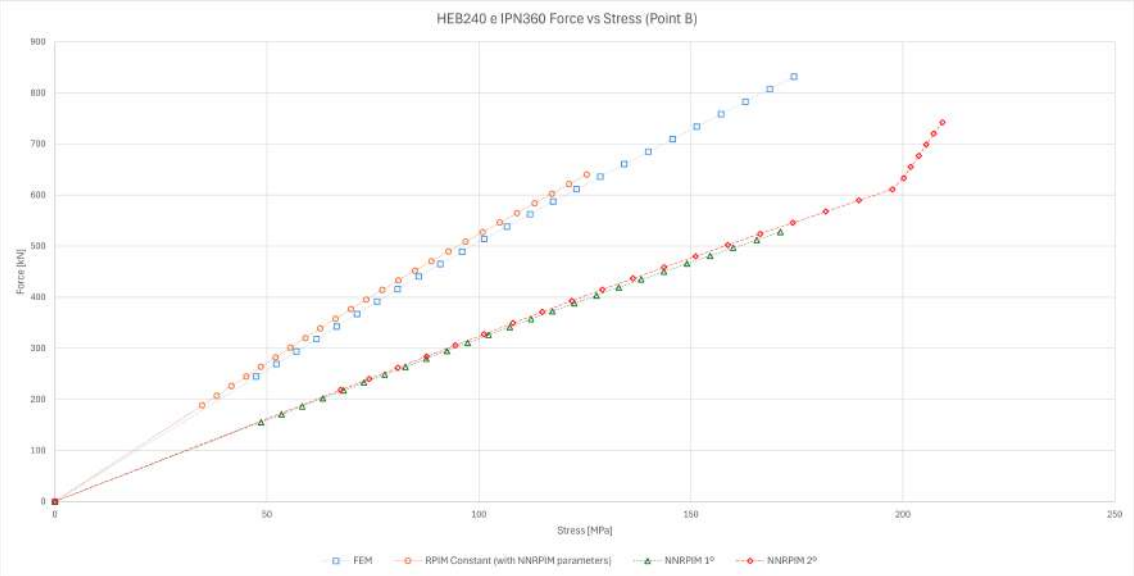

Figure 8.12: Graphic from point B of the third structure (HEB240 with IPN360), with the stress results

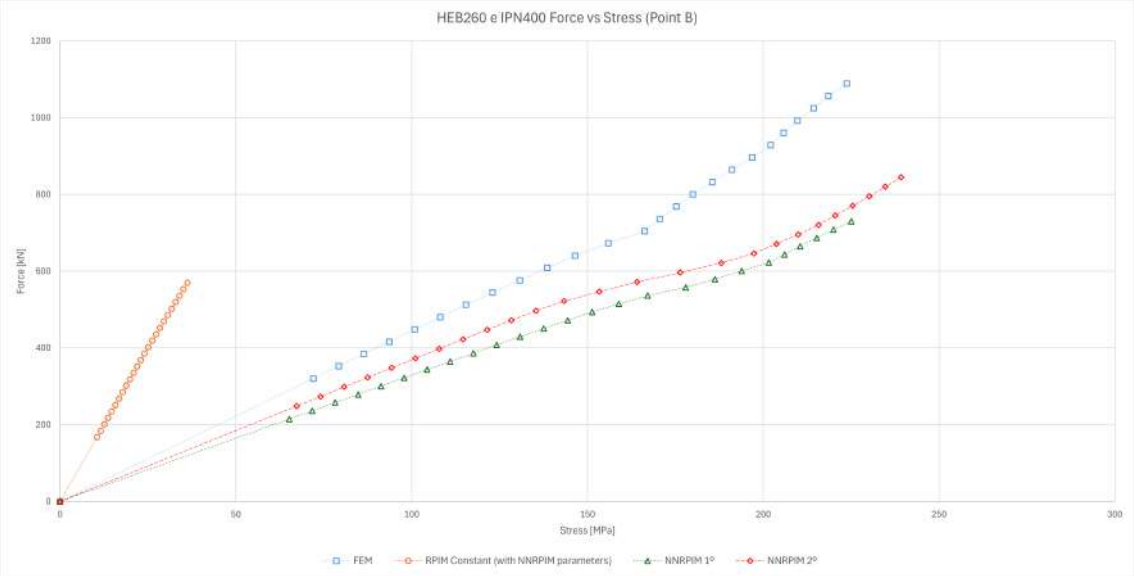

Figure 8.13: Graphic from point B of the fourth structure (HEB260 with IPN400), with the stress results

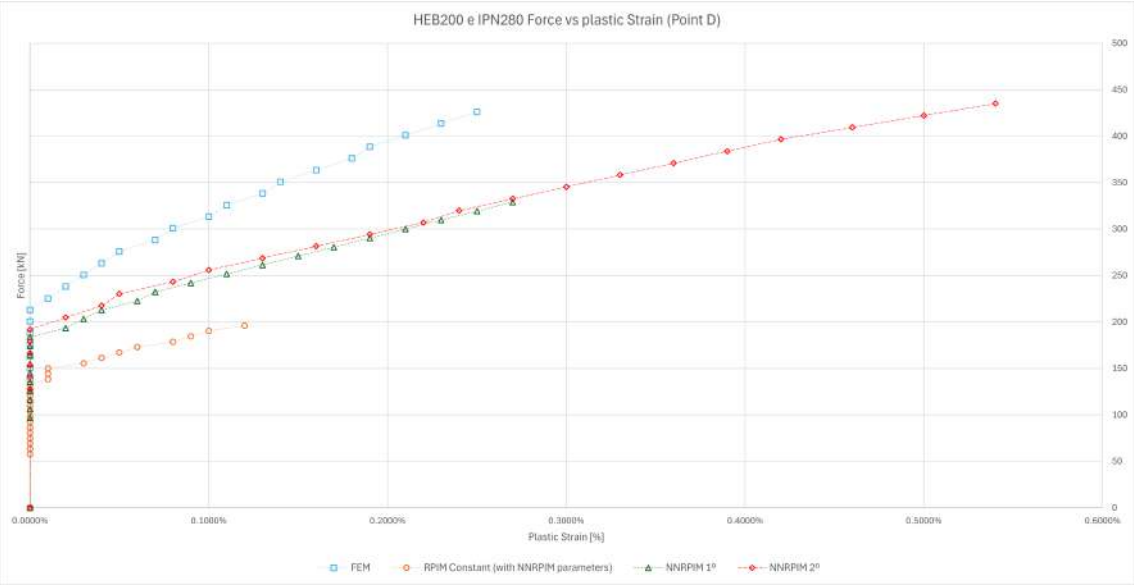

Figure 8.14: Graphic from point D of the first structure (HEB200 with IPN280), with the plastic strain results

Frame Structure HEB200 with IPN280

We begin the analysis of point D with the graphs from the first structure (figure 8.14), if we consider the FEM simulations as the industry standard and compare the other results to them, we observe that both NNRPIM simulations (first and second degree of neighborhood) are fairly close and similar to the FEM results. However, for the RPIM results, the similarity and closeness to the FEM results are not present in the first structure; the plastic strain is much lower than in the FEM and NNRPIM simulations. When compared to the FEM simulation's plastic strain results, we visualize that while FEM results don't enter a nonlinearity state, in point D, until the applied force is superior to 200 kN, on the other hand, the same state is acquired in the RPIM simulations, well below 150 kN of the applied load. We can also observe that for the RPIM simulation, the point D plastic deformation doesn't change during 3 iterations, even with the load increment; that's likely due to a small numerical volumetric issue known as "plato". It's important to point out that even though the two methods' simulations FEM and NNRPIM are relatively close, they don't overlap, and that indicates that there is still space for convergence and improvement.

Frame Structure HEB220 with IPN320

The second structure yields very similar results on all the elaborated simulations. The graphic from the second structure is presented in figure 8.15 and shows us that all simulations produce very similar results, with the RPIM simulation being even closer to the FEM simulation than the NNRPIM simulation, which is the opposite of what was observed in the first structure analysis. The difference between the NNRPIM simulations and the FEM simulation is very similar to that previously observed in the first structure (HEB280 with IPN320), and that means an incredible (comparatively) approximation from the results present in figure 8.14 to the results

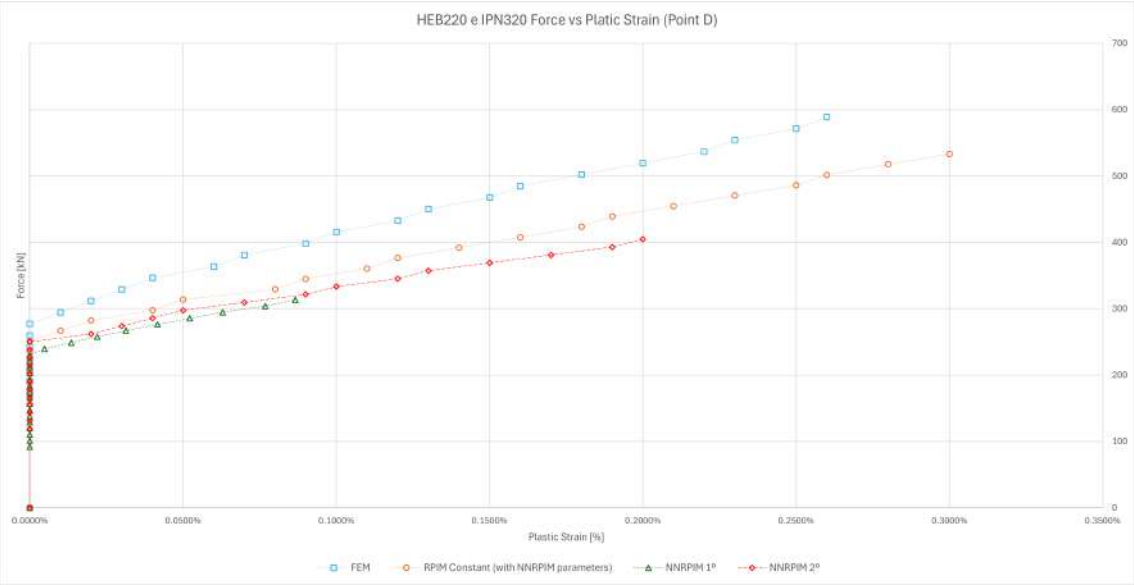

Figure 8.15: Graphic from point D of the second structure (HEB220 with IPN320), with the plastic strain results

obtained in the second structure. Despite the similarities, the simulation's behaviors aren't, just like in the first structure, considered equals.

Frame Structure HEB240 with IPN360

Analyzing now the point's D plastic strain, we can visually identify the behavioral similarities with the results obtained in the previous structure (HEB220 with IPN320). Once again, we have the same three methods' simulations moderately close, without overlap between the meshless methods' results with the FEM results. The plastic strain results can be observed in the graphic presented in figure 8.16.

Frame Structure HEB260 with IPN400

To complete the point D study, from the frame structure, we can observe figure 8.17, where it is visible that the graphic corresponds to the last structure. This graphic presents us with a behavior more similar to the first structure, where the three methods have significant differences, with the NNRPIM simulations being the ones closest to the FEM simulation. Once again, we can observe that the RPIM method's results are extremely distant from the industry norm (FEM method).

8.2.4 Point F

At point F, we will observe and analyze the displacement present in this point with respect to the three discussed methods. The following figures, from 8.18 to 8.21, correspond to the first through the fourth structures, respectively, and show the force versus displacement graphs for point F.

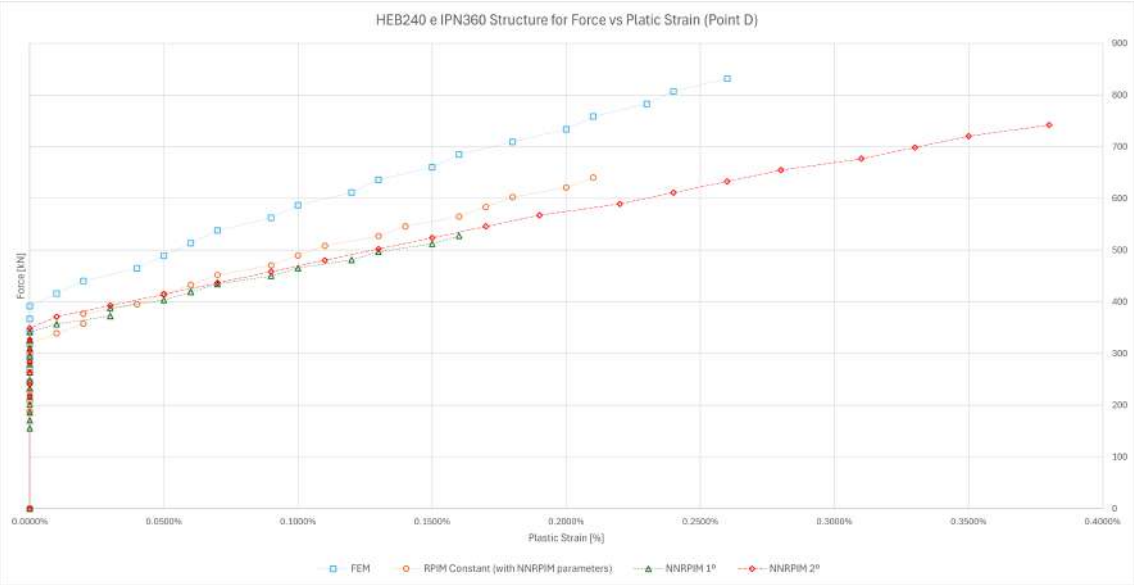

Figure 8.16: Graphic from point D of the third structure (HEB240 with IPN360), with the plastic strain results

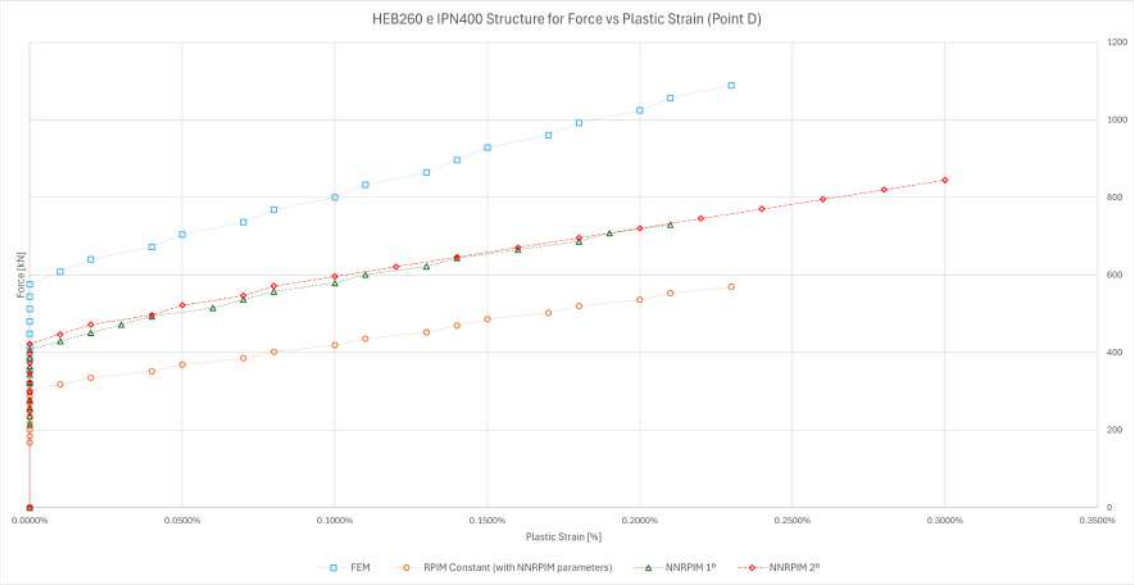

Figure 8.17: Graphic from point D of the fourth structure (HEB260 with IPN4000), with the plastic strain results

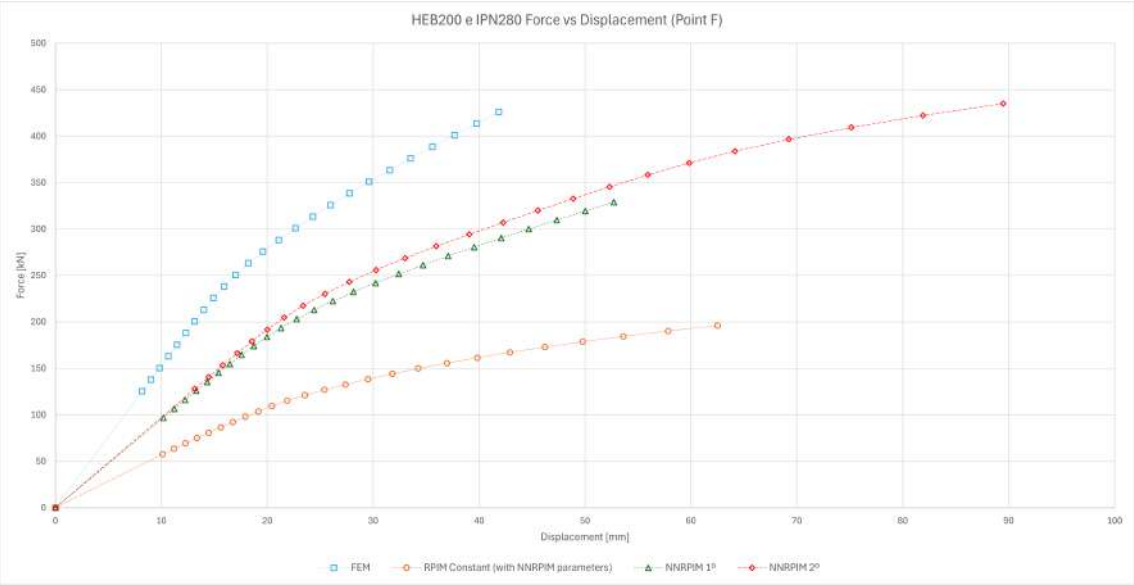

Figure 8.18: Graphic from point F of the first structure (HEB200 with IPN280), with the displacement results

8.2.5 Frame Structure HEB200 with IPN280

For point F in the first structure, we observe that the RPIM simulation curve is much farther from the FEM curve, not in terms of the final displacement achieved, but in the force required to reach the same displacement—significantly less force is needed in the RPIM simulation. In the NNRPIM simulation results, the curves are much closer to the FEM curve, however, even these simulations aren't close enough to the industry standard, the FEM method. It is worth highlight that the two NNRPIM simulations are very close to each other, as expected. The graph in question can be seen in figure 8.18.

8.2.6 Frame Structure HEB220 with IPN320

Analyzing the results for the second structure at point F, we notice that all simulations produce much closer results, with all the graph curves occupying roughly the same space. In these cases, the RPIM simulation is closest to the FEM curve, with the NNRPIM simulations being slightly apart, but still occupying a close space, compared to the first structure. Nevertheless, there are some differences between the NNRPIM simulation results and the other two. We can observe that the two NNRPIM simulations basically overlap each other, and the RPIM and FEM simulations are very close to each other. This means that, compared to the FEM simulation, the RPIM result is the one that came closest to the FEM results, in a contrary direction to what occurred in the first structure results.

8.2.7 Frame Structure HEB240 with IPN360

Figure 8.20 shows us the displacement on point F for the third structure. In this image, we can observe the similarities with the previous analysis of the second structure (HEB220 with IPN320), with the big difference being the discrepancy

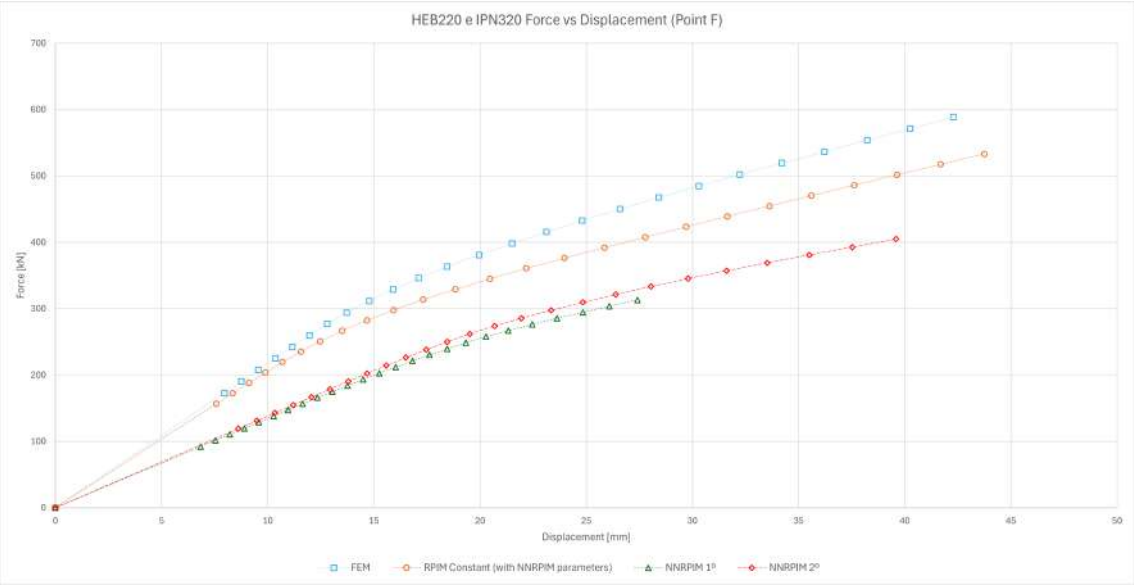

Figure 8.19: Graphic from point F of the second structure (HEB220 with IPN320), with the displacement results

between the NNRPIM simulations with the FEM and the RPIM simulation, which has increased.

Frame Structure HEB260 with IPN400

To finalize the point F study, let's direct our attention to the figure 8.21, where we can observe the fourth structure graphic for the point F displacement. In the graphic analysis, we can observe that the RPIM simulation stopped being the closest to the FEM simulation and started being the one with the most different result. The difference between the FEM results and the NNRPIM results is very considerable, and the difference between the NNRPIM simulations and the RPIM simulation is also remarkably considerable, which means that the RPIM result is exorbitantly different from the industry standard, and none of the meshless methods' simulation results are relatively close to the FEM one.

8.2.8 Point H

To conclude these studies, we now move to the analysis of point H, where we will again focus on displacement. The following figures, from 8.22 to 8.25, correspond to the first through fourth structures, respectively, and all the curves exhibit downward concavity. A quick analysis of these graphs shows that the results for the second and third structures are very similar.

Frame Structure HEB200 with IPN280

In the first structure, we can see that the NNRPIM curves are much closer to the FEM curve than the RPIM one, even though the NNRPIM curves are still significantly away from the FEM curve. That indicates that the RPIM results are grossly away from the expected ones. The NNRPIM results are very closely matched,

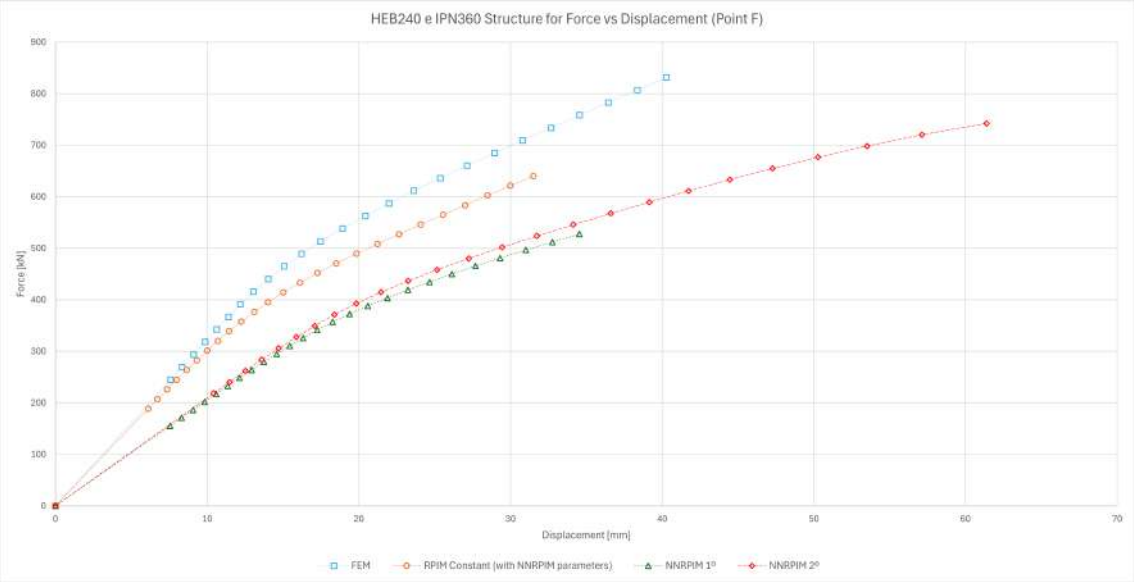

Figure 8.20: Graphic from point F of the third structure (HEB240 with IPN360), with the displacement results

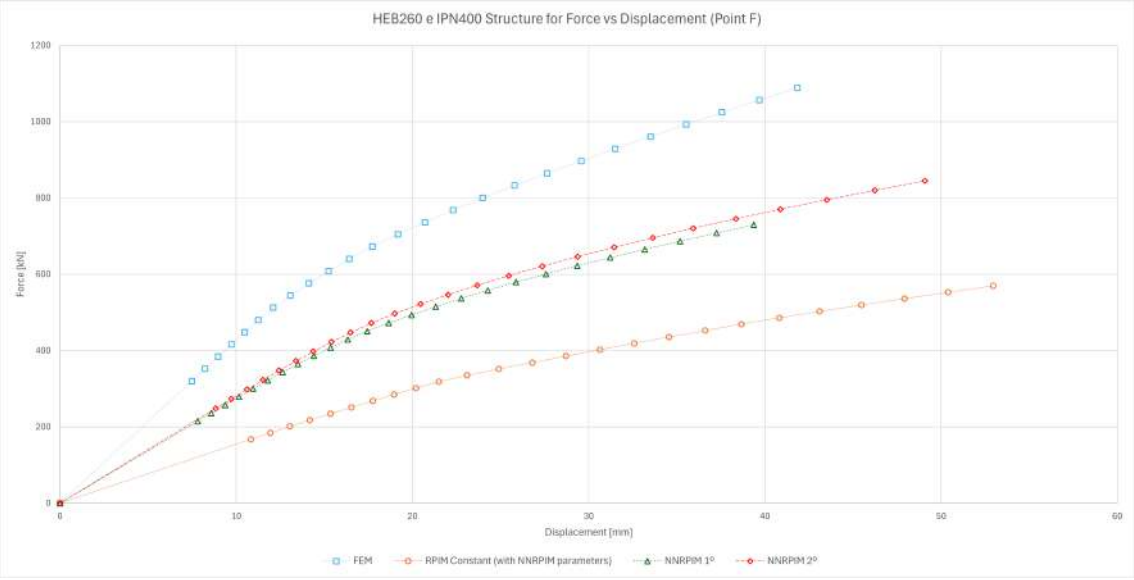

Figure 8.21: Graphic from point F of the fourth structure (HEB260 with IPN4000), with the displacement results

Figure 8.22: Graphic from point H of the first structure (HEB200 with IPN280), with the displacement results

meaning that we can consider the two results as an overlap. Additionally, the concavity of the RPIM curve is visually more distinct from the other three, appearing to approach its mathematical limit, while the FEM curve is clearly far from it. Another interesting point is that the only method with a similar applied force, in the last iteration, to the FEM simulation is the NNRPIM of second order. The difference is that, unlike FEM simulation, the NNRPIM simulations in discussion are closing their mathematical limit. These results and visual conclusions can be observed in figure 8.22.

Frame Structure HEB220 with IPN320

In the second structure, all the curves from the different simulations occupy roughly the same space, with the RPIM curve being closest to the FEM curve and the NNRPIM curves positioned considerably below the FEM and RPIM curves, as is possible to observe in figure 8.23. We can conclude, then, that for this point, in the second structure, the RPIM almost overlaps the FEM method, providing us with a more expected result. It is worth mentioning that NNRPIM simulations are, again, a very close match, overlapping each other, just like we have seen in this study.

Frame Structure HEB240 with IPN360

Analysing now results of the third structure, presented in figure 8.24, we can observe that the RPIM simulation's result is close to the FEM simulation result. The NNRPIM simulations are not very similar to the RPIM and FEM ones, presenting us with higher deflections to the same applied force level. Once again, the NNRPIM simulation gives us an overlapping sensation, maintaining the norm throughout the study (so far).

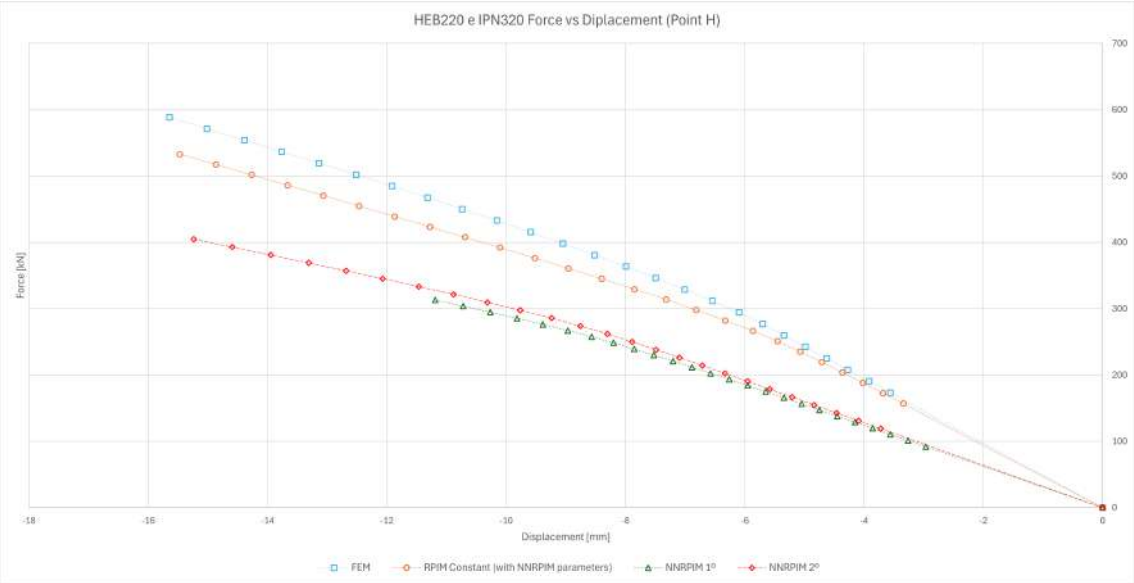

Figure 8.23: Graphic from point H of the second structure (HEB220 with IPN320), with the displacement results

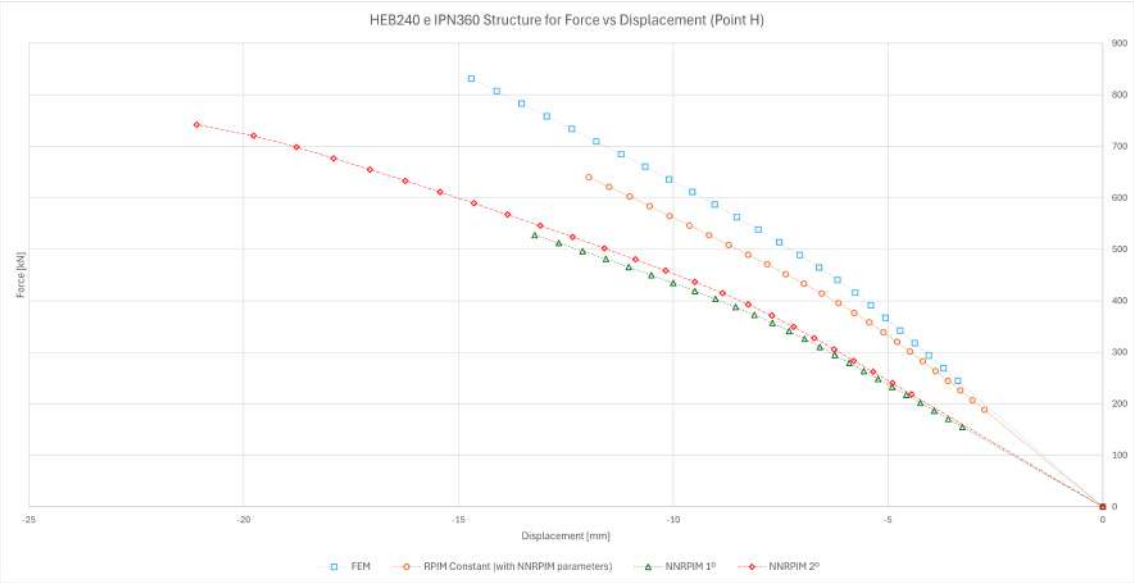

Figure 8.24: Graphic from point H of the third structure (HEB240 with IPN360), with the displacement results

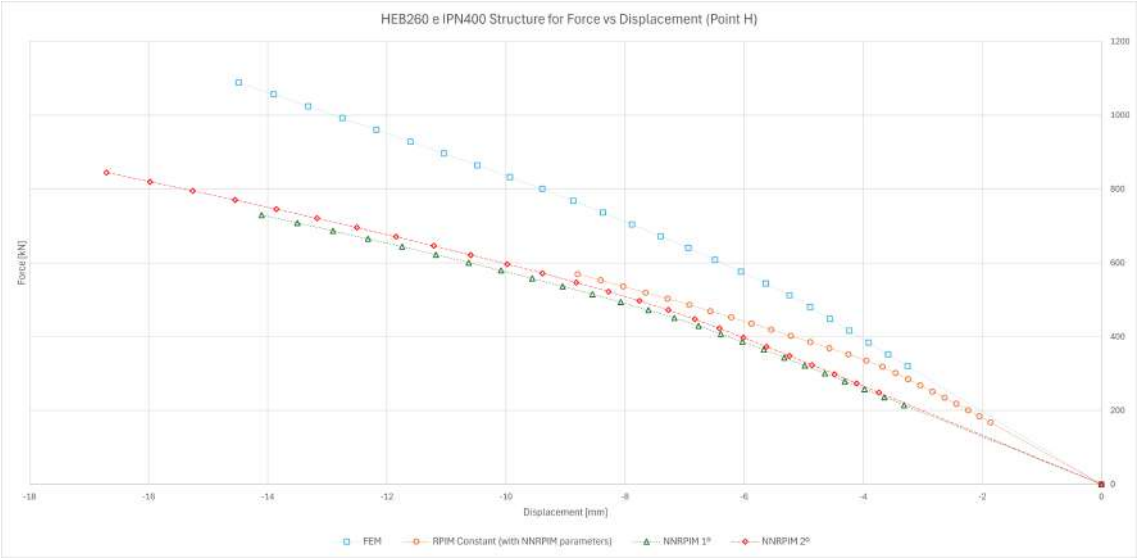

Figure 8.25: Graphic from point H of the fourth structure (HEB260 with IPN4000), with the displacement results

Frame Structure HEB260 with IPN400

And finally, to finish the graphics analysis, let's turn our awareness to the final graph present in figure 8.25. In this image, we are capable of finding a difference between the RPIM behaviors that occurred so far, and the RPIM behavior present in figure 8.25. The other three methods present to us the same behavior present throughout the study; that is, the NNRPIM curves are overlapping each other but don't occupy the same graphical space as the FEM curve. The RPIM method presents us with a behavior change, as already discussed, because its curve starts overlapping the FEM method's curve, but ends up overlapping the NNRPIM methods' curves, something that is new in the displacement analysis.

8.3 Conclusions

This study shows us certain discrepancies between the meshless methods' results compared to the FEM results; however, there are some reasonable explanations for these deviations.

For the first structure (HEB200 with IPN280) results, we can conclude that the meshless methods presented some discrepancies, with the RPIM results revealing less agreement than the NNRPIM results. However, it is important to mention that even though the NNRPIM simulations show us better results than the RPIM simulation result, it wasn't good enough to overlap with the FEM simulation result. One potential way to address these discrepancies in the obtained results could be to modify the method's basis functions from constant or linear to quadratic. These modifications would increase the calculation time and computation resources spent.

For the second structure (HEB220 with IPN320), it is possible to see an improvement in the RPIM simulation result. The RPIM curves overlapped the FEM curves

on several occasions, and that indicates a strong reliability sentiment. The NNRPIM simulations have a little discrepancy but maintain a certain consistency when compared with the first structure.

In the third structure (HEB240 with IPN360), we can conclude the same as in the second structure, with an RPIM simulation's result being very promising and with the NNRPIM simulations' results not exactly on a FEM or RPIM methods level.

In the fourth and final structure (HEB260 with IPN400), the RPIM simulation became, once again, with more discrepancy than the NNRPIM simulations. The NNRPIM simulations' results almost overlap the FEM simulation's results, in some cases. The RPIM result in question completely fails to mimic the FEM or even the NNRPIM results.

Overall, we can see that the NNRPIM was the meshless method's most consistent, having almost overlapping the FEM method in some cases, and the RPIM method was capable of mimicking and overlapping the FEM method in some simulations. This proves that the meshless methods have the potential to give precise results that can be trusted when properly used. A possible solution to fix the noted discrepancies is to simply increase the number of nodes and elements, improving the mesh; however, this possible fix creates a computational cost and requires more time, energy, and computation power.

9 Conclusion

During this work, we performed linear and nonlinear simulations with FEM and meshless methods, with the goal of show that the meshless methods can be an interesting, trustworthy, and precise alternative to the FEM, for that we analyze the performance, accuracy, and applicability of the studied meshless methods RPIM and NNRPIM comparatively to FEM.

In chapter 5, with the linear simulation results, we demonstrate that the number of nodes is correlated with the precision, accuracy, and veracity of the results, which means that a more refined mesh will offer us a better solution for our problem. This conclusion is valid for all the simulation methods used in the study (FEM, RPIM, and NNRPIM). This conversion mesh refinement/relation is perfectly normal and expected, which indicates that the chapter 5 studies were correctly elaborated. This accuracy solution came with a price; the bigger the mesh size, the more costly the simulation. As we know, the mesh size is directly correlated with the computational cost, which means that a compromise is necessary to prevent a simple simulation requiring an incredible, and expensive, computer that will cost more to run than a regular one. So the goal is to select an appropriate mesh size for each problem, which, due to the conversion occurring, will not compromise the simulated results.

The nonlinear study done in chapter 6 includes Cook's Membrane problem and beams studies in two and three dimensions. It's pertinent to remember that the beams' RPIM simulations with RPIM parameters were considered unreliable due to their suboptimal results, which forced us to redo the RPIM simulations with NNRPIM parameters, ending in much better simulation results. In Cook's Membrane problem, we tested the KT0, KT1, and KT-ALL algorithms, where we corroborated KT-ALL is the most precise algorithm, confirming the theoretical assumption made in chapter 3.

Focus our attention now on the nonlinear 3D and 2D simulations present in the same chapter. We can observe a remarkable similarity between all the simulations, with the already explained and replaced exception. The meshless simulation results, compared to the FEM ones, provide us with relatively lower percentual discrepancies in stress values, while the strain and displacement values are significantly bigger, being in some cases, extremely higher. However, it's important to highlight that the graphics visual analysis from the figures present in subchapter 6.2 is more important than the percentual values. If the simulation curves overlapped with the industry standard (FEM simulation curve), we can conclude that the simulations were extremely successful. Another conclusion from this chapter was that the 3D simulations often produce narrower, more load values and slightly less stress than the 2D simulations; however, the difference is so insignificant that, in fact, we can

consider the 2D simulations as accurate, precise, and trustworthy as the 3D simulations.

In chapter 7, we can observe the simulation of an existing study that provided us with a structure and simulation results that were essential to the FEMAS software confirmation. This study provided us with overlapping linear analysis with all the simulations, which proves the accuracy of FEMAS and validates it.

The frame structure analysis chapter 8 provided us with four frame structure results in simulations with the FEM and meshless methods, where the mesh complexity is visibly bigger than the 2D previous simulations. In this analysis, we found certain discrepancies between the meshless methods simulations and the FEM simulation that we didn't intend. The first and fourth structures present us with RPIM simulations with a significant discrepancy to the FEM results. With the NNRPIM, the meshless method more closely related to the FEM solutions, even though the NNRPIM did not exactly overlap with the FEM result. In the second and third solutions, the meshless method types' roles changed, which means that the RPIM solutions were closer to the FEM one than the NNRPIM solutions. It's important to state that the NNRPIM maintained the same discrepancy to the FEM solution that it had in the first and fourth frame structures' results, which implies that it was the RPIM method that improved its behavior. After these observations, we can confirm that the meshless method was more consistent with the NNRPIM one; it didn't provide us with the expected overlapping results, but it was constant in its results. The RPIM simulations, on the other hand, were capable of providing very good results but were also very inconsistent, being capable of providing bad solutions as well. To mitigate these nonoverlapping solutions, we could try to increase the mesh refinement and study its effects.

During this work, we achieve several important conclusions:

- we demonstrate the natural convergence between the three used methods (FEM, RPIM, and NNRPIM), showing the accuracy and precision of the meshless methods;
- we show comparative results between the nonlinear meshless methods and FEM with significant areas of conversion, proving once again that the meshless methods are trustworthy;
- we show a 2D with 3D simulations comparison, showing results overlapping for the same simulations in the different dimensions;
- the FEMAS software proved to be reliable and accurate during this work;
- finally, we see that the meshless methods have the potential to provide us with good results even for complex frame structures, even though they didn't give us the expected behavior, we could conclude that there are strong indications of their validity.

The possible next steps for the continuation of these problems can be:

- optimization of the meshless methods parameters for different structures;
- use adaptive nodal distribution to achieve more satisfactory results;
- including large deformations as a next step;
- including large deformations with elastoplasticity;
- use these methods to study possible rupture or plastic deformed zones, such as welding zones, or rivets and screws applied to holes.

References

[1] J. Belinha, Ed., *Meshless Methods in Biomechanics, Bone Tissue Remodelling Analysis*. Porto: Springer, 2014.

[2] J. A. Belinha, "Análise elasto-plástica considerando o método livre de elementos de galerkin," Master's thesis, Faculdade de Engenharia da Universidade do Porto, Porto, 2004.

[3] S. Dastjerdi, A. Alibakhshi, B. Akgoz, and Ömer Civalek, "A novel nonlinear elasticity approach for analysis of nonlinear and hyperelastic structures," *Engineering Analysis with Boundary Elements*, vol. 143, pp. 219–236, 2022.

[4] S. F. Moreira, "Elastoplastic analysis using the natural neighbour radial point interpolation method," Master's thesis, Faculdade de Engenharia da Universidade do Porto, Porto, 2013.

[5] R. A. . A. Kassimali, "Large deformation elastic-plastic analysis of space frames," *Constructional Steel Research*, vol. 35, no. 3, pp. 275–290, 1995.

[6] Available at https://www.hierroyacero.site/perfil-ipn/, (Last accessed in 06/06/2025).

[7] Available at https://www.hierroyacero.site/perfil-heb/, (Last accessed in 06/06/2025).

[8] B. Nayroles, G. Touzot, and P. Villon, "Generalizing the finite element method: Diffuse approximation and diffuse elements," *Computational Mechanics*, vol. 10, no. 5, pp. 307–318.

[9] T. Belytschko, Y. Krongauz, D. Organ, M. Fleming, and P. Krysl, "Meshless methods: An overview and recent developments," *Computer Methods in Applied Mechanics and Engineering*, vol. 139, pp. 3–47, 1996.

[10] Y. T. Gu, "Meshfree methods and their comparisons," *International Journal of Computational Methods*, vol. 2, no. 4, pp. 477–515, 2005.

[11] P. W. Randles and L. D. Libersky, "Smoothed particle hydrodynamics: Some recent improvements and applications," *Computer Methods in Applied Mechanics and Engineering*, vol. 139, pp. 375–408, 1996.

[12] V. P. Nguyen, T. Rabczuk, S. Bordas, and M. Duflot, "Meshless methods: A review and computer implementation aspects," *Mathematics and Computers in Simulation*, vol. 79, pp. 763–813, 2008.

[13] J. J. Monaghan, "Smoothed particle hydrodynamics: Theory and applications to non-spherical stars," *Monthly Notices of the Royal Astronomical Society*, vol. 181, pp. 375–389, 1977.

[14] L. D. Libersky and A. G. Petschek, "Smoothed particle hydrodynamics with strength of materials," in *The Next Free Lagrange Conference*, 1991, pp. 248–257.

[15] T. Belytschko, Y. Y. Lu, and L. Gu, "Element-free galerkin methods," *International Journal for Numerical Methods in Engineering*, vol. 37, pp. 229–256, 1994.

[16] P. Lancaster and K. Salkauskas, "Surfaces generation by moving least squares methods," *Mathematics of Computation*, vol. 37, pp. 141–158, 1981.

[17] W. K. Liu, S. Jun, S. Li, J. Adee, and T. Belytschko, "Reproducing kernel particle methods for structural dynamics," *International Journal for Numerical Methods in Engineering*, vol. 38, pp. 1655–1679, 1995.

[18] Z. T. Atluri, "A new meshless local petrov–galerkin (MLPG) approach in computational mechanics," *Computational Mechanics*, vol. 22, no. 2, pp. 117–127, 1998.

[19] B. Xu, R. Zhang, K. Yangb, G. Yua, and Y. Chenab, "Application of generalized finite difference method for elastoplastic torsion analysis of prismatic bars," *Engineering Analysis with Boundary Elements*, vol. 146, pp. 939–950, 2023.

[20] Y. Belaasilia, A. Timesl, B. Braikat, and M. Jamala, "A numerical mesh-free model for elasto-plastic contact problems," *Engineering Analysis with Boundary Elements*, vol. 82, pp. 68–78, 2017.

[21] X. L. Xin Xu, Zhenzhou Lu, "A numerical meshless method of soliton-like structures model via an optimal sampling density based kernel interpolation," *Computer Physics Communications*, vol. 192, pp. 12–22, 2015.

[22] L. M. J. S. Dinis, R. M. Natal Jorge, and J. Belinha, "Analysis of 3d solids using the natural neighbour radial point interpolation method," *Computer Methods in Applied Mechanics and Engineering*, vol. 196, pp. 2009–2028, 2007.

[23] K. M. Liew, X. Zhao, and A. J. M. Ferreira, "A review of meshless methods for laminated and functionally graded plates and shells," *Composite Structures*, vol. 93, pp. 2031–2041, 2011.

[24] G. R. Liu and Y. T. Gu, "A point interpolation method for two-dimensional solids," *International Journal for Numerical Methods in Engineering*, vol. 50, pp. 937–951, 2001.

[25] J. G. Wang, G. R. Liu, and Y. G. Wu, "A point interpolation method for simulating dissipation process of consolidation," *Computational Methods in Applied Mechanics and Engineering*, vol. 190, pp. 5907–5922, 2001.

[26] J. G. Wang and G. R. Liu, "A point interpolation meshless method based on radial basis functions," *International Journal for Numerical Methods in Engineering*, vol. 54, pp. 1623–1648, 2002.

[27] ——, "On the optimal shape parameters of radial basis functions used for 2-d meshless methods," *Computational Methods in Applied Mechanics and Engineering*, vol. 191, pp. 2611–2630, 2002.

[28] J. Braun and M. Sambridge, "A numerical method for solving partial differential equations on highly irregular evolving grids," *Nature*, vol. 376, pp. 655–660, 1995.

[29] N. Sukumar, B. Moran, A. Y. Semenov, and V. V. Belikov, "Natural neighbour galerkin methods," *International Journal for Numerical Methods in Engineering*, vol. 50, pp. 1–27, 2001.

[30] S. R. Idelsohn, E. Onate, N. Calvo, and F. Del Pin, "The meshless finite element method," *International Journal for Numerical Methods in Engineering*, vol. 58, pp. 893–912, 2003.

[31] J. Belinha, L. M. J. S. Dinis, and R. M. Natal Jorge, "The natural radial element method," *International Journal for Numerical Methods in Engineering*, vol. 93, pp. 1286–1313, 2013.

[32] ——, "Composite laminated plate analysis using the natural radial element method," *Composite Structures*, vol. 103, pp. 50–67, 2013.

[33] L. M. J. S. Dinis, R. M. Natal Jorge, and J. Belinha, "Large deformation applications with the radial natural neighbours interpolators," *Computer Modelling in Engineering and Sciences*, vol. 44, pp. 1–34, 2009.

[34] J. Belinha, R. M. Natal Jorge, and L. M. J. S. Dinis, "A meshless microscale bone tissue trabecular remodelling analysis considering a new anisotropic bone tissue material law," *Computer Methods in Biomechanics and Biomedical Engineering*, 2012.

[35] L. M. J. S. Dinis, R. M. Natal Jorge, and J. Belinha, "Analysis of plates and laminates using the natural neighbour radial point interpolation method," *Engineering Analysis with Boundary Elements*, vol. 32, pp. 267–279, 2008.

[36] ——, "Static and dynamic analysis of laminated plates based on an unconstrained third order theory and using a radial point interpolator meshless method," *Computers and Structures*, vol. 89, pp. 1771–1784, 2011.

[37] ——, "An unconstrained third-order plate theory applied to functionally graded plates using a meshless method," *Mechanics of Advanced Materials and Structures*, vol. 17, pp. 1–26, 2010.

[38] ——, "A 3d shell-like approach using a natural neighbour meshless method: Isotropic and orthotropic thin structures," *Composite Structures*, vol. 92, pp. 1132–1142, 2010.

[39] ——, "Composite laminated plates: A 3d natural neighbour radial point interpolation method approach," *Journal of Sandwich Structures and Materials*, vol. 12, pp. 119–138, 2010.

[40] ——, "The natural neighbour radial point interpolation method: Dynamic applications," *Engineering Computations*, vol. 26, pp. 911–949, 2009.

[41] ——, "The dynamic analysis of thin structures using a radial interpolator meshless method," in *Vibration and Structural Acoustics Analysis*, C. Vasques and J. Rodrigues, Eds. Springer, 2011.

[42] D. C. Gonçalves, "Structural optimization algorithms combined with advance discretization meshless techniques - a review," Master's thesis, ISEP - School of Engineering, Porto, 2020.

[43] B. V. Farahani, J. M. Berardo, R. Drgas, J. M. C. de Sá, A. J. Ferreira, and J. Belinha, "The axisymmetric analysis of circular plates using the radial point interpolation method," *International Journal for Computational Methods in Engineering Science and Mechanics*, vol. 16, no. 6, pp. 336–353, 2015.

[44] T. I. E. Sanjukta Das, "A meshless weak strong form method for the groundwater flow simulation in an unconfined aquifer," *Engineering Analysis with Boundary Elements*, vol. 137, pp. 147–159, 2022.

[45] D. Gonçalves, I. Sanchez-Arce, L. Ramalho, R. Campilho, and J. Belinha, "Fracture propagation based on meshless method and energy release rate criterion extended to the double cantilever beam adhesive joint test," *Theoretical and Applied Fracture Mechanics*, vol. 112, 2022.

[46] J. M. C. A. L. M. J. S. D. J. Belinha and R. M. N. Jorge, "The natural neighbor radial point interpolation method in computational fracture mechanics: A 2d preliminary study," *Journal of Computational Methods*, vol. 14, no. 4, 2017.

[47] S. F. Moreira, J. belinha, L. M. J. S. Dinis, and R. M. N. Jorge, "The anisotropic elasto-plastic analysis using a natural neighbour rpim version," *The Brazilian Society of Mechanical Sciences and Engineering*, 2016.

[48] J. Belinha, A. Araújo, A. Ferreira, L. Dinis, and R. N. Jorge, "The analysis of laminated plates using distinct advanced discretization meshless techniques," *Composite Structures*, vol. 143, pp. 165–179, 2016.

[49] R. N. J. Ana Guerra, Jorge Belinha, "Using a meshless method to assess the effect of mechanical loading in angiogenesis," *Mathematics and Computers in Simulation*, vol. 202, pp. 421–441, 2022.

[50] V. M. da Costa Ferreira, "Optimização da forma de uma estrutura usando um método sem malha," Master's thesis, Faculdade de Engenharia da Universidade do Porto, Porto, 2012.

[51] M. C. Aires, "Elastoplastic analysis of 2d and 3d structural elements using meshless methods," Master's thesis, Faculdade de Engenharia da Universidade do Porto, Porto, 2019.

[52] J. M. C. Azevedo, "Fracture mechanics using the natural neighbour radial point interpolation method," Master's thesis, Faculdade de Engenharia da Universidade do Porto, Porto, 2013.

[53] M. A. Crisfield, Ed., *Non-linear Finite Element Analysis of Solids and Structures - VOLUME 1: ESSENTIALS.* Chichester: JOHN WILEY & SONS, 2000.

[54] J. K. Bathe, Ed., *Finite Element Procedures in Engineering Analysis.* New Jersey: Prentice-Hall, 1982.

[55] N. A. M. F. P. Nascimento, "Numerical and experimental analysis of polymeric foams obtained by 3d printing (additive manufacturing)," Master's thesis, Faculdade de Engenharia da Universidade do Porto, Porto, 2019.

[56] J. A. O. P. Belinha, "The natural neighbour radial point interpolation method," PhD thesis, Faculdade de Engenharia da Universidade do Porto, Porto, 2010. [Online]. Available: https://repositorio-aberto.up.pt/handle/10216/57990

[57] H. Li and S. S. Mulay, Eds., *Meshless Methods and their Numerical Properties.* New York: CRC Press, 2013.

[58] "Science direct," Available at https://www.sciencedirect.com/, Jan. 2023, (Last accessed in 15/06/2025).

[59] Y. K.M.Liew, T.Y.Ng, "Meshfree method for large deformation analysis–a reproducing kernel particle approach," *Engineering Structures*, vol. 24, no. 5, pp. 543–551, 2002.

[60] R. C. Hibbeler, Ed., *Mechanics of materials*, 10th ed. Hoboken, New Jersey: Pearson, 2015.

[61] W. DS Simulia Abaqus 2016, "W3C – Cook's membrane problem," Available at http://130.149.89.49:2080/v2016/books/bmk/default.htm?startat=ch02s01ach142.html, Apr. 2005, (Last accessed in 25/05/2025).

Declaração de Integridade

Declaro ter conduzido este trabalho académico com integridade. Não plagiei ou apliquei qualquer forma de uso indevido de informações ou falsificação de resultados ao longo do processo que levou à sua elaboração. Declaro que o trabalho apresentado neste documento é original e de minha autoria, não tendo sido utilizado anteriormente para nenhum outro fim. Declaro ainda que tenho pleno conhecimento do Código de Conduta Ética do P.PORTO Instituto Superior de Engenharia do Porto (ISEP),

Hugo Daniel Pereira Torres

Porto, 14 de setembro de 2025